

ISSN 0911-5730

UVSOR-45

August 2018

UVSOR ACTIVITY REPORT 2017

UVSOR Synchrotron Facility
Institute for Molecular Science
National Institutes of Natural Sciences

UVSOR II
since 2012



Preface

This Activity Report covers scientific and technological activities carried out using the UVSOR-III Synchrotron in FY2017 (April 2017-March 2018). We present examples of how the users study at the UVSOR Synchrotron Facility.

The present UVSOR-III Synchrotron is one of the most advanced low-energy SR facilities of the 3rd generation SR in the world and is now one of the critical resources in doing molecular science. The UVSOR-III Synchrotron has a small electron storage ring but has powerful 6-undulator beamlines (3 VUV and 3 in-vacuum soft X-ray undulators) with 8-dipole beamlines. We never stop improving and upgrading our micro- and nano-scale photoabsorption and photoemission approaches and in situ/operando measurements in the VUV and soft X-ray regions, based on our strategic international collaboration program in molecular science. We are grateful to all the people who use our facility and support our efforts.

The total number of users is about 1,200 people/year; this means ca. 100 people/beamline/year and ca. 30 people/week. Most users stay for one or two weeks for the experiment. To continue high-level achievements in science and technology at the UVSOR-III Synchrotron, we in-house staff are always working hard to maintain and improve our high-performance accelerators and beamlines. The FY2018



would be a challenging year for the UVSOR staff, because many active members moved including the previous director of Prof. Kosugi who had conducted the UVSOR Synchrotron Facility with great efforts for a long time.

We created a new position title, Senior Researcher, who is working for beamline science, aiming at the development and upgrade of new methods using highly brilliant SR, according to the international direction of electronic structure analysis and is also planning future developments ranging for 10-20 years in the UVSOR Synchrotron Facility. Dr. Fumihiko Matsui from NAIST joined with this position.

After the two-major upgrade from UVSOR-I to UVSOR-III Synchrotron, now we aim continuously for serving the high-quality light sources and for developing the stability in use. On the experimental side, technology development will not stop, hence we will make a progress on the imaging-related techniques to encourage the advanced molecular science. The advanced SR-related instruments will offer opportunities to reveal the nature of properties and functions of them.

We look forward to receiving your feedback and suggestions on the continuing evolution of the UVSOR Synchrotron Facility. And we hope many users will perform excellent work by fully utilizing the UVSOR-III Synchrotron as a unique international hub for the SR research in advanced molecular science.

April 2018

Satoshi Kera

Director of the UVSOR Synchrotron Facility

KOSUGI's Memory



12. 2003 UVSOR 20th Anniversary Tour



12. 2003 UVSOR 20th Anniversary Celebration



10. 2007 Softball Competition



4. 2012 Ski Tour



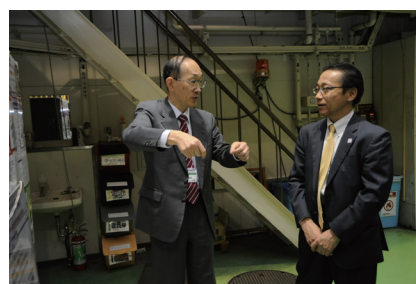
10. 2012 IMS Public Release



10. 2012 Spectrometer working



11. 2013 Celebrate the 60th birthday in the office



12. 2013 UVSOR 30th Anniversary Tour



12. 2013 UVSOR 30th Anniversary Lecture



5. 2016 Japan Chemical Society Award Celebration

KOSUGI Farewell Party Memory



Previous UVSOR director Professor Nobuhiro Kosugi moved to the Institute of Materials Structure Science, KEK as director of the institute in April 2018. He led the UVSOR synchrotron facility for a long time of 20 years. By his great efforts, UVSOR has grown into a SR facility where many researchers can use the light. We all UVSOR staff respect and appreciate Prof. Kosugi. We also wish him more success as a leader in the field of synchrotron radiation.

Ms. Hikaru Fujise was awarded “Best Poster Prize” in the 33rd Symposium on chemical Kinetics and Dynamics

Ms. Hikaru Fujise has received the Best Poster Prize for her poster presentation; “Site-specific production of H_3^+ by core ionization of CH_3Cl ”, at the 33rd Symposium on Chemical Kinetics and Dynamics. Ms. Fujise was a master student of SOKENDAI and worked as a research assistant at the UVSOR gas group.

She presented about the Auger-electron-ion coincidence experiments conducted using the double toroidal analyzer at the soft X-ray beamline BL6U at UVSOR. The experimental results targeting gaseous chloromethane (CH_3Cl) revealed that for the production of H_3^+ , the selectivity of the ionizing site is high, along with the high specificity of the Auger final state.



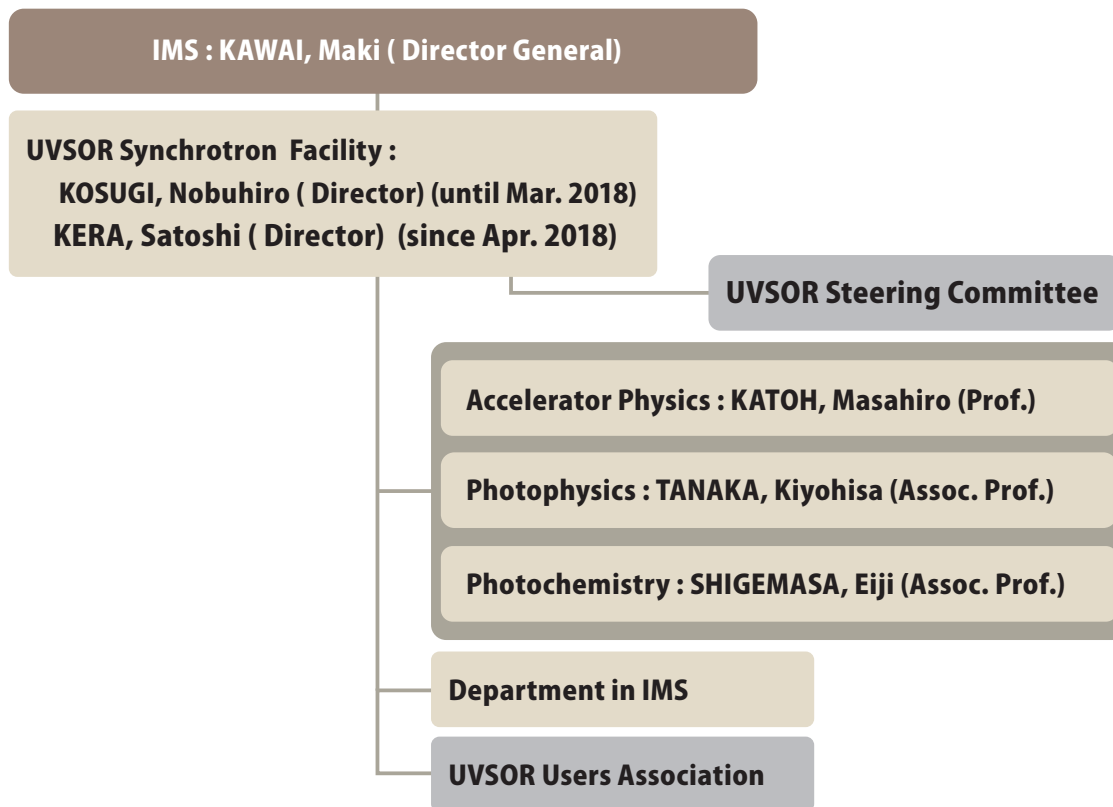
I

Organization and Staff List



UVSOR Synchrotron Facility Organization

May 2018



Staff List

UVSOR Staff

Director

KOSUGI, Nobuhiro	Professor	kosugi@ims.ac.jp	(until Mar. 2018)
KERA, Satoshi	Professor	kera@ims.ac.jp	(since Apr. 2018)

Light Source Division (Accelerator Physics)

KATOH, Masahiro	Professor	mkatoh@ims.ac.jp	
KANEYASU, Tatsuo	Visiting Associate Professor		(since Apr. 2018)
FUJIMOTO, Masaki	Assistant Professor	mfmoto@ims.ac.jp	
YAMAZAKI, Jun-ichiro	Unit Chief Engineer	yamazaki@ims.ac.jp	
HAYASHI, Kenji	Unit Chief Engineer	h-kenji@ims.ac.jp	
TESHIMA, Fumitsuna	Assistant Unit Chief Engineer	tetsu@ims.ac.jp	
MINAKUCHI, Aki	Supporting Engineer	minakuchi@ims.ac.jp	

Light Source Division (X-ray Imaging Optics)

MATSUI, Fumihiko	Senior Researcher	matui@ims.ac.jp	(since Apr. 2018)
------------------	-------------------	-----------------	-------------------

OHIGASHI, Takuji	Assistant Professor	ohigashi@ims.ac.jp	
INAGAKI, Yuichi	Engineer	yinagaki@ims.ac.jp	
YUZAWA Hayato	Engineer	hayato@ims.ac.jp	(since Apr. 2018)

Beamline Division (Photophysics)

TANAKA, Kiyohisa	Associate Professor	k-tanaka@ims.ac.jp	
HIRAHARA, Toru	Visiting Associate Professor		(until Mar. 2018)
IDETA, Shin-ichiro	Assistant Professor	idetas@ims.ac.jp	
HASUMOTO, Masami	Unit Chief Engineer	hasumoto@ims.ac.jp	(until Mar. 2018)
SAKAI, Masahiro	Unit Chief Engineer	sakai@ims.ac.jp	
TOKUSHI, Tetsuzyo	Supporting Engineer	tetsuzyo@ims.ac.jp	(until Sep. 2017)

Beamline Division (Photochemistry)

SHIGEMASA, Eiji	Associate Professor	sigemasa@ims.ac.jp	(until Sep. 2017)
IWAYAMA, Hiroshi	Assistant Professor	iwayama@ims.ac.jp	
NAKAMURA, Eiken	Facility Chief Engineer	eiken@ims.ac.jp	
KONDO, Naonori	Assistant Unit Chief Engineer	nkondo@ims.ac.jp	
YANO, Takayuki	Assistant Unit Chief Engineer	yano@ims.ac.jp	
MAKITA Seiji	Assistant Unit Chief Engineer	makita@ims.ac.jp	(since Oct. 2017)
HORIGOME, Toshio	Senior Engineer	horigome@ims.ac.jp	
HAYASHI, Kenichi	Supporting Engineer	khayasi@ims.ac.jp	(until Mar. 2018)

Secretary

HAGIWARA, Hisayo		hagiwara@ims.ac.jp	
INAGAKI, Itsuko		itsuko@ims.ac.jp	

UVSOR Steering Committee (* Chair)

KOSUGI, Nobuhiro *	UVSOR, IMS		(until Mar. 2018)
KERA, Satoshi *	UVSOR, IMS		(since Apr. 2018)
KATOH, Masahiro	UVSOR, IMS		
SHIGEMASA, Eiji	UVSOR, IMS		(until Sep. 2017)
TANAKA, Kiyohisa	UVSOR, IMS		
HIRAHARA, Toru	UVSOR, IMS (Tokyo Institute of Technology)		(until Mar. 2018)
KANEYASU, Tatsuo	UVSOR, IMS (Kyushu Synchrotron Light Research Center)		(since Apr. 2018)
YOKOYAMA, Toshihiko	IMS		
AKIYAMA, Shuji	IMS		
FUJI, Takao	IMS		(until Mar. 2018)
MASAOKA, Shigeyuki	IMS		(since Apr. 2018)
YAMAMOTO, Hiroshi	IMS		(since Apr. 2018)
ADACHI, Shinichi	KEK-PF		(until Mar. 2018)
DAIMON, Hiroshi	NAIST		(until Mar. 2018)

OHASHI, Haruhiko	JASRI	(until Mar. 2018)
SASAKI, Shigemi	Hiroshima Univ.	(until Mar. 2018)
KITAURA, Mamoru	Yamagata Univ.	
KOMORI, Fumio	Univ. of Tokyo	
OKABAYASHI, Jun	Univ. of Tokyo	
HATSUI, Takaki	JASRI	(since Apr. 2018)
OKUDA, Taichi	Hiroshima Univ.	(since Apr. 2018)
KUMIGASHIRA, Hiroshi	KEK-PF	(since Apr. 2018)
TAKAKUWA, Yuji	Tohoku Univ.	(since Apr. 2018)

UVSOR Users Association (* Chair)

FUKUI, Kazutoshi *	Fukui Univ.	(until Mar. 2018)
HIRAHARA, Toru	Tokyo Institute of Technology	(until Mar. 2018)
ITO, Takahiro	Nagoya Univ.	
KITAURA, Mamoru	Yamagata Univ.	(until Mar. 2018)
YOSHIDA, Tomoko	Osaka City Univ.	(until Mar. 2018)
KIMURA, Shin-ichi *	Osaka Univ.	(since Apr. 2018)
OKABAYASHI, Jun	Univ. of Tokyo	(since Apr. 2018)
YAMANE, Hiroyuki	RIKEN	(since Apr. 2018)
KONDO, Hiroshi	Keio Univ.	(since Apr. 2018)

Graduate Students

FUJISE, Hikaru	SOKENDAI	(until Mar. 2018)
HASEGAWA, Jun	Nagoya Univ.	(until Sep. 2017)
IMAO, Kenta	Nagoya Univ.	(until Sep. 2017)
KUSUNOKI, Naohiro	Nagoya Univ.	(until Sep. 2017)
HAMADA, Ryo	Nagoya Univ.	(since Oct. 2017)
IKEMOTO, Masashi	Nagoya Univ.	(since Oct. 2017)
KONTANI, Syouta	Nagoya Univ.	(since Oct. 2017)
TAKAHASHI, Kazuyoshi	Nagoya Univ.	(since Oct. 2017)

Visiting Scientists

SUN, Zhengyi	Nanjing Tech Univ.	Jun. 2017
WEN, Chenhaoping	Fudan Univ.	Jun. 2017, Nov. 2017
YAO, Qi	Fudan Univ.	Jun. 2017
CHUANG, Cheng-Hao	Tamkang Univ.	Jun. 2017
WANG, Yu-Fu	Tamkang Univ.	Jun. 2017
HSU, Wei-Hao	Academia Sinica	Jun. 2017
CHIOU, Jau-Wern	National Univ. of Kaohsiung	Jun. 2017
STANIA, Roland	Institute for Basic Science	Jun. 2017
FUKUTANI, Keisuke	Institute for Basic Science	Jun. 2017

JUNG, Jiwon	Pohang Univ. of Science and Technology	Jun. 2017
HAN, Sehee	Pohang Univ. of Science and Technology	Jun. 2017
JU, Huanxin	Univ. of Science and Technology of China	Jul. 2017
PATANEN, Minna	Univ. of Oulu	Jul. 2017
de JONG, Michel P.	Univ. of Twente	Jul. 2017
OCHAPSKI, Michal Witold	Univ. of Twente	Jul. 2017
CÉOLIN, Denis	Synchrotron SOLEIL	Aug. 2017
NICOLAS, Christophe	Synchrotron SOLEIL	Aug. 2017
LAI, Yu-Ling	NSRRC	Aug. 2017, Dec. 2017
SHIN, Hung-Wei	NSRRC	Aug. 2017, Dec. 2017
YU, Li-Chung	NSRRC	Aug. 2017, Dec. 2017
WHITE, James L.	Sandia National Laboratories	Aug. 2017
RÜHL, Eckart	Freie Univ. Berlin	Sep. 2017, Mar. 2018
KLOSSEK, André	Freie Univ. Berlin	Sep. 2017, Mar. 2018
YAMAMOTO, Kenji	Freie Univ. Berlin	Sep. 2017, Mar. 2018
FLESCH, Roman	Freie Univ. Berlin	Sep. 2017, Mar. 2018
RANCAN, Fiorenza	Charité-Universitätsmedizin Berlin	Sep. 2017, Mar. 2018
SALEHI DERAKHTANJANI, Elham	Institut. for Research in Fundamental Sciences	Sep. 2017
SOOHYUN, Cho	Yonsei Univ.	Sep. 2017
DONG JIN, Oh	Seoul National Univ.	Sep. 2017
LOU, Xia	Fudan Univ.(FDU)	Nob. 2017
YU, Tianlun	Fudan Univ.(FDU)	Nob. 2017
FANG, Yifei	Fudan Univ.(FDU)	Nob. 2017
DONG, Chung-Li	Tamkang Univ.	Jan. 2018
SHIROLKAR, Mandar Mukund	Tamkang Univ.	Jan. 2018
HUANG, Yu-Cheng	National Chiao Tung Univ.	Jan. 2018
HAN YOUNG, Yoo	Seoul National Univ.	Feb. 2018
HUTTULA, Marko	Univ. of Oulu	Oct. 2017, Feb. 2018
IMMONEN, Esa-Ville	Univ. of Oulu	Oct. 2017
PRISLE, Nønne L.	Univ. of Oulu	Feb. 2018
LIN, Jack J.	Univ. of Oulu	Feb. 2018
MICHAILOUDI, Gerogia	Univ. of Oulu	Feb. 2018
CORRAL, Arroyo Pabio	Paul Scherrer Institut.	Feb. 2018
PARK, Seung Ryong	Incheon National Univ.	Feb. 2018
KONG, Xiangrui	Univ. of Gothenburg	Feb. 2018
BERKEMEYER, Janis	Freie Univ. Berlin	Mar. 2018
KHODABANDEH, Aminreza	Univ. of South Australia	Mar. 2018
ARRUA, Ruben Dario	Univ. of South Australia	Mar. 2018

A large, white, stylized Roman numeral 'II' is centered in the upper half of the page. The background is a vibrant teal color with abstract, futuristic patterns. A prominent feature is a large, circular, multi-layered structure resembling a particle accelerator or light source, with concentric rings and a dashed outer boundary. Diagonal lines and a grid of small dots are also visible in the lower half of the image.

Current Status of
Light Sources and
Beamlines

Light Source in 2017

1. Status of UVSOR Accelerators

In the fiscal year 2017, we had scheduled to operate UVSOR-III from May to March, for 36 weeks for users. Although we had several machine troubles as described later, fortunately, we could operate the machine mostly as scheduled only with one day and a few hour losses. We had a scheduled shutdown period in April and May for about 6 weeks. This was mainly for the scheduled maintenance works. We had one week shut down period in August and October, two week one around the New Years day and one week one at the end of March. We had 2 weeks for machine and beamline conditioning in May after the spring shut down. In addition, we had 4 weeks for machine conditionings and studies, in October, November, January and March. The machine study week in November was mainly for the machine conditioning after the annual planned power outage.

We operated the machine for 34 weeks in the multi-bunch top-up mode, in which the beam current was kept at 300 mA, and 2 weeks in the single-bunch mode, in which the machine was operated in single-bunch top-up mode with the beam current of approximately 40 mA. The monthly statistics of the operation time and the integrated beam current are shown in Fig. 1.

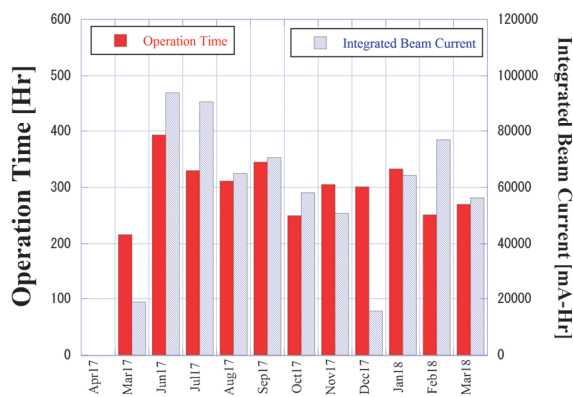


Fig. 1. Monthly statistics in FY2017.

The weekly operation schedule is as follows. On Monday, from 9 am to 9 pm, the machine is operated for machine conditionings and studies. On Tuesday and Wednesday, from 9am to 9pm, the machine is operated for users. From Thursday 9am to Friday 9pm, the machine is operated for 36 hours continuously for users. Therefore, the beam time for users in a week is 60 hours.

The most serious trouble in this year was the vacuum leakage at the booster synchrotron, which happened in July. We observed an unusual pressure rise in a part of the synchrotron. After the careful check, we

found a vacuum leakage at a beam duct (Fig. 2). Fortunately, a temporal expedient with vacuum sealant was effective, and the vacuum pressure recovered. We could restart the users operation after a shut down for one day. Another vacuum trouble was also in July. In this case, the leakage occurred at a beamline frontend. After a temporal expedient, we could restart the users time with 4 hour loss.

In February, a cooling water leakage was found at a sextupole coil wound on a pole face of a multipole (quadrupole/sextupole) magnet. Due to the space constraints, an expedient was difficult. Therefore, we decided to continue the operation for about one month as monitoring the leakage carefully. In the spring shut down, the coil will be repaired. Concerning the water leakage from the coils of quadrupole magnet in the booster synchrotron, which occurred twice in these years, the preventive treatment with sealant seems effective. No recurrence has been observed so far.

In this year, other than the troubles described above, we had a few less serious troubles on the power supplies of the injection/extraction magnets. Fortunately, in all cases the beam time for users was not lost. Due to the unusual low temperature in this winter, in the cooling tower of the cooling water system, the pipe was partly frozen and damaged. It should have been avoided by an interlock system but, unfortunately, the temperature detection system was malfunctioned. In order to prevent the recurrence, we are going to improve the routine inspection.

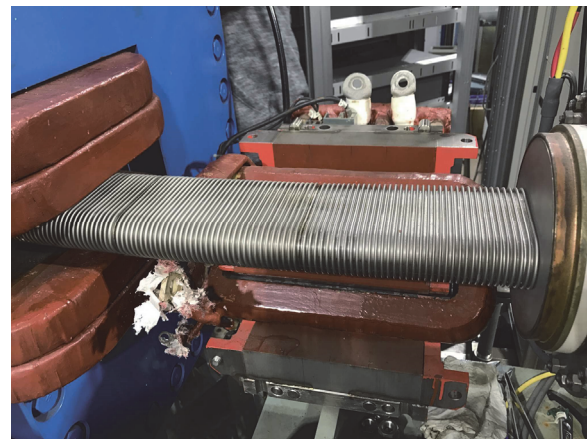


Fig. 2. The beam duct at a quadrupole in the booster synchrotron. A vacuum leakage was found in the middle of the duct.

2. Improvements and Developments

The power supply for the extraction septum magnet in the booster synchrotron was replaced in spring 2017 (Fig. 3), following the replacement of the power supply

for the injection septum magnet in the previous year. As the result, there was no pulse power supply which had been used since the beginning of the facility. The small power supplies for beam transport line were also replaced (Fig. 3), which had been used for more than 20 years.

The cooling water system of the main RF cavity in the storage ring was replaced with the one which has a good temporal stability of 0.1 degree C. We expected that this would improve the beam stability.



Fig. 3 New power supplies for the extraction septum at the booster synchrotron (left) and those for the beam transport line magnets (right).

Light Source Developments and Beam Physics Studies

We continue the efforts to develop novel light sources technologies and their applications such as free electron lasers, coherent harmonic generation, coherent synchrotron radiation, laser Compton scattering gamma-rays, intense polarized and vortex UV radiation at the source development station BL1U, which was constructed under the support of Quantum

Beam Technology Program by MEXT/JST. In these years, we continued studying the optical vortex beam from a helical undulator in collaboration with Hiroshima U., Nagoya U. and other institutes. Since the UVSOR electron beam is diffraction-limited in the UV range, we could precisely investigate the optical properties of the vortex beams from undulators using conventional optical components. In 2016, we installed a mirror and a monochromator at BL1U, which would be used for exploring the applications of novel light sources. We designed the beamline to be flexible as much as possible to various experimental configurations. By using this beam-line, we continued the experimental study on the interaction between optical vortex VUV light and atoms in collaboration with Saga LS and Niigata U.

In March 2018, we tested the operation of the optical cavity for the resonator free electron laser at BL1U, in collaboration with Kyoto U. We have checked the alignment and the length of the cavity. In FY2018, we will try the FEL oscillation, which had been terminated for several years.

The laser Compton scattering gamma-rays are powerful tools for nuclear science and technologies. By using various external lasers, we have demonstrated to generate quasi-monochromatic gamma-rays in the energy range from 1MeV to around 10MeV. We continue the experiments in collaboration with Kyoto U., AIST and QST towards imaging applications. We will start new experiments on positron lifetime spectroscopy experiments in collaboration with Yamagata U., Nagoya U. and AIST.

Some studies on the beam dynamics have been carried out in collaboration with Nagoya U. We continue studying longitudinal coupled bunch instabilities and its suppression mechanism with the harmonic cavity. We are also studying the single bunch instability which limits the single bunch beam current around 40-50mA.

Masahiro KATOH
(UVSOR Synchrotron Facility)

UVSOR Accelerator Complex

Injection Linear Accelerator

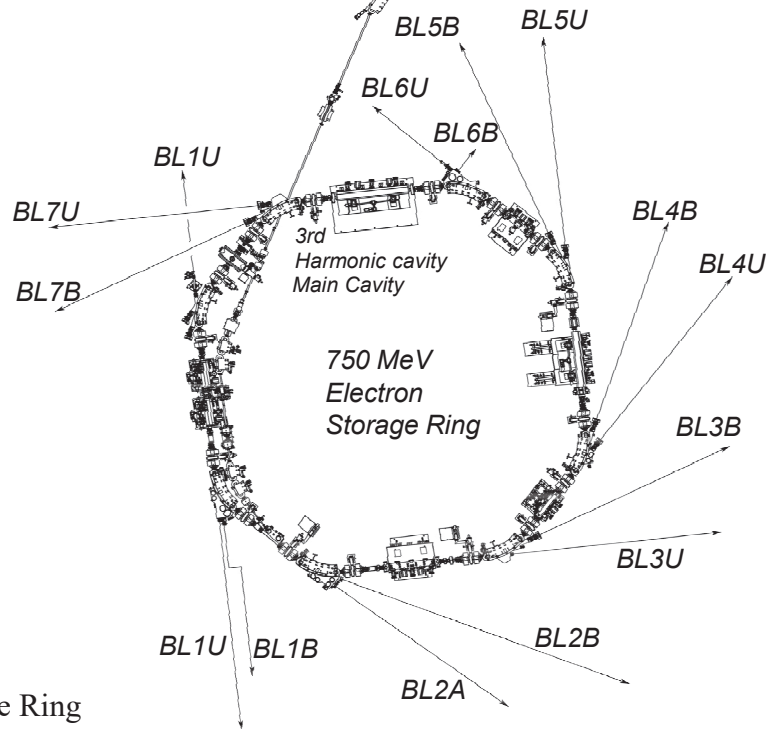
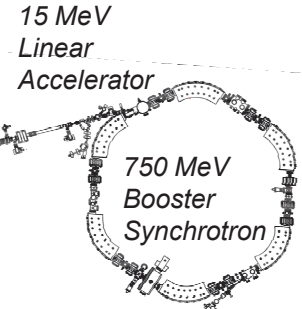
Energy	15 MeV
Length	2.5 m
Frequency	2856 MHz
Accelerating RF Field	$2\pi/3$ Traveling Wave
Klystron Power	1.8 MW
Energy Spread	~ 1.6 MeV
Repetition Rate	2.6 Hz

UVSOR-III Storage-Ring

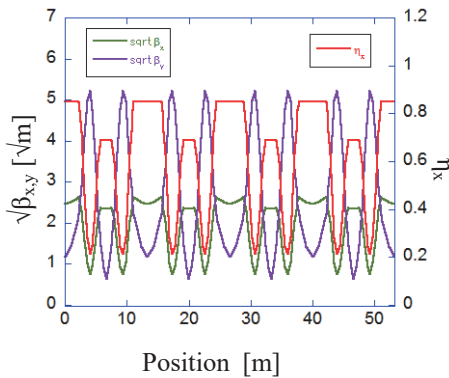
Energy	750 MeV
Injection Energy	750 MeV
Maximum Storage Current	500 mA (multi bunch) 100 mA (single bunch)
Normal operation current (Top-up mode)	300 mA (multi bunch) 50 mA (single bunch)
Natural Emittance	17.5 nm-rad
Circumference	53.2 m
RF Frequency	90.1 MHz
Harmonic Number	16
Bending Radius	2.2 m
Lattice	Extended DBA $\times 4$
Straight Section	(4 m \times 4)+(1.5 m \times 4)
RF Voltage	120 kV
Betatron Tune	
Horizontal	3.75
Vertical	3.20
Momentum Compaction	0.030
Natural Chromaticity	
Horizontal	-8.1
Vertical	-7.3
Energy Spread	5.26×10^{-4}
Coupling Ratio	1%
Natural Bunch Length	128 ps

Booster Synchrotron

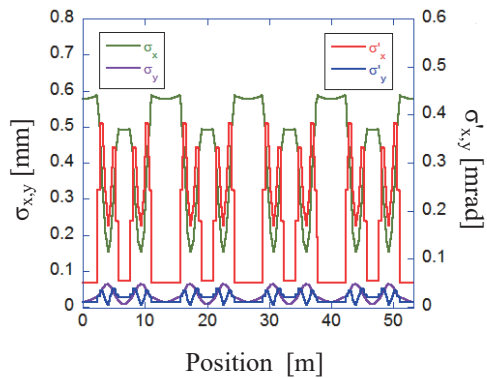
Energy	750 MeV
Injection	15 MeV
Frequency	32 mA (uniform filling)
Circumference	26.6 m
RF Frequency	90.1 MHz
Harmonic Number	8
Bending Radius	1.8m
Lattice	FODO $\times 8$
Betatron Tune	
Horizontal	2.25
Vertical	1.25
Momentum Compaction	0.138
Repetition Rate	1 Hz (750 MeV)



Electron Beam Optics of UVSOR-III Storage Ring

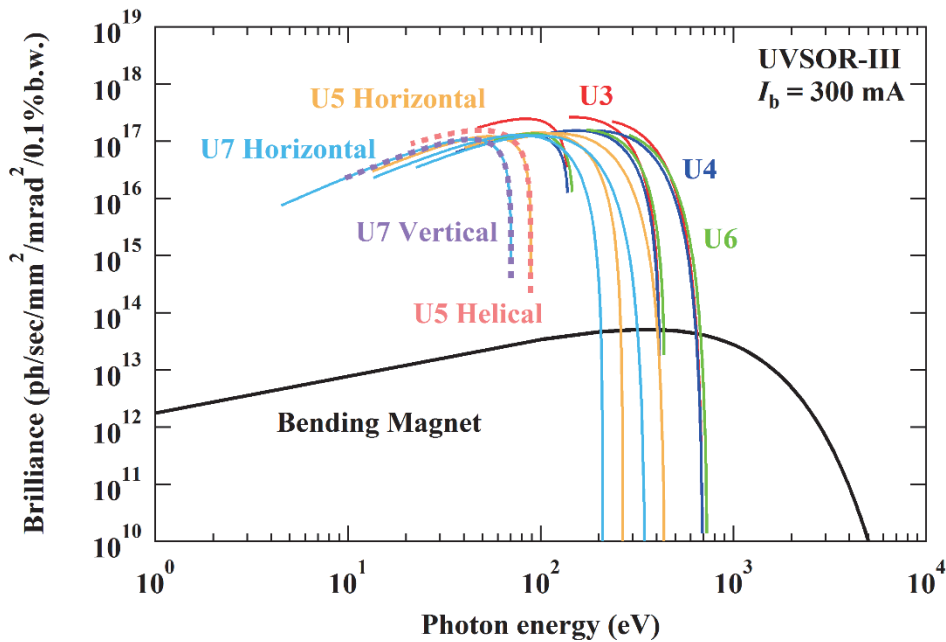


Horizontal/vertical betatron functions and dispersion function



Horizontal/vertical electron beam size and beam divergences

Insertion Device



Brilliance of radiation from the insertion devices (U3, U4, U5, U6 and U7) and a bending magnet of UVSOR-III

U1 Apple-II Undulator /

Optical Klystron

Number of Periods	10+10
Period length	88 mm
Pole Length	0.968 m + 0.968 m
Pole Gap	24-200 mm
Deflection Parameter	7.36 (Max. Horizontal) 4.93 (Max. Vertical) 4.06 (Max. Helical)

U3 In-vacuum Undulator

Number of Periods	50
Period length	38 mm
Pole Length	1.9 m
Pole Gap	16.5-40 mm
Deflection Parameter	1.8-0.24

U4 In-vacuum Undulator

Number of Periods	26
Period length	38 mm
Pole Length	0.99 m
Pole Gap	13-40 mm
Deflection Parameter	2.4-0.19

U5 Apple-II

Variable Polarization Undulator

Number of Periods	38
Period length	60 mm
Pole Length	2.28 m
Pole Gap	24-190 mm
Deflection Parameter	3.4 (Max. Horizontal) 2.1 (Max. Vertical) 1.8 (Max. Helical)

U6 In-vacuum Undulator

Number of Periods	26
Period length	36 mm
Pole Length	0.94 m
Pole Gap	13-40 mm
Deflection Parameter	1.78 - 0.19

U7 Apple-II

Variable Polarization Undulator

Number of Periods	40
Period length	76 mm
Pole Length	3.04 m
Pole Gap	24-200 mm
Deflection Parameter	5.4 (Max. Horizontal) 3.6 (Max. Vertical) 3.0 (Max. Helical)

Bending Magnets

Bending Radius	2.2 m
Critical Energy	425 eV

Beamlines in 2017

Kiyohisa TANAKA

UVSOR Synchrotron Facility, Institute for Molecular Science

UVSOR is one of the highest-brilliance light sources in the extreme-ultraviolet region among the synchrotron radiation facilities with electron energies of less than 1 GeV. The natural emittance of the UVSOR-III storage ring is as low as 17.5 nm-rad after the successful completion of the storage ring upgrade project (the UVSOR-III project) in 2012.

Eight bending magnets and five insertion devices are available as synchrotron light sources at UVSOR. As of 2016 there are a total of fourteen operational beamlines, which are classified into two categories. Eleven of them are the so-called “Open beamlines”, which are open to scientists from universities and research institutes belonging to the government, public organizations, private enterprises and also those from foreign countries. The remaining three beamlines are the “In-house beamlines”, and are dedicated to the use of research groups within Institute for Molecular Science (IMS).

There is one soft X-ray station equipped with a double-crystal monochromator, seven extreme ultraviolet and soft X-ray stations with grazing incidence monochromators, three vacuum ultraviolet (VUV) stations with normal incidence monochromators, two infrared (IR) stations equipped with Fourier-Transform interferometers, and one free electron laser beamline with no monochromator, as shown in the appended table (next page) for all available beamlines at UVSOR in 2017. The details of the updates for several beamlines are the followings.

BL2A equipped with a double-crystal monochromator, where users can use the highest energy photons in UVSOR (~4 keV), has been used mainly for photoabsorption spectroscopy. Since there are users who want to evaluate the sample surface, a new chamber for X-ray photoemission spectroscopy (XPS) has been attached to BL2A during the shutdown of 2017. XPS measurement is now available.

In BL3B, a new endstation chamber has been installed during the shutdown of 2017. High efficiency VUV emission spectroscopy will be

available soon.

BL5U has been officially opened for users from 2016 as high energy resolution angle-resolved photoemission spectroscopy (ARPES) beamline. It became one of the most popular beamline in UVSOR, whose beamtime requests are about three times more than the beamtime. Using a new mirror located close to the sample position, the beam spot size is successfully focused to ~50 μm , which make users possible to perform measurements on small samples or inhomogeneous samples. Spin-resolved ARPES will be developed and installed soon.

In BL6U, which is one of the in-house beamlines, the latest version of ARPES analyzer was installed (MB Scientific AB, A-1 analyzer Lens#5). Manipulator will be modified so that a mesh can be set in front of the sample and the sample can be biased voltages. By applying bias voltages to the sample, the wider acceptance angle (~ 60 deg.) with $h\nu = 40\text{-}60$ eV will be available.

UVSOR is now planning to introduce so-called “Momentum microscope (MM)”, which is an electronic spectroscopy with both the real space and momentum space resolution. It will be installed to the area of BL2A and BL2B. BL2B will be shut down from FY2018 and the whole BL2A, including the grating and endstation, will move to BL8A. User operation of BL8A will start from summer 2018. New normal incident monochromator beamline for MM is designed with two gratings which cover the energy of photon from 6 to 60 eV. Construction of beamline will start from FY2018 and MM analyzer will be installed in FY2019. Tender process for both the beamline and MM analyzer is now in progress.

All users are required to refer to the beamline manuals and the UVSOR guidebook (the latest revision in PDF format uploaded on the UVSOR web site in June 2010), on the occasion of conducting the actual experimental procedures. Those wishing to use the open and in-house beamlines are recommended to contact the appropriate beamline master (see next page). For updated information on UVSOR, please see <http://www.uvsor.ims.ac.jp>

Beamlines at UVSOR

Beamline	Monochromator / Spectrometer	Energy Range	Targets	Techniques	Contact
BL1U	Free electron laser	1.6 - 13.9 eV		(Irradiation)	M. Katoh mkatoh@ims.ac.jp
BL1B	Martin-Puplett FT-FIR	0.5 - 30 meV	Solid	Reflection Absorption	K. Tanaka k-tanaka@ims.ac.jp
BL2A	Double crystal	585 eV - 4 keV	Solid	Reflection Absorption	K. Tanaka k-tanaka@ims.ac.jp
BL2B	18-m spherical grating (Dragon)	23 - 205 eV	Solid	Photoemission	S. Kera kera@ims.ac.jp
BL3U	Varied-line-spacing plane grating (Monk-Gillieson)	60 - 800 eV	Gas Liquid Solid	Absorption Photoemission Photon-emission	M. Nagasaka nagasaka@ims.ac.jp
BL3B	2.5-m off-plane Eagle	1.7 - 31 eV	Solid	Reflection Absorption Photon-emission	K. Tanaka k-tanaka@ims.ac.jp
BL4U	Varied-line-spacing plane grating (Monk-Gillieson)	100 - 770 eV	Gas Liquid Solid	Absorption (Microscopy)	T. Ohigashi ohigashi@ims.ac.jp
BL4B	Varied-line-spacing plane grating (Monk-Gillieson)	25 eV - 1 keV	Gas Solid	Photoionization Photodissociation Photoemission	H. Iwayama iwayama@ims.ac.jp
BL5U	Spherical grating (SGM-TRAIN [†])	20 - 200 eV	Solid	Photoemission	K. Tanaka k-tanaka@ims.ac.jp
BL5B	Plane grating	6 - 600 eV	Solid	Calibration Absorption	K. Tanaka k-tanaka@ims.ac.jp
BL6U*	Variable-included-angle varied-line-spacing plane grating	40 - 500 eV	Gas Solid	Photoionization Photodissociation Photoemission	F. Matsui matui@ims.ac.jp
BL6B	Michelson FT-IR	4 meV - 2.5 eV	Solid	Reflection Absorption IR microscope	K. Tanaka k-tanaka@ims.ac.jp
BL7U	10-m normal incidence (modified Wadsworth)	6 - 40 eV	Solid	Photoemission	S. Ideta idetas@ims.ac.jp
BL7B	3-m normal incidence	1.2 - 25 eV	Solid	Reflection Absorption Photon-emission	K. Tanaka k-tanaka@ims.ac.jp

Yellow columns represent undulator beamlines.

* In-house beamline.

BL1U

Light Source Development Station

▼ Description

BL1U is dedicated for developments and applications of various novel photon sources including free electron laser in the range from visible to deep UV, coherent harmonic generation in the deep UV and VUV, laser Compton scattering gamma-rays and undulator radiation with various polarization properties including optical vortices.

The beam-line is equipped with a dedicated twin polarization variable undulator system with a buncher section, which can be used for a FEL oscillator and a VUV CHG. It is also equipped with a femto-second laser system synchronized with the accelerator, which is used for CHG, slicing, LCS and coherent THz radiation generation.

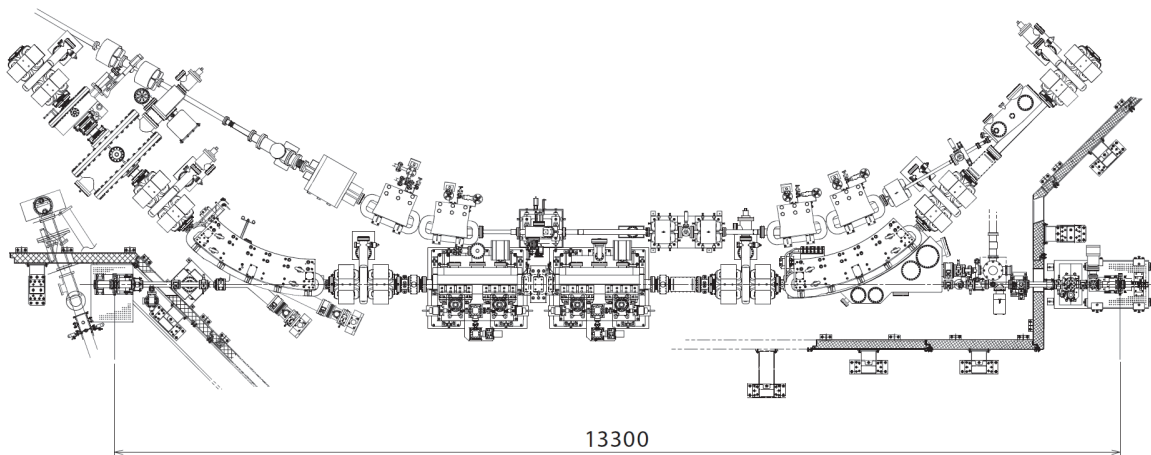


Fig. 1. Configuration of the free electron laser (under reconstruction).



Fig. 2. Twin Apple-II Undulator.

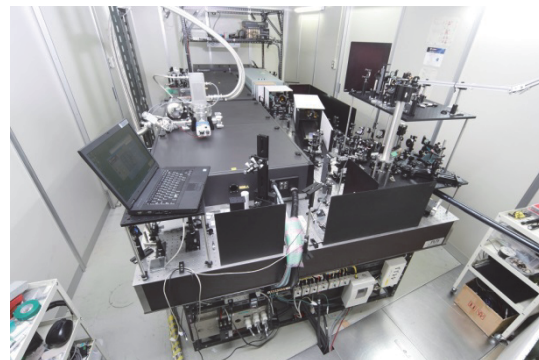


Fig. 3. Accelerator Synchronized Laser System.

▼ Technical Data of FEL

Wave Length	199-800 nm
Spectral Band Width	$\sim 10^{-4}$
Polarization	Circular/Linear
Pulse Rate	11.26 MHz
Max. Ave. Power	~ 1 W

▼ Technical Data of Ti:Sa Laser

Wave Length	800 nm
Pulse Length	130 fsec
Oscillator	90.1 MHz
Pulse Energy	2.5mJ 10mJ 50mJ
Repetition Rate	1kHz 1kHz 10Hz

BL1B

Terahertz Spectroscopy Using Coherent Synchrotron Radiation

II

▼ Description

Coherent synchrotron radiation (CSR) is a powerful light source in the terahertz (THz) region. This beamline has been constructed for basic studies on the properties of THz-CSR. However, it can be also used for measurements of reflectivity and transmission spectra of solids using conventional synchrotron radiation.

The emitted THz light is collected by a three-dimensional magic mirror (3D-MM, M0) of the same type as those already successfully installed at BL43IR in SPring-8 and BL6B in UVSOR-II. The 3D-MM was installed in bending-magnet chamber #1 and is controlled by a 5-axis pulse motor stage (x, z translation; θ_x , θ_y , θ_z rotation). The acceptance angle was set at 17.5-34 degrees (total 288 mrad) in the horizontal direction. The vertical angle was set at ± 40 mrad to collect the widely expanded THz-CSR.

The beamline is equipped with a Martin-Puplett type interferometer (JASCO FARIS-1) to cover the THz spectral region from 4 to 240 cm^{-1} ($h\nu = 500 \mu\text{eV}$ -30 meV). There is a reflection/absorption spectroscopy (RAS) end-station for large samples (\sim several mm). At the RAS end-station, a liquid-helium-flow type cryostat with a minimum temperature of 4 K is installed.

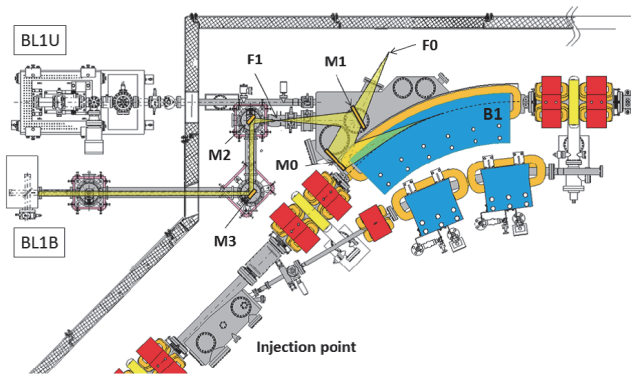


Fig. 1. Schematic top view of the beam extraction part of the THz-CSR beamline, BL1B. The three-dimensional magic mirror (3D-MM, M0) and a plane mirror (M1) are located in the bending-magnet chamber. A parabolic mirror (M2) is installed to form a parallel beam. The straight section (BL1U) is used for coherent harmonic generation (CHG) in the VUV region.

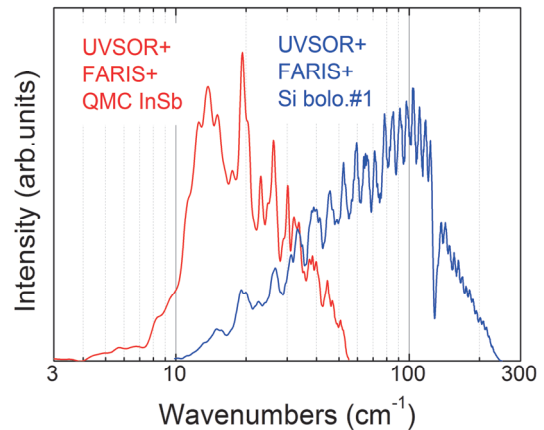


Fig. 2. Obtained intensity spectra with the combination of a light source (UVSOR), interferometer (FARIS-1), and detectors (Si bolometer and InSb hot-electron bolometer).

▼ Technical Data

Interferometer	Martin-Puplett (JASCO FARIS-1)
Wavenumber range (Energy range)	4-240 cm^{-1} (500 μeV -30 meV)
Resolution in cm^{-1}	0.25 cm^{-1}
Experiments	Reflection/transmission spectroscopy
Miscellaneous	Users can use their experimental system in this beamline.

BL2A

Soft X-Ray Beamline for Photoabsorption Spectroscopy

▼ Description

BL2A, which was moved its previous location as BL1A in 2011, is a soft X-ray beamline for photoabsorption spectroscopy. The beamline is equipped with a focusing premirror and a double-crystal monochromator [1]. The monochromator serves soft X-rays in the energy region from 585 to 4000 eV using several types of single crystals, such as β - Al_2O_3 , beryl, KTP (KTiOPO_4), quartz, InSb, and Ge. The throughput spectra measured using a Si photodiode (AXUV-100, IRD Inc.) are shown in Fig. 1. The typical energy resolution ($E / \Delta E$) of the monochromator is approximately 1500 for beryl and InSb.

A small vacuum chamber equipped with an electron multiplier (EM) detector is available. Photoabsorption spectra for powdery samples are usually measured in total electron yield mode, with the use of the EM detector. A silicon drift detector is also available for measuring partial fluorescence yields from solid samples.

[1] Hiraya *et al.*, Rev. Sci. Instrum. **63** (1992) 1264.

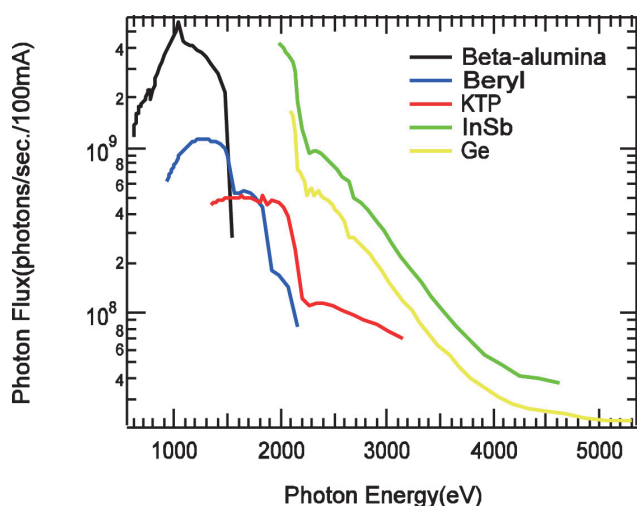


Fig. 1. Throughput spectra of the double-crystal monochromator at BL2A.



Fig. 2. Side view of BL2A.

▼ Technical Data

Monochromator	Double crystal monochromator
Monochromator crystals: (2d value, energy range)	β - Al_2O_3 (22.53 Å, 585-1609 eV), beryl (15.965 Å, 826-2271 eV), KTP (10.95 Å, 1205-3310 eV), quartz (8.512 Å, 1550-4000 eV), InSb (7.481 Å, 1764-4000 eV), Ge (6.532 Å, 2094-4000 eV)
Resolution	$E / \Delta E = 1500$ for beryl and InSb
Experiments	Photoabsorption spectroscopy (total electron yield using EM and partial fluorescence yield using SDD)

BL2B

Photoelectron spectroscopy of molecular solids

II

▼ Description

This beamline previously dedicated for experiments in the field of gas phase photoionization and reaction dynamics. Then, the beamline has been reconstructed for photoelectron spectroscopy of molecular solids with a new end station, and experiments can be performed from May 2014. The monochromator is a spherical grating Dragon type with 18-m focal length. High throughput (1×10^{10} photons s^{-1}) and high resolution ($E/\Delta E = 2000 - 8000$) are achieved simultaneously under the condition of the ring current of 100 mA [1]. The optical system consists of two pre-focusing mirrors, an entrance slit, three spherical gratings (G1 - G3), two folding mirrors, a movable exit slit, and a refocusing mirror [2]. The monochromator is designed to cover the energy range of 23–205 eV with the three gratings: G1 (2400 lines mm^{-1} , $R = 18$ m) at 80–205 eV; G2 (1200 lines mm^{-1} , $R = 18$ m) at 40–100 eV; G3 (2400 lines mm^{-1} , $R = 9.25$ m) at 23–50 eV. The percentage of the second-order light contamination at $h\nu = 45.6$ eV is 23% for G2 or 7% for G3.

A UHV chamber is placed downstream of the refocusing mirror chamber and equipped silicon photodiode, sapphire plate Au mesh and filters for absolute photon flux measurement, monitor the photon-beam position, relative photon flux measurements and attenuate higher order light, respectively.

The new end station consists of a main chamber with a hemispherical analyzer (SCIENTA R3000) and a liquid-He-cooled cryostat (temperature range of 15-400 K) with 5-axis stage, a sample preparation chamber with a fast-entry load-lock chamber and a cleaning chamber with LEED, ion gun for sputtering and IR heating unit.

[1] M. Ono, H. Yoshida, H. Hattori and K. Mitsuke, Nucl. Instrum. Meth. Phys. Res. A **467-468** (2001) 577.

[2] H. Yoshida and K. Mitsuke, J. Synchrotron Radiation **5** (1998) 774.



Fig. 1. 18 m spherical grating monochromator at BL2B.

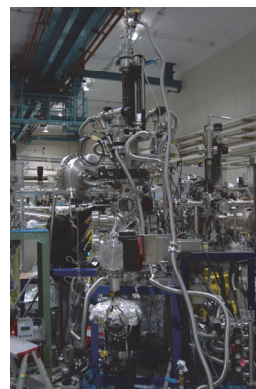


Fig. 2. End station of BL2B for photoelectron spectroscopy of molecular solids.

▼ Technical Data

Monochromator	18 m spherical grating Dragon-type
Wavelength Range	23-205 eV
Resolution	2000–8000 depending on the gratings
Experiments	Angle-resolved ultraviolet photoemission spectroscopy

BL3U

Varied-Line-Spacing Plane Grating Monochromator for Molecular Soft X-Ray Spectroscopy

II

▼ Description

The beamline BL3U is equipped with an in-vacuum undulator composed of 50 periods of 3.8 cm period length. The emitted photons are monochromatized by the varied-line-spacing plane grating monochromator (VLS-PGM) designed for various spectroscopic investigations in the soft X-ray range including soft X-ray emission studies. Three holographically ruled laminar profile plane gratings are designed to cover the photon energy range from 60 to 800 eV. The beamline has two endstations, namely, XES setup and multi-purpose setup. The XES setup is used for soft X-ray emission spectroscopy. The beam is horizontally focused onto the sample position by a plane-elliptical mirror, M2X. In the multi-purpose setup, the beam is focused by the toroidal mirror M2. Between the sample position and M2, the differential pumping is placed. XAS of liquid samples and the application of in operando observations are performed at the experimental stage of the multi-purpose setup.

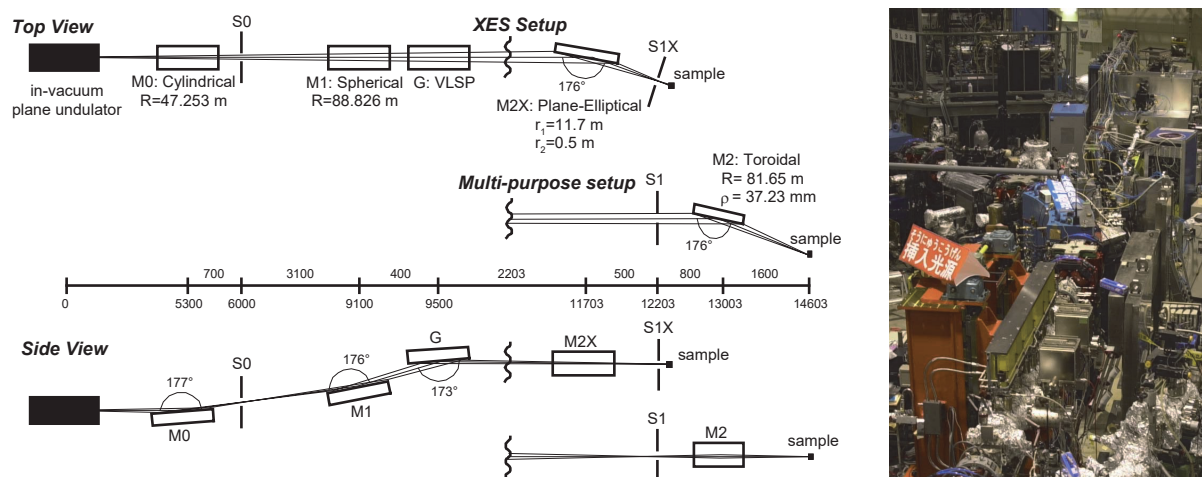


Fig. 1. Schematic layout (left) and the photography (right) of the BL3U. The distances along the beam from the center of the in-vacuum plane undulator are shown in millimeters. S1X and M2X can be replaced with the other exit slit S1 so that experiments can be carried out at either the XES or the multipurpose endstation. In the XES setup, the sample is placed 5–10 mm downstream of S1X.

▼ Technical Data

Monochromator	Varied-line-spacing plane grating monochromator
Energy Range	60-800 eV
Resolution	$E / \Delta E > 10\,000$
Experiments	Soft X-ray spectroscopy (XPS, XES, XAS)
Beam Size (XES Endstation)	Gaussian shape Vertical 5-20 μm ; Horizontal 41 μm (FWHM)

BL3B (HOTRLU)

VIS-VUV Photoluminescence and Reflection/Absorption Spectroscopy

▼ Description

BL3B has been constructed to study photoluminescence (PL) in the visible (VIS) to vacuum ultraviolet (VUV) region. This beamline consists of a 2.5 m off-plane Eagle type normal-incidence monochromator, which covers the VUV, UV, and VIS regions, i.e., the energy (wavelength) region of 1.7-31 eV (40-730 nm), with three spherical gratings having constant grooving densities of 1200, 600, and 300 l/mm optimized at the photon energies of ~ 20 , ~ 16 , and ~ 6 eV, respectively. The schematic side view and top view layouts are shown in Figs. 1(a) and 1(b), respectively. The FWHM of the beam spot at the sample position is 0.25 mm (V) \times 0.75 mm (H). Low energy pass filters (LiF, quartz, WG32, OG53) can be inserted automatically to maintain the optical purity in the G3 (300 l/mm) grating region (1.7–11.8 eV). Figure 2 shows the throughput spectra (photon numbers at a beam current of 300 mA) for each grating with entrance and exit slit openings of 0.1 mm (resolving power $E / \Delta E$ of ~ 2000 (G3, ~ 6.8 eV)). Since both slits can be opened up to 0.5 mm, a monochromatized photon flux of 10^{10} photons/s or higher is available for PL measurements in the whole energy region.

The end station is equipped with a liquid-helium-flow type cryostat for sample cooling and two detectors; one of which is a photomultiplier with sodium salicylate and the other a Si photodiode for reflection/absorption measurement. For the PL measurements in the wide energy region from VIS to VUV, two PL monochromators, comprising not only a conventional VIS monochromator but also a VUV monochromator with a CCD detector, are installed at the end station.

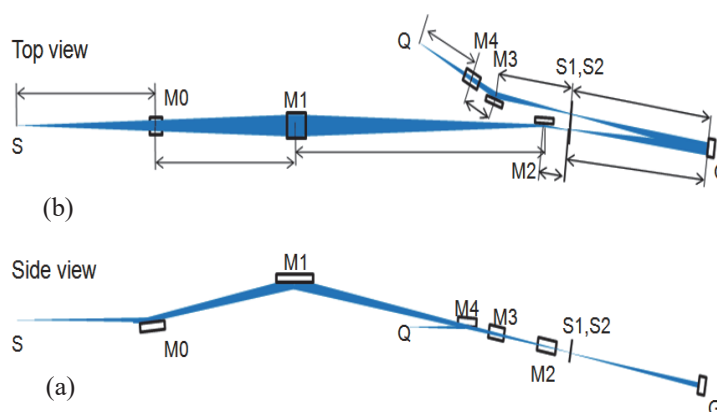


Fig. 1. Schematic layout of the BL3B (a) side view and (b) top view.

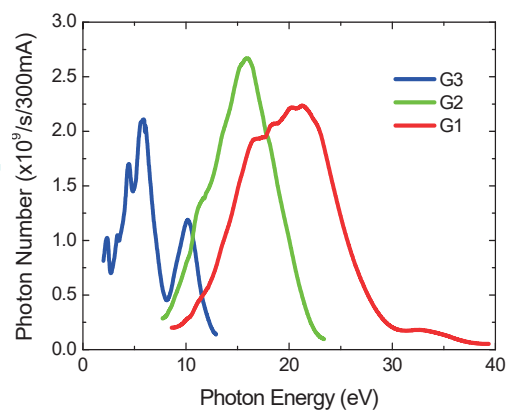


Fig. 2. Throughput spectra for each grating (G1:1200 l/mm, G2:600 l/mm and G3:300 l/mm) with $S1 = S2 = 0.1$ mm.

▼ Technical Data

Monochromator	-2.5 m normal-incidence monochromator
Energy range	1.7-31 eV (40~730 nm)
Resolution ($\Delta h\nu / h\nu$)	≥ 12000 (at ~ 6.9 eV, 0.02 mm slits, G1 (1200 l/mm))
Experiments	Photoluminescence, reflection, and absorption spectroscopy, mainly for solids

BL4U

Scanning Transmission X-ray Microscopy in the Soft X-ray Region

▼ Description

In the soft x-ray region, there are several absorption edges of light elements and transition metals. The near edge X-ray absorption fine structure (NEXAFS) brings detailed information about the chemical state of target elements. A scanning transmission X-ray microscope (STXM) in the soft X-ray region is a kind of extended technique of the NEXAFS with high spatial resolution. The STXM has a capability of several additional options, for example, in-situ observations, 3-dimensional observation by computed tomography and ptychography, by utilizing the characteristics of the X-rays. The STXM can be applied to several sciences, such as polymer science, material science, cell biology, environmental science, and so on.

This beamline equips an in-vacuum undulator, a varied-line-spacing plane grating monochromator and a fixed exit slit. The soft X-ray energy range from 100 to 770 eV with the resolving power ($E/\Delta E$) of 6,000 is available. The aperture size of the fixed exit slit determines not only the resolving power but also the size of a microprobe. A Fresnel zone plate is used as a focusing optical device through an order select aperture and its focal spot size of ~ 30 nm is available at minimum. An image is acquired by detecting intensities of the transmitted X-rays by a photomultiplier tube with scintillator with scanning a sample 2-dimensionally. By changing the energy of the incident beam, each 2-dimensional NEXAFS image is stacked. A main chamber of STXM is separated from the beamline optics by a silicon nitride membrane of 100-nm thickness; therefore, sample folders can be handled in vacuum or in helium.

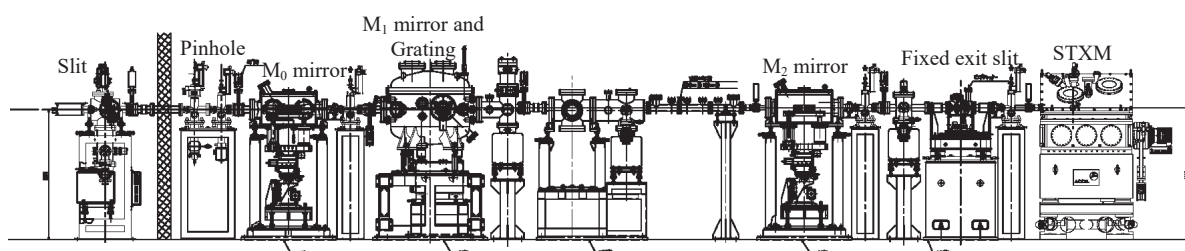


Fig. 1. Schematic image of BL4U.

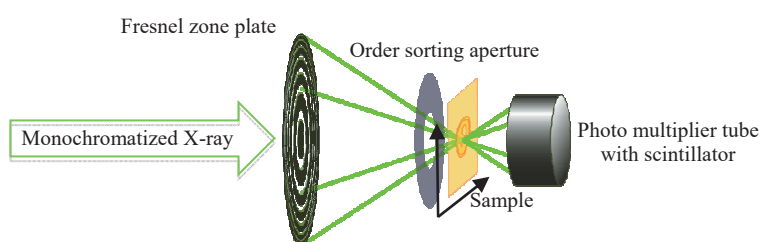


Fig. 2. Schematic image of the STXM.

▼ Technical Data

Energy range (E)	100-770 eV
Resolving power ($E / \Delta E$)	$\sim 6,000$
Focusing optical element	Fresnel zone plate
Spatial resolution	~ 30 nm
Experiments	2-dimensional absorption spectroscopy
Measurement environment	standard sample folder in vacuum or in helium, specially designed sample cell in ambient condition

BL4B

Varied-Line-Spacing Plane Grating Monochromator for Molecular Soft X-Ray Spectroscopy

▼ Description

The beamline BL4B equipped with a varied-line-spacing plane grating monochromator (VLS-PGM) was constructed for various spectroscopic investigations in a gas phase and/or on solids in the soft X-ray range. Three holographically ruled laminar profile plane gratings with SiO₂ substrates are designed to cover the photon energy range from 25 to 800 eV. The gratings with groove densities of 100, 267, and 800 1/mm cover the spectral ranges of 25–100, 60–300, and 200–1000 eV, respectively, and are interchangeable without breaking the vacuum. Figure 1 shows the absolute photon flux for each grating measured using a Si photodiode (IRD Inc.), with the entrance- and exit-slit openings set at 50 and 50 μm, respectively. The maximum resolving power ($E / \Delta E$) achieved for each grating exceeds 5000.

There is no fixed endstation on this beamline. A small vacuum chamber equipped with an electron multiplier (EM) detector is available. Soft X-ray absorption spectra of solid samples are usually measured by means of the total electron yield method using EM, and the partial fluorescence yield method using a silicon drift detector (SDD).

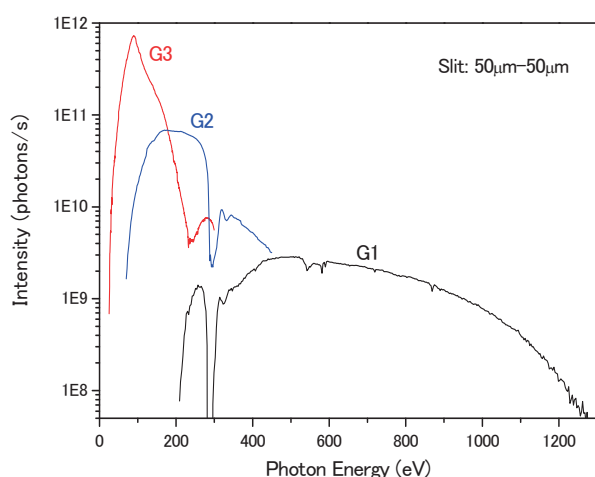


Fig. 1. Throughput from the VLS-PGM monochromator on BL4B.

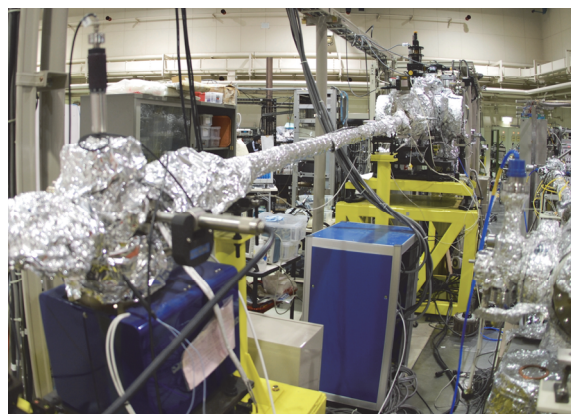


Fig. 2. Photo of BL4B.

▼ Technical Data

Monochromator	Varied-line-spacing Plane Grating Monochromator
Energy range	25-1000 eV
Resolution	$E / \Delta E > 5000$ (at maximum)
Experiments	Soft X-ray spectroscopy (mainly, photoabsorption spectroscopy for solid targets by means of total electron yield method using EM and partial fluorescence yield method using SDD)

BL5U

Photoemission Spectroscopy of Solids and Surfaces

▼ Description

Since the monochromator of BL5U was an old-style spherical grating type SGMTRAIN constructed in 1990s and the throughput intensity and energy resolution were poor, the whole beamline has been replaced to state-of-the-art monochromator and end station. The new beamline has been opened to users from FY2016 as high-energy resolution ARPES beamline. Samples can be cooled down to 3.8 K with newly developed 5-axis manipulator to perform high energy resolution measurements. Users can also obtain spatial-dependence of the electronic structure of solids using micro-focused beam ($\sim 50 \mu\text{m}$). The new electron lens system makes it possible to obtain ARPES spectra without moving samples. This beamline will also have new capability to perform high-efficient spin-resolved ARPES in the future.

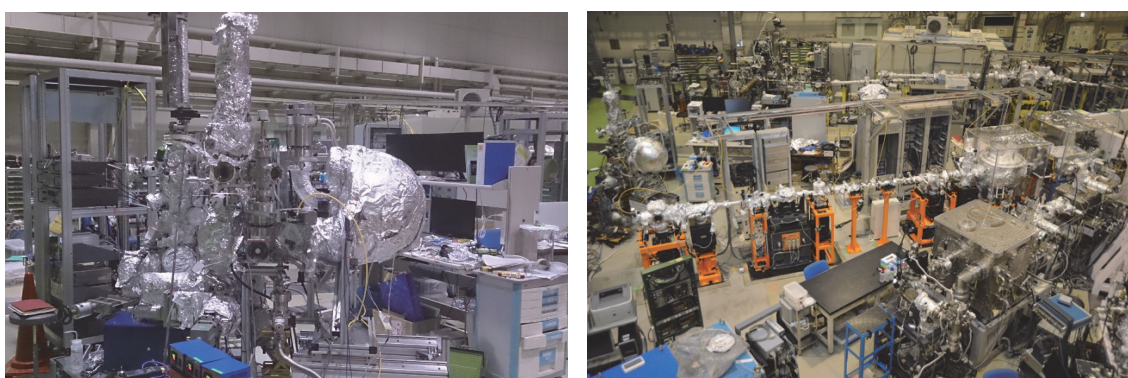


Fig. 1. Pictures of BL5U.

▼ Technical Data (Expected Performance)

Light source	APPLE-II type undulator ($\lambda_u = 60 \text{ mm}$, $N = 38$) vertical/horizontal, right/left circular (depending on $h\nu$)
Monochromator	Monk-Gillieson VLS-PGM
Energy Range	20-200 eV
Resolution	$h\nu / \Delta E > 10,000$ for $< 10 \mu\text{m}$ slits
Experiment	ARPES, Space-resolved ARPES, Spin-resolved ARPES
Flux	$< 10^{12}$ photons/s for $< 10 \mu\text{m}$ slits (at the sample position)
Beam spot size	23 (H) x 40 (V) μm
Main Instruments	Hemispherical photoelectron analyzer with deflector scan (MBS A-1 Lens#4), Liq-He flow cryostat with 5-axis manipulator (3.8 K-350 K)

BL5B

Calibration Apparatus for Optical Elements and Detectors

II

▼ Description

BL5B has been constructed to perform calibration measurements for optical elements and detectors. This beamline is composed of a plane grating monochromator (PGM) and three endstations in tandem. The most upstream station is used for the calibration measurements of optical elements, the middle one for optical measurements for solids, and the last for photo-stimulated desorption experiments. The experimental chamber at the most downstream station is sometimes changed to a chamber for photoemission spectroscopy. The calibration chamber shown in Fig. 2 is equipped with a goniometer for the characterization of optical elements, which has six degrees of freedom, X-Y translation of a sample, and interchanging of samples and filters. These are driven by pulse motors in vacuum. Because the polarization of synchrotron radiation is essential for such measurements, the rotation axis can be made in either the horizontal or vertical direction (s- or p-polarization).

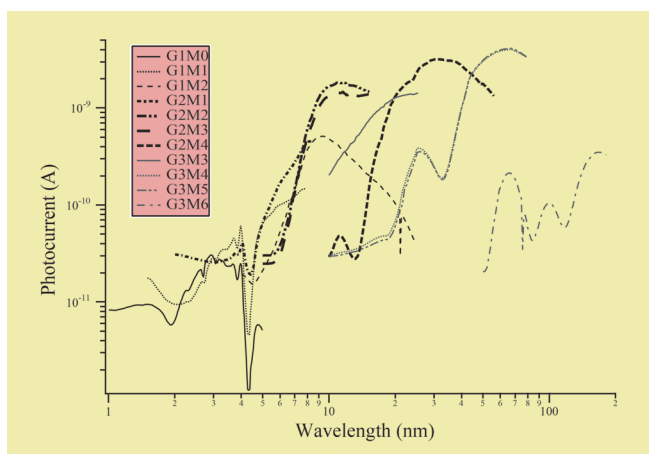


Fig. 1. Throughput spectra for possible combinations of gratings and mirrors at BL5B measured by a gold mesh.

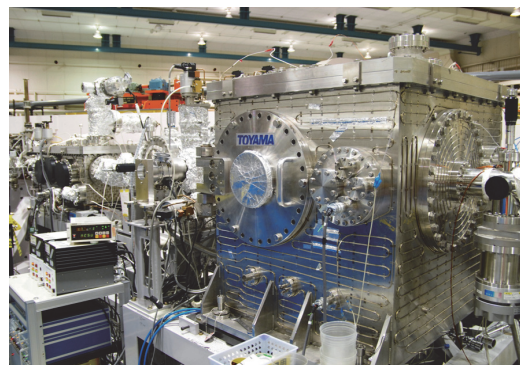


Fig. 2. A side view of the experimental chamber for calibration measurements.

▼ Technical Data

Monochromator	Plane Grating Monochromator
Energy range	6-600 eV (2-200 nm)
Resolution	$E / \Delta E \sim 500$
Experiments	Calibration of optical elements, reflection and absorption spectroscopy mainly for solids

BL6U

Variable-Included-Angle VLS-PGM for Molecular Soft X-Ray Spectroscopy

▼ Description

The beamline BL6U equipped with a variable-included-angle Monk-Gillieson mounting monochromator with a varied-line-spacing plane grating was constructed for various spectroscopic investigations requiring high-brilliance soft X-rays in a gas phase and/or on solids. Through a combination of undulator radiation and sophisticated monochromator design (entrance slit-less configuration and variable-included-angle mechanism), using a single grating, the monochromator can cover the photon energy ranging from 30 to 500 eV, with resolving power of greater than 10000 and photon flux of more than 10^{10} photons/s. Figure 1 shows an example of the monochromator throughput spectra measured using a Si photodiode, with the exit-slit opening set at $30\ \mu\text{m}$, which corresponds to the theoretical resolving power of 10000 at 80 eV.

The end station is equipped with an electron energy analyzer for angle-resolved photoelectron spectroscopy.

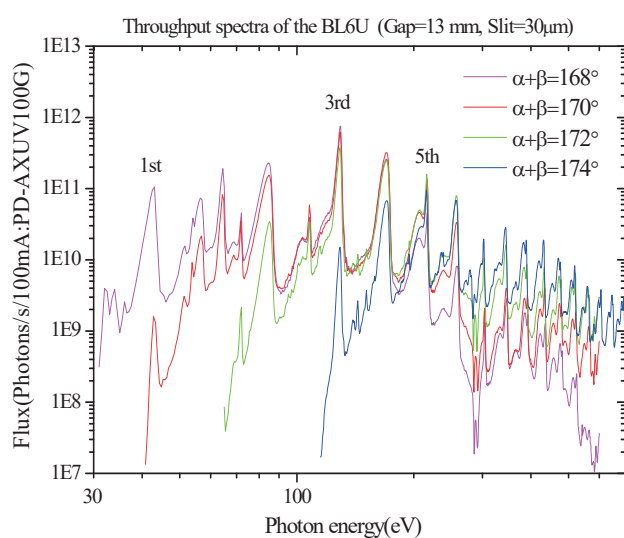


Fig. 1. Throughput spectra of the BL6U monochromator at various included angles.

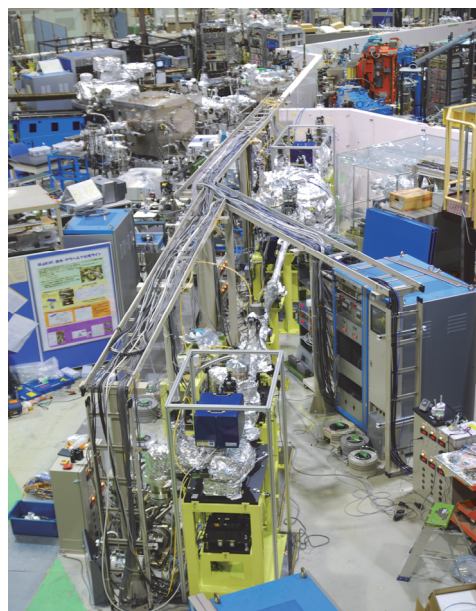


Fig. 2. Photo of BL6U.

▼ Technical Data

Monochromator	Variable-included-angle Varied-line-spacing Plane Grating Monochromator
Energy range	40-500 eV
Resolution	$E / \Delta E > 10000$ (at maximum)
Experiments	High-resolution soft X-ray spectroscopy (mainly photoelectron spectroscopy for gaseous and solid targets)

BL6B

Infrared and Terahertz Spectroscopy of Solids

II

▼ Description

Synchrotron radiation (SR) has good performance (high brilliance and high flux) not only in the VUV and soft X-ray (SX) regions but also in the infrared (IR) and THz regions. BL6B covers the IR and THz regions. The previous beamline, BL6A1, which was constructed in 1985, was the pioneer in IRSR research. The beamline was deactivated at the end of FY2003 and a new IR/THz beamline, BL6B (IR), was constructed in FY2004. The front-end part including bending duct #6 was replaced with a new part having a higher acceptance angle ($215 \text{ (H)} \times 80 \text{ (V)} \text{ mrad}^2$) using a magic mirror, as shown in Fig. 1.

There are two Michelson type interferometers in this endstation; with first one (Bruker Vertex70v), which covers a wide spectral region from 30 to $20,000 \text{ cm}^{-1}$ ($h\nu = 4 \text{ meV}$ - 2.5 eV), reflection/absorption spectroscopy measurements of large samples (up to several mm) and IR/THz microscopy measurements of tiny samples (up to several tens of μm) can be performed. For reflection/absorption spectroscopy measurements, a liquid-helium-flow type cryostat with a minimum temperature of 4 K is installed. The other interferometer (Jasco FT/IR-6100), which covers 350 to $15,000 \text{ cm}^{-1}$ ($h\nu = 45 \text{ meV}$ - 1.8 eV), has been available for IR microscopy imaging measurements from FY2014. One can also perform ATR measurements using diamond ATR prism.

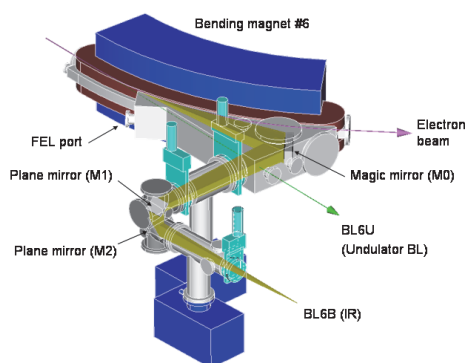


Fig. 1. Design of the optics and front end of BL6B.

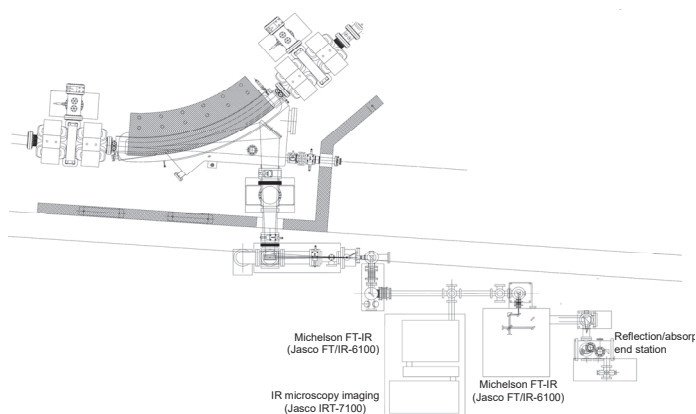


Fig. 2. Schematic top view of BL6B.

▼ Technical Data

Interferometer	Michelson (Bruker Vertex70v)	Michelson (Jasco FT/IR-6100)
Wavenumber Range (Energy range)	30 - $20,000 \text{ cm}^{-1}$ (4 meV - 2.5 eV)	350 - $15,000 \text{ cm}^{-1}$ (45 meV - 1.8 eV)
Resolution in cm^{-1}	0.1 cm^{-1}	0.5 cm^{-1}
Experiments	Reflectivity and transmission spectroscopy THz Microspectroscopy	IR microscopy imaging (JASCO IRT-7000) ATR spectroscopy

BL7U (SAMRAI)

Angle-Resolved Photoemission of Solids in the VUV Region

▼ Description

Beamline 7U, named the Symmetry- And Momentum-Resolved electronic structure Analysis Instrument (SAMRAI) for functional materials, was constructed to provide a photon flux with high energy resolution and high flux mainly for high-resolution angle-resolved photoemission spectroscopy, so-called “ARPES”, of solids [1]. An APPLE-II-type variable-polarization undulator is installed as the light source. The undulator can produce intense VUV light with horizontal/vertical linear and right/left circular polarization. The undulator light is monochromatized by a modified Wadsworth type monochromator with three gratings (10 m radius; 1200, 2400, and 3600 lines/mm optimized at $h\nu = 10, 20,$ and 33 eV). The energy resolution of the light ($h\nu / \Delta h\nu$) is more than 10^4 with a photon flux of 10^{11} - 10^{12} ph/s or higher on samples in the entire energy region. The beamline has a photoemission end-station equipped with a 200 mm-radius hemispherical photoelectron analyzer (MB Scientific AB, A-1 analyzer) with a wide-angle electron lens and a liquid-helium-cooled cryostat with 6-axis pulse motor control (AVC Co., Ltd., i-GONIO). The main function of the beamline is to determine the electronic structure of solids and its temperature dependence in order to reveal the origin of their physical properties.

[1] S. Kimura, T. Ito, M. Sakai, E. Nakamura, N. Kondo, K. Hayashi, T. Horigome, M. Hosaka, M. Katoh, T. Goto, T. Ejima and K. Soda, Rev. Sci. Instrum. **81** (2010) 053104.

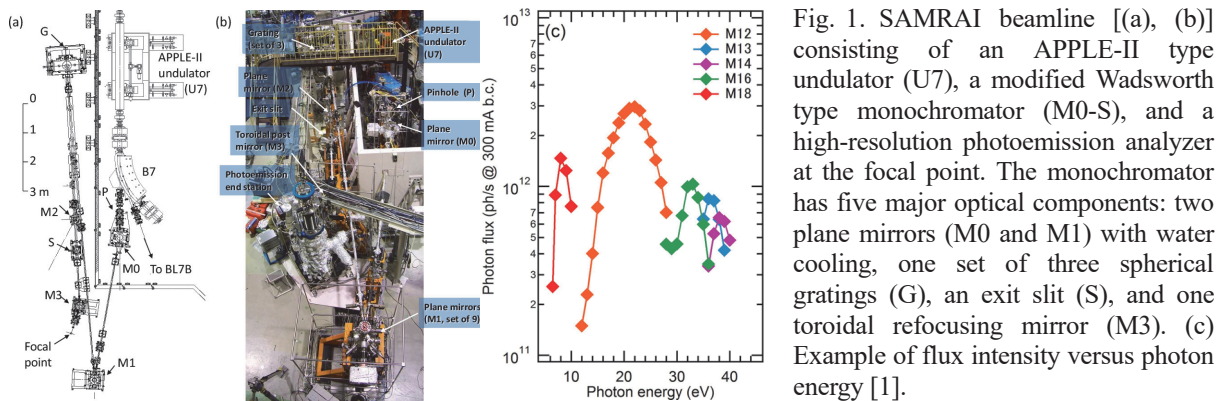


Fig. 1. SAMRAI beamline [(a), (b)] consisting of an APPLE-II type undulator (U7), a modified Wadsworth type monochromator (M0-S), and a high-resolution photoemission analyzer at the focal point. The monochromator has five major optical components: two plane mirrors (M0 and M1) with water cooling, one set of three spherical gratings (G), an exit slit (S), and one toroidal refocusing mirror (M3). (c) Example of flux intensity versus photon energy [1].

▼ Technical Data

Light source	APPLE-II type undulator ($\lambda_u = 76$ mm, $N = 36$) vertical/horizontal, right/left circular (depending on $h\nu$)
Monochromator	10 m normal-incidence monochromator (modified Wadsworth type)
Photon energy range	6-40 eV ($\lambda = 30$ -200 nm)
Resolution ($h\nu/\Delta h\nu$)	$E / \Delta E > 10000$ -50000
Photon flux on sample	$\geq 10^{12}$ - 10^{11} ph/s (depending on $h\nu$)
Beam size on sample	200 (H) \times 50 (V) μm^2
Experiments	Angle-resolved photoemission of solids (MV Scientific A-1 analyzer, acceptance angle: ± 18 deg)

BL7B

3 m Normal-Incidence Monochromator for Solid-State Spectroscopy

II

▼ Description

BL7B has been constructed to provide sufficiently high resolution for conventional solid-state spectroscopy, sufficient intensity for luminescence measurements, wide wavelength coverage for Kramers–Kronig analyses, and minimum deformation to the polarization characteristic of incident synchrotron radiation. This beamline consists of a 3-m normal incidence monochromator, which covers the vacuum ultraviolet, ultraviolet, visible, and infrared, i.e., the wavelength region of 50–1000 nm, with three gratings (1200, 600, and 300 l/mm). Two interchangeable refocusing mirrors provide two different focusing positions. For the mirror with the longer focal length, an LiF or a MgF₂ window valve can be installed between the end valve of the beamline and the focusing position. Fig.1 shows the absolute photon intensity for each grating with the entrance and exit slit openings of 0.5 mm. A silicon photodiode (AXUV-100, IRD Inc.) was utilized to measure the photon intensity and the absolute photon flux was estimated, taking the quantum efficiency of the photodiode into account.

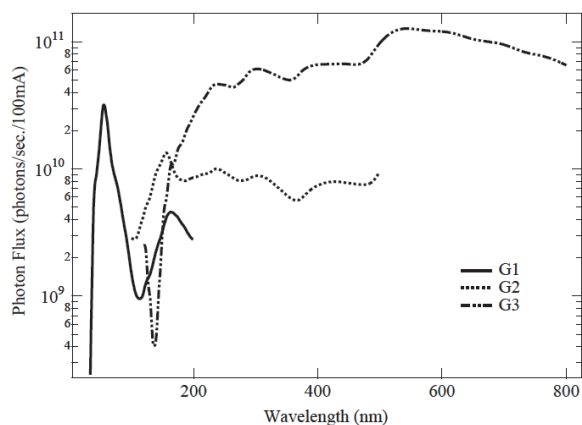


Fig. 1. Throughput spectra of BL7B measured using a silicon photodiode.

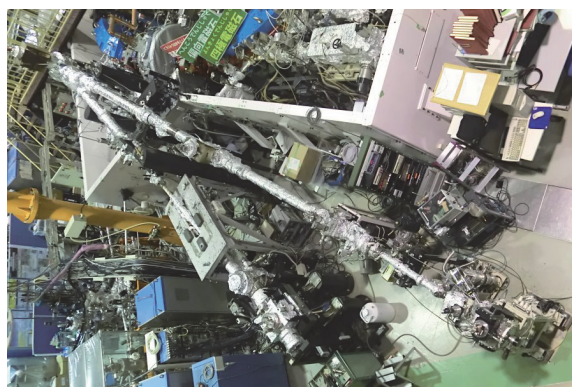


Fig. 2. Photo of BL7B.

▼ Technical Data

Monochromator	3 m Normal-Incidence Monochromator
Wavelength Range	1.2-25 eV (50-1000 nm)
Resolution	$E / \Delta E = 4000-8000$ for 0.01 mm slits
Experiments	Absorption, reflection, and fluorescence spectroscopy, mainly for solids

The background is a vibrant blue with a complex geometric design. A large, semi-transparent circular graphic is centered on the right side, featuring concentric rings and a dotted border. Diagonal lines and a grid of small dots are also visible, creating a sense of depth and movement.

III-1

Accelerators and
Instruments

BL1U

Reconstruction of Free-Electron-Laser Optical Resonator at BL1U

H. Zen¹, J. Yamazaki², M. Fujimoto^{2,3}, M. Hosaka⁴, K. Hayashi², M. Katoh^{2,3} and H. Ohgaki¹

¹*Institute of Advanced Energy, Kyoto University, Uji 611-0011, Japan*

²*UVSOR Synchrotron Facility, Institute for Molecular Science, Okazaki 444-8585, Japan*

³*School of Physical Sciences, The Graduate University for Advanced Studies (SOKENDAI), Okazaki 444-8585, Japan*

⁴*Nagoya University Synchrotron radiation Research center, Nagoya 464-8603, Japan*

An electron storage-ring-driven Free Electron Laser (FEL) had been developed at the straight section #5, of the UVSOR using an optical klystron and FEL optical resonator until 2009 [1]. The straight section #5 had been also used for developing new coherent light sources, such as the coherent synchrotron radiation, the coherent harmonic generation by combining the high energy electron beam circulating in the storage ring and the high-power femtosecond laser. In 2010, dedicated undulators with an electromagnet-based bunching section were installed in the straight section #1 of the UVSOR. Then the above activities have been moved from straight section #5 to #1.

In this work, we tried to reconstruct the FEL optical resonator at the straight section #1 and BL1U to restart the FEL which will be used for the generation of high intensity gamma-rays as same as the H γ S in Duke University [2].

The new layout of the FEL optical resonator mirrors (M1 and M2) and the optical klystron at the straight section #1 is depicted in Fig. 1. The optical klystron has been already installed in 2012. In this work, the optical resonator mirrors were installed in the beamline and some commissioning experiments of the optical resonator were carried out.

The photographs of the vacuum chamber of the optical resonator mirrors are shown in Fig. 2. The vacuum chambers are supported by large gimbal mounts equipped with a motorized actuator to control the angle of mirrors. The resonator mirrors with the diameter of 1 inch are installed in the vacuum chamber. The downstream side gimbal mount is placed on the linear stage which enables us to change the total cavity length.

The commissioning experiment was performed at

the wavelength of 540 nm. As a result, we could store the undulator radiation lights inside the optical resonator and observed strong lights from the resonator mirror as shown in Fig. 3. This indicates that the optical cavity mirrors has good alignment in the transverse direction. In the next machine time, the length of the optical resonator will be optimized to achieve the lasing of UVSOR-FEL with this new configuration.

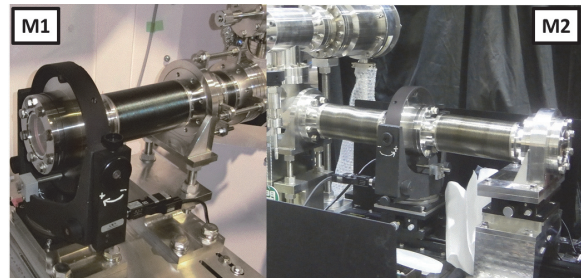


Fig. 2. Photograph of the vacuum chamber for FEL optical resonator mirrors.

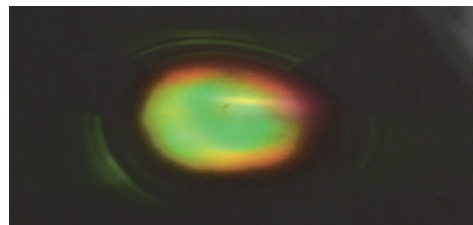


Fig. 3. Photograph of the strong lights from the optical resonator.

- [1] H. Zen *et al.*, Proc. of FEL2009 (2009) 576.
 [2] <http://www.tunl.duke.edu/web.tunl.2011a.higs.php>

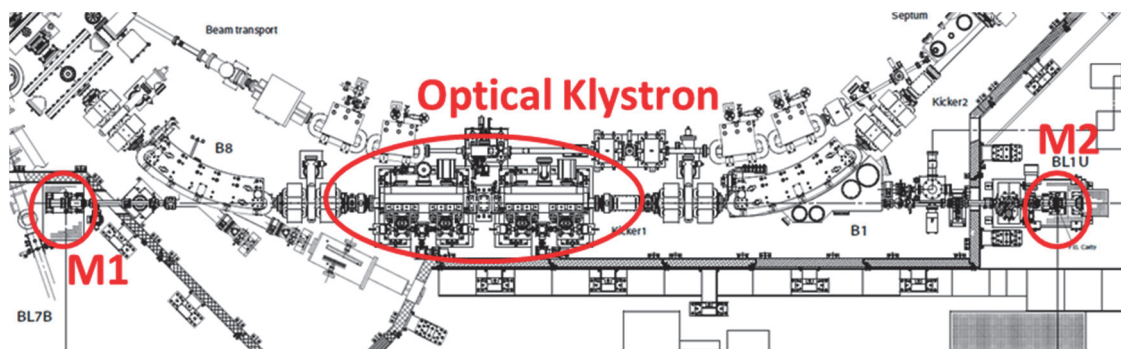


Fig. 1. Layout of FEL optical resonator mirrors (M1 and M2) and the optical klystron at the straight section #1 of UVSOR.

BL1U

Observation of XUV Vortex Beam from a Helical Undulator

T. Kaneyasu¹, Y. Hikosaka², M. Fujimoto^{3,4}, H. Iwayama^{3,4}, M. Hosaka⁵, E. Shigemasa^{3,4} and M. Katoh^{3,4}

¹SAGA Light Source, Tosu 841-0005, Japan

²Graduate School of Medicine and Pharmaceutical Sciences, University of Toyama, Toyama 930-0194, Japan

³UVSOR Synchrotron Facility, Institute for Molecular Science, Okazaki 444-8585, Japan

⁴The Graduate University for Advanced Studies (SOKENDAI), Okazaki 444-8585, Japan

⁵Synchrotron Radiation Research Center, Nagoya University, Nagoya 464-8603, Japan

An optical vortex beam carries orbital angular momentum (OAM), as well as spin angular momentum associated with its circular polarization. Recently it has been reported that the spiral motion of a relativistic electron naturally leads to the emission of photons carrying OAM [1]. A typical example of the vortex radiation is found in the harmonic radiation of a helical undulator in synchrotron light sources [2, 3]. Since the helical undulators are widely used in modern synchrotron light sources, the optical vortex beam generated as harmonic radiation may open up new opportunities in synchrotron radiation researches. Here we report on the observation of the extreme ultraviolet (XUV) vortex beam at 60 nm wavelength, produced as the second harmonic radiation from a helical undulator [4].

The experiment was carried out at the BL1U. To characterize experimentally the optical vortex beam, we observed an interference pattern between the photon beams from two helical undulators. The reference beam without OAM was produced as the fundamental radiation from the upstream undulator, while the optical vortex beam was produced as the second-harmonic radiation from the downstream undulator. The radiation wavelengths were set to 60 and 120 nm for the fundamental radiation from the upstream and downstream undulators, respectively. The spatial distribution of the photon beam was measured by scanning a pinhole.

Figure 1(a) compares the interference patterns measured for the left and right circular polarization modes. The direction of the spiral pattern changes with the helicity, as predicted in theoretical studies. The dotted curves in Fig. 1(b) show the calculated interference patterns, which agree with the experimental results. Thus, it is reasonable to conclude that optical vortex beams carrying an OAM of $l\hbar$ ($l=\pm 1$) per photon are produced in the XUV region. In the present experiment, the electron beam emittance is 17.5 nm-radian, which is about four times larger than the 4.8 nm-radian corresponding to the diffraction-limited emittance at 60-nm wavelength. Consequently, the measured spiral patterns are blurred, owing to the relatively large electron beam emittance, whereas an individual electron emits an optical vortex with a phase singularity and zero-intensity minimum. To reveal the overall features of the interference pattern

smearing by the finite emittance, we performed a simulation using the SRW code [5] as in Fig. 1(c). It can be clearly seen that the simulation reproduces the experiments, which confirms the reliability of the measurement.

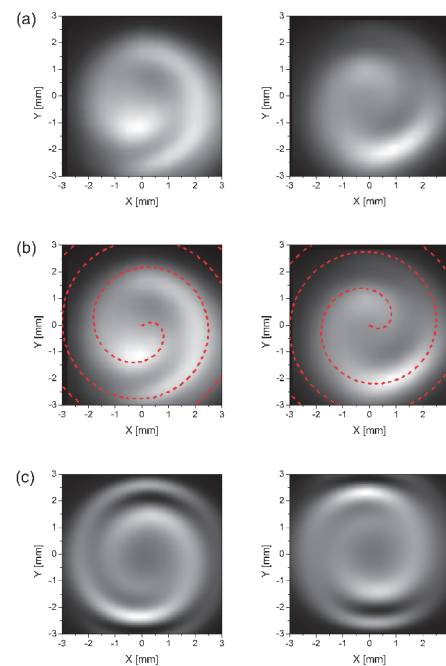


Fig. 1. Interference patterns at 60-nm wavelength produced by interfering the optical vortex beam with the reference beam without OAM. Left column: left circular polarization. Right column: right circular polarization. (a) Measurement results. (b) Same as (a) with the dotted curves representing the constructive interference patterns predicted by the theoretical model. (c) Simulation results by SRW code.

[1] M. Katoh *et al.*, *Sci. Rep.* **7** (2017) 6130.

[2] S. Sasaki and I. McNulty, *Phys. Rev. Lett.* **100** (2008) 124801.

[3] J. Bahrtdt *et al.*, *Phys. Rev. Lett.* **111** (2013) 034801.

[4] T. Kaneyasu *et al.*, *J. Synchrotron Rad.* **24** (2017) 934.

[5] O. Chubar *et al.*, *Nucl. Instrum. Meth. A* **435** (1999) 495.

BL2A

Evaluation of a Flight High-Speed Back-Illuminated CMOS Sensor in a Soft X-Ray Range for FOXSI-3 Sounding Rocket Project

N. Narukage¹ and S. Ishikawa²

¹National Astronomical Observatory of Japan, Mitaka 181-8588, Japan

²Institute of Space and Astronautical Science, Japan Aerospace Exploration Agency, Sagami-hara 252-5210, Japan

The solar corona is full of dynamic phenomena. They are accompanied by interesting physical processes, namely, magnetic reconnection, particle acceleration, shocks, waves, flows, evaporation, heating, cooling, and so on. The understandings of these phenomena and processes have been progressing step-by-step with the evolution of the observation technology in EUV and X-rays from the space. But, there are fundamental questions remain unanswered, or haven't even addressed so far. Our scientific objective is to understand underlying physics of dynamic phenomena in the solar corona, covering some of the long-standing questions in solar physics such as particle acceleration in flares and coronal heating. In order to achieve these science objectives, we identify the imaging spectroscopy (the observations with spatial, temporal and energy resolutions) in the soft X-ray range (from ~ 0.5 keV to ~ 10 keV) is a powerful approach for the detection and analysis of energetic events [1]. This energy range contains many lines emitted from below 1 MK to beyond 10 MK plasmas plus continuum component that reflects the electron temperature.

The soft X-ray imaging spectroscopy is realized with the following method. We take images with a short enough exposure to detect only single X-ray photon in an isolated pixel area with a fine pixel Silicon sensor. So, we can measure the energy of the X-ray photons one by one with spatial and temporal resolutions. When we use a high-speed soft X-ray camera that can perform the continuous exposure with a rate of 1,000 times per second, we can count the photon energy with a rate of several 10 photons / pixel / second. This high-speed exposure is enough to track the time evolution of spectra generated by dynamic phenomena in the solar corona, whose lifetimes are about from several ten seconds to several minutes.

As the first imaging spectroscopic observation of the sun in soft X-ray range, we plan to launch the NASA's sounding rocket (FOXSI-3) in the summer of 2018.

In this time, we evaluated quantum efficiency (QE) of a flight back-illuminated high-speed CMOS sensor at UVSOR BL2A (see Fig. 1). The sensor was driven with a flight camera electronics board [2]. As a reference sensor, we used the photodiode AXUV100G. The preliminary result of the measured QE is shown in

Fig. 2. The measured QE of the flight sensor is within the expected range that is calculated with the material and thickness of the sensor. Based on this QE measurement, we will finalize the thickness of the attenuation filter to adjust the incident X-ray flux into the sensor suitably for the photon counting.

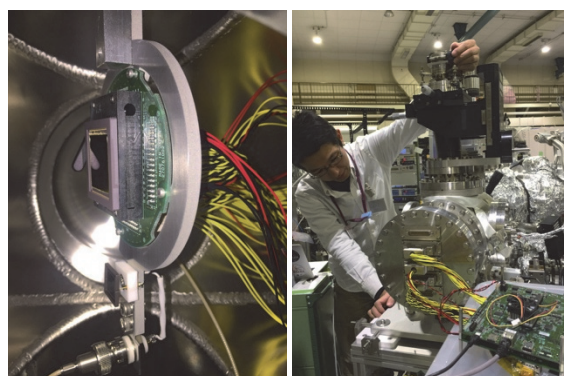


Fig. 1. Setting of CMOS sensor evaluation with a flight camera system. Left: CMOS sensor and photodiode deployed in a vacuum chamber. Right: Flight camera electronics board (green board in this picture).

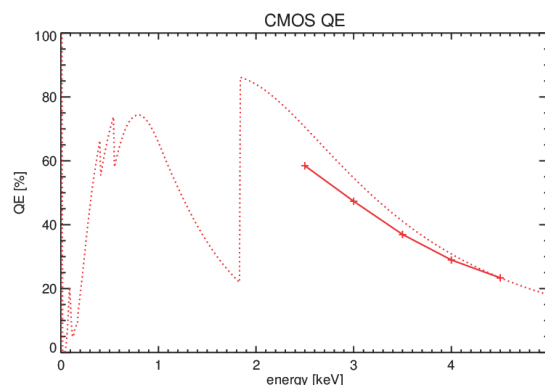


Fig. 2. Preliminary result of the measured quantum efficiency (QE) of the flight CMOS sensor. The solid and dotted lines show the measured and expected QE, respectively.

[1] N. Narukage *et al.*, White paper of the “soft X-ray imaging spectroscopy”, arXiv:1706.04536 (2017).

[2] S. Ishikawa *et al.*, arXiv:1711.04372 (2017).

BL4U

Development of a Cryo-Cooling System for Scanning Transmission X-ray Microscopy

T. Ohigashi^{1,2}, F. Kaneko³, Y. Inagaki¹, T. Yano¹, H. Kishimoto³ and N. Kosugi^{1,2}

¹UVSOR Synchrotron Facility, Institute for Molecular Science, Okazaki 444-8585, Japan

²School of Physical Sciences, SOKENDAI (The Graduate University for Advanced Studies), Okazaki 444-8585, Japan

³Sumitomo Rubber Industries, Kobe, 651-0072, Japan

A scanning transmission X-ray Microscope (STXM) is a powerful tool to obtain 2-dimensional chemical states with high spatial resolution. By using the STXM in the soft X-ray region, core-level absorption edges of light elements, carbon, nitrogen and oxygen, are available for the measurement. Generally speaking, the radiation damage by X-rays is lower than that by electron beams [1]. This means that even organic materials, such as polymers, carbon nanotubes and biological specimens that are very sensitive to radiations, can be targets of the STXM. However, in spite of the lower radiation damage of X-rays, some samples show chemical or morphological changes during the measurement. For example, rubber, one of reasonable targets for the STXM analysis [2, 3], is easily damaged by the irradiation of X-rays. It is known that the cooling of rubber samples reduces radiation effects [4]. In the present work, therefore, we have developed a cryo-cooling system.

A Dewar vessel is placed on the STXM. Liquid nitrogen in the vessel cool a sample mounting plate through copper braids. A sample holder is equipped with two sets of a heater and a temperature sensor. One of these combinations is for the temperature control of samples and the other one is for keeping the temperature of stages constant. These heaters are operated by PID controllers. Main issues of the cryo-cooling system for STXM are the vibration generated by bubbling of liquid nitrogen and the thermal stability. In the present work, by optimizing thermal insulation and stiffness of the copper braids, the vibration at the sample is successfully reduced down to 50 nm (peak to valley). By using this system, the sample mounting plate can be cooled down to -90°C.

A thin specimen (thickness of 250 nm) of vulcanized rubber was used as a sample. After measuring an energy stack at nitrogen K-edge by changing dwell time as 1, 2 and 4 ms, the energy stack at carbon K-edge was measured to evaluate damages on the sample. NEXAFS spectra around carbon K-edge at RT and at cryo condition of -85°C and an STXM image of a damaged sample are shown in Fig. 1. In Fig. 1(a) and 1(b), main peaks are 285.4 and 288.0 eV, corresponded to C=C π^* and C-H σ^* transition respectively. The damage by X-ray irradiation mainly appears on 285.4 and 288.0 eV as decrease of intensity and as broadening of peak width. Especially, the peaks

at 288.0 eV show apparent difference between RT and cryo conditions. In RT condition, peaks at 288.0 eV are dull and low rather than those in cryo condition although the lowest dose by the dwell time of 1 ms. Furthermore, height of the peaks at 285.4 in RT are lower than those in cryo condition. These differences show that using the cryo-cooling system is effective to reduce the damage on the sample. Currently, critical dose to analyze the vulcanized rubber and improvement of cryo temperature are under discussion.

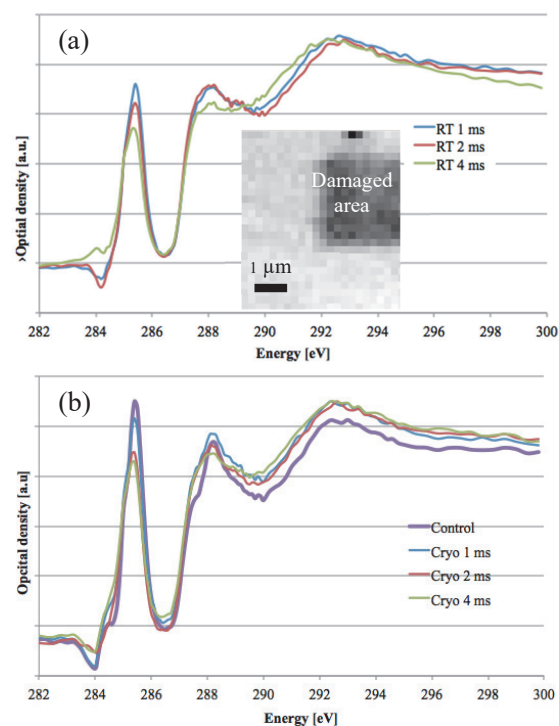


Fig. 1. NEXAFS spectra of pristine and damaged vulcanized rubber around carbon K-edge (a) at RT and (b) at -85°C. An inset in (a) is an STXM image of the damaged vulcanized rubber acquired at 285.4 eV.

- [1] H. Ade *et al.*, *Science* 258 (1992) 972.
- [2] D. A. Winesett *et al.*, *Rubber. Chem. Technol.* **76** (2003) 803.
- [3] D. A. Winesett *et al.*, *Rubber. Chem. Technol.* **80** (2007) 14.
- [4] G. Schneider, *Ultramicroscopy* **75** (1998) 85.

BL4U

High Pressure STXM Cell

P. –A. Glans¹, Y. S. Liu¹, R. M. Qiao¹, T. Ohigashi^{2, 3} and J. –H. Guo¹

¹Advanced Light Source, Lawrence Berkeley Nat'l Lab. 1 Cyclotron Road, Berkeley, CA 94720, USA

²UVSOR Synchrotron Facility, Institute for Molecular Science, Okazaki 444-8585, Japan

³School of Physical Sciences, The Graduate University for Advanced Studies (SOKENDAI), Okazaki 444-8585, Japan

Measurements of the electronic structure of materials in vacuum or even at atmospheric pressure are becoming more and more common. Some catalytic reactions, however, occur at, or create, higher pressures: gas evolution (such as water splitting), some catalytic processes are more efficient at higher pressures, some batteries operate at pressures higher than 1 atm, High pressures are also necessary to investigate phase transitions of gasses.

A high-pressure cell for the STXM has been designed and tested at the BL4U at UVSOR, see Fig. 1. The body of the cell is made out of PEEK for maximum chemical compatibility. Windows similar to what is usually used at the STXM but with a custom window size were made at the Lawrence Berkeley Lab. The window size was 75 μ m x 75 μ m, set in frames of 5 mm x 5 mm and 10 mm x 10 mm. The cell was tested off-line and could reliably hold gauge pressures up to 10 bar. Liquid can flow through the cell through PEEK tubing. Once the system is filled, a valve on the drain end is closed and the system is pressurized by running the pump until required pressure has been achieved.

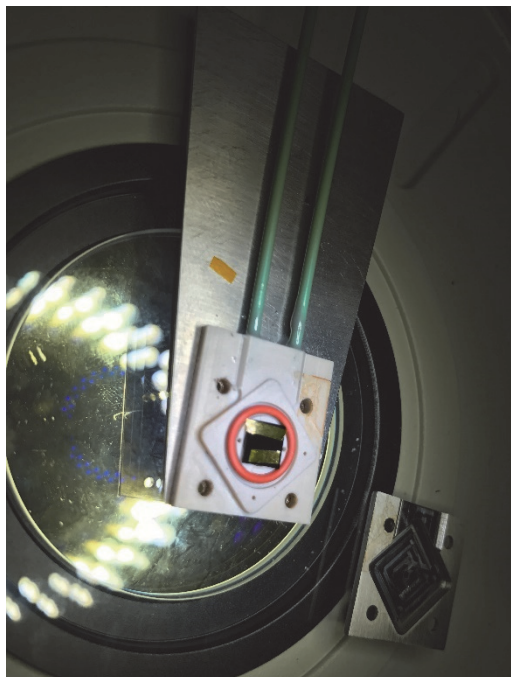


Fig. 1. Partially assembled high-pressure cell. The cell is mounted on the standard STXM sample holder.

The back window (5 mm x 5 mm frame) is visible together with Teflon spacers and the outer o-ring. A larger window (10 mm x 10 mm frame) will be mounted on top and the lid – visible to the right in the photo – will finish the ‘sandwich.’ The large window is rotated 45 degrees with respect to the smaller one.

The cell was loaded with water or CaCl₂ solutions with concentrations ranging from 0.5 M to 3.0 M. The pressure was controlled with a syringe pump and measured by a pressure gauge. In the STXM chamber we did not go past 2.0 bar gauge pressure for safety reasons. Figure 2 shows example data of the Ca L_{2,3} edge XAS from 1.5 M solution of CaCl₂ in water at 0 bar gauge pressure and 2.0 bar gauge pressure.

The cell performed very well and we could collect spectra at elevated pressures. However, the next iteration needs a way to measure I₀ and a solution to minimize the bulging of the windows. A future version of the cell will also include electrodes to allow for electrochemical reactions.

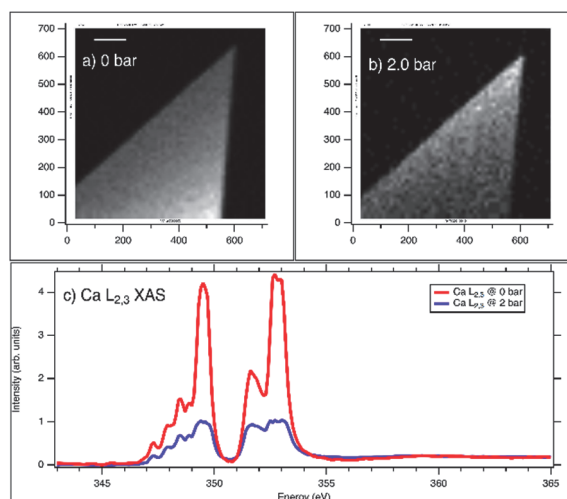


Fig. 2. STXM images of 1.5 M CaCl₂ solution at a) 0 bar gauge pressure, and at b) 2.0 bar gauge pressure. c) Ca L_{2,3} XAS extracted from the images. Unfortunately, i) there was no access to an I₀ channel to normalize the spectra, and ii) the optical density was too high at higher pressures due to bulging cells so the XAS is saturated at 2.0 bar.

BL7B

Performance Verification of the VUV Coating for the CLASP2 Flight Mirrors

D. Song¹, R. Ishikawa¹, R. Kano¹, K. Shinoda¹ and M. Yoshida²

¹National Astronomical Observatory of Japan, Mitaka 181-8588, Japan

²Department of Astronomical Science, Graduate University for Advanced Studies (SOKENDAI), Tokyo 181-8585, Japan

We are developing an ultraviolet spectro-polarimeter (SP) for a sounding rocket experiment named Chromospheric LAYER Spectro-Polarimeter (CLASP2). The CLASP2 is re-flight project of the Chromospheric Lyman-Alpha Spectro-Polarimeter (CLASP1), which successfully observed the Lyman-alpha polarization in 2015 [1], but will observe the polarization in 2019 with the different lines from the CLASP1 after a small modification in the optics. It mainly aims to achieve the high-sensitivity ($< 0.1\%$) spectro-polarimetric observations in the Mg II h & k lines (near 280 nm) for deriving the magnetic information in the upper chromosphere of the Sun and also to get solar images in the Lyman-alpha line (121.6 nm) with the high temporal resolution. Therefore, it requires the high throughput not only near 280 nm but also around 121.6 nm wavelengths.

In this fiscal year, we prepared all CLASP2 flight mirrors. On the primary mirror of the telescope (TL), a dual-band pass “cold mirror” coating targeting both the 121.6 nm ($R > 40\%$) and 280 nm ($R > 70\%$) was performed by Acton Optics. In addition, the high reflectivity mirror coating (Al+MgF₂ coating) was done by Acton Optics on the new fabricated SP mirrors ($R > 80\%$ near 280 nm for convex hyperbolic mirrors and folder mirrors, and $R > 75\%$ near 121.6 nm for a slit mirror).

To evaluate their coating performance, we measured the reflectivity of witness samples (WSs) for the p- and s-polarized beam (hereafter, R_p and R_s) at the UVSOR BL7B. The WSs are 1-inch flat mirrors simultaneously coated with the flight mirrors during the coating processes [2]. For the primary mirror coating, WSs were spread over the area corresponding to the effective area of the primary mirror to check the uniformity of the reflectivity.

Figure 1 shows the reflectivity of the WSs for the primary mirror in the wide wavelength ranges. The measured reflectivity is larger than 55% near the 121.6 nm wavelength and also larger than 76% near the 280 nm wavelength. Meanwhile, the average reflectivity in the visible light wavelength ranges is less than 5%, which had been measured by the Acton Optics. This indicates that the “cold mirror” coating performed on the primary mirror not only has high reflectivity near our required UV wavelengths, but also efficiently eliminates unwanted lights such as visible light.

From Fig. 2, we can verify the performance of the high reflectivity coating at Angle of Incidence (AOI)

as required by our SP mirrors. Note that, more information is given in Table 1.

Based on our measurements with WSs of the flight mirrors, we confirmed the following three: (1) The coatings performed on the flight mirrors (TL and SP) well satisfy our specifications. (2) The coating of the primary mirror (diameter: 290 m) is sufficiently uniform. (3) Finally, the computed throughput is about 1.8%, which is three times larger than the value of CLASP1 instrument (0.6%).

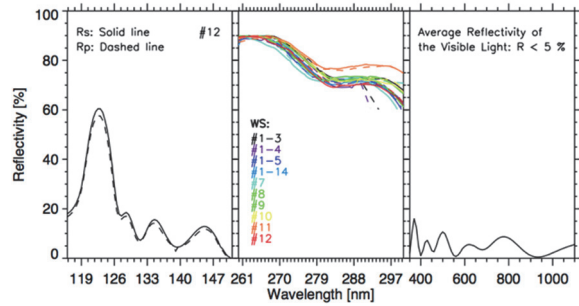


Fig. 1. Measured reflectivity of 10 witness samples for the primary mirror as a function of wavelengths.

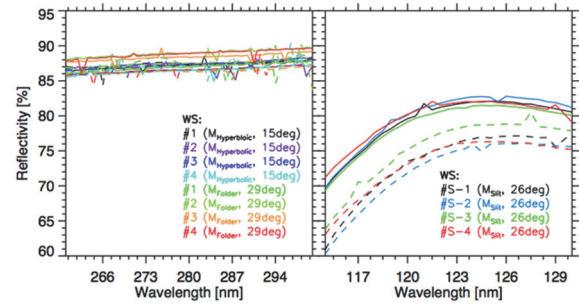


Fig. 2. Measured reflectivity of witness samples for the SP mirrors.

Table 1. Measured reflectivity of WSs for SP mirrors

Mirror	AOI (°)	R_p	R_s	$(R_p+R_s)/2$
$M_{Hyperbolic}$	11-18	87%	87.5%	87.3%
M_{Folder}	24-33	87%	88%	87.5%
M_{Slit}	22-30	73%	81%	77%

[1] R. Kano *et al.*, *ApJL*, **839** (2017), L10.

[2] N. Narukage *et al.*, *UVSOR Activity Report* **40** (2012) 46.

BL7B

Stokes Parameters Measurements of the BL7B by Using VUV Ellipsometry (III)

 F. Sawa¹, S. Takashima¹, K. Fukui¹, K. Yamamoto², T. Saito³ and T. Horigome⁴
¹Department of Electrical and Electronics Engineering, University of Fukui, Fukui 910-8507, Japan

²Far-infrared region Development Research Center, University of Fukui, Fukui 910-8507, Japan

³Department of Environment and Energy, Tohoku Institute of Technology, Sendai 982-8577, Japan

⁴UVSOR Synchrotron Facility, Institute for Molecular Science, Okazaki 444-8585, Japan

Since it is difficult to construct vacuum ultraviolet region (VUV) ellipsometers, there exists only one beamline equipped with VUV spectroscopic ellipsometer (SE) at BESSY [1] in the world to our knowledge. Saito et al. proposed the other idea for VUV SE, which is dedicated to the synchrotron radiation (SR) and used an oblique incidence detector [2, 3]. Compared with the standard SE, this type of SE has an advantage in obtaining not only optical constants of the sample, but also Stokes parameters (S_1/S_0 , S_2/S_0 , S_3/S_0) (SPs) of the incident beam. We installed this type of SE at the BL7B of UVSOR. Since these SPs must be invariant even if the sample changes, we can use this characteristics as an indicator of the reliability of unknown sample experiment results. Therefore, we have been continuing to improve the reproducibility by eliminating the causes to reduce them. On the other hand, we have not confirmed the correctness of the absolute value for these SPs. In this report, we have compared the results of our VUV SE against the results obtained by using dichroic dye film type polarizers in the visible region (300 ~ 500 nm) for the SPs of BL7B output beam to further confirm the correctness of the absolute SPs based on our SE.

Figure 1 shows schematic layout of our VUV SE with Au mirror as a standard sample. Measurement system using the VIS polarizer is shown in Fig. 2. In Fig. 2, since the polarizer set at the sample position instead of a Au mirror is a transmission type, optical conditions are the same between two methods. Figure 3 shows SPs of BL7B output beam as a function of wavelength obtained by our VUV SE (solid circles) and polarizers (open circles). It is noted that S_3/S_0 and unpolarized components cannot be distinguished in the experiment by using the polarizer. As expected from both the characteristics of SR and the optical configuration of the BL7B, the results of both experimental methods show that S_1/S_0 values are close to 1 and both S_2/S_0 and S_3/S_0 have small values. The agreements between the two methods for both S_2/S_0 and S_1/S_0 in all wavelength region validates our SE.

[1] W. Budde and R. Dittmann, PTB-Mitt. **83** (1973) 1.
 [2] T. Saito, M. Yuri and H. Onuki, Rev. Sci. Instrum. **66** (1995) 1570.

[3] T. Saito, K. Ozaki, K. Fukui, H. Iwai, K. Yamamoto, H. Miyake and K. Hiramatsu, Thin Solid Films **571** (2014) 517.

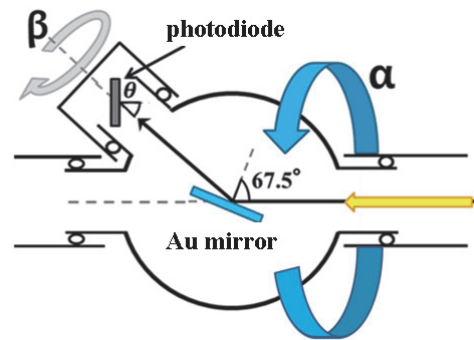


Fig. 1. Schematic layout of VUV SE.

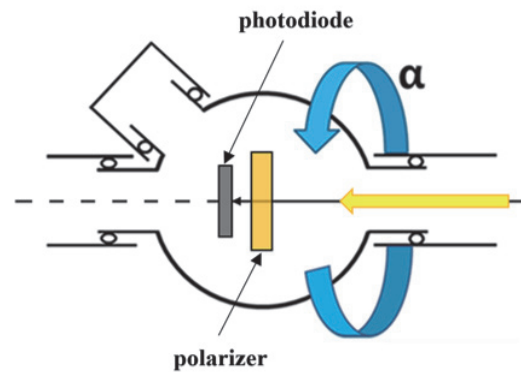


Fig. 2. Schematic layout of Stokes parameters measurement system using a polarizer.

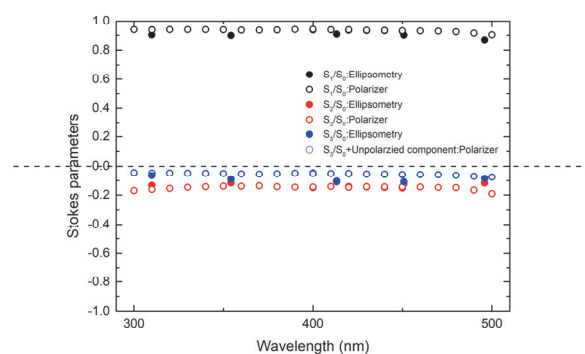
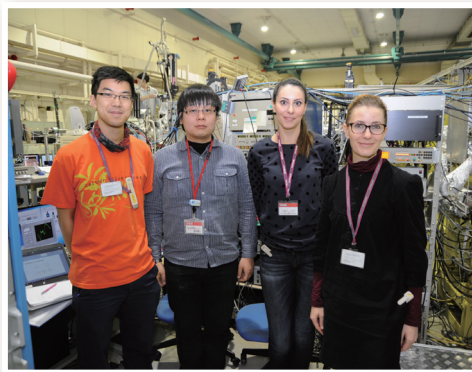
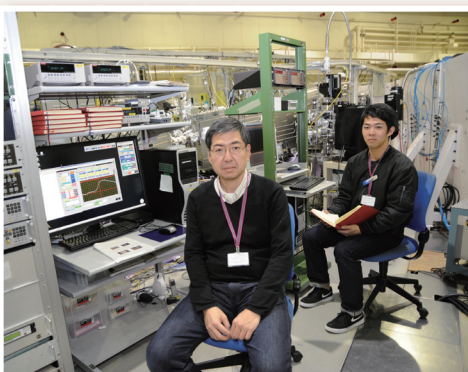
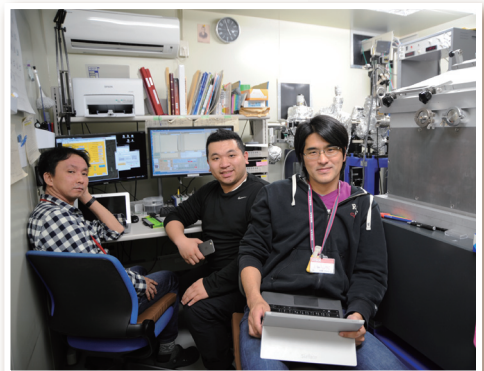
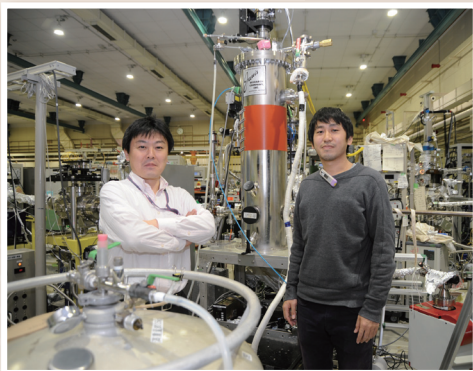
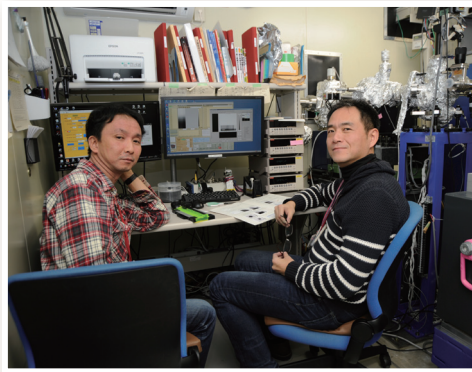
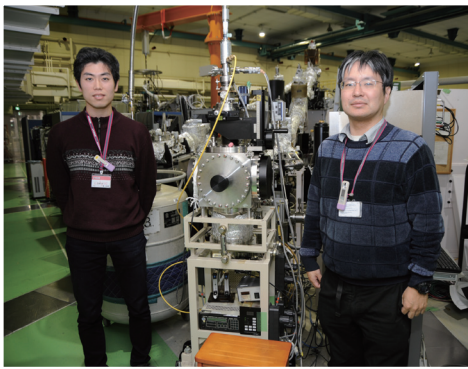
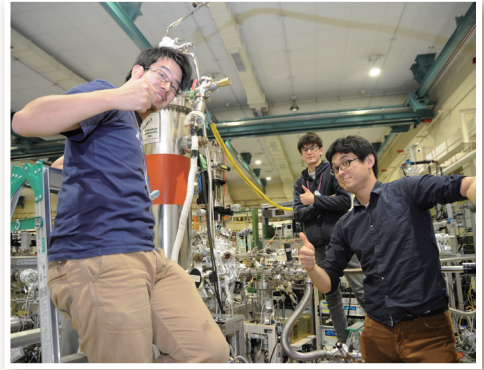
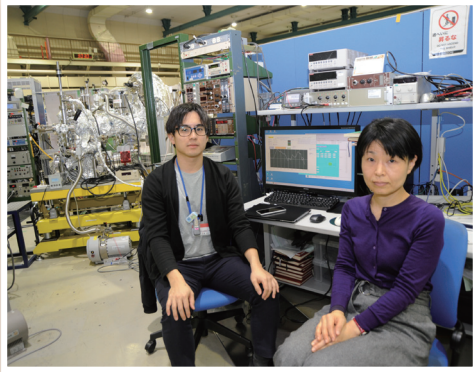
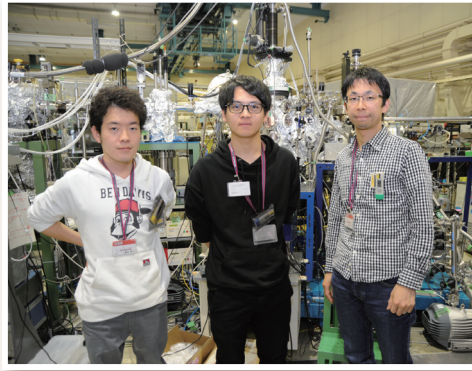
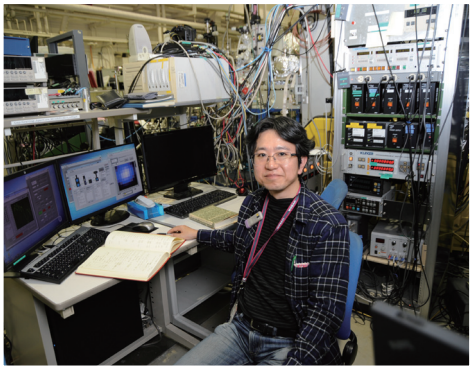


Fig. 3. Stokes parameters of BL7B.

UVSOR User 1



The background is a vibrant blue. In the upper right, there is a large, semi-transparent circular graphic composed of several concentric rings. The outermost ring features a series of small, light-blue circles. Below this graphic, the text 'III-2' is prominently displayed in a large, white, serif font. Underneath the main title, the words 'Materials Sciences' are written in a smaller, white, sans-serif font. The bottom half of the page is filled with a fine, light-blue grid of small dots.

III-2

Materials Sciences

BL7U

Electronic Structure of $\text{Sr}_{1-x}\text{Ca}_x\text{Fe}_2(\text{As}_{1-y}\text{P}_y)_2$ Revealed by Angle Resolved Photoemission Spectroscopy II

 T. Adachi¹, S. Ideta^{2,3}, K. Tanaka^{2,3}, T. Z. How¹, S. Miyasaka¹ and S. Tajima¹
¹Department of Physics, Graduate school of Science, Osaka University, Toyonaka 560-0043, Japan

²UVSOR Synchrotron Facility, Institute for Molecular Science, Okazaki 444-8585, Japan

³School of Physical Sciences, The Graduate University for Advanced Studies (SOKENDAI), Okazaki 444-8585, Japan

It is well known that there is a remarkable correlation between a crystal structure and T_c in iron based superconductor. Thus, it is essential for unraveling the superconducting (SC) mechanism in this system to clarify how the electronic structure (the topology of a Fermi surface (FS) and the SC gap structure) changes with the crystal structure. Recently we have performed ARPES measurements on $\text{Sr}_{1-x}\text{Ca}_x\text{Fe}_2(\text{As}_{1-y}\text{P}_y)_2$ ($x = 0.25, y = 0.08$) whose c/a (the ratio of a - and c -axes lattice constants), which is index of structural anisotropy, is smaller than that of $\text{BaFe}_2(\text{As}_{1-y}\text{P}_y)_2$. We have revealed two salient features of this compound. First, the innermost d_{xy} hole band is below E_F around the Γ point, while in $\text{BaFe}_2(\text{As}_{1-y}\text{P}_y)_2$, all the hole bands are above E_F in the entire k_z region [1]. Second, there is a gap minimum on one of the electron FS.

In this measurement, we have performed the ARPES measurement on $\text{Sr}_{1-x}\text{Ca}_x\text{Fe}_2(\text{As}_{1-y}\text{P}_y)_2$ ($x = 0.25, y = 0.08$) to confirm the gap minimum on one of the electron FSs and clarify the momentum dependences of the SC gaps around all the high symmetry points. Figure 1 shows the SC gaps on the electron FSs around the X point. One can see the gap minimum around 40 degrees on the δ electron FS in Fig. 1 (a). This feature has been confirmed by measurements for other 4 samples summarized in Fig. 1 (c). Therefore, we conclude that there exists the gap minimum on the δ electron FS, indicating the existence of a node. All results about the SC gaps are summarized in Fig. 2. There is weak anisotropy of the SC gap on the γ hole FS around the Z point, implying the contribution of the spin fluctuation to the SC mechanism [2]. On the other hand, other gaps on the hole FSs are nearly isotropic. As discussed above, there exist the gap minima or nodes on the δ electron FS while the SC gap on the ε electron FS is almost isotropic. This result indicates the orbital fluctuation plays an important role on the SC mechanism [3].

[1] T. Yoshida, I. Nishi, S. Ideta, A. Fujimori, M. Kubota, K. Ono, S. Kasahara, T. Shibauchi, T. Terashima, Y. Matsuda, H. Ikeda and R. Arita, Phys. Rev. Lett. **106** (2011) 117001.

[2] K. Suzuki, H. Usui and K. Kuroki, J. Phys. Soc. Jpn **80** (2011) 013710.

[3] T. Saito, S. Onari and H. Kontani, Phys. Rev. B **88** (2013) 045115.

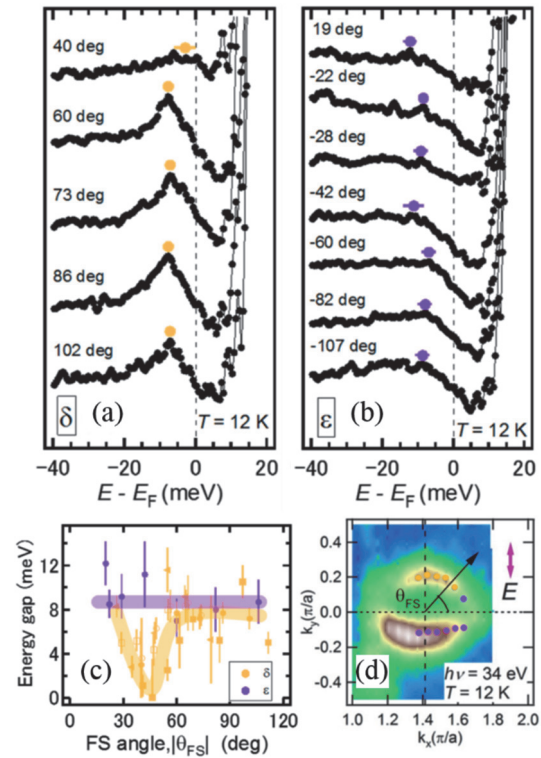


Fig. 1. (a), (b) The photoemission spectra divided by Fermi-Dirac function at various Fermi surface angles θ_{FS} for electron FSs. (c) Energy gap as a function of θ_{FS} . (d) In-plane FS mapping around the X point.

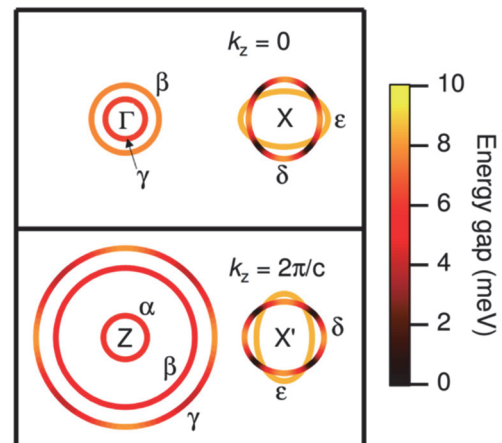


Fig. 2. Color plots of the SC gap distribution on the FSs of $\text{Sr}_{1-x}\text{Ca}_x\text{Fe}_2(\text{As}_{1-y}\text{P}_y)_2$ ($x = 0.25, y = 0.08$).

BL1B

Terahertz Spectroscopy of Ionic Liquids

T. Awano

Faculty of Engineering, Tohoku Gakuin University, Tagajo 985-8537, Japan

Terahertz absorption bands had been observed in superionic conductors of crystals and glasses[1]. These bands seems to be due to collective motion of conductive ions, although the correlational dynamics of mobile ions is not clear.

Ionic liquid (IL) is molten salt at room temperature because of large radius of component ions. Figure 1 shows molecular structures of 1-Ethyl-3-methylimidazolium [$C_2\text{min}$] cation and bis (trifluoromethyl) sulfonyl imide [Tf_2N] anion. It is interesting to compare ionic motion in ionic liquids with those in superionic conductor for investigation of dynamics of mobile ions. In superionic conducting glasses, only cation is mobile.

Temperature dependence of absorption spectra of ionic liquids in spectral range between 20 to 60 cm^{-1} have measured to investigate change of dynamics of mobile ions. Transmittance spectra of one and two filter papers with the ionic liquid of the same quantity per the paper were measured. Absorption spectra were obtained by subtracting each other. To eliminate interference fringe remaining in the spectra, absorption difference spectra of each spectrum from that at 78 K are shown in Fig. 2. Molecular dynamics (MD) simulation was executed using GROMACS5.0.

There observed some structures in the absorption spectra in terahertz region contrary to the previously reported THz-TDS result[2]. Temperature dependence of the absorption spectra showed similar tendency as the results in millimeter wave region [3]. Four types of the spectral change occurred at temperature above melting point or glass transition temperature. The intensities of the absorption bands in the ILs which are crystal in the solid state showed rapid decrease at their melting points. On the other hand, those in ILs which are vitreous in the solid state weakened and shifted gradually. Some others showed complicated change. The other type showed no absorption band in this spectral range.

Figure 3 shows MD simulation spectra of each ion in [$C_2\text{min}$] [Tf_2N] at 300 K. Terahertz absorption bands are coincident with those in observed spectra in Fig. 2.

Figure 4 shows contribution of rotation of molecules (a) and temperature dependence of that of the anion (b). A part of the observed spectral change seems to be due to the rotation of ions.

[1] T. Awano and T. Takahashi, J. Phys. Soc. Jpn. **79** (2010) Suppl. A 118.

[2] T. Yamada, Y. Tominari, A. Tanaka and M. Mizuno, J. Phys. Chem. B **119** (2015) 15696.

[3] T. Awano and T. Takahashi, KURRI rep. 2016.

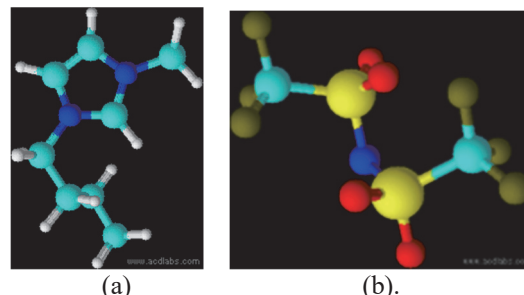


Fig. 1. Ionic structures of [$C_2\text{min}$] (a) and [Tf_2N]

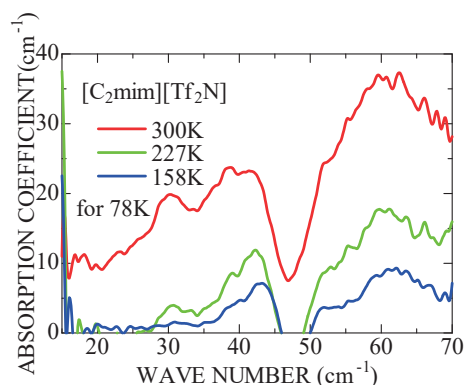


Fig 2. Absorption increment spectra of [$C_2\text{min}$] [Tf_2N] against the absorption spectrum at 78 K.

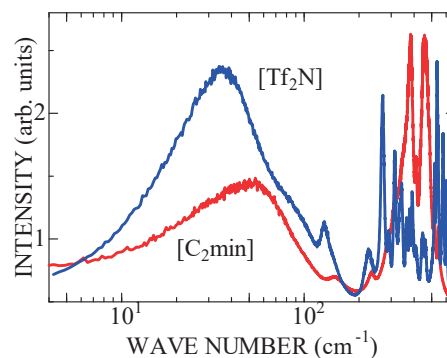


Fig. 3. Autocorrelation function of velocity of ions in [$C_2\text{min}$] [Tf_2N] at 300 K.

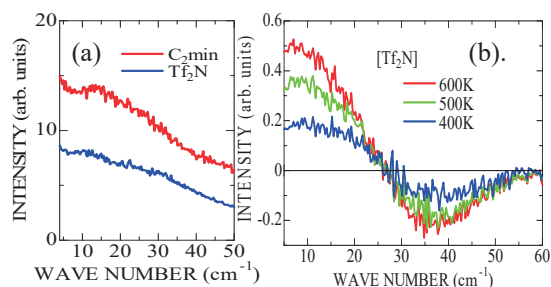


Fig. 4. (a) Rotational velocity autocorrelation function of the cation and anion at 300 K. (b) Increment spectra of anion against that at 300 K.

BL2A

XAFS Measurement for Alloying Element in Tempered Nitrogen Martensite

M. Sato and S. Shimaya

Institute for Materials Research, Tohoku University, Sendai 980-8577, Japan

It is well known that the martensite phase obtained by quenching is hard but brittle. Therefore the balance between hardness and toughness is adjusted by the subsequent tempering treatment. At that time, cementite is precipitated in case carbon steel, and Fe_4N is precipitated in case of nitrogen steel [1, 2].

Although it is known that alloying elements partially dissolve as solid solution in these precipitates, there is a little knowledge on the chemical state of these substitution elements in the precipitates. In this study, changes in the chemical state of the substitutional elements such as Si and Mo before and after tempering treatment were investigated by XAFS measurement.

Fe-1mass%Si and Fe-1mass%Mo alloys were used as starting materials. They were homogenized at 1523 K for 24h and furnace-cooled until room temperature. The Fe-1Si alloys were prepared by nitriding and quenching (N-Q) process using NH_3/H_2 mixed gas at 1273 K for 1 h. Then obtained Fe-1Si-0.3N alloys were tempered at 773 K. and precipitates generated during tempering were extracted using Iodine-alcohol procedure. The Si K-edge XANES spectra were corrected by fluorescence method using InSb double crystal monochromator and silicon drift detector (SDD) at BL2A in UVSOR, respectively. Obtained data were analyzed using Athena software.

Figure 1 shows Si K-edge XANES spectra of Fe-1Si-0.3N samples before and after tempering. The XANES spectrum of the as-quenched sample showed similar spectrum to that previously reported. the spectrum shape changed at tempering above 400°C, and the peak at 1840 eV decreased and that at 1845 and 1850 eV increased. These peaks at 1845 and 1850 eV are the same as the peak positions obtained from Si_3N_4 and SiO_2 reference samples [3]. Therefore, it is thought that Si kept a solid solution state in Fe at low tempering temperature below 300°C and it precipitated as Si_3N_4 or made a solid solution in Fe_4N precipitates at the tempering temperature above 400 °C. In addition, it is considered that the component of SiO_2 is the oxidation of the surface.

XANES spectra of Mo alloy slightly changed by tempering only at 500°C, implying the precipitation of Mo compounds, or it made a solid solution in Fe_4N precipitates. In the future, detailed examination should be carried out by analysis of the EXAFS region and calculation using FEFF code.

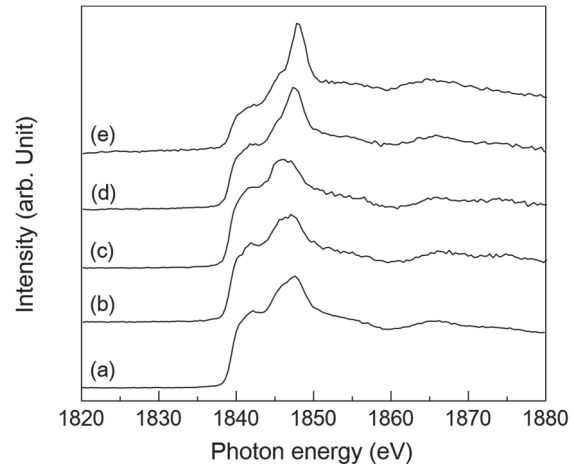


Fig. 1. Si K-edge XANES spectra of Fe-1Si-0.3N samples. (a) as-quenched sample and tempered at (b) 100°C (c) 200°C (d) 400°C and (e) 500°C for 1 hour.

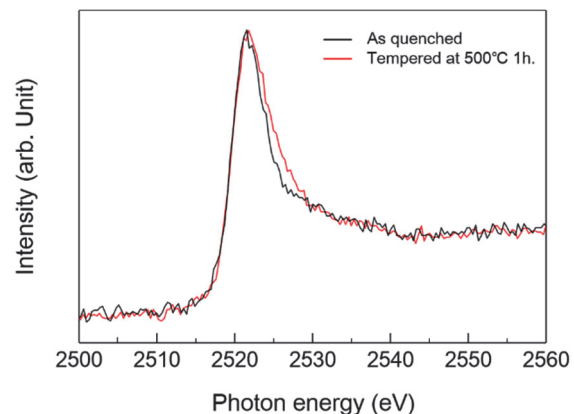


Fig. 2. Mo L-edge XANES spectra of Fe-1Mo-0.3N samples. (a) as-quenched and (b) tempered at 500 °C for 1 hour.

[1] L. Cheng and E. J. Mittemeijer, *Met. Trans. A* **21A** (1990) 13.

[2] L. Cheng, A. Bottger and E. J. Mittemeijer, *Met. Trans. A* **23A** (1992) 1129.

[3] M. Sato, UVSOR Activity Report **44** (2016).

BL2A

Catalytically Active Mo₂C Species on H-MFI Zeolites for Methane Dehydroaromatization with Hydrogen

H. Aritani¹, R. Yamazaki², M. Tsutsumi¹, H. Miyanaga¹, M. Akutsu², S. Mogi²,
K. Ogasawara², K. Kuramochi² and A. Nakahira³

¹Graduate School of Engineering, Saitama Institute of Technology, Fukaya 369-0293, Japan

²Advanced Science Research Laboratory, Saitama Institute of Technology, Fukaya 369-0293, Japan

³Graduate School of Engineering, Osaka Prefecture University, Sakai 599-8531, Japan

MoO₃-modified H-MFI (Mo/H-MFI) is a noted typical catalyst for methane dehydroaromatization, which is an important reaction for direct GTL (Gas To Liquid) processes. Since detail of the MTB reaction process is still unknown, It has been accepted that the activity is based on strong acidity and sieving effects onto MFI zeolite support. During the reaction, MoO_x species must be reduced and carbonized to form carbide-like species[1]. At the same time, catalytic deactivation is brought about by carbon contamination on MFI. The deactivation strongly depends on the strong acidity on H-MFI, and excess carbonization Mo species also affect the lowering of methane conversion. In our previous study, Mo/GaAl-MFI (using Ga-contained H-MFI) catalysts employed to MTB reaction[2]. In these cases, formation of Mo-carbide species with durable MTB activity is different from those of Mo/H-MFI catalysts. Since H₂ co-feed with CH₄ reactant is effective for suppression of carbon coking on H-MFI, reduction of active Mo species can proceeds. It is concluded that formation of active Mo carbide-like species, as well as restraint of the carbon deposits on H-MFI supports, may become the breakthrough for the design of high and durable MTB catalysts[3]. In the present report, Mo L_{III}-edge XANES study is applied to characterize the Mo/H-MFI catalysts to evaluate the Mo species after the MTB reaction with H₂.

Catalysts were prepared by impregnation of H-MFI support with MoO₂(acac)₂-CHCl₃ solution (5.0wt% as MoO₃), and followed by drying overnight and calcination at 773 K for 3 h. H-MFI supports (SiO₂/Al₂O₃ ratio is 27 or 40) were synthesized hydrothermally at 413 K for a week, and followed by ion-exchanging with NH₄Cl and calcination at 873 K. The catalytic activity of MTB was evaluated by means of fixed bed flow reaction, as described in a separate paper[1]. The reactant gas is CH₄(20%)+H₂ (0-3%)+He(base) at the flow rate of 30 mL/min, and the reactivity was evaluated at 1023 K by using the 0.25 g of each Mo/H-MFI catalyst. Mo L_{III}-edge XANES spectra were obtained in BL2A of UVSOR-IMS in a total-electron yield mode using InSb double-crystal monochromator. Photon energy was calibrated by using Mo metal-foil at Mo L_{III}-edge, and normalized XANES spectra are presented by using REX-2000 (Rigaku) software.

Figure 1 shows the XANES spectra of Mo/H-MFI

after MTB reaction with H₂. In case of the H-MFI (Si/Al₂=28) support, it is definitely that metallic Mo species are formed after the reaction with/without H₂. These catalysts shows durable reactivity, and thus, excess reduction to form the metallic Mo species act as the highly reactive sites. For the H-MFI (Si/Al₂=40) support, reduction of Mo species are slightly and almost as similar as α-Mo₂C. On these catalysts, suppressing effect for deactivation was shown by addition of H₂. However, highly reduced Mo ions are not formed on H-MFI (Si/Al₂=40) support. The relation between the reduction of Mo species and the catalytic activity and its durability for MTB is now in progress.

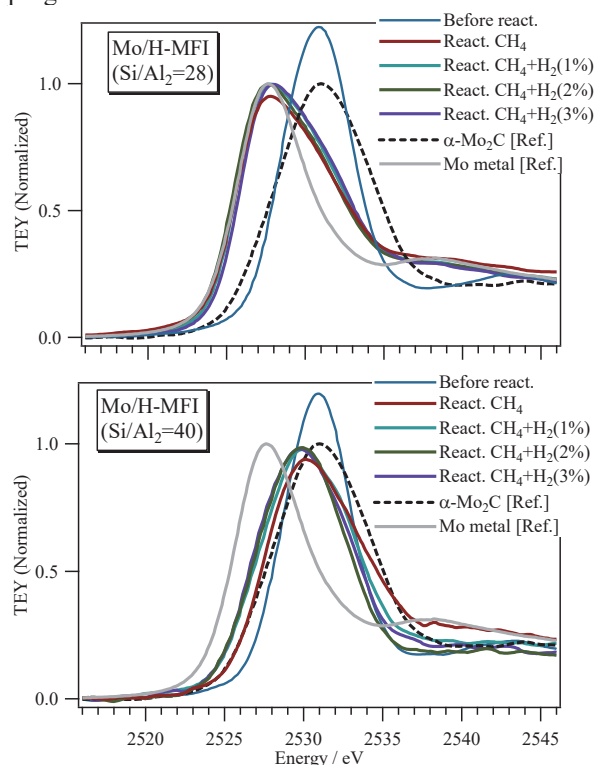


Fig. 1. Mo L_{III}-edge XANES over Mo/H-MFI [Si/Al₂ ratios are 28 (top) and 40 (bottom)] catalysts after the MTB reaction with H₂.

[1] H. Aritani *et al.*, J. Environm. Sci. **21** (2009) 736.

[2] H. Aritani *et al.*, UVSOR Activity Report, **43** (2016) 49.

[3] H. Aritani *et al.*, UVSOR Activity Report, **44** (2017) 52.

BL2A

Mg K-edge XANES of MgO Single Crystal

K. K. Okudaira¹, S. Yoshioka² and E. Kobayashi³

¹ Graduate School of Science and Engineering, Chiba University, Chiba 263-8522, Japan

² Graduate School of Engineering, Kyushu University, Fukuoka 819-0395, Japan

³ Kyushu Synchrotron Light Research Center, Tosu 841-0005, Japan

A large number of applications have lead to the study of magnesium oxide in recent years. In the field of organic electronics, magnesium oxides (MgOs) are used as encapsulation, high-k substrate, and insulating material deposited between the organic layer and the metal cathode for organic light emitting diode (OLED), organic thin film transistor (OTFT), and organic photovoltaic solar cell (OPV), respectively[1-3]. Particularly, MgOs are used as insulating barriers and play an essential role in state of the organic devices. In this context the electronic structure MgO has been widely studied. Furthermore, MgO single crystal has attracted attention due to its simple electronic structure, giving rise to a series of very interesting basic physics questions. In general, to obtain the information on electronic structure of valence band and conduction band, UPS and XANES or IPES are used, respectively [4]. The photoelectron spectroscopy such as UPS and XANES using electron yield method are not available due to low conductivity (high insulation) of MgO single crystal.

In this report, we investigated the electronic structure of MgO single crystal by means of XANES using fluorescence yield method.

Mg K-edge XANES measurements were performed at the BL2A of UVSOR Okazaki, Japan, using the partial fluorescence yield method (PFY). A KTiOPO₄ (KTP) double crystal monochromator defined Mg K absorption edges in the energy region from 1290 to 1340 eV. The samples were set with their surface perpendicular to the incident X-ray beam. Fluorescence X-rays of Mg K α were collected using an energy dispersible silicon drift detector (SDD). All measurements of XANES spectra were carried out in vacuum of 1×10^{-5} Pa at room temperature. To interpret the local structure from the experimental spectra, we used theoretical spectra by the full-potential linearized augmented plane wave (APW) plus local orbitals technique as implemented in WIEN2k code[5].

Firstly, magnesium oxide (MgO), which is typical insulating material for electronic devices, was measured. Fine structures of Mg K-edge XANES were observed in MgO, as shown in Fig. 1. Theoretical spectra of rock salt-type MgO was performed with 216 atoms supercell. The calculation of MgO successfully reproduced the major peaks (a, b, c and d) and shoulders of the experimental spectrum with respect to relative energy and intensity. In XANES experiments with fluorescence mode for highly concentrated sample, the peak intensities sometime do not be observed correctly due to thickness effect. However,

the degree of distortion in MgO spectrum in this study was improved by devising the sample-detector arrangements. We will study the interaction between MgO and organic molecules by this method.

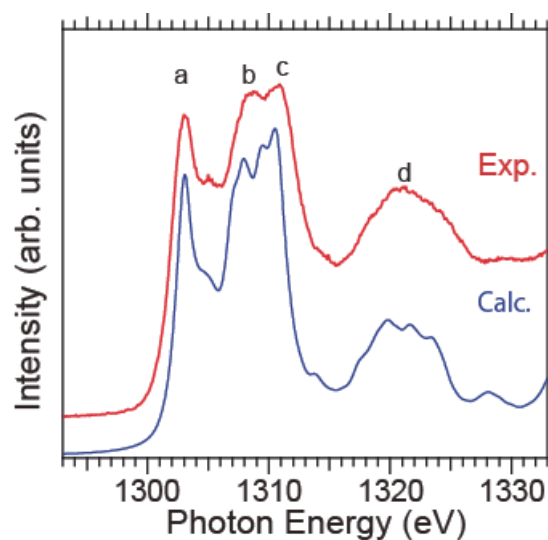


Fig. 1. Mg K-edge XANES spectra of MgO. Experimental (red) and calculated (blue) spectrum.

- [1] Y. C. Han, C. Jang, K. J. Kim, K. C. Choi, K. H. Jung, B. -S. Bae, *Org. Electron* **12** (2011) 609.
- [2] S.-S. Cheng, C.-Y. Yang, C.-W. Ou, Y.-C. Chuang, M.-C. Wu, and C.-W. Chu, *Electrochem. Solid State Lett.* **11** (2008) H118.
- [3] D.-H. Kim, J.-H. Kim, Y.-H. Hwang, J.-W. Shin, and J.-G. Park, *J. Korean Phys. Soc.* **3** (2013) 490.
- [4] NEXAFS J Stöhr Springer-Verlag Berlin 1992.
- [5] P. Blaha, K. Schwarz, G.K.H. Madsen, D. Kvasnicka, and J. Luitz, WIEN2K: An Augmented Plane Wave plus Local Orbitals Program for Calculating Crystal Properties (Vienna: Vienna University of Technology, 2001).

BL2A

Structural Evaluation and Synthesis of Various Hydroxyapatite Doped with Al Ion

A. Nakahira¹, M. Togo¹, M. Sato², T. Ujike¹, T. Sakuma¹, T. Moriya¹, M. Minami¹
and H. Aritani³

¹ Faculty of Engineering, Osaka Prefecture University, Sakai 599-8531, Japan

² Industrial Materials Research (IMR), Tohoku University, Sendai 980-8577, Japan

³ Saitama Institute of Technology, Fukaya 369-0293, Japan

Hydroxyapatite, $\text{Ca}_{10}(\text{PO}_4)_6(\text{OH})_2$, similar to the inorganic components of bone and teeth, is one of most attractive bioceramics (calcium phosphate) for implants and replacements in orthopedics fields. At the same time hydroxyapatite possesses the excellent biologically active properties and the high biocompatibility. It is well-known that natural bones have higher osteoconductive activities, because these natural bones contain generally some cations in the hydroxyapatite structure. However, the biocompatibility strongly depends on the nature and amount cation. Especially, it is inexplicit on the behaviors of aluminum ion for biocompatibility and osteoconductive activities.

The purpose in this study was to evaluate the local structure of aluminum ion for hydroxyapatite added with aluminum ion synthesized by the solution-precipitation method such as static hydrothermal process. The effect of aluminum ion amount on the microstructure for various hydroxyapatite added with aluminum ion was specially investigated.

All chemicals were analytical reagent-grade, and they used without further purification. Undoped and Al-doped hydroxyapatite samples were synthesized using the static hydrothermal process as a solution-precipitation method. Starting aqueous solutions were 0.1 mol/L solutions with $\text{Ca}(\text{NO}_3)_2 \cdot 4\text{H}_2\text{O}$, $\text{Al}(\text{NO}_3)_3 \cdot 6\text{H}_2\text{O}$ and $(\text{NH}_4)_2\text{HPO}_4$. Precipitations were matured at 353 K for 5 hours in air atmosphere and subsequently synthesized at 423 K for 12h to 24h by the static hydrothermal process. Nominal $\text{Al}/(\text{Ca}+\text{Al})$ ratio was set to 0, 1, 3, 5 and 10 at%. The samples prepared through this process were characterized with X-ray diffraction technique. The microstructures were observed by SEM.

Al-K XANES was measured at BL2A in UVSOR. The pellets of samples were mounted on carbon tapes. The incident X-ray beam was monochromatized with using beryl double crystals. Al-K XANES signals were collected with GaAsP photo-diodes (Hamamatsu: G-1127-02).

Theoretical spectra were obtained by the first-principles supercell method with a core-hole effect and evaluated for a detailed analysis of Al-K XANES.

According to the XRD results, all samples were identified to hydroxyapatite structure without another phase. In especial, aluminium phosphate and calcium phosphate were not contained for Al-doped

hydroxyapatite samples synthesized using the static hydrothermal process.

Figure 1 shows the results of Al-K XANES spectra of various Al-doped hydroxyapatite samples synthesized using the static hydrothermal process. As shown in Fig. 1, Al-K XANES spectra of sample obtained by hydrothermal process were quite similar. Furthermore, Al-doped hydroxyapatite samples with the high contents of aluminum ion were most of the same as ones with low content of aluminum ion. As a result, Al-doped hydroxyapatite samples with $\text{Al}/(\text{Ca}+\text{Al})$ ratio of 1, 3, 5 and 10 had the similar Al local structure.

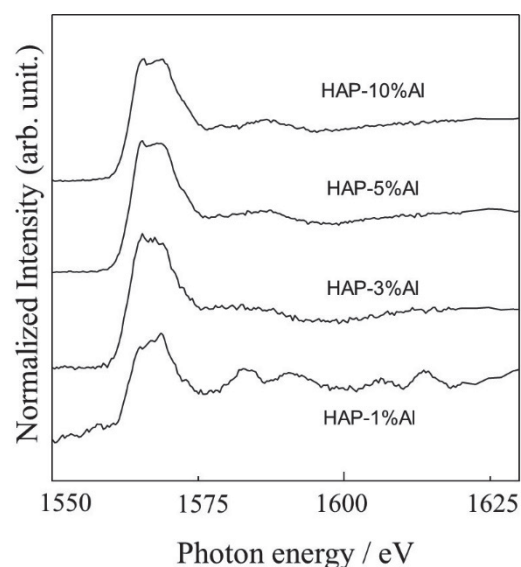


Fig. 1. Al-K XANES spectra of various products synthesized by the hydrothermal process at 423 K. Al-doped hydroxyapatite samples: $\text{Al}/(\text{Ca}+\text{Al})$ ratio of 1, 3, 5 and 10.

BL2A

Change in Charge States of Mo Ions in $\text{Sr}_2\text{FeMoO}_6$ by Incorporations of Ba and Nb Ions

S. Obunai¹ and T. Yamamoto^{1,2}¹Faculty of Science and Engineering, Waseda University, Tokyo 169-8555, Japan²Institute of Condensed-Matter Science, Waseda University, Tokyo 169-8555, Japan

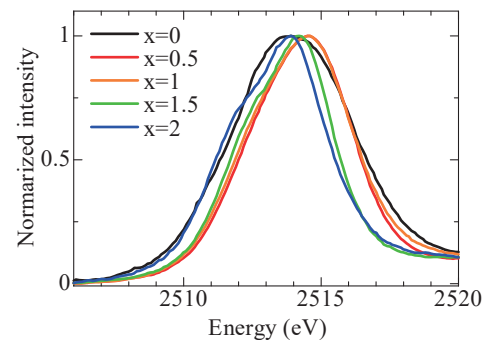
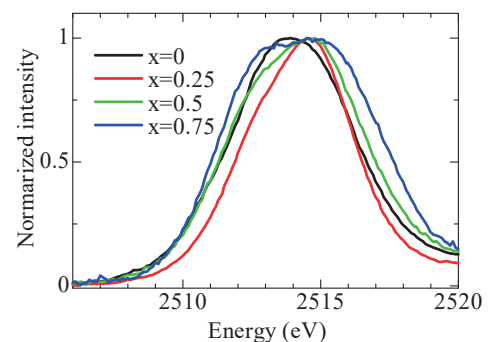
The half-metallic materials have been widely studied due to their potential applications in new technologies such as spintronics. $\text{Sr}_2\text{FeMoO}_6$ is the promising candidates of half-metals, since it has high Curie temperature (420 K) and colossal magnetoresistance (CMR) at room temperature [1]. It was studied that the partial replacements of Sr and Mo by Ba and Ta, respectively, change magnetic property. There are two aspects to understand such change in magnetic property, that is 1) change in magnetic moments on Fe and Mo and 2) change in magnetic ordering. In order to investigate the first one 1), valence states of magnetic ions should be determined. For such purpose, XANES analysis is quite powerful. In the current study, we have investigated the change in valence states of Mo ions in $\text{Sr}_2\text{FeMoO}_6$ by incorporations of Ba and Nb ions using the Mo-L XANES measurements.

$\text{Sr}_{2-x}\text{Ba}_x\text{FeMoO}_6$ and $\text{Sr}_2\text{FeMo}_{1-x}\text{Ta}_x\text{O}_6$, were synthesized by the conventional solid state reaction method changing the cation ratio, x . SrCO_3 , BaCO_3 , $\alpha\text{-Fe}_2\text{O}_3$, MoO_3 powders were used for the starting materials. Crystal structures of all the synthesized materials were examined by the powder X-ray diffraction with $\text{Cu-K}\alpha$ X-rays.

XANES measurements at Mo-L₃ of the samples here synthesized were carried out at BL2A in UVSOR with a total electron yield method. All the sample powders were put on the carbon adhesive tape, which were attached onto the Al plate, and the drain current was measured instead of counting the number of emitted electrons from the samples. The InSb double-crystal monochromator was employed.

Observed Mo-L₃ XANES spectra of Ba incorporated $\text{Sr}_2\text{FeMoO}_6$, i.e., $\text{Sr}_{2-x}\text{Ba}_x\text{FeMoO}_6$, are shown in Fig. 1. The component in lower energy side decrease as increase of Ba concentration when x is 0.5 and 1.0, and at $x = 1.5$ that of higher energy side decreases. Finally, lower energy side recovers with no change in higher energy side as that at $x = 1.5$. From this analysis, we can discuss change in magnetic moment derived from Mo ions. Same analysis have been also carried out for $\text{Sr}_2\text{FeMo}_{1-x}\text{Ta}_x\text{O}_6$, whose spectra are shown in Fig. 2. In both cases, i.e., $\text{Sr}_{2-x}\text{Ba}_x\text{FeMoO}_6$ and $\text{Sr}_2\text{FeMo}_{1-x}\text{Ta}_x\text{O}_6$, it was found that simple peak shift without spectral change does not occur due to the Ba and Ta incorporations. The first principles calculations within a density functional theory were also carried out to investigate the change in charge states of Mo ions due to the incorporations

of Ba and Nb ions, which support the experimental change in the spectral shapes.

Fig. 1. Mo-L₃ XANES spectra of $\text{Sr}_{2-x}\text{Ba}_x\text{FeMoO}_6$.Fig. 2. Mo-L₃ XANES spectra of $\text{Sr}_2\text{FeMo}_{1-x}\text{Nb}_x\text{O}_6$.

[1] K. -I. Kobayashi *et al.*, Nature **395** (1998) 677.

BL2A

Study of Local Structure of Al-K Edge for Novel Modified Layered Double Hydroxide by Rehydration Process

A. Nakahira¹, M. Iida¹, M. Togo¹, M. Sato² and H. Aritani³¹Faculty of Engineering, Osaka Prefecture University, Sakai 599-8531, Japan²Industrial Materials Research (IMR), Tohoku University, Sendai 980-8577, Japan³Saitama Institute of Technology, Fukaya 369-0293, Japan

Layered double hydroxide (LDH) is one of unique clay minerals with a layered structure and possess the excellent exchangeable anions ability owing to substitution to various cations and anions in LDH. Its composition formula is $[M(II)_{1-x}M(III)_x(OH)_2]_{x+} \cdot [An-x/n \cdot YH_2O]$. M(II), M(III) for layered double hydroxide. Here, we focus on the structure evaluation of novel modified NiAl-LDH synthesized from MgAl-LDH composed of Al^{3+} and Mg^{2+} , which is called hydrotalcite. In special, it was found that in our experiments the rehydration treatment for MgAl-LDH samples heat-treated at 473 K to 773 K in air atmosphere resulted in the synthesis of novel modified NiAl-LDH. The purpose in this study was to evaluate the local structure of aluminum ion for novel modified NiAl-LDH synthesized by the rehydration treatment for MgAl-LDH in aqueous nickel acetate solution. The effect of concentration of aqueous nickel acetate solution on the microstructure for novel modified NiAl-LDH through the rehydration treatment was specially investigated.

Mixing solution was adjusted by mixing 0.2 mol/dm³ MgCl₂ aqueous solution and 0.1 mol/dm³ AlCl₃ aqueous solution. MgAl-LDH with $M^{2+}/M^{3+}=2$ were synthesized by adding mixing solution into 0.05 mol/dm³ NaHCO₃ at room temperature through the co-precipitation process. 1 mol/dm³ NaOH was simultaneously added into the aqueous solution in order to keep pH 10. After precipitation was finished, the products for MgAl-LDH were aged at room temperature for 2 hours. They were separated from liquid phase with Buchner funnel and sufficiently washed by deionized water and finally air-dried at 323 K for 24 hours. Mixed oxides (Mg-Al double oxide) were prepared by calcination at 473 K to 773 K in air atmosphere for 2 hours of MgAl-LDH. The rehydration treatment for mixed oxides (Mg-Al double oxide) was carried out in aqueous nickel acetate solution with 0.1 M to 0.5 M at room temperature. The samples prepared through this process were characterized with X-ray diffraction technique. The microstructures were observed by SEM. The local structures around Al were characterized by measuring X-ray adsorption near edge structure (XANES) at BL01A in UV-SOR with KTP. Al-K XANES was measured at BL2A in UVSOR. The pellets of samples were mounted on carbon tapes. The incident X-ray beam was monochromatized with using KTP crystals.

Al-K XANES signals were collected with GaAsP photo-diodes (Hamamatsu: G-1127-02). Theoretical spectra were obtained by the first-principles supercell method with a core-hole effect and evaluated for a detailed analysis of Al-K XANES.

XRD results indicated that MgAl-LDH samples prepared by the co-precipitation process were identified to hydrotalcite structure without another phase. After calcination at 573 K to 773 K in air atmosphere for 2 hours of MgAl-LDH, samples were identified to amorphous mixed oxides (Mg-Al double oxide), not hydrotalcite structure. Using these amorphous mixed oxides, the rehydration in aqueous nickel acetate solution was attempted to synthesize the modified NiAl-LDH. According to XRD, samples after the rehydration in aqueous nickel acetate solution were identified to hydrotalcite structure and modified NiAl-LDH was successfully obtained by the rehydration in aqueous nickel acetate solution. Figure 1 shows the results of Al-K XANES spectra for modified NiAl-LDH synthesized by the rehydration process. As shown in Fig. 1, Al-K XANES spectra of sample obtained by rehydration process were quite similar aluminum hydroxide. As a result, NiAl-LDH prepared by rehydration process the same structure as the coprecipitation process.

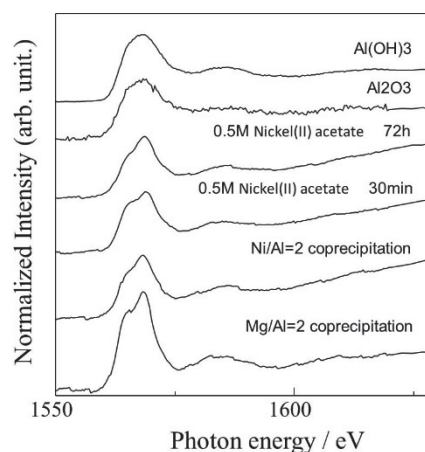


Fig. 1. Al-K XANES spectra of various products.

BL2A

Local Structure Investigations of $\text{Gd}_3\text{Ga}_5\text{O}_{12}$ Irradiated with Swift Heavy Ions

S. Yoshioka¹, K. K. Okudaira² and E. Kobayashi³¹ Graduate School of Engineering, Kyushu University, Fukuoka 819-0395, Japan² Graduate School of Science and Engineering, Chiba University, Chiba 263-8522, Japan³ Kyushu Synchrotron Light Research Center, Tosu 841-0005, Japan

Gadolinium gallium garnet ($\text{Gd}_3\text{Ga}_5\text{O}_{12}$ or GGG) is considered as an important material for laser optical application. Ion irradiations are currently used to tailor materials properties. In particular, for garnet structure materials, swift heavy ion irradiations, produce amorphous tracks that can change the microstructure and the magnetic or magneto-optical properties. In the present study, we made a combined study of NEXAFS measurements and first principles calculations on $\text{Gd}_3\text{Ga}_5\text{O}_{12}$ with special interests on the local environment of Ga and Gd after irradiated with swift heavy ions.

Synthetic single crystals of $\text{Gd}_3\text{Ga}_5\text{O}_{12}$ were used in this study. The crystals were cut into sheets with a (111) plane surface and were polished to a mirror finish. The specimens were irradiated with 200 MeV Xe ions to fluences of $1 \times 10^{13} \text{ cm}^{-2}$ at the H1 beamline of the tandem ion accelerator facility at the Japan Atomic Energy Agency (JAEA) in Tokai. Ga L_3 -edge XANES measurements were performed at the BL2A beamline of UVSOR Okazaki, Japan, using the partial fluorescence yield method (PFY). A Beryl double crystal monochromator defined Ga L_3 absorption edges in the energy region from 1105 to 1160 eV. The samples were set with their surface perpendicular to the incident X-ray beam. Fluorescence X-rays of Ga $L\alpha$ were collected using an energy dispersible silicon drift detector (SDD). All measurements of XANES spectra were carried out in vacuum of $1 \times 10^{-5} \text{ Pa}$ at room temperature. To interpret the local structure from the experimental spectra, we used theoretical spectra by the full-potential linearized augmented plane wave (APW) plus local orbitals technique as implemented in WIEN2k code[1].

Figure 1 shows calculated Ga L_3 -edge XANES spectrum of monoclinic type gallium oxide ($\beta\text{-Ga}_2\text{O}_3$) as standard samples together with experimental spectra. Theoretical spectrum was performed with 120 atoms supercell. The calculation of Ga_2O_3 successfully reproduced the major peaks and shoulders of the experimental spectrum with respect to relative energy and intensity. Detailed analyses on the local environment of $\text{Gd}_3\text{Ga}_5\text{O}_{12}$ irradiated with swift heavy ions are in progress by combined use of the NEXAFS and the first principles band structure calculations.

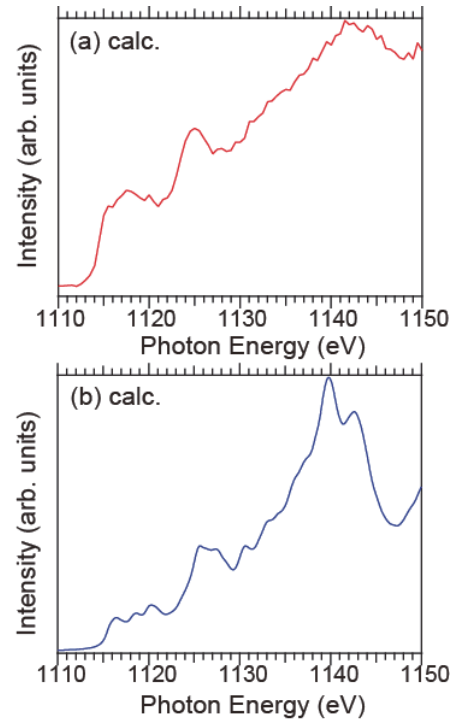


Fig. 1. Ga L_3 -edge XANES spectra of Ga_2O_3 . Experimental (a) and calculated (b) spectra.

[1] P. Blaha, *et al.*, WIEN2k, *An Augmented Plane Wave + Local Orbitals Program for Calculating Crystal Properties* (Karlheinz Schwarz, Techn. Universität Wien, Austria, 2001).

BL2B

Ultraviolet Photoelectron Spectroscopy Reveals Small Intermolecular Band Dispersion in an Acceptor-donor Blend

 N. Aghdassi¹, Q. Wang^{1,2}, R.-R. Ji¹, B. Wang¹, J. Fan¹ and S. Duhm¹
¹Institute of Functional Nano & Soft Materials (FUNSOM), Soochow University, Suzhou 215123, P. R. China

²Institut für Angewandte Physik, Universität Tübingen, 72076 Tübingen, Germany

7,8,15,16-tetraazaterrylene (TAT) thin films grown on highly oriented pyrolytic graphite (HOPG) substrates were studied by means of ultraviolet photoelectron spectroscopy (UPS). Photon energy-dependent UPS performed perpendicular to the molecular planes of TAT multilayer films at room temperature clearly reveals band-like intermolecular dispersion of the TAT highest occupied molecular orbital (HOMO) energy. Based on a comparison with a tight-binding (TB) model, a relatively narrow bandwidth of 54 meV is derived. Upon additional deposition of 2,2':5',2'':5'':2'''-quaterthiophene (4T), a 4T/TAT donor-acceptor blend is formed. The 4T/TAT blend likewise exhibits intermolecular dispersion of the TAT HOMO energy, yet with a significant decreased bandwidth.

Photon energy-dependent UPS measurements of TAT thin films were carried out at BL2B of UVSOR III in a UHV chamber with a base pressure of 1×10^{-8} mbar at normal electron emission and at room temperature (300 K). Energy calibration of the spectra was enabled by separately recording the particular Fermi edge on metallic components of the sample manipulator for each photon energy. TAT and 4T molecules were deposited by in-situ sublimation from quartz crucibles.

Figure 1 shows the photon energy-dependent UPS of a) a TAT thin film on HOPG and b) a TAT thin film in a heterostructure with 4T. Figure 1 c) shows the maxima of the HOMO-derived peak of the pristine TAT film. In a TB-model the dispersion can be expressed as

$$E_B(k_{\perp}) = E_B^0 - 2t \cos(a_{\perp} k_{\perp})$$

with the normal component of the electron momentum

$$k_{\perp} = \frac{\sqrt{2m_e^*(h\nu - E_B - V_0)}}{\hbar}$$

In this context, E_B^0 denotes the energy of the band centre, t the transfer integral, a_{\perp} the lattice spacing along the surface normal, $h\nu$ the photon energy, V_0 the inner potential and E_b the HOMO binding energy with respect to the vacuum energy. The data points were fitted by a least-squares fitting procedure with E_B^0 , t and V_0 being treated as fitting parameters. In this way, $t = 13.5$ meV, $E_B^0 = 6.546$ eV and $V_0 = -0.5$ eV were obtained for the TAT HOMO energy dispersion. Regarding the 4T:TAT blend, the TB model yields $t = 6.065$ meV, $E_B^0 = 6.423$ eV and $V_0 = -5.6$ eV.

In conclusion, intermolecular energy-band dispersion of the TAT HOMO perpendicular to the molecular planes, is clearly identified for both the TAT

multilayer film and the 4T:TAT blend. Comparatively narrow bandwidths well below 0.1 eV are identified, with the 4T:TAT bandwidth being significantly decreased compared to the initial TAT multilayer film. Therefore, suchlike donor-acceptor heterojunctions are rendered promising candidates as integral parts of organic-based devices. We further demonstrate that an experimental determination of very narrow bandwidths at room temperature is indeed feasible by means of UPS.

The results have been published in [1].

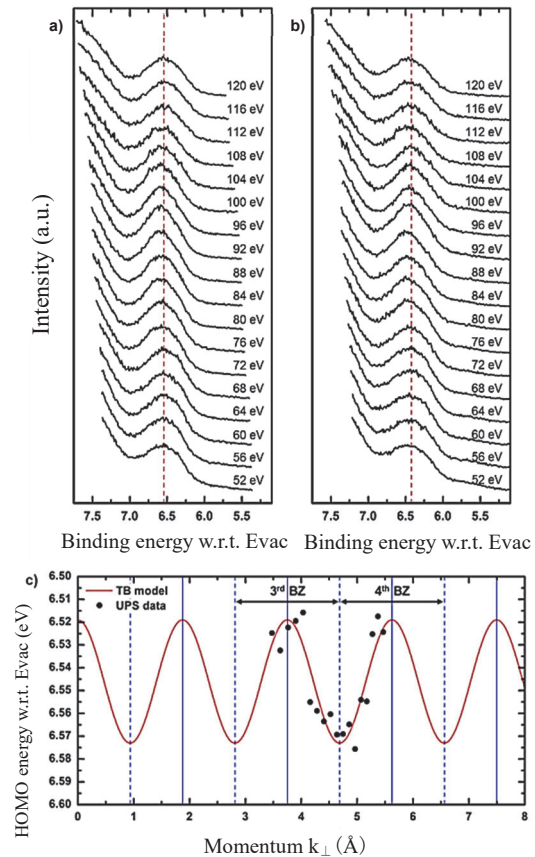


Fig. 1. HOMO region of photon energy-dependent normal emission UPS spectra of a) a TAT thin film with a nominal thickness of 150 Å and b) a 120 Å 4T/150 Å TAT blend on HOPG. c) TAT HOMO energy dispersion perpendicular to the molecular planes as derived from photon energy-dependent UPS. Black dots denote experimental data, whereas red curves are associated with the TB mode.

[1] N. Aghdassi, Q. Wang, R.-R. Ji, B. Wang, J. Fan and S. Duhm, *Nanotechnology* **29** (2018) 194002.

BL3B

Characterization of Intrinsic Luminescence from Orthophosphate and Borophosphate Crystals with Multiple Nonequivalent Oxoanions upon Vacuum UV Excitation

N. Kodama, C. Takahashi, H. Kubota and T. Takahashi

Graduate School of Engineering Science, Akita University, Akita 010-8502, Japan

To date, there has been very little work focusing on the formation of molecular-type excitons in the local structure of low-symmetry complex rare-earth oxides with multiple nonequivalent oxoanions of the PO_4^{3-} or BO_3^{3-} group. To the best of our knowledge, for these complex oxoanion crystals, a comprehensive understanding of the correlation between intrinsic luminescence bands and the number and symmetry of nonequivalent oxoanion groups such as PO_4^{3-} and/or BO_3^{3-} is still lacking. We focused on orthophosphate and borophosphate crystals with multiple nonequivalent PO_4^{3-} and/or BO_3^{3-} oxoanion groups. The first type is $\text{Li}_3\text{Sc}_2(\text{PO}_4)_3$ (LSP) with three nonequivalent PO_4^{3-} groups. The second type is $\text{CaK}(\text{PO}_4)_2$ (CKP) with two nonequivalent PO_4^{3-} groups. The third type is $\text{Ba}_3(\text{BO}_3)(\text{PO}_4)$ (BBP) with one PO_4^{3-} group and one BO_3^{3-} group.

We report intrinsic luminescence from self-trapped excitons (STEs) as intra-anion excitons in these crystals. In addition, we discuss the correlation between intrinsic luminescence bands from STEs and the number of nonequivalent PO_4^{3-} and/or BO_3^{3-} groups in LSP, CKP, and BBP.

Luminescence and excitation spectra of STEs in LSP, CKP, and BBP polycrystals were measured at twelve temperatures in the range of 8-293 K using the undulator BL3B at the UVSOR Synchrotron Facility. The emission spectra were corrected for the wavelength dependence of the diffraction monochromator and CCD detector using calibrated deuterium and halogen lamps as standard light sources. Time-resolved spectra were measured using a pulse with a width of 10 ns from a F_2 pulsed laser operating at 157 nm, and the decay times were determined.

All samples were found to exhibit multiple STE luminescence bands in the UV region under VUV excitation at 70 and 160 nm. The excitation spectral intensity in the 70-220 nm wavelength range for the orthoborate and borophosphate crystals increased rapidly below about 175-180 nm. Broad excitation bands were assigned to bandgap excitations or molecular transitions of the PO_4^{3-} or BO_3^{3-} group.

Figures 1(a)-1(f) show the luminescence spectra for LSP, CKP, and BBP at 8 and 293 K, excited at 70 nm. In order to estimate the number and peak energy of the bands, the spectra are deconvoluted into Gaussians in Figs. 1(a)-1(d). The luminescence spectra of LSP at 293 K and 8 K comprised, respectively, three distinct broad bands associated with STE(I), (II), and (III) having peaks at 263-247, 351, 430-476 nm, as shown in Figs. 1(a) and 1(b). These three intrinsic bands are assigned to STE(I), STE(II), and STE(III) in three sets of nonequivalent PO_4^{3-} groups. The spectra of CKP at 8 K consisted of two broad bands with peaks at 245 and 303 nm, and 281 and 364 nm, respectively, as shown in Figs. 1(c) and 1(d), associated with STE(I) and STE(II) in two sets of nonequivalent PO_4^{3-} groups. On the other hand, as shown in Figs. 1(e) and 1(f), BBP exhibited one broad band at 8 and 293 K. In LSP and

CKP, the number of intrinsic luminescence bands corresponds to the number of nonequivalent PO_4^{3-} groups, whereas in BBP, only one band appears, despite the presence of a PO_4^{3-} group and a BO_3^{3-} group. The number of bands is inconsistent with the number of PO_4^{3-} and BO_3^{3-} groups. A possible explanation for this discrepancy is that a self-trapping of excitons takes place in either the PO_4^{3-} or BO_3^{3-} group with different geometries. The peaks of the STE luminescence bands in all samples (LSP, CKP, BBP) shifted to shorter wavelengths with decreasing temperature from 293 to 8 K.

The radiative decay curves consist of a fast and a slow component due to high-spin and low-spin STEs associated with the two possible spin orientations for the exciton electron-hole pair, as observed in alkali halides [1]. For LSP, the decay times for STE(I) luminescence at 243 nm are 15 ns and 174 ns, and those for STE(II) at 300 nm are 28 ns and 148 ns.

The fast decay components for STE(I) and STE(II) in LSP may originate from singlet STE states in two PO_4^{3-} groups with C_1 symmetry. In contrast, the slow decay components for STE(I) and STE(II) are attributed to triplet STEs in two PO_4^{3-} groups in which triplet STE states occur.

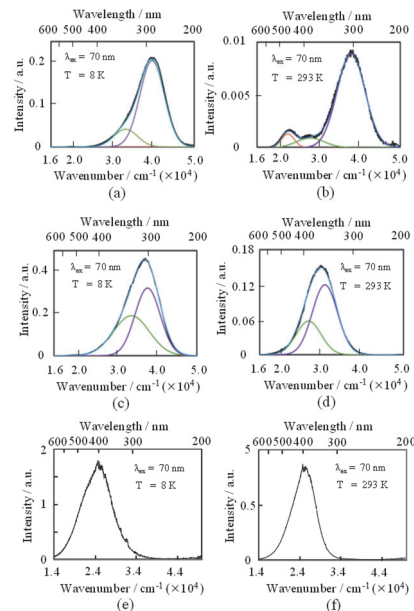


Fig. 1. The decompositions of intrinsic luminescence spectra excited at 160 nm in (a) and (b) LSP, (c) and (d) CKP, and in (e) and (f) BBP at 8 K and 293 K. The calculated components of the Gaussians are represented by yellow, orange, and gray lines.

[1] T. T. Williams, K. S. Song, *J. Phys. Chem. Solids* **51** (1990) 679.

BL3B

Bandgap Energy of La and Y admixed $Gd_{2-x}Si_2O_7$ Crystals Using the UVSOR Facility

T. Horiai¹, S. Kurosawa^{2,3}, A. Yamaji¹, S. Kodama¹, S. Yamato¹, Y. Shoji^{1,4}, M. Yoshino¹, Y. Ohashi², K. Kamada^{2,4}, Y. Yokota² and A. Yoshikawa^{1,2,4}

¹Institute for Materials Research, Tohoku University, Sendai 980-8577, Japan

²New Industry Creation Hatchery Center (NICHe), Tohoku University, Sendai 980-8579, Japan

³Department of Physics, Yamagata University, Yamagata 990-8560, Japan

⁴C&A Corporation, Sendai 980-8579, Japan

Scintillation crystals convert energy of ionizing radiation such as gamma-ray and X-ray into multiple photons of energy 2~8 eV. Scintillators are used in several fields, and oil-well exploration is one of the application fields [1-3]. Specifically, scintillators are used in gamma-ray detectors in combination with a photodetector to discriminate geologic layers at oil well exploration sites. Since the ground temperature in shale layer is reached approximately 200°C, the noise by dark current of the photomultiplier tube (PMT) is become larger. On the other hand, the light outputs are dropped for conventional scintillators. To solve degrading the signal-to-noise ratio, the development of new scintillator which could keep high light output even at high temperature is required.

To satisfy this requirement, Ce-doped $(Gd,La)_2Si_2O_7$ (Ce:La-GPS) has been investigated. Ce:La-GPS has a light output of ~42,000 photons/MeV, and the light output is maintained even at 150°C [4]; however, for high temperature applications, further improvement is needed. In this study, we focus on Y-admixed Ce:La-GPS and optimize Y concentration to improve the temperature dependence. Here, in previous studies, the thermal quenching of Y-admixed Ce-doped Lu_2SiO_5 (Ce:LYSO) was suppressed when compared to Y-free sample (Ce:LSO) [5, 6].

We prepared $(Gd_{0.59-x}Ce_{0.01}La_{0.40}Y_x)_2Si_2O_7$ (Ce:LaY-GPS) single crystals grown by the micro-pulling-down method, and UV absorption edge for these samples were evaluated with a photo diode (IRD, AXUV 100) at BL3B of UVSOR. The bandgap energies were calculated from the UV absorption edge.

From the result of the temperature dependence of light output at 25°C and 175°C, Y5% substituted Ce:La-GPS was improved (Table 1). On the other hand, the light output of Y15% substituted Ce:La-GPS was degraded.

Figure 1 shows the UV absorption spectra of Y0% and 15% substituted Ce:La-GPS. From this figure, the UV absorption edge wavelength were constant regardless of Y concentration (~174 nm), and the bandgap energies were determined appoloximately 7.14 eV. Thus, the improvement factor of temperature dependence of light output was not the effect of the bandgap energy.

Table 1. Light outputs of $(Gd_{0.59-x}Ce_{0.01}La_{0.40}Y_x)_2Si_2O_7$ at 25°C and 175°C

Sample	Light output @ 25°C [photons/MeV]	Light output @ 175°C [photons/MeV]
x = 0.00	42,000	34,000
x = 0.05	43,000	40,000
x = 0.10	36,000	34,000
x = 0.15	33,000	24,000

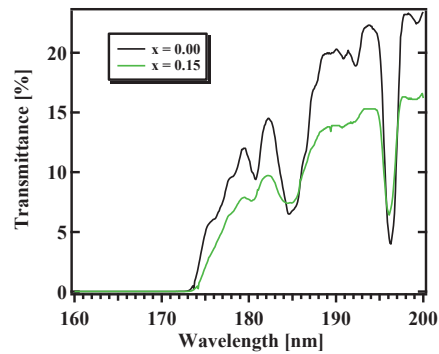


Fig. 1. UV absorption spectra of $(Gd_{0.59-x}Ce_{0.01}La_{0.40}Y_x)_2Si_2O_7$ at 6 K.

- [1] C. Rozsa, R. Dayton, P. Raby, M. Kusner and R. Schreiner, IEEE Trans. Nucl. Sci. **37** (1996) 966.
- [2] A. Baberdin, A. Dutova, A. Fedorov, M. Korzhik, V. Ligoun, O. Missevitch, V. Kazak, A. Vinokurov and S. Zagumenov, IEEE Trans. Nucl. Sci. **55** (2008) 1170.
- [3] C.L. Melcher, J.S. Schweitzer, R.A. Manente and C.A. Peterson, J. Crystal Growth **109** (1991) 37.
- [4] S. Kurosawa, T. Shishido, T. Sugawara, A. Nomura, K. Yubuta, A. Suzuki, R. Murakami, J. Pejchal, Y. Yokota, K. Kamada and A. Yoshikawa, Nucl. Instrum. Methods Phys. Res. A **772** (2015) 72.
- [5] H. Suzuki, T.A. Tombrello, C.L. Melcher and J.S. Schweitzer, IEEE Trans. Nucl. Sci. **40** (1993) 380.
- [6] L. Pidol, A. Kahn-Harari, B. Viana, E. Virey, B. Ferrand, P. Dorenbos, J.T.M. Haas and C.W.E. Eijk, IEEE Trans. Nucl. Sci. **51** (2004) 1084.

BL3B

Insight into the High Light Output of Ce:(Gd, La)₂Si₂O₇ Scintillator

S. Kurosawa^{1,2}, A. Yamaji³, T. Horiai³, S. Kodama³, S. Yamato³, Y. Shoji^{3,4}, Y. Ohashi³,
Y. Yokota¹, K. Kamada^{1,4}, A. Yoshikawa^{1,3,4} and M. Kitaura²

¹ New Industry Creation Hatchery Center (NICHe), Tohoku University, Sendai 980-8579, Japan

² Faculty of Science, Yamagata University, Yamagata 990-8560, Japan

³ Institute for Materials Research (IMR), Tohoku University, Sendai 980-8577, Japan

⁴ C&A Corporation, Sendai 980-8577, Japan.

Crystalline scintillators have been used in various fields such as medical imaging, astronomy and so on. Recently, scintillation properties of (Ce_{0.01}, Gd_{0.90}, La_{0.09})₂Si₂O₇ (Ce:La-GPS) have been studied. The Ce:La-GPS crystal had the light output of around 4,000 photons/MeV and the FWHM energy resolution of 5.0% at 662 keV [1, 2]. Moreover, the light output was constant in the temperature range from 10 to 423 K [3]. Thus, the Ce:La-GPS crystal is applicable to radiation detection at high temperatures.

The evaluation of the bandgap energy is very much important for the development of more functional scintillators. From this viewpoint, we have evaluated the bandgap energy of La-GPS crystals at the BL3B of UVSOR. The bandgap energy of La-GPS was estimated to be over 7.13±0.03 eV. Compared with other oxide scintillators, Ce:La-GPS was found to have wider bandgap. Generally, the light output of scintillator is inversely proportional to the band-gap energy. Despite such a large bandgap energy, the light output is larger than those of other oxide scintillators with small bandgap energies. This result implies that the product of transfer efficiency and/or electron-hole pair generation efficiency in Ce:La-GPS is higher than those in others. The cause may be due to small number of traps in Ce:La-GPS. In order to clarify high light output in Ce:La-GPS, we have investigated thermoluminescence (TL) properties under irradiation with vacuum ultraviolet (VUV) radiation.

Figure 1 and 2 show TL emission spectra and TL glow curve for Ce:La-GPS, respectively, where the TL intensity is the integrated value from the TL emission spectrum at each temperature. The TL glow peak is found at around 120 K. The TL glow curve for 1.5% Ce-doped Gd₂SiO₅ (Ce:GSO) was also measured for a reference. Apparently, the integrated value of the 120 K peak for Ce:La-GPS is smaller than the sum of integrated values of a number of peaks for Ce:GSO up to 300 K. Since Ce:La-GPS have small number of the traps which block the electron transportation into luminescence center, the transfer efficiency becomes high, compared to Ce:GSO. Details of the present study will be reported in Ref. 4.

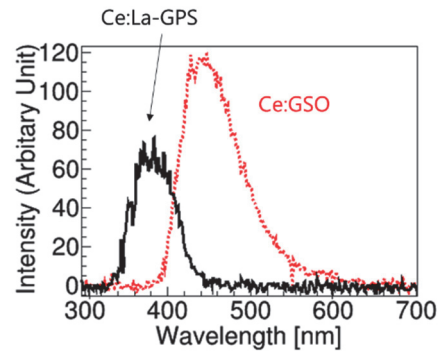


Fig. 1. TL-emission spectra for Ce:La-GPS at 120K and Ce:GSO at 282K.

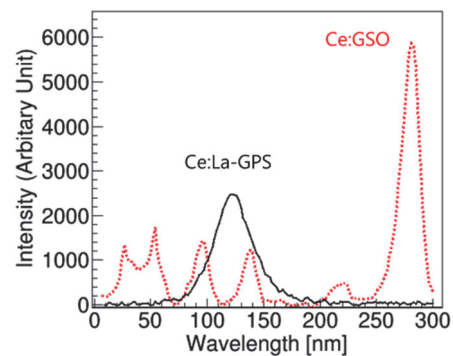


Fig. 2. TL glow curves of Ce:La-GPS (solid line) and Ce:GSO (dotted line).

- [1] A. Suzuki *et al.*, Applied Physics Express **5** (2012) 102601.
- [2] S. Kurosawa *et al.*, Nucl. Inst. and Meth. in Phys. Res. **A774** (2014)30.
- [3] S. Kurosawa *et al.*, Nucl. Inst. and Meth. in Phys. Res. **A772** (2015)72.
- [4] S. Kurosawa *et al.*, IEEE Trans. Nucl. Sci. Accepted.

BL3B

PL Decay Times of Trans-stilbene and 1,4-Bis(2-methylstyryl) Benzene (BisMSB)-doped Trans-stilbene at 13-300 K

S. Yamato¹, A. Yamaji¹, S. Kurosawa^{2, 3}, M. Yoshino¹,
Y. Ohashi², K. Kamada^{2, 4}, Y. Yokota² and A. Yoshikawa^{1, 2, 4}

¹Institute for Materials Research (IMR), Tohoku University, Sendai 980-8577, Japan

²New Industry Creation Hatchery Center (NICHe), Tohoku University, Sendai 980-8579, Japan

³Faculty of science, Yamagata University, Yamagata 990-8560, Japan

⁴C&A Corporation, Sendai 980-8577, Japan.

Neutron detectors can be used in several fields such as homeland security and maintenance of social infrastructure. In such applications, gaseous detectors can be used due to high and low detection efficiency for neutron and gamma rays as background noise, respectively. However, gaseous detectors contain expensive gas or toxic gas like ³He and BF₃, and scintillators are expected to be an alternative detector. Here, neutron energy is evaluated using Time-of-Flight (TOF) method, and the energy resolution depends on the timing response of the scintillator. Therefore, inorganic scintillators with long decay time are not suitable for measurements of neutron energies.

Organic scintillators are used as neutron detectors, and trans-stilbene crystals, for example, have decay time of 6.4 ns [1] and good pulse shape discrimination (PSD) property, which is often operated to discriminate neutron/gamma [2]. Organic non-single-crystal scintillators such as liquid scintillators (LSs) and plastic scintillators (PSs) are applied to detection of underground environment neutron and energy spectrum measurement of fast neutrons, etc., because these scintillators have faster scintillation decay than organic “crystal” scintillators. However, LSs are flammable and toxic, and PSs have low radiation hardness. Therefore, we focused on organic crystal scintillators which are safer and more stable than LSs and PSs.

We grew pure trans-stilbene crystal and 1,4-Bis(2-methylstyryl) benzene (BisMSB)-doped trans-stilbene crystal, by the self-seeding vertical Bridgman method using an enclosed chamber [3]. The doping amount of BisMSB was 1wt%. Pulling down rate for growth was 1.44 mm/h. BisMSB was used as solutes in LSs and PSs, and BisMSB doped LSs have fast decay times of ~2 ns [4].

We measured the photoluminescence (PL) emission spectra of the samples excited by 260-nm photons at 13 and 300 K as shown in Fig. 1, with the BL3B at UVSOR Synchrotron Facility, using a photo multiplier tube (PMT) (C5594, Hamamatsu Photonics) and a CCD camera (MODEL:TN/CCD/100PBVISAR, Princeton Instruments). At 300 K, the emission peaks ranged from 400 to 550 nm were appeared for the BisMSB-doped crystal. Although the spectrum was shifted by doping BisMSB at 13 K, the peak was blue-shifted compared to that at 300 K.

The PL decay times of the samples excited by 260-

nm photons at 13-300 K are summarized in Table 1. The ranges of excitation wavelength and emission wavelength for PL decay measurements were from 226 to 293 nm and from 295 to 680 nm, respectively. The PL decay time of trans-stilbene matched the value in previous report [5]. Despite the difference of luminescence spectra, there was almost no difference in photoluminescence decay times between the two crystals. Further study is necessary to reveal the reason.

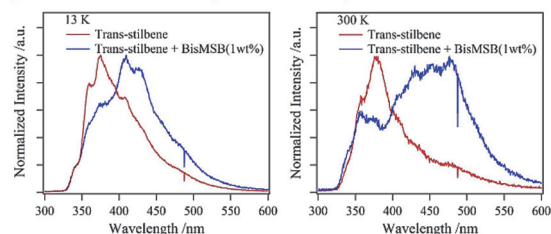


Fig. 1. Emission spectra of grown crystals excited by 260 nm at 13 K and 300 K.

Table 1. Photoluminescence decay times of grown crystals excited by 260 nm at 13-300 K

T [K]	Trans-stilbene	Trans-stilbene + BisMSB(1wt%)
	τ_1 [ns]	τ_1 [ns]
13	1.9	1.8
50	1.9	1.8
100	1.7	1.7
200	1.2	1.5
250	1.1	1.5
300	1.0	1.1

[1] J. B. Birks, *The Theory and Practice of Scintillation Counting*, (Pergamon, Oxford, 1964).

[2] N. Zaitseva *et al.*, *IEEE Trans. Nucl. Sci.* **58** (2011) 3411.

[3] A. Arulchakkaravarthi *et al.*, *J. Crystal Growth* **234** (2002) 159.

[4] M. M. de Souza *et al.*, *Synth. Metals* **101** (1999) 631.

[5] D. J. S. Berch *et al.*, *Chem. Phys. Lett.* **38** (1976) 432.

BL3B

Temperature Dependence of Cs₂HfI₆ Transmittance Spectra

S. Kodama¹, S. Kurosawa^{2,3}, A. Yamaji¹, M. Yoshino¹, Y. Ohashi¹, K. Kamada^{2,4},
Y. Yokota² and A. Yoshikawa^{1,2,4}

¹ Institute for Materials Research (IMR), Tohoku University, Sendai 980-8577, Japan

² New Industry Creation Hatchery Center (NICHe), Tohoku University, Sendai 980-8579, Japan

³ Faculty of Science, Yamagata University, Yamagata 990-8560, Japan

⁴ C&A Corporation, Sendai 980-8577, Japan

A₂HfX₆ (A: monovalent cation, X: halogen ion) compounds are host-emitting materials originated from self-trapped exciton. Since the crystal lattice of A₂HfX₆ compounds can be a well-ordered and high symmetry cubic structure (space group: *Fm-3m*), producing a transparent single crystal is easy. Actually, Cs₂HfCl₆ (CHC) or anion-admixed Cs₂HfCl₂Br₄ had been reported as single-crystalline scintillators so far [1-2], and CHC has a high scintillation light-output of over 50,000 photons/MeV.

Generally, the light output of scintillator (*Y*) is inversely proportional to band-gap energy of the host material (E_{gap}); $Y \propto (E_{\text{gap}})^{-1}$. In order to realize the higher light output than CHC, Cs₂HfI₆ (CHI) is investigated in this study, because the E_{gap} of CHC and CHI were calculated as ~6.4 eV and ~3.9 eV, respectively [3].

A single-crystalline CHI specimen was synthesized from 99%-pure HfI₄ and 99.999%-pure CsI using the vertical Bridgman growth method. CHI was revealed to emit orange-red light around 650 nm, and had a high light output of ~70,000 photons/MeV, a moderate fast scintillation decay of ~2.5 μs. We found that CHI is a first noble red-emitting scintillator applicable to the photon-counting detect technique.

To develop CHI furthermore, the evaluation of fundamental optical properties should be necessary, and we measured transmittance spectra of CHI at room temperature and 8 K cooled by liquid Helium in a cryostat chamber of UVSOR BL3B. Transmittance spectra were measured with a photo-diode (IRD, AXUV 100). The light source was a synchrotron light.

Figures indicate the obtained transmittance spectra of CHI at room temperature and 8 K. The transmittance gradually decreased towards shorter wavelength from 700 nm. We observed a transmittance drop around ~480 nm at room temperature, and the dropping wavelength was revealed to shift to ~440 nm at 8 K due to lattice vibration. Since CHI was revealed to absorb the blue-yellow visible light around ~480 nm, CHI crystal had the orange color. CHI should have an absorption edge around ~320 nm based on the calculated E_{gap} of ~3.9 eV. The transmittance drop at ~480 nm was considered to be an absorption of the self-trapped exciton.

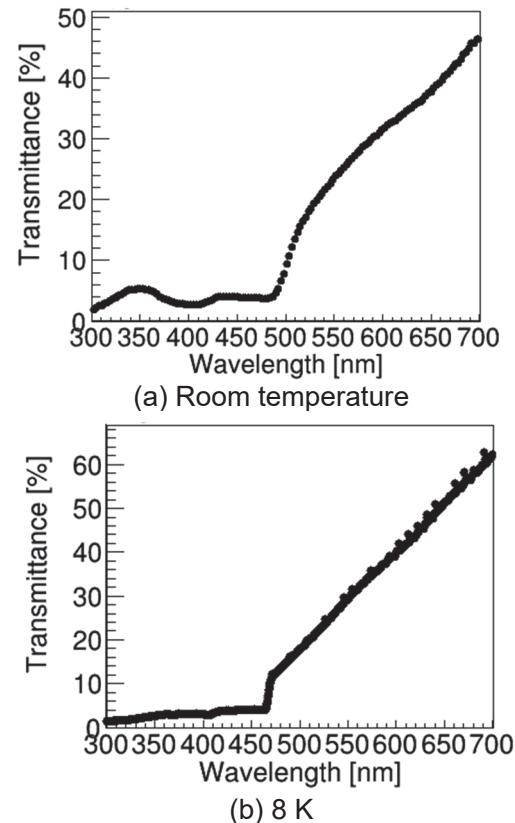


Fig. Transmittance spectra of CHI crystal. (a) and (b) are spectra at room temperature and 8 K, respectively.

- [1] A. Burger *et al.*, Appl. Phys. Lett. **107** no. 14 (2015) 34.
[2] S. Lam, C. Guguschev, A. Burger, M. Hackett, and S. Motakef, J. Cryst. Growth **483** (2018) 121.
[3] B. Kang and K. Biswas, J. Phys. Chem. C **120** no. 22 (2016) 12187.

BL3B

Evaluation of Optical Basic Properties of Ultra-Violet Emitting Zinc Aluminate Phosphor

H. Kominami¹, K. Hada¹, S. Kubota¹, K. Kijima¹, M. Ohkawa¹, Y. Kato¹,
T. Matsuura², M. Arimura², K. Imagawa² and K. Warita²

¹Graduate School of Integrated Science and Technology, Shizuoka University, Hamamatsu 432-8651, Japan

²Faculty of Engineering, Shizuoka University, Hamamatsu 432-8651, Japan

The UV light is used for various applications depending on the wavelength as well as the sterilization described above. The lights of 200-280 nm (UV-C) region as for the sterilization, 280-320 nm (UV-B) region as the treatment of the skin disease, 320-400nm (UV-A) region as application of purification of water and air, and photocatalysts. Recently, from the viewpoint of consideration to the environment, the mercury free UV emission devices have been demanded for the application of catalyst and medical situations. In our previous work, it was clarified that ZnAl₂O₄ phosphor was suitable for the UV field emission lamp because of its stability and luminescent property. It shows strong UV emission peaked around 250 nm which suitable for sterilization. In ZnAl₂O₄, the application as the sterilization light source is expected from the luminescence wavelength area, but it is not sure about the application as other ultraviolet light sources. Therefore, the possibility of the application of the ultraviolet light source is thought about by controlling composition of ZnAl₂O₄.

Zn(Al_{1-x}Ga_x)₂O₄ powders were prepared by solid phase synthesis using ZnO (99.999%), α -Al₂O₃ (99.99%) and Ga₂O₃ (99.9%) powders. The Ga ratio x was changed from 0 ~ 1 for control the phase. The powders were fired at 1000 ~ 1300 °C for 3 hours in air. And the powders were evaluated using X-ray diffraction (XRD), Cathodoluminescence (CL) and Photoluminescence (PL, PLE).

Figure 1 shows cathodoluminescent spectra of Zn(Al_{1-x}Ga_x)₂O₄ phosphors fired at 1300°C in air. The emission peak was shifted from 250 nm to 350 nm according to increasing of Ga ratio x . However, CL intensity of phosphors were quite different by Ga composition. Especially, the powders at $x = 0.5$ and 1 showed poor luminescence. It is thought that the distortion of crystallinity was occurred for the powder of $x = 0.5$. On the other hand, for the powder of $x = 1$, the optimum firing condition of ZnGa₂O₄ was different from ZnAl₂O₄.

Figure 2 shows Photoluminescent excitation spectra of Zn(Al_{1-x}Ga_x)₂O₄ phosphors fired at 1300°C in air, measured at 8K. The excitation band was shifted to longer wavelength according to increase of Ga ratio x . From our previous work, the PLE absorption edge of ZnAl₂O₄ was equivalent to forbidden gap. It indicates that forbidden gap of Zn(Al_{1-x}Ga_x)₂O₄ phosphors became narrower according to increase of Ga ratio. The energy of absorption edge was changed linearly. From XRD measurement also shows Zn(Al_{1-x}Ga_x)₂O₄

phosphors successfully synthesized at 1300°C firing because of the shift of diffraction peak obeyed Begard's law. it seems that the replacement of Ga to Al-site was occurred smoothly.

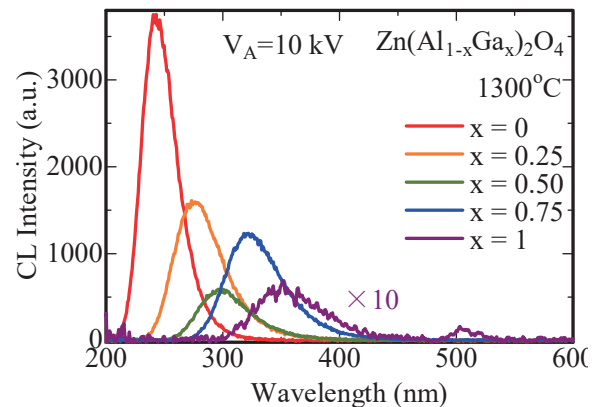


Fig. 1. CL spectra of Zn(Al_{1-x}Ga_x)₂O₄ alloy phosphor.

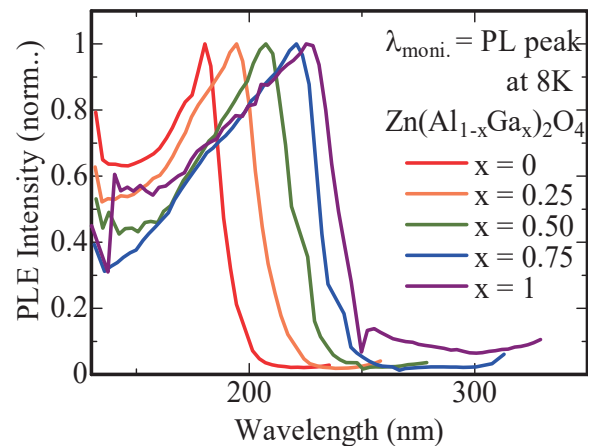


Fig. 2. PLE spectra of Zn(Al_{1-x}Ga_x)₂O₄ phosphor at 8K monitored at CL peak.

BL3B

Emission Spectra of Pr-doped SrY₂O₄

M. Yoshino, S. Nishiki, T. Kuyama and S. Watanabe

Graduate School of Engineering, Nagoya University, Nagoya 464-8603, Japan

The trivalent lanthanide ions (e.g., Ce³⁺, Nd³⁺, Er³⁺) in oxide crystals have drawn attentions due to their application for luminescent materials in NIR to UV regions such as solid-state lasers, phosphors or scintillators. The trivalent praseodymium ion, Pr³⁺, has also attracted attentions as luminescence centers. In this work, the excitation spectra and emission spectra for Pr³⁺ in SrY₂O₄ crystal have been measured. The Pr-doped SrY₂O₄ samples are synthesized by solid state reactions. The samples are annealed in N₂-H₂ atmosphere in order to reduce Pr⁴⁺ to Pr³⁺. The concentration of Pr in the samples are 0.5, 1.0, 1.5, 2.0 and 3.0 mol%.

The excitation spectrum monitored at 520 nm emission contains absorption around 315 nm and 273 nm and they originate the *4f-5d* transitions of Pr³⁺ [1]. The emission spectra at 315 and 273 nm excitation in 300 K are shown in Fig. 1 and Fig. 2, respectively.

Peaks A, B, C, D, E exist in the each spectra. On the other hand, peak F appears only in 273 nm excitation and has different dependency to Pr concentration compared with the other peaks. The intensity of F decrease with Pr concentration while it decreases after the increase in A, B, C, D and E. The emission spectra at 315 and 273 nm excitation in different temperatures are shown in Fig. 3 and Fig. 4, respectively. It is found that the peak F has also different dependency to temperature compared with the other peaks. The intensity of F is high when it measured in high temperature while it decreases monotonously with temperature in the other peaks. The peak F is not seen in the spectrum of 315 nm excitation in each temperature.

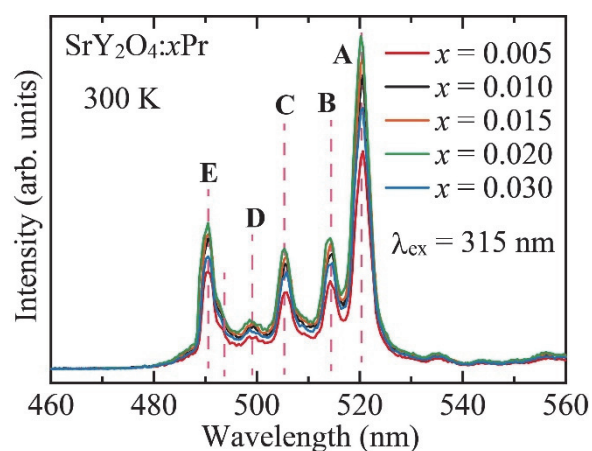


Fig. 1. Emission spectra of SrY₂O₄:xPr. ($\lambda_{\text{ex}} = 315$ nm, 300 K).

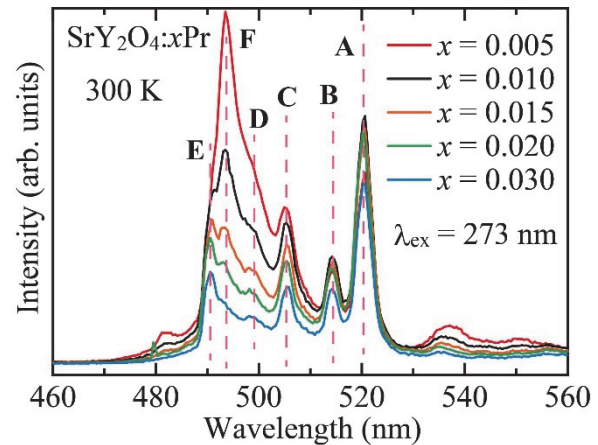


Fig. 2. Emission spectra of SrY₂O₄:xPr. ($\lambda_{\text{ex}} = 273$ nm, 300 K).

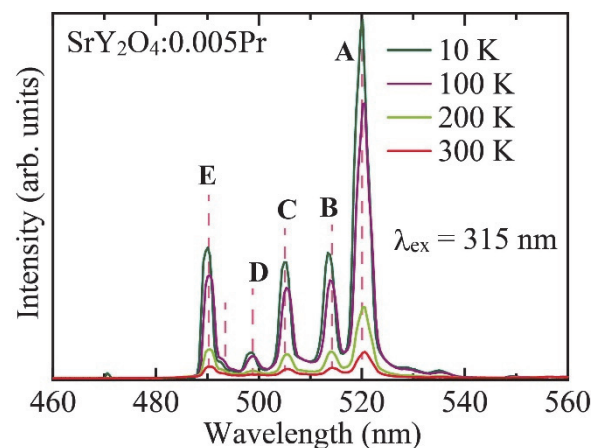


Fig. 3. Emission spectra of SrY₂O₄:0.005Pr. ($\lambda_{\text{ex}} = 315$ nm).

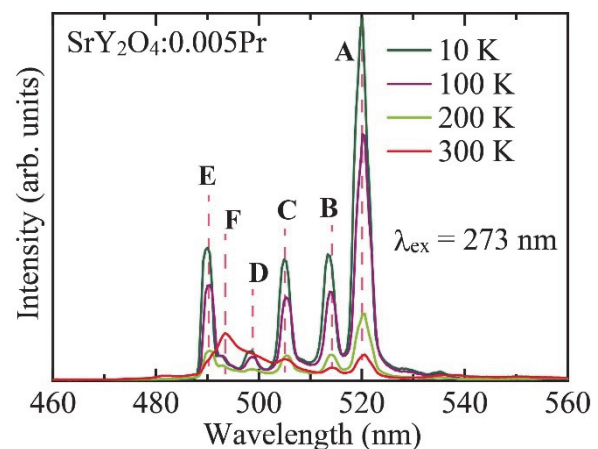


Fig. 4. Emission spectra of SrY₂O₄:0.005Pr. ($\lambda_{\text{ex}} = 273$ nm).

[1] M. Yoshino, S. Nishiki and S. Watanabe, UVSOR Activity Report **43** (2016) 95.

BL3B

Energy Transfer from Γ^- Centers to TI^+ Centers in Co-Doped $\text{NaCl:}\Gamma^-, \text{TI}^+$ Crystals

O. Yagi and T. Kawai

Graduate School of Science, Osaka Prefecture University, Sakai 599-8531, Japan

Energy transfer mechanism in solid crystals is one of the interesting research topics in solid state physics. Many experimental investigations have been performed on the crystals co-doped with two kinds of impurities. The resonant transfer and the emission reabsorption are well-known as the mechanism of the energy transfer. Both the mechanisms can occur if there is the overlap between the donor's luminescence band and the acceptor's absorption band [1].

In this study, we have investigated the NaCl crystals co-doped with Γ^- and TI^+ ions ($\text{NaCl:}\Gamma^-, \text{TI}^+$) to discuss the existence and the mechanism of the energy transfer. NaCl crystals have the wide band-gap up to the vacuum ultraviolet energy region and are a suitable candidate host for doping of impurity ions. NaCl crystals doped with iodine anion ($\text{NaCl:}\Gamma^-$) exhibit intense luminescence in deep ultra-violet region even at room temperature (RT), so iodine anions in NaCl are a suitable donor impurity.

Figure 1 shows the absorption spectrum of NaCl:TI^+ and the luminescence spectrum of $\text{NaCl:}\Gamma^-$ at RT. NaCl:TI^+ produces three absorption bands labeled with A, B, and C at 4.8, 5.3, and 6.2 eV respectively. These absorption bands are attributed to the intra-ionic transitions from the ground $^1\text{S}_0$ state to the excited $^3\text{P}_1$, $^3\text{P}_2$, and $^1\text{P}_1$, states. $\text{NaCl:}\Gamma^-$ shows the luminescence band appearing around 5.2 eV. It is called the NE luminescence band and comes from the one-center type localized exciton, which is localized on the central site of a substituted Γ^- impurity with small lattice relaxation [2]. The NE luminescence band in $\text{NaCl:}\Gamma^-$ has almost no overlap with the absorption bands in NaCl:TI^+ . This fact indicates that the resonant energy transfer and the emission reabsorption from the Γ^- centers to the TI^+ centers are hard to occur.

Figure 2 shows the decay profiles of the NE luminescence in the $\text{NaCl:}\Gamma^-, \text{TI}^+$ under the excitation on the Γ^- absorption band (6.8 eV) at 6, 160, 200, and 240 K. The decay profiles at 6~160 K exhibit a single exponential decay. The decay time constants at 10 and 160 K are 88 and 43 ns, respectively, which are the same as the decay time of the $\text{NaCl:}\Gamma^-$. On the other hand, the decay profiles at 200~300 K exhibit two exponential decay components. Both decay components become faster with increasing temperature. The behavior of the decay profiles indicates the existence of the energy transfer from the Γ^- centers to the TI^+ centers at more than 200 K. We are analyzing the decay profiles with the energy transfer model via carrier diffusion reaction.

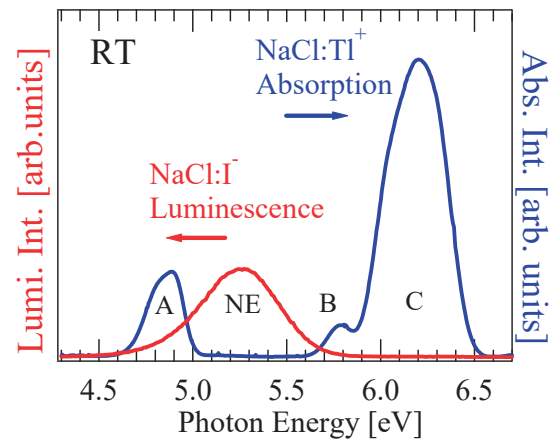


Fig. 1. Luminescence spectrum (Red) of $\text{NaCl:}\Gamma^-$ and absorption spectrum (blue) of NaCl:TI^+ at RT.

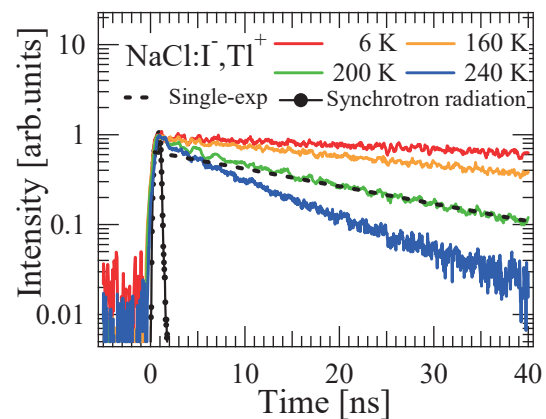


Fig. 2. Decay profiles of the NE luminescence in the $\text{NaCl:}\Gamma^-, \text{TI}^+$ at 6, 160, 200, and 240 K.

[1] A. Iguchi, T. Kawai and K. Mizoguchi, *Phys. Status Solidi. C* **13** (2015) 85.

[2] I. Akimoto, M. Shimozato and K. Kan'no, *Phys. Status Solidi. C* **6** (2009) 342.

BL3B

Comparison of Luminescence Properties at Room Temperature between NaI:TI⁺ and NaI:In⁺ Crystals

S. Watanabe and T. Kawai

Graduate School of Science, Osaka Prefecture University, Sakai 599-8531, Japan

Alkali halide crystals doped with TI⁺-type centers have been extensively studied until now. The TI⁺-type centers exhibit the optical bands called A, B, and C, which are attributed to intra-ionic transitions from the ¹A_{1g} ground state to the ¹T_{1u}, ³T_{2u}+³E_u, and ³T_{1u} excited states, respectively [1,2].

Among the alkali halides doped with the TI⁺-type centers, CsI:TI⁺ and NaI:TI⁺ crystals have been widely used as a scintillator and investigated in detail. Especially, NaI crystals doped with the TI⁺ centers have the high scintillation yield and faster time response. On the other hand, optical studies on NaI crystals doped with In⁺ centers have not been reported to our knowledge. In this study, optical properties of the NaI:In⁺ crystals have been investigated at room temperature (RT).

NaI:In⁺ and NaI:TI⁺ crystals were grown by the Bridgman method from NaI beads and InI or TII powders, respectively. The samples used for the measurements were cleaved in a nitrogen-filled glove box. Optical measurements were performed at the BL3B of UVSOR.

Figure 1 shows the luminescence spectra of NaI:In⁺ and NaI:TI⁺ under excitation at 200 nm at RT. In NaI:TI⁺, the A' luminescence band due to the radiative transition from the relaxed excited state of ³T_{1u} is confirmed at 425 nm [3]. The NaI:In⁺ crystal exhibits a broad luminescence band around 520 nm, which would be assigned to the A' luminescence of the In⁺ centers from the comparison with NaI:TI⁺.

Figure 2 shows the absorption (broken curve) and the excitation (solid curve) spectra for the A' luminescence of NaI:In⁺ and NaI:TI⁺ at RT. The absorption band at 295 nm in NaI:TI⁺ corresponds to the A absorption band [3]. Since the absorption bands of the In⁺ center in alkali halide crystals are located at the lower energy region than those of the TI⁺ centers, the band at 275 nm in NaI:In⁺ would correspond to the C band. The A' luminescence bands in both the crystals are efficiently excited at the respective absorption bands. Furthermore, both excitation spectra demonstrate that the A' luminescence bands have responses even in the higher energy range than about 230 nm, where correspond to the energy region above the fundamental absorption edge of NaI host crystals. The fact indicates that the energy absorbed by the host crystals transfers to the energy level of the impurity centers. The luminescence properties of NaI crystals activated with various kind of impurity centers should be extensively investigated.

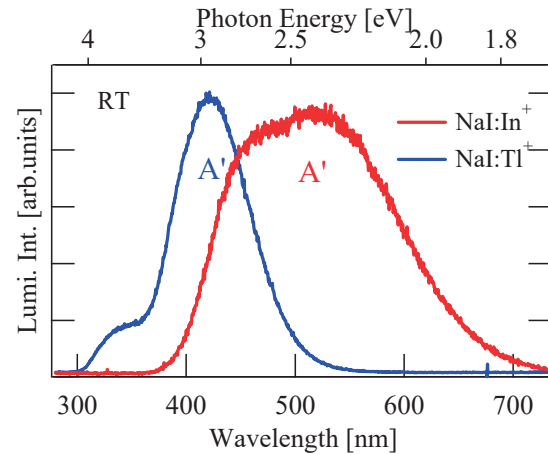


Fig. 1. Luminescence spectra of NaI:In⁺ (red) and NaI:TI⁺ (blue) crystals excited at 200 nm at RT.

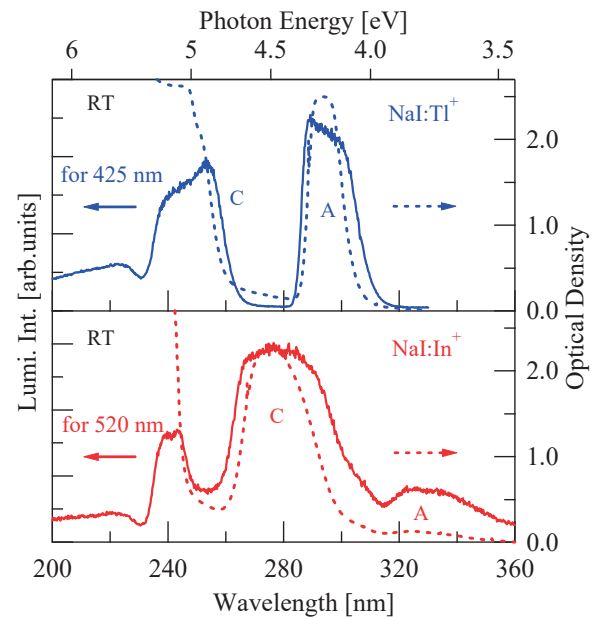


Fig. 2. Absorption (broken) and Excitation (solid) spectra for the A' luminescence of NaI:In⁺ and NaI:TI⁺ at RT.

[1] A. Ranfagni *et al.*: *Advances in Physics* **32** (1983) 823.

[2] P. W. M. Jacobs: *J. Phys. Chem. Solids* **52** (1991) 35.

[3] M. P. Fontana and W. J. Van Sciver: *Phys. Rev.* **168** (1968) 960.

BL3B, BL7B

Total Photoelectron Yield Spectroscopy on 3d Transition Metal Doped AlN Films

N. Tatemizo¹, S. Imada¹, S. Hirata², W. Kamihigoshi² and K. Fukui²

¹Faculty of Electrical Engineering and Electronics, Kyoto Institute of Technology, Kyoto, 606-8585, Japan

² Faculty of Electrical and Electronics Engineering, University of Fukui, Fukui, 910-8507, Japan

Intermediate band (IB) materials proposed by Luque *et al.*, have gained attention for use in absorption layers of solar cells to increase their conversion efficiency [1]. Heavy 3d-transition metal (3d-TM) doped AlN films are one of the candidates of IB materials. Exploring the possibility of them, we have synthesized Ti [2], V [3] and Cr [4,5] doped AlN films and investigated their band structures.

The films were deposited on SiO₂ glass or Ti metal polycrystalline substrates by RF sputtering from an AlN target with Ti or Cr metal chips on it. Results of XRD, TEM and 3d-TM K-edge EXAFS showed that the films have wurtzite structures with Ti and Cr atoms occupied the Al sites of AlN [2,5]. To investigate the potentials of the electron occupied states (Valence band and/or a part of IB), we carried out total photoelectron yield spectroscopy (TPYS) [6] for the films deposited on Ti metal substrates. As show in Fig. 1. electrical contacts with the film were made both back (thorough the Ti substrate) and front (a Cu metal plate with hole). A photoelectron corrector was set in front of the film with around 1mm interspace. A negative bias was applied to the sample against the grounded photoelectron corrector. The number of photoelectrons was obtained by measuring the current needed to compensate for the photoexcited holes at the sample with an ammeter. The photoemission yield was measured as a function of incident photon energy.

Figure 2 shows TPYS spectra of AlN films doped with 11.0 and 8.3% Ti and 12.3 and 9.3% Cr. It is clear that the Cr-doped films have threshold at around 5.5 eV, while threshold of the Ti-doped films is at around 6.0 eV. These results agree well with the theoretical levels of Cr and Ti in AlN [7]. We have obtained different thresholds for other different 3d-TM elements, which means the potential of IB can be controlled via choice of 3d-TM elements and adjust the band structure for the effective photoconversion. To reveal all potentials of the electron occupied band of the films, we will extend the energy region of the measurements to larger one.

- [1] A. Luque *et al.*, Phys. Rev. Lett. **78** (1997) 5014.
- [2] N. Tatemizo *et al.*, J. Mater. Chem. A **5** (2017) 20824.
- [3] N. Tatemizo *et al.*, J. App. Phys., **123** (2018) 161546.
- [4] N. Tatemizo *et al.*, J. of Phys.: Condens. Matter, **29** (2017) 085502.
- [5] N. Tatemizo *et al.*, AIP advances, **7** (2017) 055306.
- [6] M. Honda *et al.*, J. Appl. Phys. **102** (2007) 103704.
- [7] U. Gerstmann *et al.*, Phys. Rev. B, **63** (2001) 1.

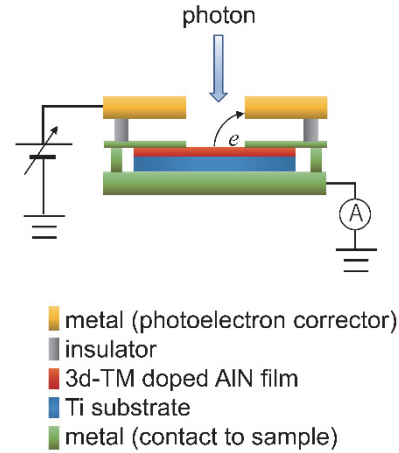


Fig. 1. Schematic of sample setting for the TPYS measurements.

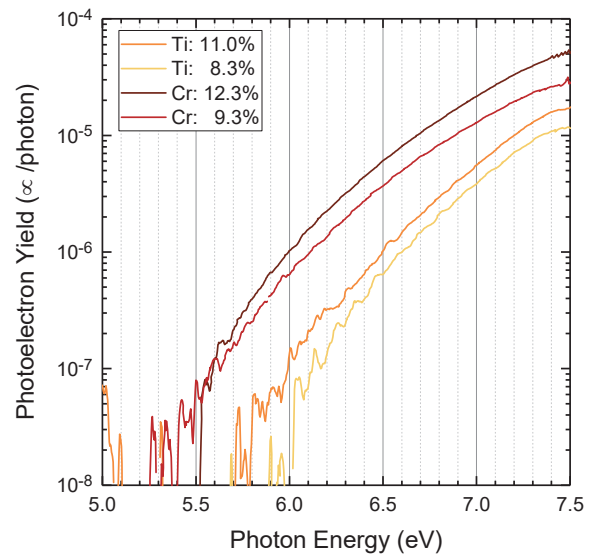


Fig. 2. Total photoelectron yield spectra of 3d-TM doped AlN films (12.3 and 9.3 % of Cr and 11.0 and 8.3 % of Ti) deposited on Ti metal substrates.

BL3B

Study of Defect Induced by Hydrogen Reduction in MgO Single Crystal by UV Absorption Spectroscopy

E. Kobayashi¹, K. K. Okudaira², S. Yoshioka³, K. K. Bando⁴ and O. Takahashi⁵

¹*Kyushu Synchrotron Light Research Center, Tosu 841-0005, Japan*

²*Chiba University, Chiba 263-8522, Japan*

³*Graduate School of Engineering, Kyushu University, Fukuoka 819-0395 Japan*

⁴*National Institute of Advanced Industrial Science and Technology, Tsukuba 305-8565, Japan*

⁵*Institute for Sustainable Science and Development, Hiroshima University, Higashi-Hiroshima, 739-8526, Japan*

Magnesium oxide (MgO) is a typical wide band gap insulator and is used in a wide range of devices [1-4]. Physical characteristics such as optical or electrical performances are greatly affected by the presence of defects. Various types of defects are found in metal oxides, which are composed of points, lines and planes. The electronic state derived from those defects controls electrical, optical, or magnetic functions of devices. Therefore, a lot of efforts have been made so far to understand the effect of point defects on the electronic states of metal oxides so far, but more detailed atomic level investigation of defects is still desired.

In this study, we focused on magnesium oxide to see the effect of typical oxygen point defects on the electronic states derived from oxygen. We investigated the correlation between the defects and the electronic states using near-edge X-ray absorption fine structure (NEXAFS) spectroscopy and ultraviolet absorption spectroscopy.

The MgO single crystals were annealed at several temperatures at 673 K ~1173 K in a hydrogen atmosphere for 4 hours. The sample was gradually cooled to room temperature, exposed to the air, then introduced into a vacuum apparatus, and the spectrum was measured. UV spectra of MgO single crystal were measured at the BL3B of UVSOR in the Institute of Molecular Science.

The change in the band gap created by oxygen defects was investigated with transmission spectra in the ultraviolet region. Figure 1 shows UV spectra of MgO(100). A distinct increase in absorption from 5.6 eV to 7.2 eV was observed for the samples treated under hydrogen, compared to an untreated sample. On the other hand, in the NEXAFS measurement, a new maximum appeared in the pre-edge area. The appearance of pre-edge peaks suggested that defects created new electronic states in the conduction band.

The results of both UV and NEXAFS indicated that a new electronic state was formed in the conduction band due to the oxygen defect produced by the hydrogen reduction treatment, which made the band gap narrower.

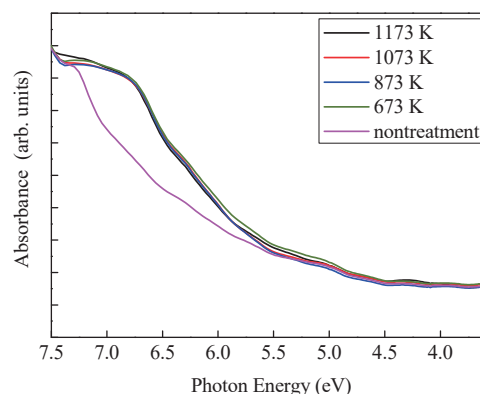


Fig. 1. UV spectra of MgO(100).

- [1] D. M. Roessler and W. C. Walker, *Phys. Rev.* **159** (1967) 733.
- [2] E. A. Colbourn, *Surf. Sci. Rep.* **15** (1992) 281.
- [3] G. H. Rosenblatt, M. W. Rowe, G. P. Williams, Jr., R. T. Williams and Y. Chen, *Phys. Rev. B* **39** (1989) 10309.
- [4] M. M. Freund, F. Freund and F. Batllo, *Phys. Rev.Lett.* **63** (1989) 2096.

BL3B

Luminescence Possibly Due to Localized Excitons in $\text{CH}_3\text{NH}_3\text{Pb}(\text{I},\text{Cl})_3$ Alloyed Thin Films

T. Makino and K. Waza

Department of Electrical and Electronics Engineering, University of Fukui, Fukui 910-8585, Japan

Perovskite-halide semiconductors ($\text{CH}_3\text{NH}_3\text{PbI}_3$) have attracted intense research interest due to their potential applications in solar-cells. The radiative and nonradiative recombination processes between the light harvesting and the hole transport layers are very important to understand the light-electricity conversion mechanism. However, the emission mechanism which is intimately related to the abovementioned recombination in $\text{CH}_3\text{NH}_3\text{PbI}_3$ is not understood completely.

Here, we are rather interested in the optical properties of its alloyed system, namely, $\text{CH}_3\text{NH}_3\text{Pb}(\text{I},\text{Cl})_3$. The physical origin of spontaneous emission in $\text{CH}_3\text{NH}_3\text{Pb}(\text{I},\text{Cl})_3$ may be attributed to the recombination of localized excitons. No photoluminescence (PL) studies have been reported in this alloy, whereas the corresponding PL studies have been reported in unalloyed $\text{CH}_3\text{NH}_3\text{PbI}_3$. An S-shaped (red–blue–redshift) temperature dependence has been observed for the peak positions of the PL spectra even in $\text{CH}_3\text{NH}_3\text{PbI}_3$. This strongly suggests inhomogeneities in $\text{CH}_3\text{NH}_3\text{PbI}_3$. Stronger inhomogeneity is expected to exist in the alloy because of the microscopic fluctuation of the concentration. This anomalous behavior is reminiscent to what one observed in alloys or quantum structures in nitride semiconductors. Essentially, no quantitative approach has been made to interpret the temperature dependence of the PL spectra in $\text{CH}_3\text{NH}_3\text{Pb}(\text{I},\text{Cl})_3$.

Let us briefly review the history for the explanation of the exciton localization mechanism in nitride semiconductors. Several simulation-based studies have been performed. The band-tail-filling model has been adopted to describe the recombination of the localized excitons. However, this model failed to explain the low-temperature dynamics of excitons. Low-temperature excitonic localization has been interpreted using numerical solutions of Schrödinger equations. This numerical approach has not successfully been applied to high temperature exciton dynamics. Finally we successfully interpreted the temperature dependence based on Monte Carlo simulation of phonon-assisted exciton hopping and relaxation, considering effects of the earlier-mentioned potential fluctuations.

We are interested in the anomalous optical behaviors of $\text{CH}_3\text{NH}_3\text{Pb}(\text{I},\text{Cl})_3$. Whether can it be interpreted along the abovementioned model applicable for nitrides?

In this work, we currently study about the temperature dependence of the PL spectra in

$\text{CH}_3\text{NH}_3\text{Pb}(\text{I},\text{Cl})_3$.

As a preparation of its detailed analysis, we show in Fig. 1 the PL spectrum taken in a low temperature (10 K). It should be noted that this spectrum has not been yet corrected with the instrumental function. Therefore, the final line-shape has possibility to be changed significantly during the correction.

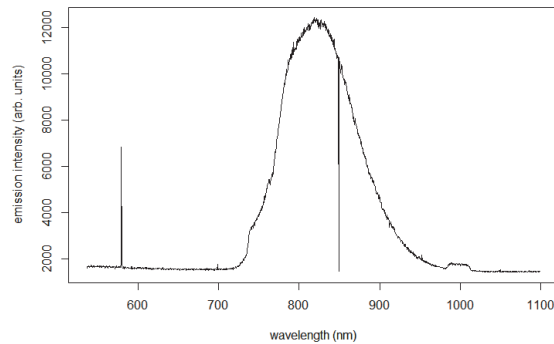


Fig. 1. Photoluminescence from alloyed thin film taken at 10 K. Excitation is made with the light source at the UVSOR Synchrotron Facility.

[1] Md. S. Hasan, Md. S. Islam, Md. R. Islam, I. M. Mehedi, T. Makino, *J. Comput. Electron.* **17** (2018) 373.

BL3B

Improvement of Persistent Luminescence Intensity of Ba₂SiO₄:Eu²⁺ Phosphor by Lanthanide Ion Co-doping Based on VRBE Diagram

K. Asami, K. Yasuda, J. Ueda and S. Tanabe

Graduate School of Human and Environmental Studies, Kyoto University, Kyoto 606-8501, Japan

The Eu²⁺ doped barium silicate phosphors are attracting much attention in optical application for scintillation materials [1] and persistent phosphors [2]. In this study, we focused on Ba₂SiO₄ host in which Eu²⁺ doped persistent luminescence property has not been investigated. For understanding the electron transfer processes and a suitable trap ion for long persistent luminescence, a vacuum referred binding energy (VRBE) diagram is useful[3]. Thus, we constructed the diagram by the spectroscopic data obtained from photoluminescence excitation (PLE) spectra of both Ce³⁺ and Eu³⁺- singly doped Ba₂SiO₄ phosphors. Based on the VRBE diagram, we found the suitable lanthanide ion co-dopant as a trap center for improvement of persistent luminescence intensity.

Figure 1 shows the PLE spectrum of the Ce³⁺- doped Ba₂SiO₄ phosphor at 15 K which was measured at BL3B. In the PLE spectrum, the host exciton peak was observed at around 7.05 eV and three bands derived from Ce³⁺ were observed at 3.2-5.8 eV. From the host exciton peak, the bandgap energy was estimated to be 7.61 eV.

Figure 2 shows PLE spectrum of the Eu³⁺- doped Ba₂SiO₄ phosphor at 10 K. The strong broad band was observed at around 4.0-7.0 eV, which is attributed to the charge transfer (CT) transition of Eu³⁺. The CT band is deconvoluted into two bands because there are two Ba sites in Ba₂SiO₄ structure. From the peak of lower CT band shown as red curve in Fig. 2, the CT energy was estimated to be 4.40 eV.

From the obtained spectroscopic data, VRBE diagram of Ba₂SiO₄ host with 4f ground states of divalent and trivalent lanthanide ions was constructed as shown in Fig. 3 based on the procedure developed by Dorenbos [3]. From the constructed diagram, we selected Er³⁺ ion as a trap center of Ba₂SiO₄:Eu phosphor. This is because estimated trap depth of Er³⁺ in Ba₂SiO₄ host (0.64 eV) from the VRBE diagram is similar to that of Dy³⁺ in SrAl₂O₄:Eu²⁺-Dy³⁺ bright persistent phosphor (~0.60 eV)[4].

Figure 4 shows the photographs of Eu²⁺ doped (left) and Eu²⁺-Er³⁺codoped (right) Ba₂SiO₄ phosphors under white light (upper), UV light (middle) and without light (lower). By co-doping Er³⁺ into Ba₂SiO₄:Eu phosphor, persistent luminescence was clearly observed. Persistent luminescence duration time on 0.32 mcd/m² is 7 min and 3.5 h for Eu²⁺- and Eu²⁺-Er³⁺ co-doped Ba₂SiO₄ phosphor, respectively.

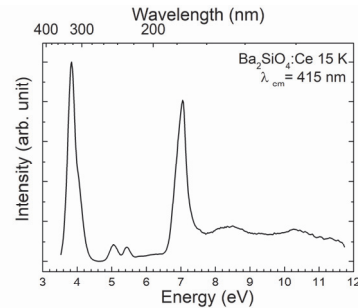


Fig. 1. PLE spectrum of Ba₂SiO₄:Ce³⁺.

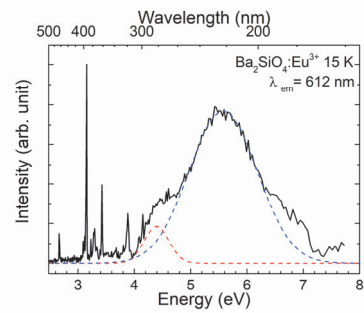


Fig. 2. PLE spectrum of Ba₂SiO₄:Eu³⁺.

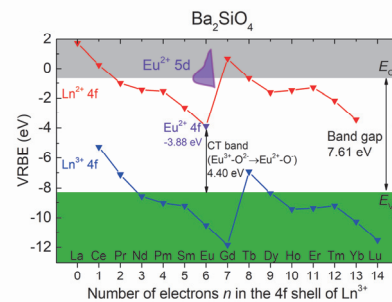


Fig. 3. VRBE diagram of Ba₂SiO₄ host.

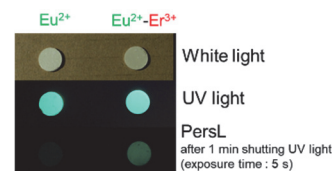


Fig. 4. Photographs of Eu²⁺ doped and Eu²⁺-Er³⁺codoped Ba₂SiO₄ phosphors.

- [1] Y. Eagleman, *et al.*, IEEE Trans. Nucl. Sci. **59** (2012) 479.
- [2] Y. Jia, *et al.*, Mater. Des. **90** (2016) 218.
- [3] P. Dorenbos, J. Lumin. **135** (2013) 93.
- [4] H. Takasaki, S. Tanabe and T. Hanada, J. Ceram. Soc. Japan. **104** (1996) 322.

BL4U

In-situ Studied the Oxygen 2*p*-vacancy in the TaO_x Interlayers of Resistive Switching Materials

J. W. Chiou¹, Y. F. Wang², W. F. Pong², J. S. Chen³, T. Ohigashi⁴ and N. Kosugi⁴

¹Department of Applied Physics, National University of Kaohsiung, Kaohsiung 811, Taiwan

²Department of Physics, Tamkang University, Tamsui 251, Taiwan

³Department of Materials Science and Engineering, National Cheng Kung University, Tainan 701, Taiwan

⁴UVSOR Synchrotron Facility, Institute for Molecular Science, Okazaki 444-8585, Japan

Resistance random access memory (ReRAM) using the change in resistance between crystalline and amorphous states of a chalcogenide compound has attracted a great deal of attention for use as next-generation nonvolatile memories. The ReRAM memory cell has a capacitor-like structure composed of insulating or semiconducting materials sandwiched between two metal electrodes. Due to its simple structure, highly scalable cross-point and multilevel stacking memory structures have been proposed. In the resistive switching phenomenon, A. Sawa [1] reports that a large change in resistance (>1000%) occurs on applying pulsed voltages and the resistance of the cell can be set to a desired values by applying the appropriate voltage pulse.

In this work, we have in-situ studied the electronic structure and the location of oxygen 2*p*-vacancy in the TaO_x interlayers and identified the type of conducting path by scanning transmission x-ray microscopy (STXM) and x-ray absorption near-edge structure (XANES). During the STXM measurements, a various voltage, 0, +50, -50, 0 volts, has exerted on both ends of the Ta/TaO_x/Pt thin film, respectively, to specify the electronic structure associated with the conducting path. The amorphous TaO_x thin film of thickness of ~75 nm was deposited on Pt/SiO₂/Si substrate by electron beam evaporation method. Active electrodes of Ta were thermally evaporated respectively on the TaO_x thin film with an equivalent thickness of ~130 nm. As shown in Fig. 1, the STXM stack mapping displays the cross-sectional views of the Ta/TaO_x/Pt thin film under various applied voltages. The experiments were performed at the BL4U. The corresponding O *K*-edge STXM-XANES spectra of the Ta/TaO_x/Pt thin film were recorded at TaO_x interlayers, as shown in Fig. 2. According to the dipole-transition selection rule, the features at ~530-545 eV are attributed to the electron excitations from O 1*s* core level to O 2*p*-derived states, which are approximately proportional to the density of the unoccupied O 2*p*-derived states. The intensities of the O *K*-edge STXM-XANES spectra are significantly lower as a voltage applied on both ends of the Ta/TaO_x/Pt thin film, which reflects the decrease in the number of unoccupied O 2*p*-derived states. In other words, the STXM-XANES results demonstrate that the population of defects at the O sites in the TaO_x interlayers and intensely support the phenomena that the existence of O 2*p*-vacancy in the TaO_x interlayers

plays a main role for the mechanics of charge transfer in resistive switching materials.

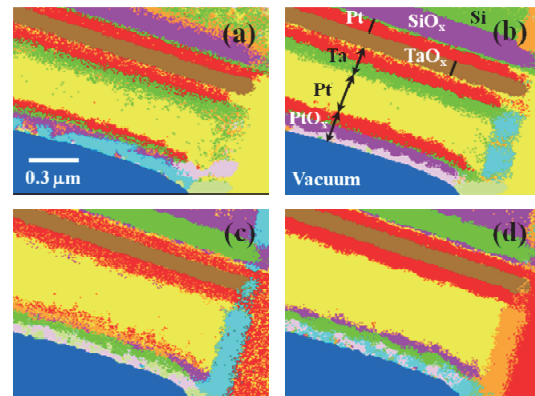


Fig. 1. The STXM stack mapping obtained in applying (a) 0, (b) +50, (c) -50, and (d) 0 volts on both ends of the Ta/TaO_x/Pt thin film, respectively.

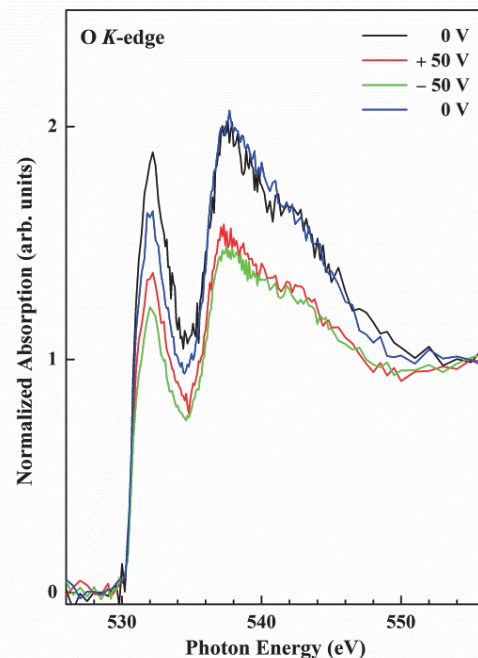


Fig. 2. The corresponding O *K*-edge STXM-XANES spectra were recorded at TaO_x interlayers under various applying voltages.

[1] A. Sawa, *Materials Today* **11** (2008) 28.

BL4U

Nano-Scale Chemical Mapping of Vapor Processed-(PEA)₂(MA)_{n-1}Pb_nI_{3n+1} Quasi-2D Perovskite Solar Cells

H. W. Shiu¹, M. S. Li², L. C. Yu¹, Y. L. Lai¹, T. Ohigashi³, N. Kosugi³, P. Chen² and Y. J. Hsu¹¹National Synchrotron Radiation Research Center, Hsinchu 300, Taiwan²Department of Photonics, National Cheng Kung University, Tainan 701, Taiwan³Institute for Molecular Science, Okazaki 444-8585, Japan

In the last couple years, a dimensionally tuned quasi-2D perovskite thin film was developed which is systematically synthesized by introducing a large organic cation, phenylethylammonium (PEA = C₈H₉NH₃) at a judiciously-chosen stoichiometry [1]. The quasi-2D perovskite exhibits the capability of combination of enhanced stability of 2D perovskite and outstanding optoelectronic properties of 3D perovskite [2]. In this work, we systematically studied the layer number dependent behavior of (PEA)₂(MA)_{n-1}Pb_nI_{3n+1} Quasi-2D perovskite by X-ray photoelectron spectroscopy (XPS), Near-edge X-ray absorption fine structure (NEXAFS), and scanning transmission X-ray microscopy (STXM).

In our previous studies, we have successfully synthesized dimensional tunable quasi-2D perovskite by mixing stoichiometric quantities of lead iodide (PbI₂), MAI (CH₃NH₃I) and PEA to yield a series of compounds, (PEA)₂(MA)_{n-1}Pb_nI_{3n+1} with different layer numbers of n. The MAI vapor-assisted method can control the morphology to achieve compact and highly stable crystalline layer. The PCEs up to 19.1% and 18.69% were achieved for n = 40 and n = 60 layers compound, respectively. Both of them showed better performance than the pristine 3D perovskite of MAPbI₃ (PCEs = 17.31%, n = ∞) and 2D perovskite of (PEA)₂MAPb₂I₇ (PCEs < 15%). Besides, compare with the SEM results, it indicated that PEA may play an important role for the photovoltaic performance, because the change of the morphology was correlated with the amount of large organic cation.

To further confirm the correlation between the morphology, photovoltaic properties and the effect of MAI vapor, chemical mapping of carbon, nitrogen and titanium in the aggregation of SiN/TiO₂/(PEA)₂(MA)_{n-1}Pb_nI_{3n+1} (n = 1, 2, 20, 40 and ∞) are studied by NEXAFS and STXM. Figure 1 shows the STXM OD images of n = 2, quasi-2D perovskite with and without MAI vapor treatment at 293.5 eV, which is corresponding to the C-Cσ* resonances. As shown in Fig. 1 (a), most of the areas is covered by the plump caterpillar-like perovskite films without MAI treatment. In contrast, the perovskite becomes slim and aggregating on to TiO₂ nano-structures as observed in Fig. 1 (b). Some bright spots with intense spherical shapes in carbon mapping is observed at low dose of the MAI treatments while it is not observed at higher dosage.

The corresponding micro NEXAFS spectra at carbon K-edge with circular marks in Fig. 1 are shown

in Fig. 2a. Figure 2b shows the reference NEXAFS spectra of n = 1, n = 20, n = 40 and MAPbI₃ (n = ∞) for comparison. When the PEA is doped into the PbI₂ film for n = 2 without MAI vapor reaction, the absorption profile along with characteristic peaks are similar to the 2D (PEA)₂PbI₄ perovskite (n = 1). After MAI vapor treatment, the n = 2 film starts growing in the mixture phase containing CH₃NH₃⁺ (MA⁺) cation and aggregates onto TiO₂ substrate. The spectrum is similar to the measurement of MAPbI₃. For lower MAI dosage, an intermediate state is observed as shown in Fig. 2a that may explain the reaction process of MAI vapor treatment.

(a) (b)

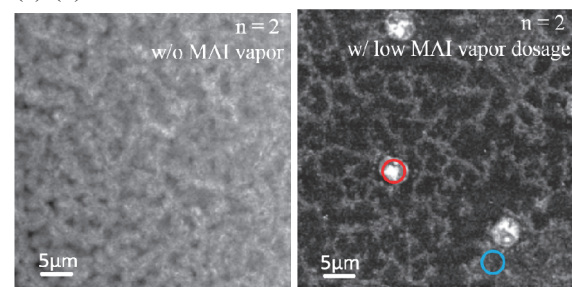


Fig. 1. C K-edge optical density images of n = 2 quasi-2D perovskite (a) without and (b) with MAI vapor treatment onto SiN/TiO₂ substrate. The carbon OD images are obtained at 293.5 eV.

(a) (b)

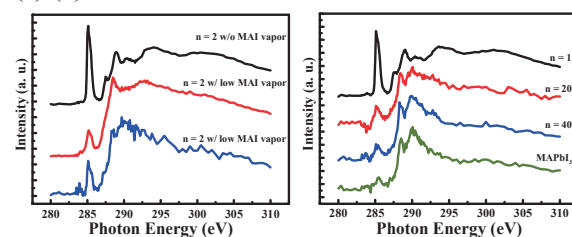


Fig. 2. (a) C K-edge spectra of n = 2 quasi-2D perovskite without (Fig.1a) and with low (Fig.1b) MAI vapor dosage. (b) C K-edge reference spectra for n = 1, n = 20, n = 40 and MAPbI₃ (n = ∞).

[1] I. C. Smith, E. T. Hoke, D. S.-Ibarra, M. D. McGehee, H. I. Karunadasa, *Angew. Chem. Int. Ed.* **53** (2014) 1.

[2] L. N. Quan, M. Yuan, R. Comin, O. Voznyy, E. M. Beauregard, S. Hoogland, A. Buin, A. R. Kirmani, K. Zhao, A. Amassian, D. H. Kim, E. H. Sargent, *J. Am. Chem. Soc.* **138** (2016) 2649.

BL4U

Phase Evolution of Complex Metal Hydrides during De/Rehydrogenation

J. L. White^{1,2}, T. Ohgashi³, K. G. Ray^{2,4}, Y.-S. Liu^{2,5}, V. Stavila^{1,2}, M. D. Allendorf^{1,2}
and J. Guo^{2,5}

¹Sandia National Laboratories, Livermore, CA 94551, United States

²Hydrogen Materials–Advanced Research Consortium (HyMARC), Livermore, CA 94551, United States

³UVSOR Synchrotron Facility, Institute for Molecular Science, Okazaki 444-8585, Japan

⁴Lawrence Livermore National Laboratory, Livermore, CA 94550, United States

⁵Lawrence Berkeley National Laboratory, Berkeley, CA 94720, United States

Lightweight complex metal hydrides are of interest for use as energy-dense on-board vehicular hydrogen stores [1]. One material of particular interest, magnesium borohydride ($\text{Mg}(\text{BH}_4)_2$), has very high hydrogen capacity, at 14.9 wt.% H, but suffers from slow kinetics and the need for extreme conditions for both dehydrogenation and rehydrogenation from magnesium diboride (MgB_2) [2]. In order to establish methods to improve the kinetic properties of this system, a greater understanding of the nucleation and growth of various solid phases is essential.

Several samples of partially dehydrogenated $\text{Mg}(\text{BH}_4)_2$ and partially hydrogenated MgB_2 were examined by Scanning Transmission X-Ray Microscopy (STXM) at the boron K-edge using the transfer system from a glovebox to BL4U to prevent oxidation upon exposure to air. The resulting series of X-ray absorption images were analyzed using computed spectra for several B containing species (Fig. 1), since the experimental XAS spectra showed substantial amounts of oxidized boron.

The STXM maps revealed some intriguing phase propagation patterns not heretofore observed. MgB_2 partially hydrogenated at 400 °C and either 200 or 700 bar H_2 over the course of 72 h (Fig. 2) showed that hydrogenation to $\text{Mg}(\text{BH}_4)_2$ began at the exterior of the particles and spread inward, with greater conversion evident at the higher pressure, as expected.

However, the $\text{Mg}(\text{BH}_4)_2$, partially dehydrogenated at 400 °C and H_2 overpressures of 200 and 360 bar, showed a much more counterintuitive phase transformation (Fig. 3). It has commonly been hypothesized that the dehydrogenated phase forms first on the outside of hydride particles as the hydride releases H_2 from the surface [3]. Instead, our STXM results on $\text{Mg}(\text{BH}_4)_2$ show that the hydride remains on the exterior, whereas the interior becomes dehydrogenated first. The higher overpressure sample decomposed less, and consequently its interior retained more of the hydride phase. Therefore, nucleation of the dehydrogenated material begins in the bulk, and hydrogen atoms diffuse toward the surface where they can combine and desorb as H_2 gas. Information regarding the phase evolution in the Mg-B-H system provides valuable insights into the rate-limiting step of hydrogen desorption.

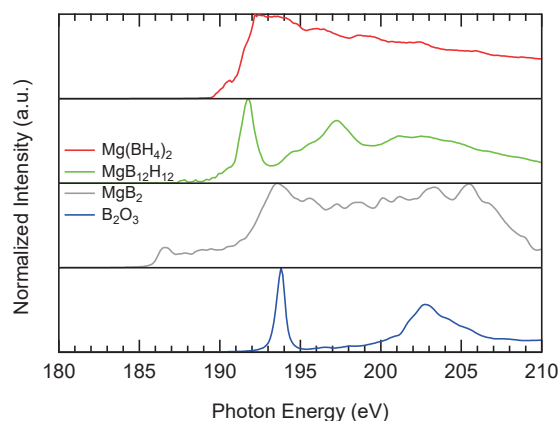


Fig. 1. Simulated B K-edge XAS spectra of relevant chemical species used in STXM analyses.

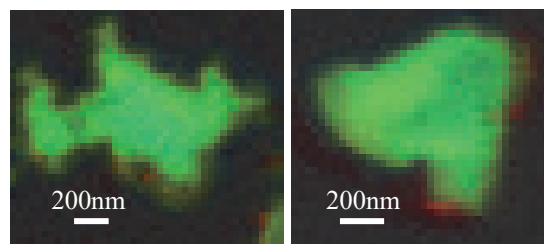


Fig. 2. STXM maps of MgB_2 hydrogenated for 72 h at 400 °C and (a) 200 or (b) 700 bar H_2 . Red indicates $\text{Mg}(\text{BH}_4)_2$, green $\text{MgB}_{12}\text{H}_{12}$, and blue B_2O_3 .

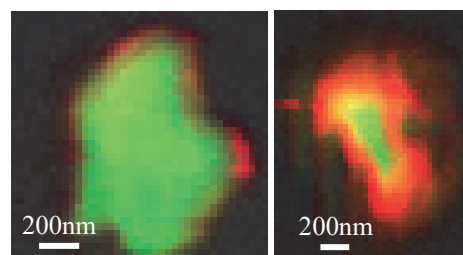


Fig. 3. STXM maps of $\text{Mg}(\text{BH}_4)_2$ dehydrogenated for 72 h at 400 °C and H_2 overpressures of (a) 200 and (b) 360 bar H_2 . Red indicates $\text{Mg}(\text{BH}_4)_2$, green $\text{MgB}_{12}\text{H}_{12}$, and blue B_2O_3 .

[1] S.-i. Orimo *et al.*, *Chem. Rev.* **107** (2007) 4111.

[2] K. G. Ray *et al.*, *Phys. Chem. Chem. Phys.* **19** (2017) 22646.

[3] B. C. Wood *et al.*, *Adv. Mater. Interfaces* **4** (2017) 1600803.

BL4U

Probing the Electronic Structure of BiVO₄ Coated ZnO Nanodendrite Core - Shell Nanocomposite Using Spatially Resolved Scanning Transmission X-ray Microscopy Studies

M. M. Shirolkar¹, J.-W. Chiou², T. Ohigashi³, N. Kosugi³ and W.-F. Pong¹

¹Department of Physics, Tamkang University, Tamsui 251, Taiwan

²Department of Applied Physics, National University of Kaohsiung, Kaohsiung 811, Taiwan

³Institute for Molecular Science, Okazaki 444-8585, Japan

Recently, it has been reported that ZnO nanodendrites (NDs) coated with BiVO₄ nanolayers core-shell nanocomposite thin film structure forms a multiple-level hierarchical heterostructure, which is remarkably beneficial for light absorption and charge carrier separation for the competent photoelectrochemical (PEC) properties compared to their individual counterparts [1]. As PEC properties are essentially a function of band alignment and atomic – electronic structures, we studied the nanocomposite thin film using various X-ray spectroscopic and microscopy studies. We have probed the origin and nature of localized electron states in core-shell structures using valance band spectroscopy, X-ray absorption spectroscopies and spatially resolved scanning transmission X-ray microscopy (STXM). The valance band studies show band alignment at the core-shell interface, which allows efficient charge transfer between heterostructure. While, X-ray absorption studies essentially show that in core-shell structure tetrahedral environment of V⁵⁺ in BiVO₄ is unusually distorted and the inter-band gap states related to another valance state of vanadium, namely, V⁴⁺ is present. The presence of multiple valance states of vanadium gives favorable conditions for small polaron formation in BiVO₄, thereby degrading PEC activities. However, it was observed that V⁴⁺ coordinates with ZnO lattice thereby giving rise to conditions similar to vanadium doped ZnO. These studies reveal electronic structure over few micrometers length scale within the thin film, which contains hundreds of nanostructures and precise locations of the coordination within individual nanostructure remain unrevealed. Moreover, high-resolution transmission electron microscopy - electron energy loss spectroscopy could not effectively resolve above-mentioned coordination features.

On the other hand, STXM is powerful technique and retains the ability to efficiently resolve the observed coordination features efficiently within single or cluster of nanocomposite structure because of its high spatial resolution features [2]. Figure 1 depicts STXM results obtained on the core – shell nanostructure. With STXM measurements, we able to probe core-shell coordination and the sites in ZnO NDs contributing to V⁴⁺ doped ZnO within single nanocomposite structure. Consequently, our STXM investigations strongly support our other synchrotron measurements.

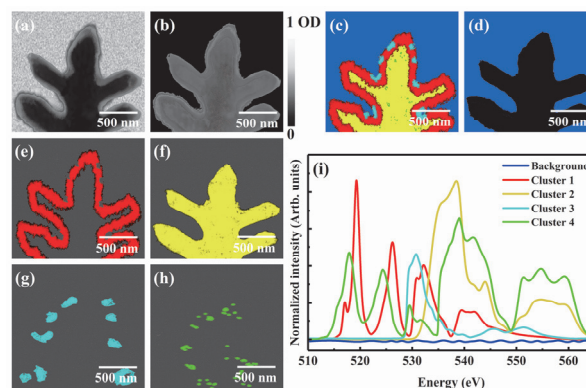


Fig. 1. (a) shows transmission electron microscope micrograph of BiVO₄ coated ZnO nanodendrite core-shell nanostructure, (b) shows magnified STXM optical image of core-shell nanodendrite highlighted in (a), (c) – (h) shows STXM mapping of O – K edge representing various coordination among core and shell structures: Bi – V – O (red), Zn – O (yellow), Bi – O (cyan) and Zn – V – O (green) and (i) represents O – K edge spectra obtained on various clusters.

[1] J.-S. Yang and J.-J. Wu, *Nano Energy* **32** (2017) 232.

BL4B

X-ray Irradiation Effect on the Local Structural Modification in Charge Transfer Salts (BEDT-TTF)₂X

T. Sasaki

Institute for Materials Research, Tohoku University, Sendai 980-8577, Japan

It has been known that X-ray irradiation to the organic materials causes molecular defects and disorders. We have investigated the X-ray irradiation effect widely in the series of molecular materials κ -(BEDT-TTF)₂X showing superconductivity or Mott insulating state from the viewpoint of the relation between the correlated electronic states and disorders [1, 2]. The experimental and theoretical investigations suggest that the -CN parts in the anion molecules X are mainly damaged and the modification of the local structure may occur.

In this study, we investigated the soft X-ray absorption spectra in the nitrogen K-edge region for the anion layers X of the charge transfer salts of (BEDT-TTF)₂X with X = Cu[N(CN)₂]Br, Cu₂(CN)₃ and RbZn(SCN)₄. X-ray irradiation to the crystals was done by using the tungsten tube with 40 kV, 20 mA at room temperature. The dose amount was controlled by the irradiation time. BL4B soft X-ray beamline was used for X-ray Absorption Near Edge Structure (XANES) spectroscopy measurements in the nitrogen K-edge region. The spectra were taken by means of the total electron yield method using EM at room temperature.

Figure 1 shows the nitrogen K-edge XANES spectra around 400 eV for (a) the non-irradiated pristine and (b) 500 hours X-ray irradiated κ -(BEDT-TTF)₂Cu₂(CN)₃. The angle θ indicates the soft X-ray incidence angle from the a^* -axis in the a^* -($b+c$) plane. The structure of anion molecules and the configuration to the incident soft X-ray beam are shown in Fig. 2. In the spectra, several absorption peak structures originating from the nitrogen atoms are observed. The major sharp A and broad B peaks can be attributed to the π^* and σ^* orbitals, respectively, coupled to the carbon or copper atoms in the anion molecule layer. The peak intensity of A and B show characteristic dependence of the incident beam angle θ , which should contain the information of the local bonding structure around the nitrogen atoms. In these results, we found that the incident beam angle dependence changes in the X-ray irradiated crystals. These observations clearly show that X-ray irradiation causes the local modification of the anion structure around the nitrogen. The details are under analysis in parallel with the comparison to the results of the other compounds with X = Cu[N(CN)₂]Br and RbZn(SCN)₄.

[1] T. Sasaki, *Crystals* **2** (2012) 374.

[2] L. Kang, K. Akagi, K. Hayashi and T. Sasaki, *Phys. Rev. B* **95** (2017) 214106.

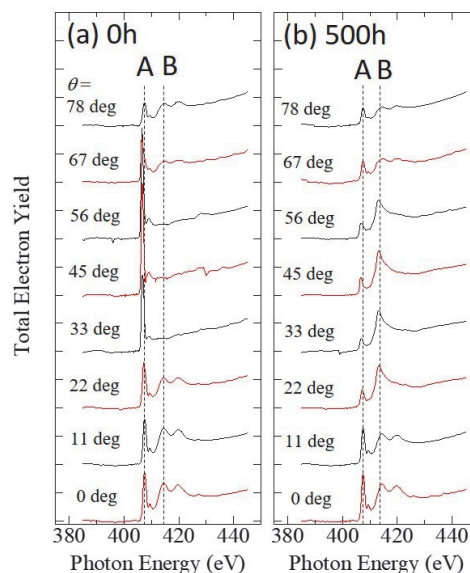


Fig. 1. Nitrogen K-edge XANES spectra of (a) non-irradiated pristine and (b) 500 hours X-ray irradiated κ -(BEDT-TTF)₂Cu₂(CN)₃. The angle θ indicates the incidence angle from the a^* -axis in the a^* -($b+c$) plane.

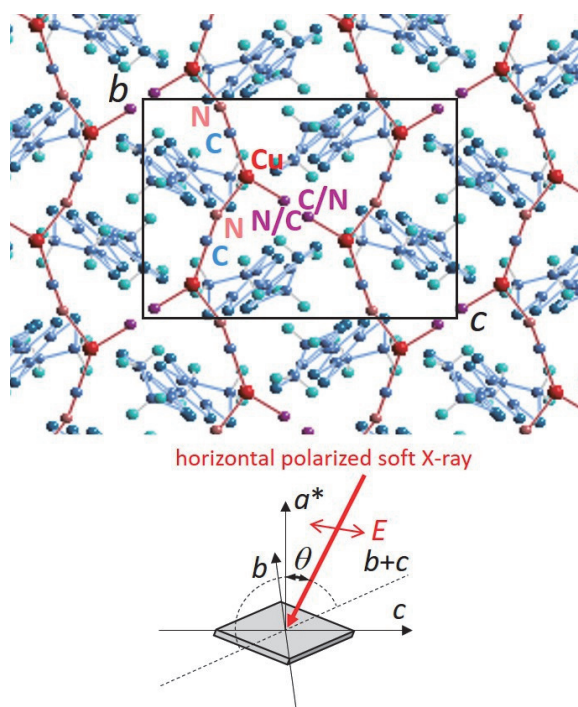


Fig. 2. The anion Cu₂(CN)₃ structure from the view along the long direction of BEDT-TTF molecule.

BL4B

Preparation of TiO₂ Film Photocatalysts for Effective Nitrogen Doping to Provide Visible Light Response

T. Yoshida¹, S. Niimi², M. Yamamoto², Y. Kato³, A. Ozawa³ and S. Yagi⁴

¹ Advanced Research Institute for Natural Science, Osaka City University Osaka 558-8585, Japan

² Graduate School of Engineering, Nagoya University, Nagoya, 464-8603, Japan

³ Graduate School of Engineering, Osaka City University, Osaka 558-8585, Japan

⁴ Institute of Materials and Systems for Sustainability, Nagoya University, Nagoya 464-8603, Japan

Photocatalytic reactions at the surface of titanium dioxide (TiO₂) under UV light irradiation have been attracting much attention in view of their practical applications to environmental cleaning such as self cleaning of tiles, glasses, and windows. Recently, Asahi *et al.* reported that the doping of nitrogen into TiO₂ contributes to band gap narrowing to provide visible-light response.

The photocatalysis of TiO₂ and nitrogen-doped TiO₂ are derived from the formation of photogenerated electrons and holes. Therefore, from a perspective of the improvement of photocatalytic properties of TiO₂, the effective depth (TiO₂ thickness) in which the electron-hole pairs capable to diffuse and contribute photocatalysis at the surface should be determined.

In the present work, we employed a pulsed laser deposition (PLD) method to fabricate the TiO₂ thin film and tried to estimate the effective depth by comparison of photocatalytic activities for TiO₂ film samples with various thicknesses. In addition, we tried to dope nitrogen into the effective depth region of TiO₂ by nitrogen implantation method, and investigated the chemical states of nitrogen effective for the visible light response of a TiO₂ photocatalyst by XAFS analysis.

Thickness-controlled TiO₂ film samples were fabricated on the (001)-face of LaAlO₃ or (LaAlO₃)_{0.3}-(SrAl_{0.5}Ta_{0.5}O₃)_{0.7} single-crystal insulator substrates by a pulsed laser deposition (PLD) with a KrF excimer laser at 973 K in an atmosphere with oxygen pressure of 5 Pa.

High-resolution X-ray diffraction measurements revealed that the deposited TiO₂ thin films on the substrates are highly (001)-oriented crystalline phase of anatase TiO₂. TEM and SIMS measurements confirmed the formation of homogeneous TiO₂ thin films. The thicknesses of the TiO₂ thin film samples have been estimated as 3, 10, 16, 19, 30 and 59 nm. We also have prepared a thick anatase TiO₂ film with the thickness of 167nm as a reference bulk sample.

The prepared TiO₂ film samples promoted photocatalytic degradation of methylene blue (MB) under UV-light irradiation. Decrease of MB concentration well obeyed the first-order kinetics, and the reaction rate constant was calculated. The reaction rate constant increased with increasing the TiO₂ thickness up to 10 nm. Then, it decreased until the thickness becomes ca. 30 nm, followed by staying

constant. Thus, it is notable that the 10 nm thickness of TiO₂ on the insulator substrate would be the optimum structure.

We also doped nitrogen into the effective depth region (ca. 10 nm) of TiO₂ by 5 keV N⁺ implantation and the nitrogen doped TiO₂ samples promoted photocatalytic degradation of MB under visible-light irradiation. Figure 1 shows N K-edge XANES spectra of a TiN powder, the photocatalytic active and inactive samples. The XANES profile of the active sample was well reproduced by the theoretical prediction using FEFF code when N occupies one of the O sites of TiO₂. On the other hand, the XANES spectrum of the inactive sample showed a distinct single peak around 401 eV. This peak could be empirically attributed to formation of NO₂ species.

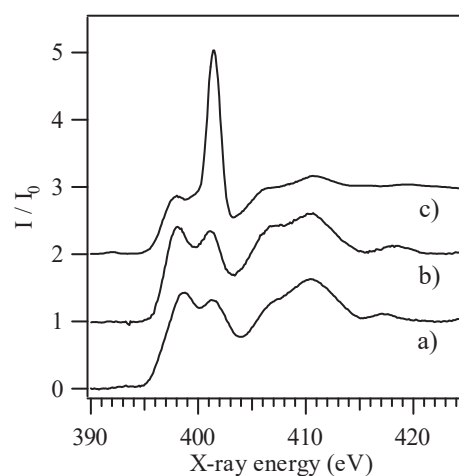


Fig. 1. N K-edge XANES spectra of (a) TiN, (b) the photocatalytic active sample and (c) the photocatalytic inactive sample.

[1] A. Fujishima, X. Zhang and D. A. Tryk, *Surf. Sci. Rep.* **63** (2008) 515.

[2] R. Asahi, T. Morikawa, T. Ohwaki, K. Aoki and Y. Taga, *Science* **293** (2001) 269.

[3] T. Yoshida and E. Kuda, *Stud. Surf. Sci. Catal.*, T. Yoshida and E. Kuda, *Stud. Surf. Sci. Catal.* **175** (2010) 267.

BL4B

Valence State Analysis of Mn Ions in Mg_2TiO_4 and Mg_2SnO_4

T. Yamamoto^{1,2} and K. Akiya¹¹Faculty of Science and Engineering, Waseda University, Tokyo 169-8555, Japan²Institute of Condensed-Matter Science, Waseda University, Tokyo 169-8555, Japan

Phosphor materials are widely studied because of their useful application for industrial use. Doping technique, i.e., incorporation of new elements in the host materials, have been widely employed to synthesize an effective phosphors, in which rare-earth elements have been often used as dopants. Recently, rare-earth free phosphors has become a new target, in which Mn has been selected as an emission center for the red-emitting phosphor. Although it is essential to know the charge state of the doped Mn ions for the understanding of emission spectra and efficiency, most of the research did not reveal it. In the current study, Mn doped Mg_2TiO_4 and Mg_2SnO_4 have been synthesized and the valence states of Mn ions in these materials were investigated by the Mn-L XANES measurements.

Mn doped Mg_2TiO_4 and Mg_2SnO_4 were synthesized by the solid state reaction method, in which high purity powders of MgO , TiO_2 , SnO_2 and Mn_2O_3 were used for starting materials. Concentrations of doped Mn are 0, 0.005, 0.1, 0.05 and 0.1 with respect to Ti or Sn. The crystal structures of all the synthesized powders were examined by the conventional powder X-ray diffraction technique, which suggested all the samples crystallized in a single-phased spinel structure. The photoluminescence spectra of these synthesized materials were measured, in which Mn-doped Mg_2TiO_4 and Mg_2SnO_4 showed red and green emissions, respectively, as shown in Fig. 1. XANES spectra at Mn L-edge were collected at BL4B in UVSOR with the total electron yield method. Incident beam was monochromatized by the varied-space grating (800 l/mm). Samples were attached on the carbon adhesive tape, which were put on the first Cu-Be dinode of the electron multiplier.

Observed Mn-L₃ XANES spectra of Mn-doped Mg_2TiO_4 and Mg_2SnO_4 are shown in Fig. 2 with those of standard Mn compounds. It is widely accepted that the Mn-L XANES profile is sensitive to change in charge states and fingerprint type analysis is possible. As shown in this figure, spectral profile of Mn-doped Mg_2TiO_4 and Mg_2SnO_4 are different, which suggest charge states of Mn ions in these two host materials are different. From the comparison of the profiles with those of standard materials, that of Mn-doped Mg_2TiO_4 shows similar profiles as that of MnO_2 , which suggests majority of the doped Mn ion is 4+ in Mg_2TiO_4 . On the other hand, the profile of Mn-doped Mg_2SnO_4 seems to be derived mainly from Mn^{2+} . These charge states of Mn ions in Mg_2TiO_4 and Mg_2SnO_4 deduced from the XANES results can explain their emission colors, i.e., red and green

emissions.

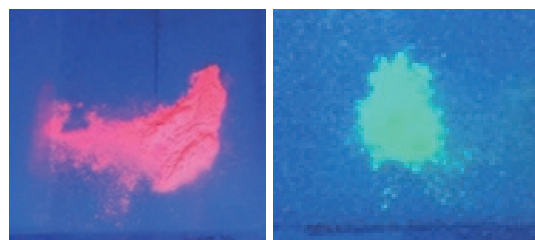


Fig. 1. Photograph of red (left) and green (right) emissions from Mn doped Mg_2TiO_4 and Mg_2SnO_4 , respectively, by UV irradiation.

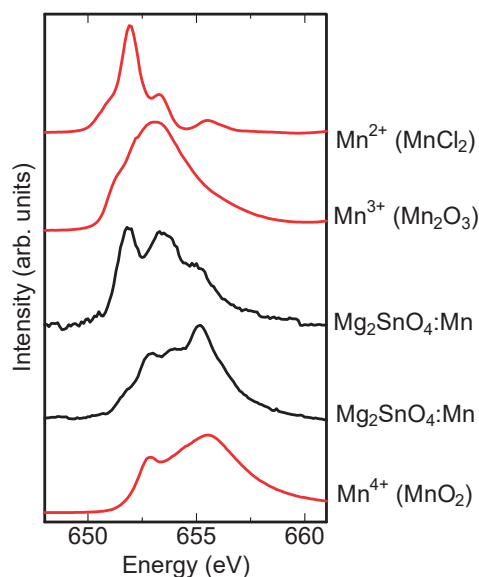


Fig. 2. Observed Mn-L₃ XANES spectra of MnCl_2 (Mn^{2+}), Mn_2O_3 (Mn^{3+}), Mn-doped Mg_2SnO_4 , Mn-doped Mg_2TiO_4 and MnO_2 (Mn^{4+}). Mn concentration in Mg_2TiO_4 and Mg_2SnO_4 are 0.05.

BL4B

Evaluation of Chemical State of Nitrogen in Nitrided Alloy by Soft X-ray Spectroscopy

M. Sato and S. Matsumoto

Institute for Materials Research, Tohoku University, Sendai 980-8577, Japan

Machinery structural materials such as gears, shafts and molds are required to have high surface hardness and high toughness because of the severe friction and/or abrasion at the surface.

Nitriding is a surface hardening technique widely used industrially and flows nitrogen from the surface and combining with strong nitride forming elements (for example, Al, Cr, V, Ti, etc.) contained in steel to precipitate clusters and alloy nitrides at near the surface. Compared to other surface hardening methods such as carburizing and shot peening, the nitriding has advantages of less strain because it does not involve phase transformation and deformation during treatment. Therefore, the importance of nitriding process is increasing in recent high-precision materials. In the nitriding treatment, a sufficient amount of nitrogen flows in the vicinity of the surface to precipitate the alloy nitride at the initial stage of nitriding, whereas precipitation is delayed at the inside of the sample because it takes long time for the nitrogen diffusion. As a result, the concentration gradient of nitrogen is formed in a sample.

In this research, we aimed to investigate whether such gradient change of nitrogen can be captured by XAFS method. Since this measurement is our first beam time at BL4B, it is also an important object to acquire how to use the devices and to obtain the correct data.

A sample with a nitrogen concentration gradient from the surface to the inside was prepared by plasma nitriding treatment at 550 °C for 16 hours using the Fe-0.5V-1.5Al alloy. In addition, nitrogen martensite steel including 0.3, 0.5 and 2 mass% N prepared by nitriding and quenching (N-Q) treatment using the pure iron, and the γ' -Fe₄N and the BN powder were used as reference materials.

XAFS measurement was carried out at the BL4B, and the N-K edge (380 ~ 450 eV) and the Fe-L edge (700 ~ 760 eV) XANES spectra were collected by the total electron yield method, respectively. Since the SDD detector had been out of order, we could not measure by fluorescence method during beam time. The measurement time was kept to 30 minutes for one scan. The measurement on the low concentration sample was performed a plurality of times, and the obtained spectrum was merged.

In the measurement of the Fe-L edge, the similar spectrum to pure iron was obtained for all bulk

samples, and it had the same shape as the spectrum reported in various papers. Therefore, it is considered that acquisition of measurement method was carried out without problems. On the other hand, the XANES spectrum obtained from the Fe₄N powder had the same shape as the Fe₂O₃, suggesting the possibility that the surface is oxidized. Since Fe₄N sample was extracted from tempered N-Q sample, it is necessary to pay attention to handling and storage conditions in the future.

Figure 1 shows the N-K edge XANES spectra of samples. Since the SDD detector could not be used in this beam time, low concentration samples could not measure. Therefore, only the spectrum of the relatively high nitrogen concentration of BN, Fe₄N and 2mass%N alloy are shown. It was also confirmed that the obtained spectrum of BN powder was similar to that previously reported one [1].

The nitrogen atom in the N-Q treated sample is considered to be in a solid solution state. However, spectrum of nearly the same shape with Fe₄N was obtained. Therefore, further investigation is necessary in combination with simulation using FEFF code in the next time.

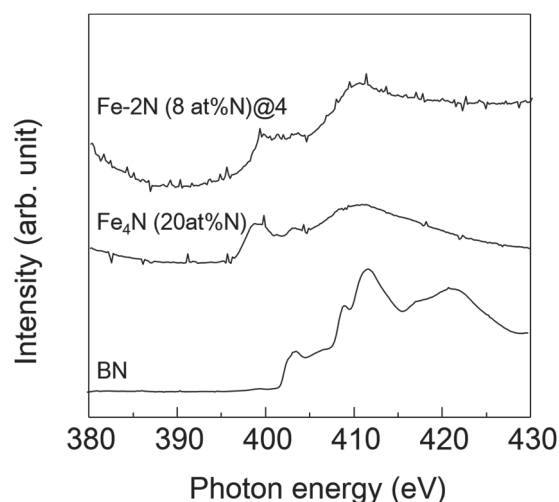


Fig. 1. N-K edge XANES spectra of BN, Fe₄N and N-Q treated Fe specimen.

[1] L. Liu *et al.*, Phys. Chem. Chem. Phys. **15** (2013) 6929.

BL5U

High-Resolution ARPES Study of TaSe₂ Atomic-Layer Ultrathin Film

Y. Nakata¹, K. Sugawara^{2,3}, T. Yoshizawa¹, T. Nakamura¹, H. Oinuma¹, T. Takahashi^{1,2,3} and T. Sato^{1,3}

¹Department of Physics, Tohoku University, Sendai 980-8578, Japan

²WPI Research Center, Advanced Institute for Materials Research, Tohoku University, Sendai 980-8577, Japan

³Center for Spintronics Research Network, Tohoku University, Sendai 980-8577, Japan

Atomic-layer materials (single-layer nano-sheet in the thinnest limit of bulk layered materials) have been a target of intensive investigations since they exhibit novel physical phenomena related to the degree of freedoms in electrons such as charge, orbital, spin, and valley. Amongst layered bulk materials, transition metal dichalcogenide (TMD) NbSe₂ has attracted considerable attention more than half century because of the coexistence of superconductivity and charge density wave (CDW). On the other hand, atomic-layer NbSe₂ show physical properties distinct from the bulk counterpart, such as two-dimensional superconductivity with the giant enhancement of upper-critical magnetic field due to spin-momentum locking at the Brillouin zone corners (K and K') in the electronic state arising from the strong spin-orbit coupling and the breaking of space inversion symmetry [1]. However, the physical properties such as the transport properties and the electronic state in single-layer TaSe₂ (the same family as IV group with spin-orbit interaction stronger than that of NbSe₂) has not been experimentally reported yet, despite theoretical studies [2].

In this study, we carried out high-resolution angle-resolved photoemission spectroscopy (ARPES) on single-layer TaSe₂ grown on bilayer graphene substrate. By utilizing energy-tunable photons from synchrotron radiation, we determined the overall VB structure and Fermi surface of single-layer TaSe₂.

Monolayer TaSe₂ films were grown on bilayer graphene by using MBE system constructed at Tohoku University. Bilayer graphene was fabricated by annealing Si-terminated 6H-SiC(0001) single crystal. Monolayer TaSe₂ films were grown by evaporating Ta on the bilayer-graphene/SiC substrate in Se atmosphere. The as-grown film was annealed at 450 °C for 30 min. Then, we additionally deposited Se atoms on monolayer TaSe₂ films to protect the surface from the atmosphere. Se-capped monolayer TaSe₂ films was then installed to a preparation chamber at BL5U and the Se capping-layer was removed by radiation heating.

Figure 1(b) shows the ARPES-intensity plot at Fermi energy (E_F) as a function of 2D wave vectors measured along the Γ KM direction at $h\nu = 50$ eV with linear polarization. We clearly find a large hole-like Fermi surface (FS) centered at the Γ point of both first and second Brillouin zone, indicating the well-ordered samples. Around the M point of the second

Brillouin zone, a small FS with the strong intensity which is assigned as the π^* band of bilayer graphene, was found. On the other hand, the spin-polarized FSs which are theoretically expected around the K point are not clearly observed because of the matrix-element effect. Figures 1(c) and (d) show the valence-band structure along the Γ -M and the Γ -K cuts. The energy band with the top of 1 eV at the Γ point and the metallic band near the Fermi level can be found along both Γ -M and the Γ -K cuts. Although the theoretical calculation has predicted the spin-split band at the Γ -K cut due to protection with the mirror symmetry at the Γ -M cut [2], it is unclear from the present experiment that whether such band splitting exists or not, likely because of the quite small domain sizes of our films.

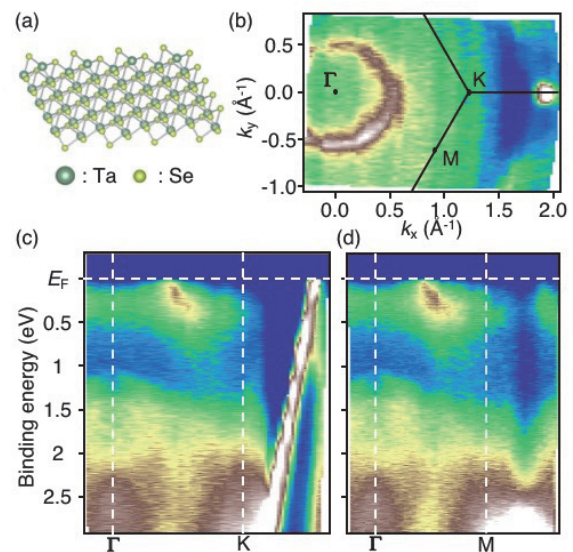


Fig. 1. (a) Crystal structure of monolayer TaSe₂. (b) Plot of ARPES intensity at E_F as a function of 2D wave vector measured at $T = 40$ K along the Γ M cut with linearly polarized 50 eV photons. (c) and (d) ARPES intensity plots in the VB region measured at $T = 40$ K along the Γ -M and the Γ -K line with linearly polarized 50 eV photons, respectively.

[1] X. Xi *et al.*, Nat. Phys. **12** (2016) 139.

[2] J. -A. Yan *et al.*, Sci. Rep. **5** (2015) 16646.

BL5U

Search for Nematicity in the Cuprate Superconductor $\text{YBa}_2\text{Cu}_3\text{O}_y$ by Angle-Resolved Photoemission Spectroscopy

S. Nakata¹, K. Koshiishi¹, K. Hagiwara¹, C. Lin¹,
S. Ideta², K. Tanaka², T. Nishizaki³ and A. Fujimori¹

¹Department of Physics, University of Tokyo, Tokyo 113-0033, Japan

²UVSOR Synchrotron Facility, Institute for Molecular Science, Okazaki 444-8585, Japan

³Department of Electrical Engineering, Kyushu Sangyo University, Fukuoka 813-8503, Japan

In cuprate superconductors, to understand the origin of the pseudogap region in the phase diagram remains a most significant issue. Recently, experimental evidence for several kinds of order (e.g. charge density wave, spin density wave, nematic order) has been reported in the pseudogap region [1]. Nematicity, which does not break the translational symmetry but breaks the fourfold rotational symmetry of the lattice, has been reported below the pseudogap temperature and may play an important role in the pseudogap region [2]. For instance, evidence for nematicity appeared in $\text{YBa}_2\text{Cu}_3\text{O}_y$ (YBCO) from transport [3,4], neutron scattering [5] and magnetic susceptibility [6] measurements and in $\text{Bi}_2\text{SrCaCu}_2\text{O}_{8+\delta}$ from resistivity measurement [7].

Nematicity has been discussed also in Fe-based superconductors [8] and studied by angle-resolved photoemission spectroscopy (ARPES) [9], which is the most direct way to reveal the electronic structure. However, at the moment, there has been no report that reveals the nematicity in cuprates by ARPES. We performed ARPES measurements in order to study the nematicity in cuprates. Furthermore, by ARPES one can investigate whether the nematicity is specific to the pseudogap state or remains in the superconducting state.

YBCO single crystal samples were grown by the flux method. It was nearly optimally doped sample and T_c and T^* were 92 K and 180 K, respectively. ARPES measurements were carried out at UVSOR BL5U. We used linearly polarized light with $h\nu = 57.1$ eV. The total energy resolution was set at 32 meV. The samples were cleaved *in-situ* under the pressure of $\sim 2 \times 10^{-8}$ Pa.

Figure 1 shows Fermi surface mapping at the Fermi level taken at various temperatures. Figure 2 shows energy distribution curves (EDCs) around $\mathbf{k} = (-\pi, 0)$ (X point) and $(0, \pi)$ (Y point). As one can expect from the symmetry of the CuO_2 plane, the difference between EDCs around the X and Y points can be seen throughout all temperatures. So far, it is difficult to identify whether this anisotropy originate from nematicity or merely from the anisotropy of the crystal structure although the difference seems to depend on temperature. More detailed measurements with many temperatures especially in the pseudogap state are necessary.

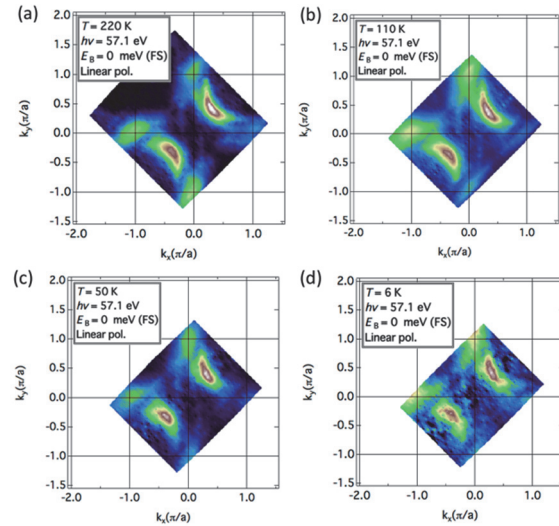


Fig. 1. Fermi surface mapping integrated over ± 10 meV of the Fermi level taken at (a) 220 K, (b) 110 K, (c) 50 K and (d) 6 K, respectively.

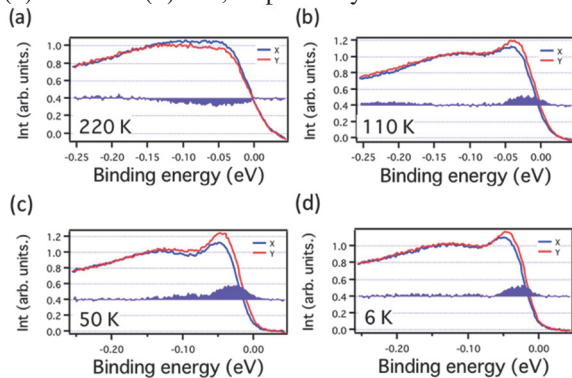


Fig. 2. EDCs of YBCO at various temperatures. Each EDC has been integrated from $k_x = -1.2$ to -0.75 (from $k_y = 0.75$ to 1.2). The difference between the lineshape of EDCs around the X and Y points are also shown.

- [1] B. Keimer *et al.*, Nature **518** (2015) 179.
- [2] S. A. Kivelson *et al.*, Nature **393** (1998) 550.
- [3] Y. Ando *et al.*, Phys. Rev. Lett. **88** (2002) 137005.
- [4] R. Daou *et al.*, Nature **463** (2010) 519.
- [5] V. Hinkov *et al.*, Science **319** (2008) 597.
- [6] Y. Sato *et al.*, Nat. Phys. **13** 1074 EP (2017).
- [7] K. Ishida *et al.*, JPS fall meeting (2016) 14pJC-12.
- [8] S. Kasahara *et al.*, Nature **486** (2012) 382.
- [9] M. Yi *et al.*, PNAS **108** (2011) 6878.

BL5U, BL7U

Electronic Structure of a Bi Atomic Chain on InAs(110) Surface

T. Nakamura¹, Y. Ohtsubo^{2,1}, Y. Yamashita¹, S. Ideta³, K. Tanaka³, K. Yaji⁴, A. Harasawa⁴, S. Shin⁴, F. Komori⁴, R. Yukawa⁵, K. Horiba⁵, H. Kumigashira⁵ and S. Kimura^{2,1}

¹Department of Physics, Graduate School of Science, Osaka University, Toyonaka 560-0043, Japan

²Graduate School of Frontier Biosciences, Osaka University, Suita 565-0871, Japan

³Institute for Molecular Science, Okazaki 444-8585, Japan

⁴Institute for Solid State Physics, The University of Tokyo, Kashiwa 277-8581, Japan

⁵Photon Factory, Institute of Materials Structure Science, High Energy Accelerator Research Organization (KEK), Tsukuba 305-0801, Japan

Low dimensional electronic structures on a solid surface has been studied extensively, such as Rashba-type spin split states due to the space-inversion asymmetry [1], and non-Fermi liquid electrons in one-dimensional (1D) metal [2, 3]. In this study, to investigate the 1D state with spin splitting due to Rashba effect, we have observed the surface electronic structures of Bi/InAs(110)-(2×1) by angle-resolved photoelectron spectroscopy (ARPES). The Bi atoms on an InAs(110) substrate form strongly buckled zig-zag atomic chains along $[\bar{1}10]$ [4]. This quasi-1D (Q1D) structure formed by heavy Bi atoms, which would play an important role for Rashba effect on this surface due to its strong spin-orbit interaction, is a good candidate for a research about Rashba-type spin splitting in 1D surface states.

The InAs(110) surface was prepared by cleaving the side face of the InAs(001) wafer in an ultra-high vacuum chamber. Then, a Bi layer with the thickness of ~ 5 monolayers was evaporated from a Knudsen cell at room temperature. After annealing at 563 K for 15 minutes, a (2×1) periodic structure was observed, consistent with an earlier report [4]. The surface electronic structure of Bi/InAs(110) was observed at BL5U and 7U of UVSOR-III.

Figure 1 shows the ARPES constant energy contour at a binding energy at 700 meV measured with polarized photons at 85 eV. k_x (k_y) is defined parallel to $[001]$ ($[\bar{1}10]$). The contour shows quasi-1D shape along k_x direction. A waving feature along k_y in Fig. 1 indicates a finite inter-chain interaction.

Figure 2 displays the second derivative ARPES intensity plot along k_y at the k_x point indicated by the dashed line in Fig. 1. A pair of the hole bands lies slightly below the Fermi level, indicating almost metallic but semiconducting electronic structure. Photon-energy-dependent ARPES data (not shown here) suggest that the hole bands are surface states because of no photon energy dependence.

Assuming parabolic dispersions (dashed lines in Fig. 2) with spin splitting along k_x , the size of the Rashba spin splitting is evaluated as 5.5 eV \AA^{-1} . This value is the largest among other 1D and Q1D Rashba systems [5, 6] and is comparable with typical giant Rashba systems such as BiTeI and Bi/Ag surface alloys [7, 8].

The giant spin splitting in the Q1D surface state

discovered here would be a promising template for future spintronic devices.

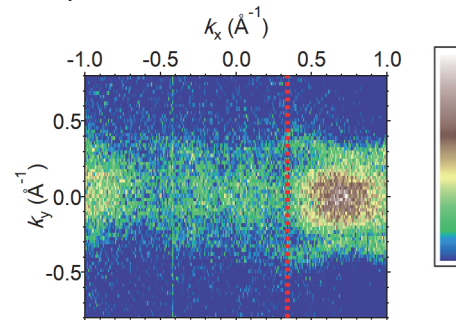


Fig. 1. A constant energy contour at the binding energy of 700 meV ($h\nu = 85 \text{ eV}$).

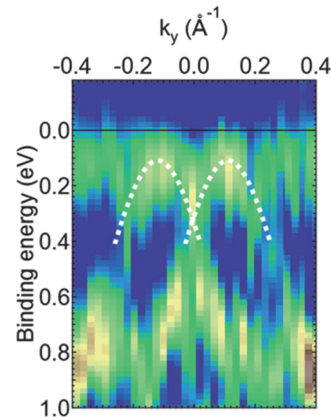


Fig. 2. Second derivative ARPES intensity plots along k_y at $k_x = 0.34 \text{ \AA}^{-1}$ ($h\nu = 85 \text{ eV}$).

[1] Y. A. Bychkov and E. I. Rashba, JETP Lett. **39** (1984) 78.

[2] M. Grioni *et al.*, J. Phys.: Condens. Matter **21** (2009) 023201.

[3] C. W. Nicholson *et al.*, Phys. Rev. Lett. **118** (2017) 206401.

[4] M. G. Betti *et al.*, Phys. Rev. B **59** (1999) 15760.

[5] J. Park *et al.*, Phys. Rev. Lett. **110** (2013) 036801.

[6] A. Takayama *et al.*, Phys. Rev. Lett. **114** (2015) 066402.

[7] C. R. Ast *et al.*, Phys. Rev. Lett. **98** (2007) 186807.

[8] K. Ishizaka *et al.*, Nat. Mater. **10** (2011) 521.

BL5U

ARPES Study of Transition-Metal Dichalcogenides NbSe₂ and NbS₂

I. Watanabe¹, K. Sugawara^{2,3}, Y. Nakata¹, K. Shigekawa¹, K. Ueno⁴, T. Takahashi^{1,2,3} and T. Sato^{1,3}

¹Department of Physics, Tohoku University, Sendai 980-8578, Japan

²WPI Research Center, Advanced Institute for Materials Research, Tohoku University, Sendai 980-8577, Japan

³Center for Spintronics Research Network, Tohoku University, Sendai 980-8577, Japan

⁴Department of Chemistry, Graduate School of Science and Engineering, Saitama University, Saitama 338-8570, Japan

Transition-metal dichalcogenides (TMDs) have attracted considerable attention since they show variety of physical properties such as magnetic ordering, charge-density wave (CDW), Mott-insulator, and superconductivity. Amongst TMDs, *2H*-NbSe₂ [see Fig. 1(a)] has been intensively studied since it exhibits coexistence of CDW ($T_{\text{CDW}} \sim 33$ K) and superconductivity ($T_{\text{C}} \sim 7$ K) [1], and there has been an intensive discussion on whether the CDW is the precursor of superconductivity or competes with the superconductivity. It is known that a cousin material of *2H*-NbSe₂, *2H*-NbS₂, shows the superconductivity below 5.7 K without any indication of CDW [2]. Thus, a comparative study of NbS₂ and NbSe₂ would enable us to clarify the interplay between the superconductivity and CDW in great detail. Very recently, it has been suggested from the theoretical calculation that the two-gap superconductivity can be realized in *2H*-NbSe₂, and it could originate from strong coupling of electrons with low-energy anharmonic phonons [3]. To elucidate these important issues, electronic states of *2H*-NbSe₂ and *2H*-NbS₂ need to be investigated by angle-resolved photoemission spectroscopy (ARPES) with energy-tunable photons from synchrotron radiation.

In this study, we have performed high-resolution ARPES on *2H*-NbSe₂ and *2H*-NbS₂. By utilizing energy-tunable photons from synchrotron radiation, we determined the electronic states near the Fermi level and found that Fermi surface topology of *2H*-NbS₂ is the same as that of *2H*-NbSe₂, while FS volume centered at the K point of *2H*-NbS₂ is slightly smaller than that of *2H*-NbSe₂. These results play an important role to understand the origin of CDW in TMDs.

Figures 1(b) and (c) show experimental Fermi surfaces on *2H*-NbSe₂ and *2H*-NbS₂ determined by ARPES. One can immediately recognize that the Fermi-surface topology of *2H*-NbSe₂ resembles to that of *2H*-NbS₂. The Fermi surface consists of the large pockets centered at the Γ and K points, respectively, which originate from Nb *4d* orbitals. These Fermi surfaces commonly have hole-like character as recognized from the Fermi level (E_{F}) crossing of the valence band (VB) in Figs 1(d) and (e). By comparing the Fermi-surface volume between *2H*-NbS₂ and *2H*-NbSe₂, we found that a large hole pocket centered at the K point in NbS₂ is slightly larger than that in NbSe₂.

It has been experimentally shown in bulk *2H*-NbSe₂ that there exist three “hot spots” on K/K’-centered FS which are interconnected by *three* equivalent 3×3 CDW vectors (Q_{CDW}) [Fig. 1(b)], which enhance the electron-phonon interaction, leading to the CDW instability [4]. The present result indicates that K/K’-centered FS in *2H*-NbS₂ is not well interconnected by 3×3 Q_{CDW} because of the suppression of CDW in *2H*-NbS₂. Therefore, the present result suggests that Fermi-surface topology plays an important role to the CDW instability in TMDs.

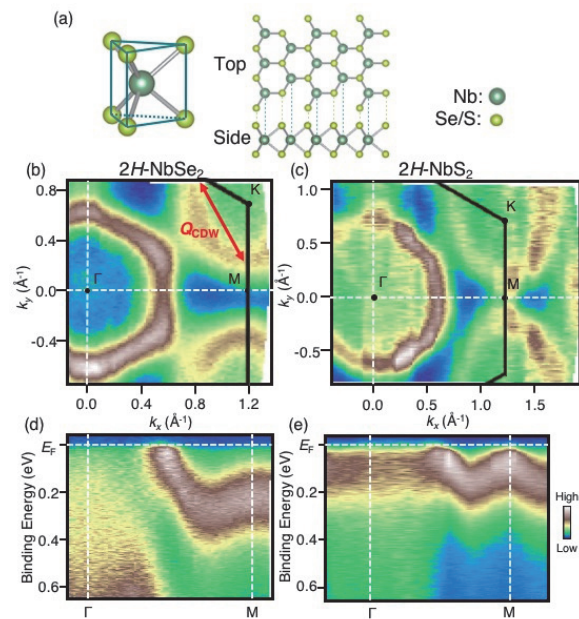


Fig. 1. (a) Crystal structure of *2H*-NbSe₂ and *2H*-NbS₂. (b) and (c) ARPES intensity at E_{F} in *2H*-NbSe₂ and *2H*-NbS₂ plotted as a function of two-dimensional wave vector measured at $h\nu = 50$ and 40 eV, respectively. (d) and (e) Experimental band dispersion along the Γ -M high-symmetry line in NbSe₂ and NbS₂, respectively.

[1] J. A. Wilson *et al.*, Adv. Phys. **24** (1975) 117.

[2] M. Naito *et al.*, J. Phys. Soc. Jpn. **51** (1982) 219.

[3] C. Heil *et al.*, Phys. Rev. Lett. **119** (2017) 087003.

[4] S. V. Borisenko *et al.*, Phys. Rev. Lett. **102**, (2009) 166402.

BL5U

Possible CDW Effects on ARPES Spectra in the Antinodal Region of Bi2212

C. Lin¹, K. Koshiishi¹, S. Nakata¹, M. Suzuki¹, S. Ideta², K. Tanaka²,
D. Song³, Y. Yoshida³, H. Eisaki³ and A. Fujimori¹

¹Department of Physics, University of Tokyo, Tokyo 113-0033, Japan

²UVSOR Synchrotron Facility, Institute for Molecular Science, Okazaki 444-8585, Japan

³National Institute of Advanced Industrial Science and Technology (AIST), Tsukuba 305-8568, Japan

With more and more recent observations of various symmetry-breaking orders found in the pseudogap state of high- T_c cuprates [1], the understanding of this intertwined phase becomes increasingly important. The ubiquitous charge density wave (CDW) has been discovered in all hole-doped cuprates and even in some electron-doped cuprates, nevertheless whether CDW competes with superconductivity and whether it is related to the pseudogap are still under hot debate.

The signature of CDW-associated band folding has not been observed by angle-resolved photoemission spectroscopy (ARPES) with one exception that may be the closest—the revelation of particle-hole symmetry breaking in the pseudogap state of single-layer Bi2201, which refutes the preformed superconductivity nature of the pseudogap and suggests a possible association between the pseudogap and CDW [2]. In order to investigate whether particle-hole symmetry is broken in the bilayer Bi2212 due to possible charge ordering, we have performed temperature-dependent ARPES measurements at UVSOR BL5U.

To avoid ultra-high energy scale and complex band structure due to super-modulation, over-doped Bi_{1.7}Pb_{0.5}Sr_{1.9}CaCu₂O₈ ($T_c = 87$ K, OD87) single crystals with Pb doping were used and cleaved *in-situ* under the pressure of $\sim 2 \times 10^{-8}$ Pa. The photon energy of the incident light was 57 eV with linear polarization perpendicular to the analyzer slit and the total energy resolution was set to 20 meV. Samples were grown by the floating-zone method and the hole concentration was controlled by annealing the samples in N₂ or O₂ flow.

Figure 1 shows the temperature evolution of the antinodal electronic states. The antibonding band was enhanced by using current photon energy [3]. By plotting the peak positions of the energy distribution

curves (EDCs) and summing up in Fig. 2, a clear misalignment between the Fermi momenta ($k_F(\pm)$) determined in the normal state and the band bending momenta ($k_G(\pm)$) can be observed, indicating the particle-hole symmetry breaking for OD87 Pb-Bi2212. Currently, we suppose a similar CDW nature of this broken particle-hole symmetry as in the case of Bi2201 [2,4], detailed explanation is planned in the near future.

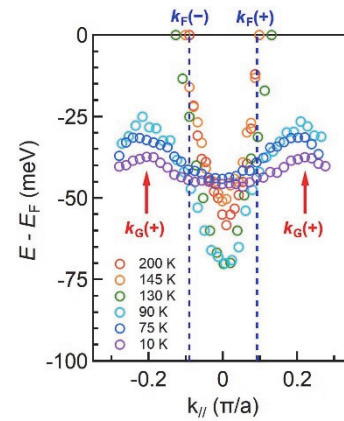


Fig. 2. Misalignment between the Fermi momenta ($k_F(\pm)$) determined in the normal state and the band bending momenta ($k_G(\pm)$) indicating the particle-hole symmetry breaking in the pseudogap state of OD87 Pb-Bi2212.

- [1] R. Comin and A. Damascelli, *Annu. Rev. Condens. Matter Phys.* **7** (2016) 369.
 [2] M. Hashimoto *et al.*, *Nat. Phys.* **6** (2010) 414.
 [3] A. A. Kordyuk *et al.*, *Phys. Rev. Lett.* **89** (2002) 077003.
 [4] R. He *et al.*, *Science*. **331** (2011) 1579.

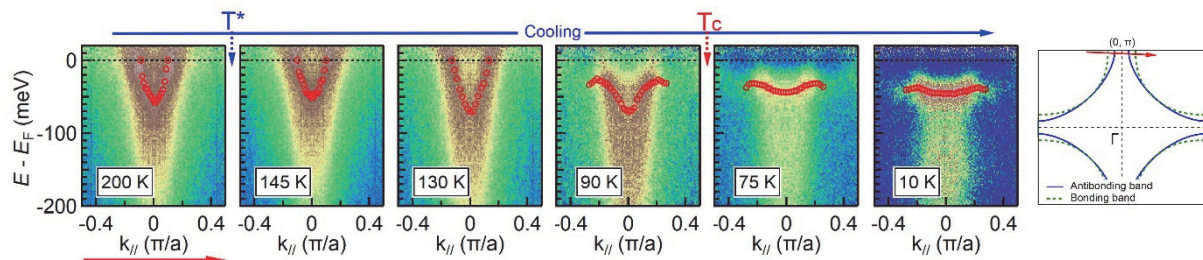


Fig. 1. Temperature evolution of the antinodal dispersions of OD87 Pb-Bi2212. The antibonding band was enhanced and the symmetrized spectra were divided by the resolution-convolved Fermi-Dirac function (FD) to effectively remove the Fermi cutoff. Red circles indicate the peak positions of the FD-EDCs and red arrow shows the cut position in the first Brillouin zone.

BL5U

Detwinned Electronic Structure of $\text{Ba}_{0.75}\text{K}_{0.25}\text{Fe}_2\text{As}_2$ Observed by ARPES

S. Ideta^{1,2}, M. Nakajima³ and K. Tanaka^{1,2}

¹UVSOR Synchrotron Facility, Institute for Molecular Science, Okazaki, 444-8585, Japan

²The Graduate University for Advanced Studies (SOKENDAI), Okazaki, 444-8585, Japan

³Department of Physics, Graduate School of Science, Osaka University, Toyonaka 560-0043, Japan

Iron-based superconductors have an interesting phase diagram with the antiferromagnetic (AFM) transition and the structural phase transition. Recently, nematicity, defined as broken rotational symmetry [a trigonal(C_4)-to-orthorhombic (C_2) structural transition], has shed light on the understanding of the mechanism on the iron-based superconductivity [1-4]. In hole-doped BaFe_2As_2 (Ba122) system, $\text{Ba}_{1-x}\text{Na}_x\text{Fe}_2\text{As}_2$ and $\text{Ba}_{1-x}\text{K}_x\text{Fe}_2\text{As}_2$ (K-Ba122) have shown the magnetic order without C_4 symmetry breaking [5, 6] and the moment's direction would be swapped from in-plane to out-of-plane [7]. Besides, the superconductivity is suppressed between the superconductivity and the C_4 -magnetic phase. The electronic structure at the C_4 magnetic phase has been unclear yet, and it would give us a great interest to elucidate the mechanism of the hole-doped Ba122.

Here, we demonstrated a temperature dependent angle-resolved photoemission spectroscopy (ARPES) experiment to elucidate the electronic structure of detwinned K-Ba122 ($x \sim 0.25$) with the C_4 -magnetic phase in order to prevent from two domains in the orthorhombic (C_2) phase below the structural and AFM transition temperatures ($T_{N,S} \sim 60$ K).

High-quality single crystals of $\text{Ba}_{0.75}\text{K}_{0.25}\text{Fe}_2\text{As}_2$ ($T_c \sim 25$ K) were grown by self-flux technique. ARPES experiments were carried out at BL5U of UVSOR-III Synchrotron using the linearly s polarized light of $h\nu = 60$ eV. Temperature was set at $T = 6$ K-230 K and clean sample surfaces were obtained for the ARPES measurements by cleaving single crystals *in-situ* in an ultrahigh vacuum better than 1×10^{-8} Pa.

Figures 1(a) and 1(b) show the second-derivative ARPES intensity plots along the Z-X and Z-Y directions, respectively, corresponding to the Z points. In Figs. 1(a) and 1(b), the direction of the uniaxial pressure is parallel or perpendicular to the s polarization vector, respectively [4], and both band dispersions are considered to be the electronic structure from the strain free single domain. Here, we confirmed that the electronic structure for both directions (Z-X and Z-Y) was the same at 230 K. In future work, we focus on the d_{yz} and d_{xz} orbitals as shown in Figs. 1(a) and 1(b) and will analyze the temperature dependent ARPES spectra. In the electronic structure of the Z-X and Z-Y directions, we expect that the occupation of the d_{yz} and d_{xz} orbitals might be the same due to the reentrant C_4 -magnetic phase.

In summary, we have performed an ARPES study of detwinned K-Ba122 ($x \sim 0.25$) and measured the

electronic structure in the Z-X and Z-Y directions. We found that the electronic structure in both Z-X and Z-Y directions shows different band dispersions, reflecting the electronic structure from the single domain due to the uniaxial pressure. We will analyze the detailed temperature dependence of the ARPES spectrum of d_{yz} and d_{xz} in future work.

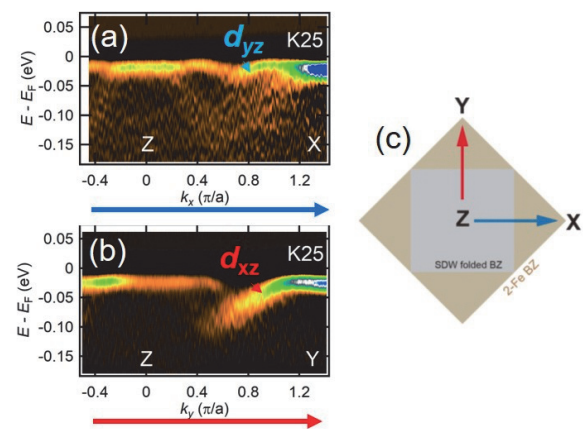


Fig. 1. (a), (b) Second-derivative ARPES intensity plots of detwinned $\text{Ba}_{0.75}\text{K}_{0.25}\text{Fe}_2\text{As}_2$ taken at $h\nu = 60$ eV ($T = 6$ K), corresponding to the Z point. The d_{yz} and d_{xz} bands are clearly observed differently. (c) Schematic Brillouin Zone. Blue and red arrows indicate the direction of the momentum cut of panels (a) and (b).

- [1] R. M. Fernandes *et al.*, Nat. Phys. **10** (2014) 97.
- [2] R. M. Fernandes *et al.*, Phys. Rev. Lett. **111** (2013) 127001.
- [3] T. Shimojima *et al.*, Phys. Rev. B **90** (2014) 12111 (R).
- [4] Y. Ming *et al.*, PNAS **108** (2011) 6878.
- [5] L. Wang *et al.*, Phys. Rev. B **93** (2016) 014514.
- [6] A. E. Böhrer *et al.*, Nat. Commun. **6** (2015) 7911.
- [7] D. D. Khalyavin *et al.*, Phys. Rev. B **90** (2014) 174511.

BL5U

Observation of Dirac Cone in Layered NiTe₂ by Angle Resolved Photoelectron Spectroscopy

M. Nishino¹, S. Miyasaka¹, Z. H. Tin¹, T. Adachi¹, S. Tajima¹, S. Ideta^{2,3} and K. Tanaka^{2,3}

¹Department of Physics, Graduate School of Science, Osaka University, Toyonaka 560-0043, Japan

²UVSOR Synchrotron Facility, Institute for Molecular Science, Okazaki 444-8585, Japan

³School of Physical Sciences, The Graduate University for Advanced Studies (SOKENDAI), Okazaki 444-8585, Japan

Transition metal dichalcogenides MX₂ (M=transition metal elements, X=S, Se and Te) has a layered structure. These systems show various physical phenomena such as charge density wave (CDW), superconductivity and so on. MX₂ has been attracted significant attention because of their interesting properties.

Recently PdTe₂ and PtX₂(X=Se,Te) revisited from a viewpoint of Dirac fermion [1, 2]. Several experimental and theoretical studies has confirmed the existence of type-II Dirac cone with Dirac point at (0,0,k_z) between Γ -A points. We have investigated the angle resolved photoemission spectroscopy (ARPES) of the related system NiTe₂ to confirm the existence of the type-II Dirac cone and to clarify its different features between NiTe₂ and other systems.

The single crystals of NiTe₂ were synthesized by a flux method in an evacuated silica tube [3]. The results of the energy dispersive X-ray spectroscopy (EDX) indicated that the actual Ni/Te ratio is 1.17:2. The ARPES spectra were measured at BL5U of UVSOR Synchrotron Facility in Institute for Molecular Science using incident photons with $h\nu=60-80$ eV. All the measurements were carried out at 20 K.

Figure 1 shows the APRES intensity plot along k_y at various k_z ($=0, 0.25$ and $0.38c^*$). At $k_z=0$, there is a hole band near Fermi level around the zone center ($k_y=0, \Gamma$ point), indicated by red break lines in Fig. 1(a). As shown in Figs. 1(a)-(c), this hole band systematically sinks down with increasing k_z . Around $k_z=0.38c^*$, the top of this band is located very near Fermi level, and the band show the linear dispersion along k_y .

We also measured the band dispersion along k_z (Γ -A direction), and found the band crossing point near Fermi level around $k_z=0.38c^*$. The present result of ARPES indicates that the Dirac point is located around (0,0,0.38c^{*}) near Fermi level in this compound. In addition, the Dirac cone is tilted along k_z , i.e., NiTe₂ is a type-II Dirac fermion system.

The band calculation in consideration of the spin-orbit interaction suggests the existence of type-II Dirac cone with Dirac point around (0,0,0.36c^{*}), which is consistent with the present ARPES results [4]. On the other hand, the energy level of the calculated Dirac point is +0.1 eV above Fermi level, and slightly different from the present experimental result. In the present work, we used the single crystals of Ni_{1.17}Te₂,

which includes excess Ni. This excess Ni introduces the electrons into this material. As a result, the electron doping shifts up to the Fermi level and the energy level of Dirac point is located very near Fermi level in the present compound.

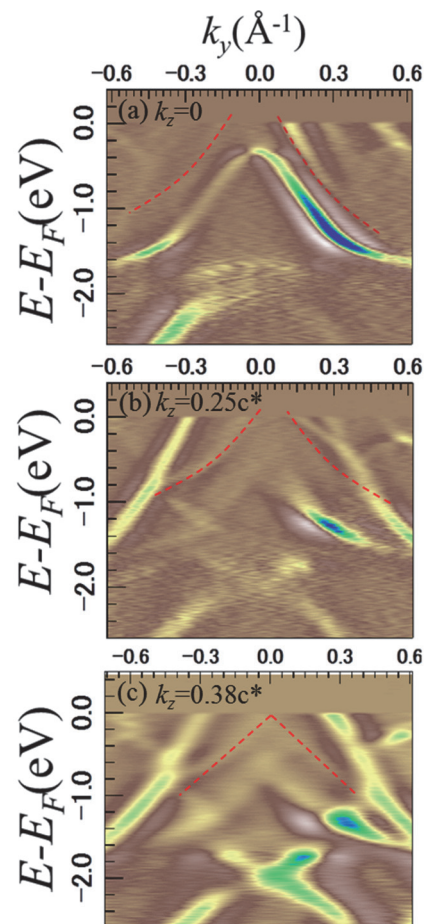


Fig. 1. ARPES intensity mapping along k_y direction at different k_z ($=0, 0.25c^*$, and $0.38c^*$) in Ni_{1.17}Te₂.

- [1] K. Zhang *et al.*, Phys. Rev. B **96** (2017) 125102.
- [2] H. -J. Noh *et al.*, Phys. Rev. Lett. **119** (2017) 016401.
- [3] J. A. Wilson and A. D. Yoffe, Adv. Phys. **18** (1969) 193.
- [4] H. Usui and K. Kuroki, private communication.

BL5U

Polarization-dependent Angle-resolved Photoemission Study of V₂AIC

 T. Ito^{1,2}, M. Ikemoto², D. Pinek³, M. Nakatake⁴, S. Ideta^{5,6}, K. Tanaka^{5,6} and T. Ouisse³
¹Nagoya University Synchrotron radiation Research center (NUSR), Nagoya University, Nagoya 464-8603, Japan

²Graduate School of Engineering, Nagoya University, Nagoya 464-8603, Japan

³Univ. Grenoble Alpes, CNRS, Grenoble INP, LMGP, F-38000 Grenoble, France

⁴Aichi Synchrotron Research Center, Seto, 489-0965, Japan

⁵UVSOR Synchrotron Facility, Institute for Molecular Science, Okazaki 444-8585, Japan

⁶The Graduate University for Advanced Studies, Okazaki 444-8585, Japan

MAX phase compounds, i.e., M_{n+1}AX_n where M is a transition metal, A belongs to groups 13-16 and X is the C or N element, have recently been attracted much attention due to their possible application for new class of two-dimensional systems called MXenes by removing A atoms [1]. On the other hand, the bulk electronic structure of MAX phase has been studied mostly by calculations, mainly because of lack of well-established single crystalline samples. In this study, we have performed angle-resolved photoemission spectroscopy (ARPES) on MAX phase compound V₂AIC [2] to directly investigate the electronic structure of this system.

ARPES measurements were performed at the UVSOR-III BL5U. Data were acquired at T = 30 K with hν = 70 eV which enables us to trace around the ΓKM plane with inner potential of V₀=22.5 eV estimated from the photon energy dependent measurement (not shown). With using horizontally (P) and vertically (S) polarized photons, we have obtained the orbital dependent ARPES image. It should be noted that all ARPES images were obtained at the normal emission geometry without changing the photon incident angle relative to the sample surface by utilizing 2D mapping lens mode of MBS A-1 analyzer.

Figures 1(a) and (b) show the polarization dependent band structure along the ΓM line obtained by P- and S-polarized photons, respectively. We found that the highly dispersive electron band (e) around the Γ point dominates in Fig. 1(b). On the other hand, the spectral weight of electron band seems to be suppressed around 300 meV in Fig.1(a) where hole-like dispersive feature (h) appears below the Fermi level (E_F). From the comparison with the band calculation (Fig. 1(c)), the observed electron and hole band are correspond to larger electron and a hole pocket, respectively. To investigate the band structure near E_F in detail, we have shown the comparison of polarization-dependent EDC and MDC spectra in Figs.1(e) and (f), respectively. Here the measured momentum point of each EDC spectrum is indicated at the top of Fig.1(f). It has clearly been observed on the S-polarized spectra that the band e shows continuous dispersive feature similarly to the calculation. On the other hand, the band e on the P-polarized ones appears as intense narrow peak just below E_F together with a sudden decrease of spectral weight as approaching to the h band. As a result, the

dispersive feature on the P-polarized seems to form the narrow band with its bottom locates around 200meV (h'). Though the observed narrow dispersive feature on the P-polarized electronic structure is not reproduced by the band calculation, it suggests that a orbital-dependent electron correlation effect plays a role for the mass enhancement on V₂AIC [1].

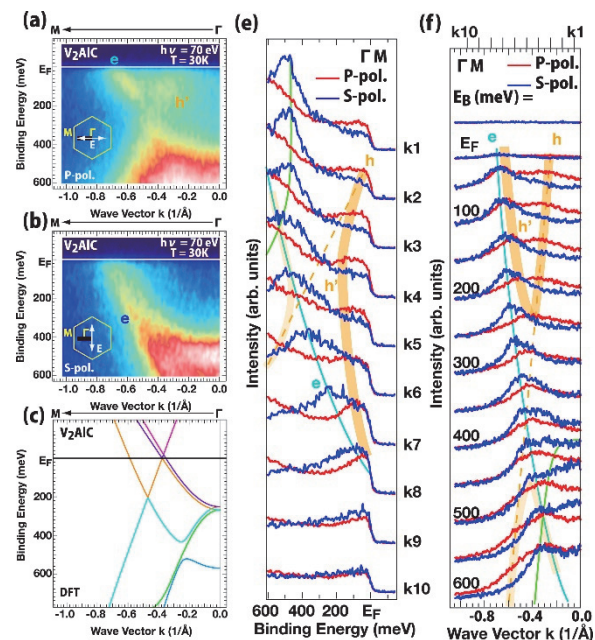


Fig. 1 Band structure along the ΓM line of V₂AIC obtained by P-(a) and S- (b) polarized photons. (c) Band calculation of V₂AIC. EDC (e) and MDC (f) spectra of V₂AIC obtained by P- (red) and S- (blue) polarized photons. In (e) and (f), solid and dashed lines are guide for eyes.

[1] M. Barsoum, *MAX phases* (Wiley, Weinheim, 2013).

[2] T. Ouisse *et al.*, *J. Cryst. Growth* **384** (2013) 88.

BL6B

Large Size Crystal Growth of p-terphenyl Crystal

A. Yamaji¹, S. Yamato¹, S. Kurosawa^{2,3}, T. Horiai¹, S. Kodama¹, Y. Ohashi², Y. Yokota²,
K. Kamada² and A. Yoshikawa^{1,2}

¹Institute for Materials Research, Tohoku University, Sendai 980-8577, Japan

²New Industry Creation Hatchery Center, Tohoku University, Sendai 980-0845, Japan

³Faculty of Science, Yamagata University, Yamagata 990-8560, Japan

Novel neutron imaging methods using a pulsed neutron source and neutron-resonance-absorption spectroscopy technique have been developed. These methods require position sensitive detectors for neutron with the Time-of-Flight (TOF), and one of the issues is development of fast response scintillator. Although some halide scintillators show high light yield and fast decay time, most halide materials have hygroscopic nature. Then, we focused on the organic scintillator crystals, which have fast decay time in the nanosecond range and no hygroscopic nature.

The organic scintillators include hydrogen with high reaction cross-section for thermal and fast neutron. However, conventional organic scintillator has low melting temperatures, and scintillation properties would degrade with overheating. Therefore, we have developed organic crystals for neutron scintillators with high melting temperatures and fast decay times.

As a first step, we grew p-terphenyl crystals by the self-seeding vertical Bridgman technique (SSVBT) [1]. In this report, we tried to grow large size p-terphenyl crystals for the neutron detector.

Growth of p-terphenyl crystals was performed in the double-wall quartz ampoule by using the SSVBT, as shown in Fig. 1. Raw material of p-terphenyl powders (98% up purity, Tokyo Chemical Industry) was loaded into both the inner and outer ampoules. The ampoule was set in a closed chamber, and was heated by using a resistive heater under nitrogen atmosphere. Due to the low purity of raw material, the ampoule was moved up and down several times like zone melting for purification, and pulling rate was 0.7 mm/h.

We succeeded in growing the p-terphenyl crystal with a diameter of 22 mm as shown in Fig. 2. This crystal had some pores, and the tail portion was not flat. The surface of the tail portion (Fig. 2(a)) and the first position at the bottom of the outer ampoule (Fig. 2(c)) looked brownish and black, respectively.

Since different phases can be generated, the phases of these portions and the inner of the grown crystal (Fig. 2(b)) were measured by using transmission Fourier Transform infrared spectroscopy (FT-IR). The FT-IR transmittance spectra as shown in Fig. 3 show that only p-terphenyl phase, and no impurity phase peaks were observed, and these brownish and black parts can be some impurities such as carbon.

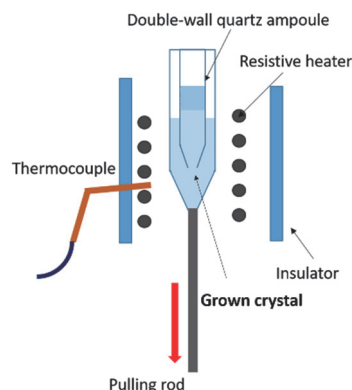


Fig. 1. Schematic of crystal growth setup by using SSVBT.

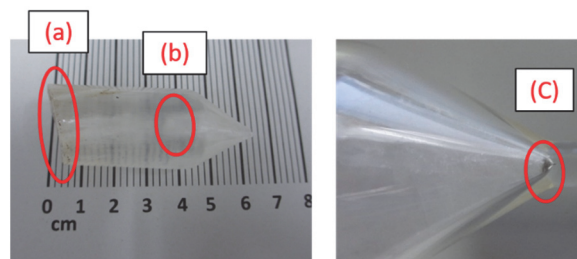


Fig. 2. Photographs of the grown crystal (left) and the bottom of the outer ampoule (right).

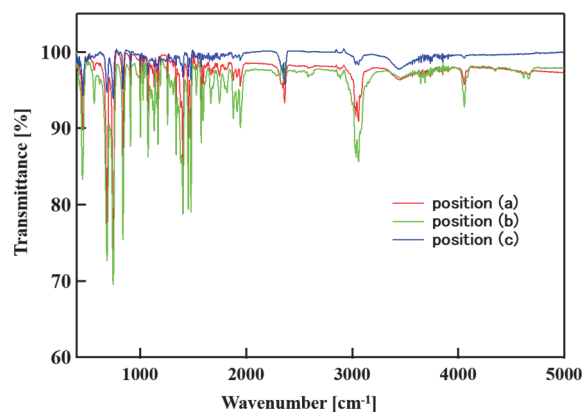


Fig. 3. FT-IR transmittance spectra of the grown p-terphenyl crystal.

[1] A. Arulchackkar avarthi *et al.*, *J. Cryst. Growth* **234** (2002) 159.

BL6B

Upper Ground State of Ultrashallow Thermal Donors in Silicon

A. Hara and T. Awano

Faculty of Engineering, Tohoku Gakuin University, Tagajo 985-8537, Japan

We have found ultrashallow thermal donors (USTDs) in carbon-doped and hydrogen-doped Czochralski silicon (CZ Si) crystals.[1, 2] To the best of our knowledge, these are the shallowest energy levels among those of currently reported donors in Si crystals. In addition, the ground state (1S state) of the USTDs was found to be split into at least two states.[3] This is direct evidence that the ground state of the USTDs is composed of a linear combination of the wave functions of the conduction band minimum. To evaluate the upper ground states, we measured the transmittances of various samples with different USTD concentrations between 8 and 60 K.

Carbon-doped CZ Si samples were doped with hydrogen by annealing in wet oxygen at 1300°C for 60 min. The samples were then cooled to room temperature by rapid exposure to air. For carbon doping, the Si melt used to prepare the ingot was doped with carbon powder during CZ Si crystal growth. Transmittance spectra were obtained with a far-IR spectrometer at the BL6B using a flowing cryostat.

Figure 1 shows the transmittance spectra of two samples, where sample A shows features related to USTD-1, but sample B shows weak USTD-1 features. Both samples show spectral features of USTD-3. Figure 2 shows $\text{Trans. (40 K)}/\text{Trans. (8 K)}$, where Trans. (T K) represents the transmittance at T K. According to our previous research, the two broad dips observed at approximately 100 and 150 cm^{-1} at 40 K originate in the transition from the upper ground state to the $2P_0$ and $2P_{\pm}$ states. The upper ground states are occupied by thermal excitation of electrons from the ground state. After comparing these data, we conclude the following. Features c and c^* are correlated with USTD-3, but not USTD-1. Thus, feature c (c^*) corresponds to the transition from the upper ground state of USTD-3 to the $2P_{\pm}$ ($2P_0$) state. Namely, the energy levels of the upper ground state are inverted compared to those of the ground state. The electronic transitions are summarized in Fig. 3.

In summary, the ground-state splitting of USTDs was evaluated. The energy levels of the upper ground state are inverted compared to those of the ground state.

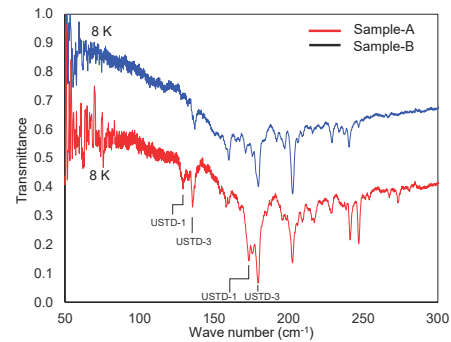


Fig. 1. Transmittance of USTDs observed in two different samples at 8 K.

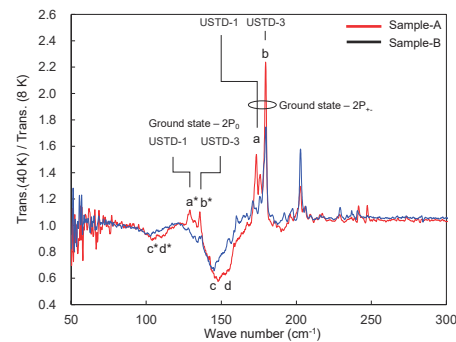


Fig. 2. $\text{Trans. (40 K)}/\text{Trans. (8 K)}$ for two different samples in Fig. 1.

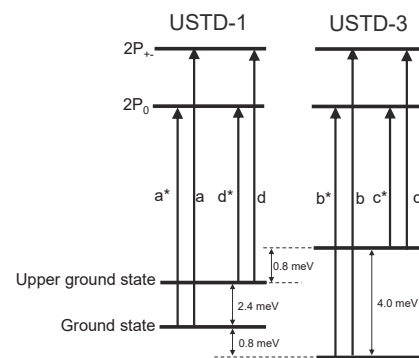


Fig. 3. The energy levels of upper ground state are inverted against those of ground state.

- [1] A. Hara, T. Awano, Y. Ohno and I. Yonenaga, *Jpn. J. Appl. Phys.* **49** (2010) 050203.
- [2] A. Hara and T. Awano, *Jpn. J. Appl. Phys.* **54** (2015) 101302.
- [3] A. Hara and T. Awano, *Jpn. J. Appl. Phys.* **56** (2017) 068001.

BL6B

UV-induced Infrared Absorption Band in Ce:Lu_{3-x}Gd_xAl₂Ga₃O₁₂ Crystals

T. Yagihashi¹, M. Kitaura¹, K. Kamada², S. Kurosawa^{1,2},
S. Watanabe³, A. Ohnishi¹ and K. Hara⁴

¹Faculty of Science, Yamagata University, Yamagata 990-8560, Japan

²New Industry Creation Hatchery Center, Tohoku University, Sendai 990-8560, Japan

³Graduate School of Engineering, Nagoya University, Nagoya 464-8603, Japan

⁴Research Institute of Electronics, Shizuoka University, Hamamatsu 432-8011, Japan

We have investigated shallow electron traps in Ce:Gd₃Al₂Ga₃O₁₂ (Ce:GAGG) crystals, which have been known as a scintillator with high-light out. From infrared absorption spectroscopy under irradiation with ultraviolet (UV) light, it was found that a broad band appears at around 12000 cm⁻¹ [1]. This band quenched at 60 K, the depth was estimated 80 meV. These facts indicate that the infrared absorption band originates in shallow electron traps. It was also clarified that the infrared absorption band is enhanced by high-temperature annealing in a reduced atmosphere. At first glance, it seems likely that shallow electron traps in Ce:GAGG crystals are associated with oxygen vacancies. However, since absorption bands due to such oxygen vacancies appear in UV region, the origin of the infrared band is different from simple oxygen vacancies. The origin of shallow electron traps in Ce:GAGG crystals still remain unclear, and is an open subject to be solved for better understanding of the development of optical materials such as scintillators and long-persistent phosphorescent phosphors [2, 3].

The purpose of the present study is to clarify whether shallow electron trap centers are formed by constituents. To do so, we have chased the change of the UV-induced infrared absorption band at cm⁻¹ for Ce:Lu_{3-x}Gd_xAl₂Ga₃O₁₂ mixed crystals. The crystals were grown by the micro pulling down method. The concentration of cerium ions was set 0.5 mol% in all of crystals. Experiment was performed at the BL6B of UVSOR synchrotron facility in the Institute for Molecular Science.

Figure 1 shows UV-induced absorption spectra of Ce:Lu_{3-x}Gd_xAl₂Ga₃O₁₂ mixed crystals at 12 K. The data were obtained by subtracting UV-unirradiated spectra from UV-irradiated spectra. As Gd³⁺ ions are replaced by Lu³⁺ ions, the infrared absorption band at 12000 cm⁻¹ is gradually weakened. It disappears completely for x=0 (Ce:Lu₃Al₂Ga₃O₁₂). From the creation spectra for photostimulated luminescence, it was confirmed that the bottom of the conduction band is almost unchanged for Lu_{3-x}Gd_xAl₂Ga₃O₁₂ mixed crystals. It is thus apparent that the low-energy shift of the conduction band is not responsible for the disappearance of the UV-induced absorption band.

The present result demonstrates that Gd³⁺ ions participate in the formation of shallow electron traps centers in Ce:GAGG crystals. It is, therefore, most

likely that excited electrons are shallowly trapped by Gd³⁺ ions adjacent to oxygen vacancies. The Gd³⁺ ions may locate at the octahedral cation sites (B site). This type of the cation is named as antisite defect [4], because Gd³⁺ ions normally occupy the dodecahedral sites (A site). The theoretical calculation for the formation energy of such antisite defects revealed that they are more stable at the octahedral site rather than the tetrahedral site (C site) [5]. On this basis, Gd²⁺ ions at B sites adjacent to oxygen vacancies are most plausible candidate for the origin of shallow electron traps in Ce:GAGG crystals.

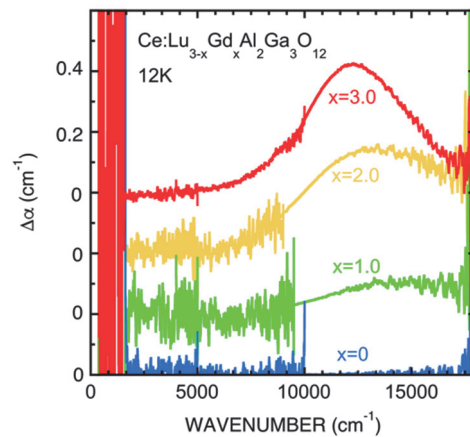


Fig. 1. UV-induced absorption spectra for Ce:Lu_{3-x}Gd_xAl₂Ga₃O₁₂ mixed crystals at 12 K. The data were obtained by subtracting UV-unirradiated spectra from UV-irradiated spectra.

- [1] M. Kitaura *et al.*, APEX **9** (2016) 072602.
- [2] K. Kamada *et al.*, J. Cryst. Growth **352** (2012) 88.
- [3] K. Asami *et al.*, Opt. Mater. **62** (2016) 171.
- [4] M. Nikl *et al.*, Appl. Phys. Lett. **88** (2006) 141916.

BL6B

Far-Infrared Reflective Spectrum of Lattice Vibration Modes in Lead-Free Alkali Niobate Piezoelectric Materials

H. Nishiyama, D. Ando, D. Xie, R. Hasegawa, S. Maeda, T. Fuchigami and K. Kakimoto
Graduate School of Engineering, Nagoya Institute of Technology, Nagoya 466-8555, Japan

Piezoelectric materials are widely used in the industry to convert electrical energy to mechanical energy. The piezoelectric property deteriorates by applying repeated electric field. This phenomenon is called as fatigue and serious problem for long use. Elucidation of the fatigue phenomenon is necessary to produce piezoelectric materials with high fatigue resistance. There are two origins of piezoelectric effect: lattice expansion and domain structure change. Some researchers attributed the fatigue phenomenon to pinning of the domain structure, however, there have been no investigation about the change of intrinsic effect. In previous reports, we have tried to investigate domain structure from the permittivity change in the line mapping measurement and a vibration mode of Nb - O oxygen octahedra for (Na, K)NbO₃ piezoceramics before and after fatigue processing using far-infrared (FIR) reflective analysis [1, 2]. However, we had not reached identification of the vibration mode in detail because ceramics have a lot of grains and randomly-oriented polarization structure. Therefore, vibration modes of KNbO₃ single crystal which has crystal system same as (Na, K)NbO₃ piezoceramics were investigated by FIR reflective analysis to clarify intrinsic effect in ceramics.

KNbO₃ single crystal was prepared by self flux method. It was confirmed that stripe domain structure appeared on the mirror polished surface. FIR measurement was conducted by a FT-IR spectrometer in BL6B from 100 to 660 cm⁻¹. BL1B was also used to obtain an information of optic mode TO1 at low wave number area, 15 – 110 cm⁻¹. Synchrotron light was used for polarized FIR light source in both BL1B and BL6B. The spectrum was fitted to obtain complex permittivity according to Drude-Lorentz equation and Fresnel equation. Fitting details are shown in the previous report [2].

Figure 1 shows angle of polarized light dependence of FIR reflectivity for KNbO₃ crystal. Reflectivity spectra changed every 15° periodically. This result showed the KNbO₃ crystal had a periodical structure on the surface. Figure 2 (a) shows FIR reflectivity for KNbO₃ crystal. Large FIR attenuations were appeared at 22.1, 190.0, 427.9 cm⁻¹. Figure 2 (b) shows imaginary part of permittivity ϵ'' calculated from the fitting spectrum shown in Fig.2 (a). Three transverse optic modes, TO1, TO2 and TO3, were appeared corresponding to the FIR attenuations. These results indicated that it is possible to investigate vibration modes of piezoelectric materials by combining of FIR reflectivity measurements of BL1B and BL6B. Vibration mode of ceramics should be clarified by

referring to the TO modes detected in crystal.

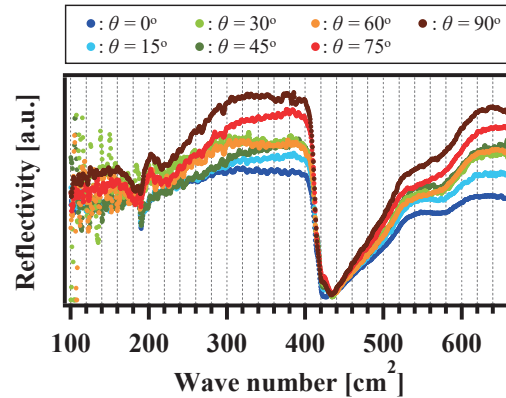


Fig. 1. Angle of polarized light dependence of FIR reflectivity for KNbO₃ crystal. $\theta = 0^\circ$ means polarized light of incident FIR is parallel to the stripe domain structure.

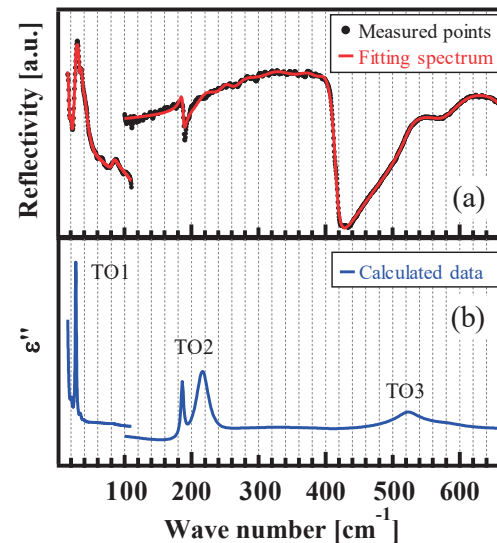


Fig. 2. FIR reflective analysis for KNbO₃ crystal in a wide range of wave number from 15 to 660 cm⁻¹. Angle of polarized light θ was zero in this measurement. (a) Measurement points of FIR reflectivity and fitting spectrum (b) Imaginary part of permittivity ϵ'' calculated from the fitting spectrum.

- [1] J. Hlinka *et al.*, Phys. Rev. Lett. **101** (2008) 167402.
 [2] H. Nishiyama, N. Matsubara, K. Yoshida, D. Ando, T. Fuchigami and K. Kakimoto, UVSOR Activity Report 2016 **44** (2017) 84.

BL6B, BL7B

Anisotropic Metal-to-Insulator Transition of RuAs Probed by Polarized Infrared Micro-Spectroscopy

Y. Nakajima¹, Z. Mita², J. Hibi², S. Kamei², H. Watanabe^{2, 1}, H. Kotegawa³, H. Sugawara³, H. Tou³, T. Ito⁴ and S. Kimura^{2, 1}

¹Department of Physics, Osaka University, Toyonaka 560-0043, Japan

²Graduate School of Frontier Biosciences, Osaka University, Suita 565-0871, Japan

³Department of Physics, Kobe University, Kobe 657-8501, Japan

⁴Synchrotron Radiation Research Center, Nagoya University, Nagoya 464-8603, Japan

Ruthenium mono-pnictides, RuX ($X = \text{P, As, Sb}$), with orthorhombic crystal structure (space group $Pnma$) attract attention because of the relationship to iron-arsenide (Fe-As) superconductors. These materials also have various physical properties such as metal-to-insulator transition (MIT) in RuAs [1], charge density wave in RuP [2] and superconducting transition in Rh-doped RuP, RuAs, and non-doped RuSb [1]. These properties are believed to be related to the superconducting property of Fe-As's, but the origin has not been clarified yet.

Recently, thanks to the successful synthesis of single-crystalline RuAs, its physical properties have now been investigated [3]. There are two structural transition at $T_{MI1} = 255 \text{ K}$ and $T_{MI2} = 195 \text{ K}$, which are second-order and first-order transitions, respectively. The electrical resistivity slightly (rapidly) increases below T_{MI1} (T_{MI2}) suggesting that a partial (full) energy gap opens. However, there is no information of the gap opening T_{MI1} and T_{MI2} because of the limited sample size of $0.8 \times 0.3 \text{ mm}^2$ at most.

To investigate the origin of MIT and the anisotropic energy gap of RuAs, we performed a polarized optical reflection spectroscopy on single-crystalline RuAs along b and c axes using IR and THz microscopes in the photon energy ranges of $0.05 - 1 \text{ eV}$ and $20 - 60 \text{ meV}$, respectively, at BL6B combined with VUV reflectivity spectra at BL7B. To obtain more information, we have also performed an angle-integrated photoelectron spectroscopy (PES) at Aichi-SR.

Figure 1 shows temperature-dependent PES spectra of RuAs along the c axis. The spectrum does not change so much with changing temperature. This suggests that the overall electronic structure does not change by MIT. The PES spectra are consistent with the calculated density of states without any electron correlations [3]. It suggests that the intensity of the electron correlation in RuAs is weak.

Figure 2 shows polarized optical conductivity [$\sigma(\omega)$] spectra of RuAs in the IR region along two independent axes derived from the Kramers-Kronig analysis of the polarized reflectivity spectra. The strong temperature dependence is visible below the photon energy of 0.5 eV in $E // c$ and 0.4 eV in $E // b$, but weak temperature dependence appears above these photon energies. The result is consistent with the PES result shown in Fig. 1, where the overall spectrum has

almost no temperature dependence. Along the c axis ($E // c$), the $\sigma(\omega)$ intensity below 0.5 eV gradually decreases below the temperature of 230 K ($< T_{MI1}$) and suddenly drops below 190 K ($\sim T_{MI2}$). This spectral change seems to be consistent with the structural transition. In contrast, along the b axis, the $\sigma(\omega)$ intensity below 0.4 eV gradually decreases with decreasing temperature.

The different behavior along the different axes is considered to be important for the origin of MIT of RuAs.

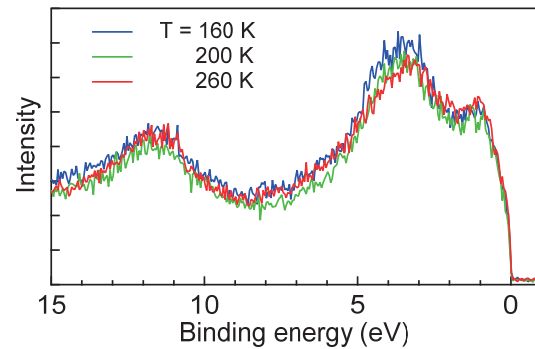


Fig. 1. Temperature-dependent angle-integrated photoelectron spectra of RuAs along the c axis.

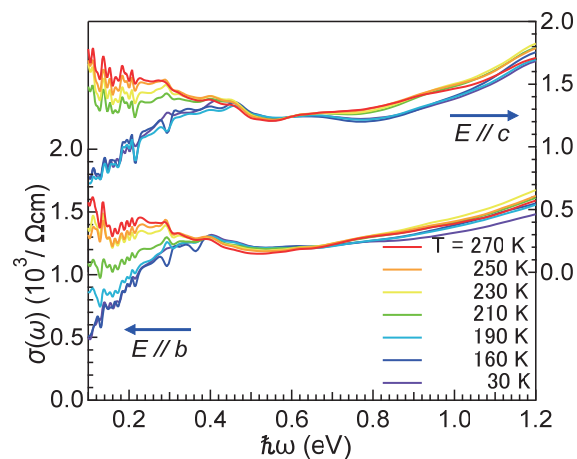


Fig. 2. Temperature-dependent optical conductivity [$\sigma(\omega)$] spectra of RuAs along the b and c axes.

[1] D. Hirai *et al.*, Phys. Rev. B **85** (2012) 140509(R).

[2] R. Y. Chen *et al.*, Phys. Rev. B **91** (2015) 125101.

[3] H. Kotegawa *et al.*, submitted.

BL6B

Infrared Microspectroscopy Using UVSOR BL6B

A. Irizawa¹, S. Suga¹, T. Nagashima², A. Higashiya², M. Hashida³ and S. Sakabe³

¹The Institute for Scientific and Industrial Research, Osaka University, Ibaraki 567-0047, Japan

²Faculty of Science and Engineering, Setsunan University, Neyagawa 572-8508, Japan

³Advanced Research Center for Beam Science, Institute for Chemical Research, Kyoto University, Uji 611-0011, Japan

Optical study is one of the most powerful techniques for investigating electronic states of solids. Great deal of information about electronic state, band structure, crystal structure, and dielectric response can be obtained by using spectroscopic techniques. From its handling for experiments, the optical study is extremely compatible with microscopy and under multiple conditions such as low temperature, high magnetic field, and high pressure. In the case of solids, it is well known that the temperature is one of the decisive factors for the electronic states. In case of strongly correlated systems, the considerable types of phase transition are induced by the change of the temperature. Particularly, the multiferroic compounds can be controlled of its physical properties mutually by the external fields such as magnetic, electronic, and elastic ones. The other particular condition, the pressure will directly affect the electron-electron interactions through the change of lattice constants. There we need microscopic technique for probing the small space in DAC. IN other cases, 2D scanning microspectroscopy can detect the change of electronic and/or chemical states in particular regions such as changed and damaged by beam irradiations. The BL6B in UVSOR is adjusted for the investigations at low temperature and microscopy in the low-energy infrared region. There equips two type interferometers of both Michelson and Martin-Puplett types for FIR region and microscopy for MIR region.

In this report, we have performed the optical transmittance measurements in MIR region for several compounds having damages by THz-FEL irradiation. THz-FEL at The Institute of Science and Industrial Research (ISIR) in Osaka University is a FEL light source in the terahertz band or the far-infrared region (frequency: 2.5 - 7.5 THz, wavelength: 40 - 120 μm , wavenumber: 83 - 250 cm^{-1}) which is the boundary region of electromagnetic wave between radio waves and lights. The electric field of this intense monochromatic laser reaches several MV/cm which is enough to make ablations and/or discharge phenomena for materials. Recently, our group can be found a strange mark constructed on a surface of semiconductors, Si [1]. This stripe mark has been known as LIPSS (laser induced periodic surface structure) for the damage by NIR fs-laser irradiation, but in THz-FIR region, this is the first observation in quite different wavelength. LIPSS has been known for its fine structures having smaller period compared for the wavelength. In case of THz-FIR LIPSS, the period

is about 10 times smaller than that of NIR fs-laser LIPSS. Therefore, the models of LIPSS formation considered for NIR laser can not be explicable for THz LIPSS.

Experiments are performed by using MIR microscope installed in BL6B. 2D mapping was performed for THz-FEL irradiated sample of Si. The size of aperture is 100*100 μm and 10*10 areas are measured. Both thermal light source and SR light source were used for the measurement. The spectra of irradiated and non-irradiated areas are compared right now. We will discuss the difference of spectra and the effects of THz-FEL irradiation constructing LIPSS on Si in the article under construction.

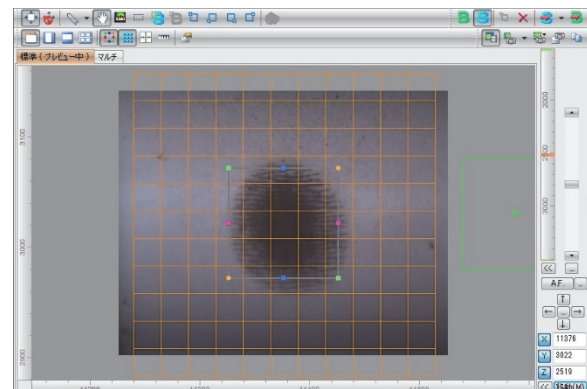


Fig. 1. MIR spectroscopic 2D mapping of THz-FEL irradiated Si.

[1] A. Irizawa, S. Suga, T. Nagashima, A. Higashiya, M. Hashida and S. Sakabe, *Appl. Phys. Lett.* **111** (2017) 251602.

BL7U

ARPES Study of Van Der Waals Ferromagnet $\text{Cr}_2\text{Ge}_2\text{Te}_6$

M. Suzuki¹, B. Gao², A. Solomon², K. Koshiishi¹, S. Nakata¹, K. Hagiwara¹, C. Lin¹,
S. Ideta³, K. Tanaka³, M. Kobayashi⁴, S-W. Cheong² and A. Fujimori¹

¹Department of Physics, The University of Tokyo, Tokyo 113-0033, Japan

²Rutgers Center for Emergent Materials, Rutgers University, Piscataway, New Jersey 08854, USA

³Editorial Board, UVSOR Facility, Institute for Molecular Science, Okazaki 444-8585, Japan

⁴Center for Spintronics Research Network, The University of Tokyo, Tokyo 113-0033, Japan

In recent years, van der Waals (vdW) ferromagnets, which have attractive physical properties, have been intensively studied in order to investigate the origin of their ferromagnetism with 2D crystalline [1]. A representative vdW ferromagnetic insulator $\text{Cr}_2\text{Ge}_2\text{Te}_6$ (CGT) exhibits ferromagnetism below ~ 61 K [2]. It has also been reported that the magnetic behavior of CGT atomic layer is well described as ideal 2D Heisenberg model [3].

We have conducted angle-resolved photoemission spectroscopy (ARPES) measurement of CGT with using two linearly polarization in order to clarify its electronic states directly. As shown in Fig. 1, hole-like band along the Γ point below Fermi level was observed, confirming its insulating property. We have also performed DFT calculations. The spectra nearby Fermi level obtained by the experiments and calculated partial density of states (PDOS) of Cr $3d$ electrons are shown in Fig. 2. We found that the spectrum for p-polarization has a large peak around binding energy of 2eV different from the case of s-polarization showing a peak at lower binding energy. Comparison between the experiments and the calculations suggests that the peak for p-polarization comes mainly from Cr $3d_{x^2-y^2}$ and $3d_{xy}$ orbitals, and the spectrum for s-polarization reflects Cr $3d_z^2$ PDOS.

For the future prospect, we would like to perform ARPES measurements for other vdW compounds such as $\text{Cr}_2\text{Si}_2\text{Te}_6$ in order to investigate the effect by the difference in composition.

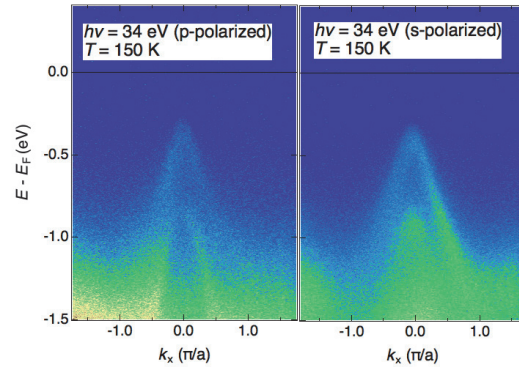


Fig. 1 ARPES spectra for different polarization.

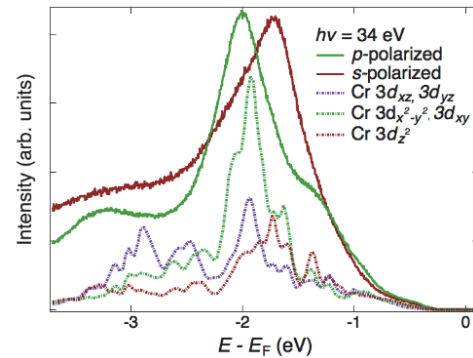


Fig. 2 The experimental spectra near E_F for different polarization and Cr $3d$ PDOS by DFT calculation.

[1] N. Smith, Nature **546** (2017) 216.

[2] X. Zhang *et al.*, Jpn. J. Appl. Phys. **55** (2016) 033001.

[3] C. Gong *et al.*, Nature **546** (2017) 265.

BL7U

ARPES Study of Topological Line-Node Semimetal CaAgAs

D. Takane¹, K. Nakayama¹, S. Souma^{2,3}, T. Wada⁴, Y. Okamoto^{4,5}, K. Takenaka⁴,
Y. Yamakawa^{5,6}, A. Yamakage^{5,6}, T. Takahashi^{1,2,3} and T. Sato^{1,2}

¹Department of Physics, Tohoku University, Sendai 980-8578, Japan

²WPI Research Center, Advanced Institute for Materials Research, Tohoku University, Sendai 980-8577, Japan

³Center for Spintronics Research Network, Tohoku University, Sendai 980-8577, Japan

⁴Department of Applied Physics, Nagoya University, Nagoya 464-8603, Japan

⁵Institute for Advanced Research, Nagoya University, Nagoya 464-8601, Japan

⁶Department of Physics, Nagoya University, Nagoya 464-8602, Japan

Topological semimetals are recently attracting a considerable attention. In contrast to conventional semimetals with a finite band overlap between valence band (VB) and conduction band (CB), topological semimetals show the touching of the VB and CB at the discrete points (called Dirac/Weyl semimetals) or along a one-dimensional curve (line-node semimetals; LNSMs) in the bulk Brillouin zone. Such Dirac/Weyl-cone states are known to provide a platform to realize exotic physical properties. The existence of three-dimensional Dirac semimetals was first confirmed in Cd_3As_2 and Na_3Bi , where the VB and CB touch with each other at the point (Dirac point) protected by rotational symmetry of the crystal. Recent studies on noncentrosymmetric transition-metal monopnictides (TaAs family) have clarified pairs of bulk Weyl-cone bands and Fermi-arc surface states, supporting their Weyl-semimetallic nature. While Dirac/Weyl semimetals with point nodes have been intensively studied experimentally, the experimental studies of LNSMs with line nodes are relatively scarce despite many theoretical predictions.

Recently, it was theoretically proposed that noncentrosymmetric ternary pnictides CaAgX [$X = \text{P}, \text{As}$] are the candidate of LNSM and topological insulator [1]. These materials crystallize in the ZrNiAs -type structure [see Figs. 1(a) and 1(b)]. First-principles band-structure calculations have shown that, under negligible spin-orbit coupling, CaAgX displays a fairly simple band structure near the Fermi level (E_F) with a ring-like line node (nodal ring) surrounding the Γ point of bulk hexagonal Brillouin zone (BZ). In this study, we performed an angle-resolved photoemission spectroscopy (ARPES) study on CaAgAs . By utilizing low-energy bulk sensitive ARPES at BL-7U, we determined the VB structure near E_F and revealed the LNSM nature of CaAgAs [2].

Samples were cleaved in situ along the $(11\bar{2}0)$ crystal plane. This indicates that the cleaved plane is the k_y - k_z plane in the hexagonal bulk BZ. Figures 1(c) and 1(d) show the momentum distribution curves at various binding energies (E_B 's) and the corresponding second-derivative intensity plot, respectively, measured at $T = 40$ K along a cut crossing the Γ point. One can recognize linearly-dispersive hole-like bands approaching E_F [see orange dashed lines in Fig. 1(d)].

The observed band dispersions are well reproduced by the band calculations and assigned as the lower branch of the Dirac-like energy bands. Through the detailed band mapping over three-dimensional BZ, we observed ring-shaped Fermi surface on the (0001) mirror plane. These observations strongly suggest that CaAgAs is characterized by the bulk Dirac-like band and ring-torus Fermi surface associated with the line node on the mirror plane, in line with the band calculations.

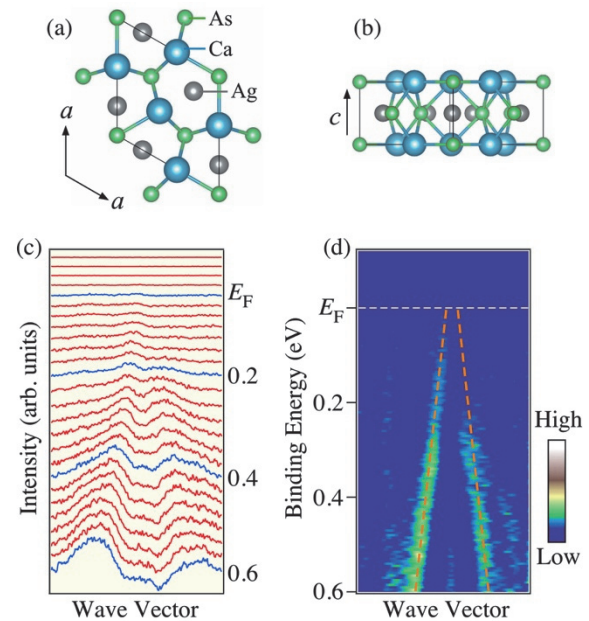


Fig. 1. (a) and (b) Two different views of crystal structure of CaAgAs . (c) Momentum distribution curves at various E_B 's measured along a cut near the Γ point at $T = 40$ K with linearly-polarized 16 eV photons. (d) Second-derivative intensity of (c) plotted as a function of E_B and wave vector. Orange dashed lines are a guide for the eyes to trace the linear band dispersions.

[1] A. Yamakage *et al.*, J. Phys. Soc. Jpn. **85** (2016) 013708.

[2] D. Takane *et al.*, npj Quantum Materials **3** (2017) 1.

BL7U

Mott Insulating State in $\text{Eu}_2\text{Ir}_2\text{O}_7$ Revealed by ARPES

M. Nakayama¹, T. Kondo¹, Z. Tian¹, J. J. Ishikawa¹, M. Halim¹, C. Bareille¹, K. Kuroda¹, T. Tomita¹, S. Ideta², K. Tanaka², M. Matsunami³, S. Kimura⁴, L. Balents⁵, S. Nakatsuji¹ and S. Shin¹

¹ISSP, University of Tokyo, Kashiwa, Chiba 277-8581, Japan

²UVSOR Synchrotron Facility, Institute for Molecular Science, Okazaki 444-8585, Japan

³Toyota Technological Institute, Nagoya 468-8511, Japan

⁴Graduate School of Frontier Biosciences, Osaka University, Suita, Osaka 565-0871, Japan

⁵Kavli Institute for Theoretical Physics, Santa Barbara, California 93106, USA

The $5d$ iridium oxides (iridates), having comparable scales for their kinetic energy, Coulomb interaction, and spin-orbit coupling, provide an excellent platform for studying new types of strongly correlated phenomena. Amongst them, the pyrochlore iridates ($\text{Ln}_2\text{Ir}_2\text{O}_7$, where Ln is a lanthanide), endowed with frustrated geometry and cubic symmetry, have a particularly fascinating phase diagram. $\text{Pr}_2\text{Ir}_2\text{O}_7$, with the largest Ln ion, is a metallic spin liquid and exhibits an anomalous Hall effect. For Ln ions with a smaller ionic radius, an antiferromagnetically ordered insulating phase appears at low temperature.

Theoretically, topological band structures have been ascribed to the $\text{Ln}_2\text{Ir}_2\text{O}_7$ series. The metallic phase is predicted to exhibit quadratically dispersing conduction and valence bands touching at the Γ point close to the Fermi level (E_F). We have indeed identified this structure by angle-resolved photoemission spectroscopy (ARPES) in $\text{Pr}_2\text{Ir}_2\text{O}_7$ [1]. Theory predicts that such a quadratic Fermi node state may be converted into various topological states such as a topological insulator or a Weyl semimetal by appropriate symmetry breaking.

Antiferromagnetism in these materials is of the Ising type, consisting of an “all-in–all-out” (AIAO) configuration of Ir moments on alternating tetrahedra. This can be considered an “octupolar” spin order which breaks time-reversal but preserves cubic symmetry, and does not enlarge the unit cell. Early density functional studies predicted the magnetic state to be a Weyl semimetal, and general arguments imply that, if a quasiparticle picture applies at low energy in the antiferromagnetic phase, and the magnetic ordering is weak, it must exhibit Weyl points and cannot have a true gap. Nevertheless, optical and transport measurements indicate a gapped insulating ground state for $\text{Nd}_2\text{Ir}_2\text{O}_7$, despite its low antiferromagnetic–metal–insulator (MI) transition temperature $T_{\text{MI}} \approx 30$ K and proximity to metallic $\text{Pr}_2\text{Ir}_2\text{O}_7$. We have investigated the evolution of the electronic structure through the MI transition in $\text{Nd}_2\text{Ir}_2\text{O}_7$ by ARPES, and found a dramatic Slater to Mott crossover with reducing temperature [2].

We further investigated the electronic properties of $\text{Eu}_2\text{Ir}_2\text{O}_7$, an insulator with all-in all-out antiferromagnetic ordering. While the band dispersion deep below the Fermi level ($\sim 1\text{eV}$) is similar to that

of the metallic $\text{Pr}_2\text{Ir}_2\text{O}_7$, the spectral weight at the Fermi level is completely diminished in $\text{Eu}_2\text{Ir}_2\text{O}_7$ (Fig.1). The gapped state lacking long-lived quasiparticles indicate that this material is a Mott insulator. We find a significant reduction of Mott gap with a little amount of carrier doping due to off-stoichiometry, and an anomalous filling of spectral weight at E_F across Neel temperature in the doped samples. These features imply that $\text{Eu}_2\text{Ir}_2\text{O}_7$ is situated near the border between the Mott- and Slater-insulating phases, suggesting a tunability by carrier doping to realize correlated topological states theoretically predicted.

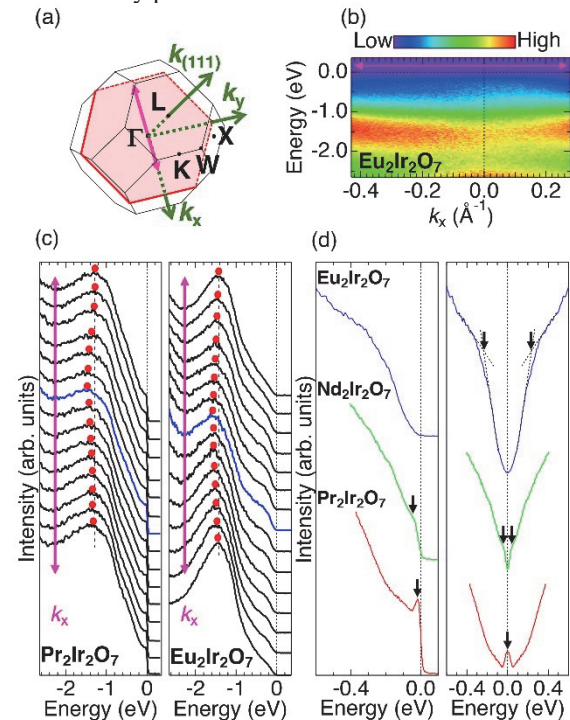


Fig. 1. (a) The Brillouin zone of $\text{Eu}_2\text{Ir}_2\text{O}_7$. (b) The ARPES dispersion map, measured along k_x crossing Γ . (c) EDCs of (b). The red points indicate peak positions. (d) Comparison of EDCs at the Γ point for three compounds.

[1] T. Kondo *et al.*, Nature communications **6** (2015) 10042.

[2] M. Nakayama *et al.*, Phys. Rev. Lett. **117** (2016) 056403.

BL7U

Superconducting Gap and Pseudogap in the Surface States of PrFeAsO_{1-y} Observed by Angle-resolved Photoemission Spectroscopy

K. Hagiwara¹, M. Horio¹, K. Koshiishi¹, S. Nakata¹, C. Lin¹, M. Suzuki¹, M. Ishikado^{2,3,4}, S. Ishida³, H. Eisaki³, S. Shamoto⁴, S. Ideta⁵, K. Tanaka⁵, T. Yoshida⁶ and A. Fujimori¹

¹Department of Physics, The University of Tokyo, Tokyo 113-0033, Japan

²Comprehensive Research Organization for Science and Society, Tokai 319-1106, Japan

³National Institute of Advanced Industrial Science and Technology, Tsukuba 305-8568, Japan

⁴Japan Atomic Energy Agency, Tokai, 319-1184, Japan

⁵UVSOR Synchrotron Facility, Institute for Molecular Science, Okazaki 444-8585, Japan

⁶Graduate School of Human and Environmental Studies, Kyoto University, Kyoto 606-8501, Japan

In the 1111-type iron pnictides, superconductivity is realized by electron doping through substituting F for O or Co for Fe, or introducing oxygen deficiencies [1]. According to previous angle-resolved photoemission spectroscopy (ARPES) studies [2, 3], however, the 1111 compounds exhibit heavily hole-doped electronic structures for cleaved surfaces, which has been attributed to charge transfer due to the polar surfaces. In some ARPES studies, it has been reported that the heavily hole-doped surfaces are superconducting, but the nature of the superconductivity nor relationship between the surface electronic structure and the superconductivity has not been known yet. Therefore, more detailed knowledge about the superconducting gap at the surface is required.

In this work, we have performed ARPES studies on the 1111 compounds and have measured the temperature dependence of the energy gap in the surface states in order to study possible superconductivity at the surface of the 1111 system.

High-quality single crystals of the electron-doped superconductor PrFeAsO_{1-y} ($T_c = 16$ K) were synthesized by the high pressure technique as described in Ref. [4]. ARPES measurements were performed at BL7U of UVSOR using linearly polarized light with the photon energy of 22.5 eV. A MBS A1 electron analyzer was used. The total energy resolution of ~ 10 meV. The crystals were cleaved *in situ* at $T = 12$ K. The measurements were carried out in an ultrahigh vacuum of $\sim 10^{-10}$ Torr.

Figure 1 shows a Fermi surface (FS) mapping for the PrFeAsO_{1-y} at $T = 12$ K using s-polarization. One can clearly observe a large circular hole pocket and a small hole pocket around zone center, referred to as “Outer” and “Inner”, respectively. This result is consistent with previous reports [2, 3]. Figure 2 shows the analysis of the energy gap on the “Outer” hole pocket, which originates from the surface. Panel (a) shows symmetrized energy distribution curves (EDCs) after the background subtracted at the Fermi wave vector (k_F) of the “Outer” hole pocket. The background spectra are defined by an orange line in Fig. 1. One can find an energy gap opening and a coherence peak at low temperatures. In order to quantify the energy gap,

we have estimated gap size from the position where deviation from the normal-state EDCs starts indicated by triangles as shown in panel (a). We also estimated the gap area surrounded by the symmetrized EDC and the normal-state EDC. As shown in panel (c), the energy gap remains open above T_c , which may indicate a pseudogap opening. In the case of low temperature, one can observe coherence peaks, which may indicate a superconducting gap caused by proximity effect.

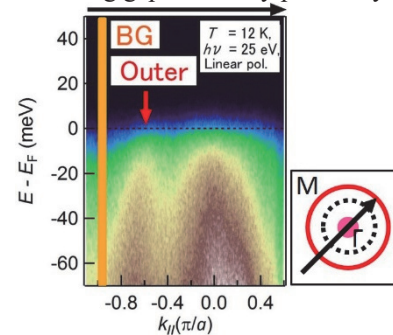


Fig. 1. E - k plot. Inset shows schematic FS.

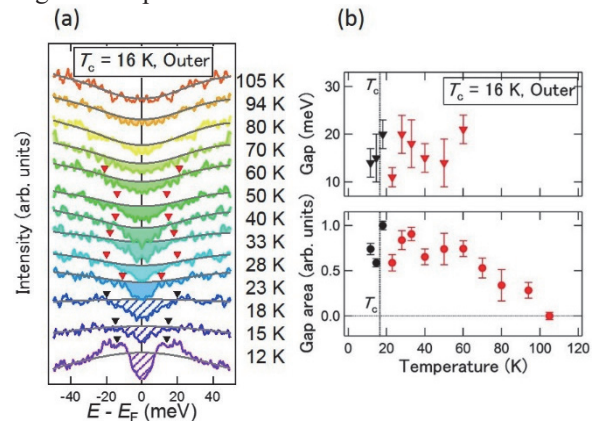


Fig. 2. Analysis of the energy gap at the “Outer” k_F . (a) Temperature dependence of the symmetrized EDCs. (b) Temperature dependence of the gap magnitude.

[1] Y. Kamihara, *et al.*, J. Am. Chem. Soc. **130** (2008) 3296.

[2] I. Nishi *et al.*, Phys. Rev. B **84** (2011) 014504.

[3] A. Charnukha *et al.*, Sci. Rep. **5** (2015) 10392.

[4] M. Ishikado *et al.*, Physica C **469** (2009) 901.

BL7U

Temperature Dependent Angle-resolved Photoemission Study of $(\text{TMTCF})_2\text{AsF}_6$

 T. Ito^{1,2}, S. Ideta^{3,4}, K. Tanaka^{3,4}, S. Kimura^{5,6} and T. Nakamura⁷
¹Nagoya University Synchrotron radiation Research center (NUSR), Nagoya University, Nagoya 464-8603, Japan

²Graduate School of Engineering, Nagoya University, Nagoya 464-8603, Japan

³UVSOR Synchrotron Facility, Institute for Molecular Science, Okazaki 444-8585, Japan

⁴The Graduate University for Advanced Studies, Okazaki 444-8585, Japan

⁵Graduate School of Frontier Biosciences, Osaka University, Suita 565-0871, Japan

⁶Department of Physics, Osaka University, Toyonaka 560-0043, Japan

⁷Institute for Molecular Science, Okazaki 444-8585, Japan

The Bechgaard salts $(\text{TMTCF})_2\text{X}$ ($\text{C} = \text{S}, \text{Se}$; $\text{X} = \text{PF}_6, \text{AsF}_6$, etc.) belong to a family of quasi-one-dimensional (Q1D) organic conductors. These materials allow for a variety of ground states from antiferro-magnetism, a Peierl's-like spin density wave, to a superconducting state by tuning the chemical pressure with the combination of TMTSF/TMTTF and anion X [1]. Among these compounds, $(\text{TMTTF})_2\text{X}$ system is especially important to elucidate the relation between the electronic structure and the origin of anomalous properties, because of its relatively high transition temperature from metallic to Mott localized (loc), charge ordered (CO), and antiferro-magnetic (AF) states [2]. In this study, we have performed temperature dependent angle-resolved photoemission spectroscopy (ARPES) on single-crystalline $(\text{TMTCF})_2\text{AsF}_6$ to clarify the relation between the electric structure and the thermodynamic properties, especially the intrinsic temperature dependence originating in the phase transitions.

ARPES measurement were performed at UVSOR-III BL7U by utilizing the bulk-sensitive low photon energy ($h\nu = 8 \text{ eV}$) as well as the micro focus beam ($15 \times 100 \mu\text{m}^2$).

Figures 1 (a-d) and (e-h) show the temperature dependence of the band structure near the Fermi level (E_F) of $(\text{TMTSF})_2\text{AsF}_6$ and $(\text{TMTTF})_2\text{AsF}_6$, respectively. It is evident that the clear dispersive feature of TMTCF molecular orbital has been observed at $T = 30 \text{ K}$ (Figs. 1(a) and (e)) for both case. With increasing temperature, the dispersive TMTSF band on metallic $(\text{TMTSF})_2\text{AsF}_6$ remain existing until $T = 260 \text{ K}$ (Fig. 1(d)). On the other hand, TMTTF features on $(\text{TMTTF})_2\text{AsF}_6$ show anomalous temperature dependence. At CO state ($T = 30 \text{ K}$), the electronic structure of $(\text{TMTTF})_2\text{AsF}_6$ is dominated with the dispersive feature folded around $k_x = 0.30 \text{ \AA}^{-1}$. With increasing temperature at the loc. state, the top of dispersive feature gradually shifts to higher binding energy side while the spectral weight of non-dispersive broad feature around 1 - 1.5 eV increases as shown in Fig. 1 (j). Then the electronic structure at the metallic state is dominated with the localized feature on $(\text{TMTTF})_2\text{AsF}_6$ in contrast to the dispersive feature on $(\text{TMTSF})_2\text{AsF}_6$. We expect that the observed

characteristic itinerant to localized transition of the TMTTF states play a dominant role in the CO-loc.-metal phase transition on $(\text{TMTTF})_2\text{AsF}_6$.

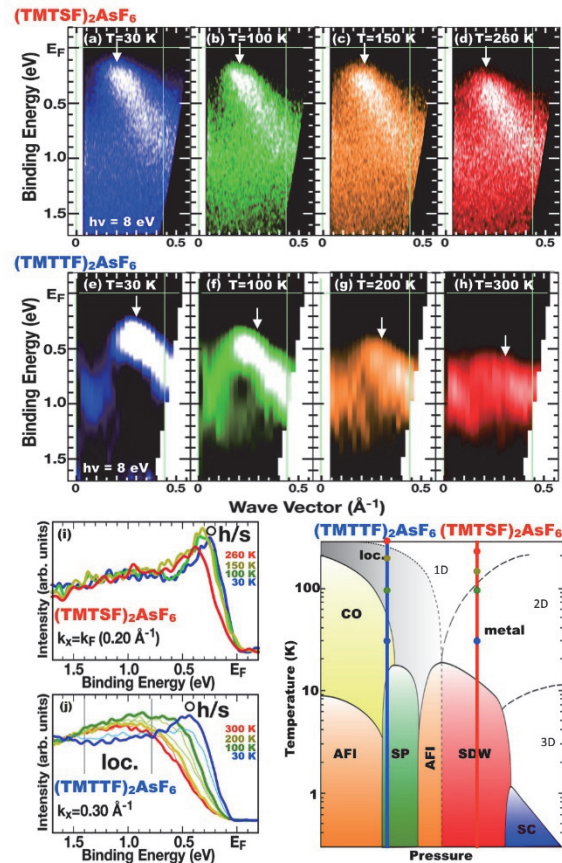


Fig. 1. Temperature dependent ARPES images and EDC spectra at $k_x=0.20 \text{ \AA}^{-1}$ and 0.30 \AA^{-1} of $(\text{TMTSF})_2\text{AsF}_6$ (a-d and i) and $(\text{TMTTF})_2\text{AsF}_6$ (e-h and j), respectively. Phase diagram of $(\text{TMTCF})_2\text{X}$ [2] is also indicated.

[1] T. Ishiguro *et al.*, Organic Superconductors (Springer-Verlag, Berlin, 1998).

[2] E. Rose *et al.*, J. Phys.: Condens. Mat. **25** (2013) 014006.

BL7U

Low-Energy Heavy-Fermion Bands in YbCdCu₄ Observed by Angle-Resolved Photoemission Spectroscopy

H. Shiono¹, S. Ishihara¹, K. Mimura¹, H. Sato², E. F. Schwier², K. Shimada², M. Taniguchi², S. Ideta³, K. Tanaka³, T. Zhuang⁴, K. T. Matsumoto⁴, K. Hiraoka⁴ and H. Anzai¹

¹Graduate School of Engineering, Osaka Prefecture University, Sakai 599-8531, Japan

²Hiroshima Synchrotron Radiation Center, Hiroshima University, Higashi-Hiroshima 739-0046, Japan

³UVSOR Synchrotron Facility, Institute for Molecular Science, Okazaki 444-8585, Japan

⁴Graduate School of Science and Engineering, Ehime University, Matsuyama 790-8577, Japan

In rare-earth compounds, the hybridization effect between conduction and localized- $4f$ electrons (c - f hybridization) leads to the formation of heavy electrons, and it is characterized by a renormalized band structure near the Fermi level (E_F). According to the single-impurity Anderson model, the Yb²⁺ $4f_{7/2}$ peak of Yb compounds appears at the energy scales of the Kondo temperature T_K , which is a measure of the hybridization strength [1]. Hence, the electronic band structure near E_F provides important clues to heavy fermion state.

The Laves-phase structure YbCdCu₄ is known as a heavy fermion compound with the electronic specific heat coefficient $\gamma \sim 175$ mJ/K²mol [2] and as a good reference for studies the first-order valence transition of YbInCu₄ [3]. To understand the heavy-fermion state in YbCdCu₄, it is essential to unveil the nature of the Yb $4f$ and conduction-band states.

Angle-resolved photoemission spectroscopy (ARPES) is a direct probe to measure the electronic excitation as functions of energy and momentum. Here, we report on a study of the hybridization effect in YbCdCu₄ based on ARPES data of the electronic band structure near E_F . The experiments were performed at BL7U of UVSOR and BL-1 of Hiroshima Synchrotron Radiation Center (HSRC).

Figure 1(a) shows ARPES spectra of YbCdCu₄ taken along the $\bar{\Gamma}$ - \bar{K} direction of the surface Brillouin zone. Two flat bands at $|\omega| \sim 0.02$ and 1.3 eV are assigned to the spin-orbit split Yb²⁺ $4f_{7/2}$ and $4f_{5/2}$ states, respectively. A dispersive band was observed over an energy range of $0.1 < |\omega| < 1.2$ eV. This conduction band intersects with the $4f_{7/2}$ state and reaches E_F , as seen from the peaks of momentum distribution curves in Fig. 1(b). Thus, Fermi surface of YbCdCu₄ at least consists of one hole band around the $\bar{\Gamma}$ point.

For quantification of the hybridization strength, we have measured the temperature dependence of the Yb²⁺ $4f_{7/2}$ state. A significant shift and an intensity enhancement in the $4f_{7/2}$ peak are observed, as shown by angle-integrated photoemission spectra in Fig. 1(c). We plotted the peak positions as a function of temperature in Fig. 1(d), which reveals a continuous decrease in the energy with decreasing temperature. The peak energies extrapolated to zero temperature is estimated to be ~ 26 meV and corresponds to $T_K \sim 300$ K, which is roughly consistent with T_K reported from

the magnetic susceptibility measurements [2]. This consistency implies that the heavy-fermion state in YbCdCu₄ stems from the hybridization between the observed $4f_{7/2}$ and conduction bands. Further experiments in wide momentum ranges are needed to understand the evolutions of the heavy-fermion bands of YbCdCu₄.

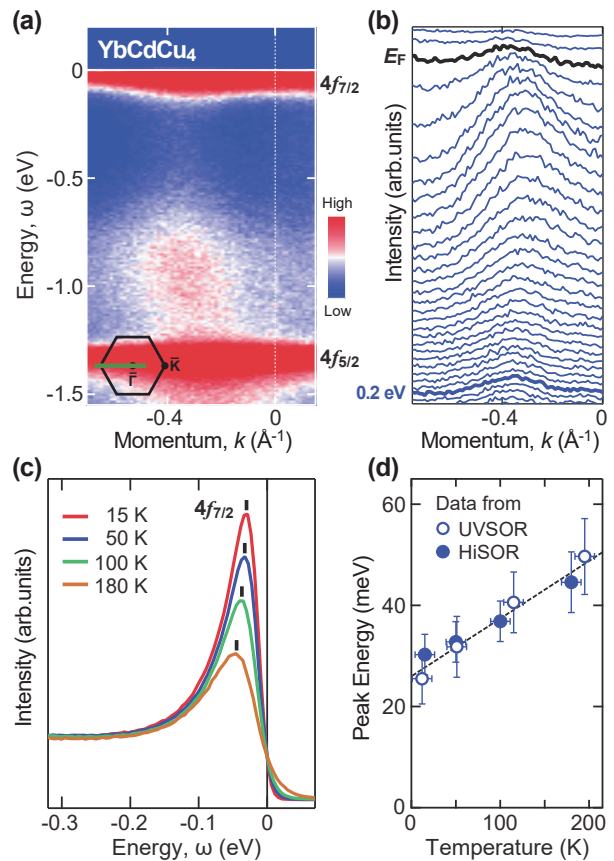


Fig. 1. (a) ARPES spectra of YbCdCu₄ taken along the $\bar{\Gamma}$ - \bar{K} direction at 15 K. The data were obtained at BL-1 of HSRC. (b) Momentum distribution curves near E_F . (c) Angle-integrated spectra at various temperatures. (d) Energy shift of the Yb²⁺ $4f_{7/2}$ peak in panel (c), together with the data from UVSOR.

[1] R. I. R. Blyth *et al.*, Phys. Rev. B **48** (1993) 9497.

[2] J. L. Sarrao *et al.*, Phys. Rev. B **59** (1999) 6857.

[3] I. Felner *et al.*, Phys. Rev. B **35** (1987) 6935.

BL7U

High-Resolution ARPES Study of FeSe Superconductor

G. Phan¹, K. Nakayama¹, H. Oinuma¹, T. Nakamura¹, D. Takane¹, Y. Nakata¹,
T. Urata², Y. Tanabe¹, K. Tanigaki^{1,3}, F. Nabeshima⁴, M. Kawai⁴, Y. Imai¹,
A. Maeda⁴, T. Takahashi^{1,3,5} and T. Sato^{1,5}

¹Department of Physics, Tohoku University, Sendai 980-8578, Japan

²Department of Crystalline Material Science, Nagoya University, Nagoya 464-8603, Japan

³WPI Research Center, Advanced Institute for Materials Research, Tohoku University, Sendai 980-8577, Japan

⁴Department of Basic Science, The University of Tokyo, Tokyo 153-8902, Japan

⁵Center for Spintronics Research Network, Tohoku University, Sendai 980-8577, Japan

Iron chalcogenides FeSe_{1-x}Te_x, the structurally simplest iron-based superconductors, are the target of intensive research because of rich physical properties such as superconductivity, antiferromagnetism, structural transition, and electronic nematicity. It was also reported that the physical properties of FeSe_{1-x}Te_x show gigantic pressure effects. For instance, the superconducting transition temperature (T_c) of FeSe is dramatically enhanced from 8 K to 36 K by the application of high pressure. Elucidating the origin of such pressure effects would provide a key to understanding the mechanism of high- T_c superconductivity.

Recent advances in fabricating epitaxial thin films of FeSe_{1-x}Te_x have opened a door to controlling the lattice parameters by tuning the lattice mismatch with substrate. This strain engineering has capability for manipulating various physical properties. For FeSe_{1-x}Te_x, compressive strain enhances the T_c up to 12 K in FeSe [1] and further to 23 K in FeSe_{0.8}Te_{0.2} [2]. In addition, strain-induced drastic changes in the structural, magnetic, and nematic properties have been discovered [3]. These discoveries have provided a great opportunity for investigating the interplay between the physical properties and the lattice parameters at ambient pressure. In this study, we have performed high-resolution angle-resolved photoemission spectroscopy (ARPES) on compressive strained FeSe_{1-x}Te_x thin films on CaF₂ substrate at BL-7U and compared their electronic structure with that of strain-free FeSe. We have revealed the evolution of electronic structure with epitaxial strain.

High-quality FeSe thin films were grown on CaF₂ substrate by pulsed laser deposition. The film thicknesses are approximately 300 monolayers. In Fig. 1, we show representative electronic structure measured in the normal state of bulk FeSe. One can recognize hole-like and electron-like band dispersions at the Brillouine-zone center (Γ point) and corner (M point), respectively, indicative of semimetallic nature of FeSe. When compressive strain is applied on CaF₂ substrate, hole-like and electron-like bands shift upward and downward, respectively. This observation indicates a strain-induced change in the semimetallic band overlap [4]. We have also determined the electronic structure of Te-substituted films on CaF₂

and found a marked change in the electronic structure compared with that in pristine FeSe. Our observations provide important insights into the interplay between T_c enhancement and lattice parameters.

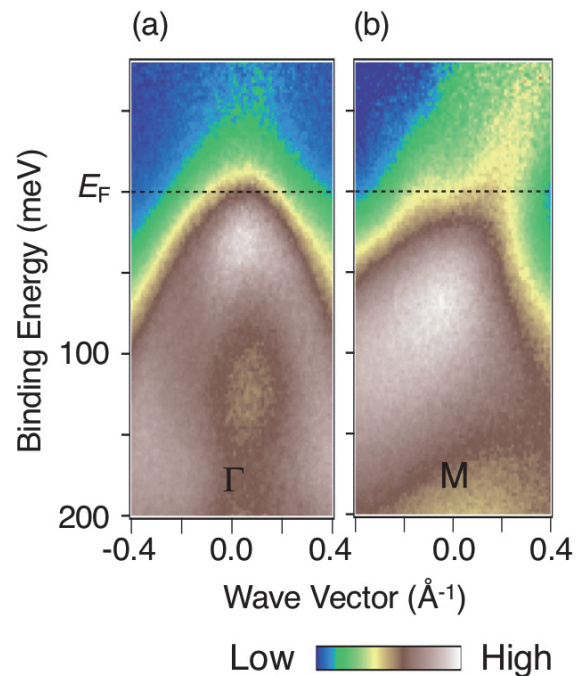


Fig. 1. (a) and (b) ARPES intensity plot around the Brillouin-zone center and corner, respectively, on FeSe at $T = 280$ K, obtained after dividing by the Fermi-Dirac function convoluted with the instrumental resolution. The data have been obtained with linearly-polarized 21-eV photons.

[1] F. Nabeshima *et al.*, Appl. Phys. Lett. **103** (2013) 172602.

[2] Y. Imai *et al.*, Proc. Natl. Acad. Sci. USA **112** (2015) 1937.

[3] Y. Imai *et al.*, Sci Rep. **7** (2017) 46653.

[4] G. Phan *et al.*, Phys. Rev. B **95** (2017) 224507.

BL7U

Electronic Structures of Methylammoniumlead Trihalides Single Crystals

S. Yamanaka¹, K. Tonami¹, S. Ideta², K. Tanaka², K. Yamada³, H. Yoshida⁴ and Y. Nakayama¹

¹Department of Pure and Applied Chemistry, Tokyo University of Science, Noda, 278-8510, Japan

²UVSOR Synchrotron Facility, Institute for Molecular Science, Okazaki 444-8585, Japan

³College of Industrial Technology, Nihon University, Narashino 275-8575, Japan

⁴Graduate School of Engineering, Chiba University, Chiba 263-8522, Japan

$\text{CH}_3\text{NH}_3\text{PbX}_3$ ($X = \text{Br}, \text{I}$) thin films are used as light absorption and charge separation materials of perovskite solar cells [1]. However, many structural defects (such as crystal grain boundaries) and impurities remain in polycrystalline thin films, which may cause problems in evaluating the precise electronic structure of the substances. In this study, we aimed to clarify the intrinsic electronic structures of $\text{CH}_3\text{NH}_3\text{PbX}_3$ by using single crystal samples.

$\text{CH}_3\text{NH}_3\text{PbBr}_3$ was produced from $\text{CH}_3\text{NH}_3\text{Br}$ and PbBr_2 in *N, N*-dimethylformamide; $\text{CH}_3\text{NH}_3\text{PbI}_3$ was synthesized from $\text{CH}_3\text{NH}_3\text{I}$ and PbI_2 in γ -butyrolactone. In either case, single crystal samples (typically as Figs. 1(a) and 1(b)) were prepared by inverse temperature crystallization methods [2, 3]. For the sake of obtaining the clean surface of the $\text{CH}_3\text{NH}_3\text{PbX}_3$ single crystals, cleavage of the crystal surface in vacuum was examined by breaking a ceramic post bounded on top of each sample. Ultraviolet photoelectron spectroscopy (UPS) measurements on the $\text{CH}_3\text{NH}_3\text{PbX}_3$ single crystals were conducted at BL7U of UVSOR. The excitation energy was set at 40 eV. In order to avoid charging of the sample during the measurements, the samples were irradiated with a laser beam (512 nm) at the same time.

Figure 2 (a) shows UPS spectra of a $\text{CH}_3\text{NH}_3\text{PbBr}_3$ single crystal before and after cleavage. It was confirmed that the peak intensity derived from Pb5d (binding energy (BE) around -20 eV) was enhanced and valence band structures (BE of -2 to -15 eV) were defined as a result of cleavage. This suggests that the clean surface is successfully obtained by cleavage in vacuum. Nevertheless, a new peak derived from metallic Pb (Pb^0) appeared at BE \sim -18 eV. This is plausibly due to damages in the $\text{CH}_3\text{NH}_3\text{PbBr}_3$ sample caused by irradiation with ultraviolet light during the measurements.

Figure 2 (b) shows UPS spectra of a $\text{CH}_3\text{NH}_3\text{PbI}_3$ single crystal before and after cleavage. Similarly to the $\text{CH}_3\text{NH}_3\text{PbBr}_3$ case, enhanced intensities of the Pb5d peaks suggest successful cleaning of the $\text{CH}_3\text{NH}_3\text{PbI}_3$ surface by cleavage in vacuum. Furthermore, in the case of $\text{CH}_3\text{NH}_3\text{PbI}_3$, it was confirmed that the peaks of Pb5d shifted by +0.20 eV, which suggests change in band bending. On the other hand, shift in the secondary electron cutoff measured with a separate equipment ("off-line ARPES" device) indicated that the vacuum level moves by 0.7 eV on the high energy side after cleavage in vacuum. These results suggest that impurities on $\text{CH}_3\text{NH}_3\text{PbI}_3$ single crystals induce a negative vacuum level shift of -0.5

eV and downward band bending of -0.2 eV. This implies the formation of a surface electric double layer due to the electrons being donated from the surface impurities to the $\text{CH}_3\text{NH}_3\text{PbI}_3$ side. In addition, it was revealed that the Pb^0 peak intensity was minor in comparison to the $\text{CH}_3\text{NH}_3\text{PbBr}_3$ case, suggesting that $\text{CH}_3\text{NH}_3\text{PbI}_3$ is more robust to the ultraviolet light.

This work was conducted as Joint-Studies-Programs [27-545 and 27-835] of IMS.

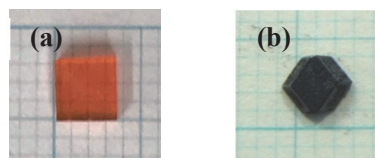


Fig. 1. Photographs of the (a) $\text{CH}_3\text{NH}_3\text{PbBr}_3$ and (b) $\text{CH}_3\text{NH}_3\text{PbI}_3$ single crystal samples.

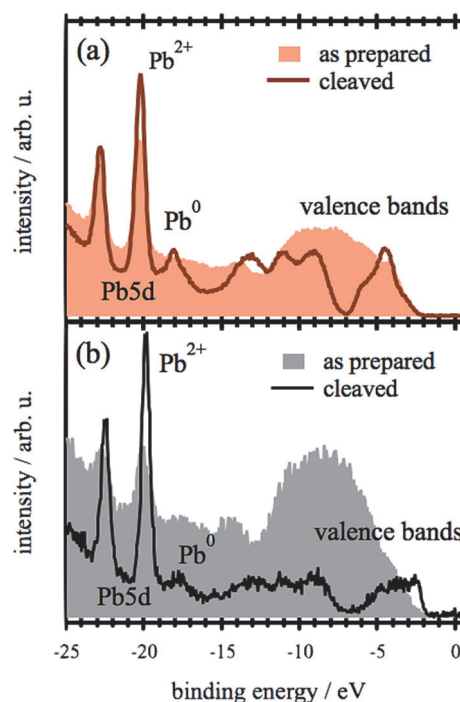


Fig. 2. UPS spectra of the (a) $\text{CH}_3\text{NH}_3\text{PbBr}_3$ and (b) $\text{CH}_3\text{NH}_3\text{PbI}_3$ single crystal samples before and after cleavage in vacuum.

[1] A. Kojima *et al.*, *J. Am. Chem. Soc.* **131** (2009) 6050.

[2] F. Zhang *et al.*, *J. Mater. Chem. C* **5** (2017) 8431.

[3] H. Wei *et al.*, *Nat. Mater.* **16** (2017) 826.

BL7U

Superconducting Gap of Iron-Based Superconductor $\text{Ba}_{0.75}\text{K}_{0.25}\text{Fe}_2\text{As}_2$

 S. Ideta^{1,2}, M. Nakajima³, N. Murai⁴, R. Kajimoto⁴ and K. Tanaka^{1,2}
¹UVSOR, Synchrotron Facility, Institute for Molecular Science, Okazaki, 444-8585, Japan

²The Graduate University for Advanced Studies (SOKENDAI), Okazaki, 444-8585, Japan

³Department of Physics, Graduate School of Science, Osaka University, Toyonaka, 560-0043, Japan

⁴Materials and Life Science Division, J-PARC Center, Japan Atomic Energy Agency, Tokai 319-1195, Japan

Iron-based superconductors have a complex phase diagram with the antiferromagnetic (AFM) transition and the structural phase transition. Recently, nematicity, defined as broken rotational symmetry [a trigonal (C_4)-to-orthorhombic (C_2) structural transition], has shed light on the understanding of the mechanism on the iron-based superconductivity [1-4]. In hole-doped BaFe_2As_2 (Ba122) system, thermal expansion, specific heat, and neutron diffraction measurements of $\text{Ba}_{1-x}\text{Na}_x\text{Fe}_2\text{As}_2$ and $\text{Ba}_{1-x}\text{K}_x\text{Fe}_2\text{As}_2$ (K-Ba122) have shown the magnetic order without C_4 symmetry breaking [5, 6]. Besides, the superconductivity is suppressed between the superconducting (SC) and the C_4 -magnetic phase. The mechanism of the suppressed superconductivity has been unclear yet, and it would give us a great interest to elucidate the hole-doped Ba122 superconductor.

Here, we have investigated the electronic structure of $\text{Ba}_{0.75}\text{K}_{0.25}\text{Fe}_2\text{As}_2$ focusing on the superconducting gaps using high energy resolution angle-resolved photoemission spectroscopy (ARPES). We found that the hole Fermi surfaces (FSs) showed the FS dependent SC gap, and the suppressed SC gap would be responsible for the low T_c in K-Ba122 with $x \sim 0.25$.

High-quality single crystals of $\text{Ba}_{0.75}\text{K}_{0.25}\text{Fe}_2\text{As}_2$ ($T_c \sim 25$ K) were grown by self-flux technique. ARPES experiments were carried out at BL7U of UVSOR-III Synchrotron using the linearly polarized light of $h\nu = 18$ eV-32 eV photons. Temperature was set at $T = 12$ K and 35 K and clean sample surfaces were obtained for the ARPES measurements by cleaving single crystals *in-situ* in an ultrahigh vacuum better than 6×10^{-9} Pa.

Figures 1(a1) and 1(a2) show the ARPES intensity plot as a function of energy and momentum taken at $h\nu = 21$ eV and 32 eV, corresponding to the Γ and Z points, respectively. We observe at least two hole bands for Γ and Z points, indicating that the degenerated inner bands (d_{yz}, d_{xz}) and outer (d_{xy}/d_z^2) bands. Taking into account the electronic structure of K-Ba122 ($x \sim 0.25$) in the k_z direction [7], we observed the SC gap at the Γ and Z points on the hole FSs. In Figs. 1(c1)-1(d2), energy distribution curve (EDC) at Fermi momentum (k_F) for inner (α) and outer (γ) hole bands are shown. EDCs are divided by the Fermi-Dirac (FD) distribution function and the peak position corresponds to the SC gap shown by a gray circle. Here, we found that the energy gap is suppressed on the outer hole FS (γ) only for K-Ba122 ($x \sim 0.25$) compared with the nearly optimally doped K-Ba122 ($x = 0.3$).

The present study reveals that the SC gap on hole FSs shows finite nodeless gaps but is strongly suppressed in K-Ba122 ($x \sim 0.25$), and therefore, we propose that the suppressed outer hole FS reflects the suppressed T_c in this material.

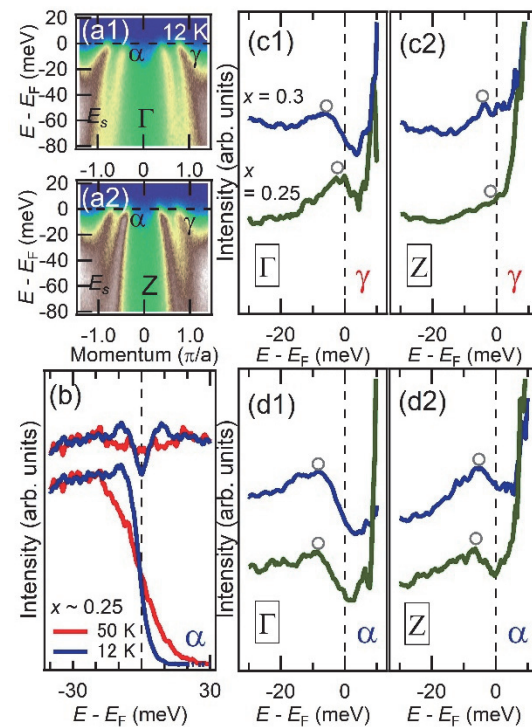


Fig. 1. (a1), (a2) Energy-momentum plots of the hole FSs at the Γ and Z points ($T = 12$ K) (b) Temperature dependence of ARPES spectrum. (c1)-(d2) EDCs of the α and γ bands at the k_F position divided by Fermi-Dirac (FD) distribution function for K-Ba122 ($x \sim 0.25$ and 0.3).

- [1] R. M. Fernandes *et al.*, Nat. Phys. **10** (2014) 97.
- [2] R. M. Fernandes *et al.*, Phys. Rev. Lett. **111** (2013) 127001.
- [3] T. Shimojima *et al.*, Phys. Rev. B **90** (2014) 12111.
- [4] Y. Ming *et al.*, PNAS **108** (2011) 6878-6883.
- [5] L. Wang *et al.*, Phys. Rev. B **93** (2016) 014514.
- [6] A. E. Böhrer *et al.*, Nat. Commun. **6** (2015) 7911.
- [7] S. Ideta *et al.*, UVSOR Activity Report **44** (2016) 76.

BL7U

Temperature Dependence of Mott Gap in Ca_2RuO_4 Investigated by ARPES

D. Shibata¹, M. Kawamoto¹, K. Yamawaki¹, D. Ootsuki¹, C. Sow², Y. Maeno², F. Nakamura³ and T. Yoshida¹

¹Graduate School of Human and Environmental Studies, Kyoto University, Kyoto 606-8501, Japan

²Department of Physics, Graduate School of Science, Kyoto University, Kyoto 606-8502, Japan

³Kurume Institute of Technology, Fukuoka 830-0052, Japan

A t_{2g} -electron system $\text{Ca}_{2-x}\text{Sr}_x\text{RuO}_4$ with a layered perovskite structure shows a rich phase diagram [1]. Sr_2RuO_4 is a leading candidate of a spin triplet superconductor. On the other hand, Ca_2RuO_4 is an antiferromagnetic insulator below $T = 110$ K and a paramagnetic insulator between $T = 110$ K and 357 K. Ca_2RuO_4 undergoes a metal to insulator (MI) transition at $T_{\text{MI}} = 357$ K accompanied by a first-order structural phase transition. The RuO_4 octahedra shrink along the c -axis and d_{xy} orbital becomes dominant in the insulating phase [2]. The insulator to metal transition can be achieved not only by raising temperature, but also by chemical substitution, applying pressure and electric field. In this work, we studied temperature dependence of the Mott gap in Ca_2RuO_4 using angle-resolved photoemission spectroscopy (ARPES).

Figure 1 shows ARPES spectra of Ca_2RuO_4 taken with $h\nu = 23$ eV. In order to determine the orbital character of the band structure near E_F , we measured the incident light polarization dependence of the spectra. The intensity at ~ -1.8 eV is enhanced with p -polarized light, indicating $d_{yz/zx}$ orbital character. On the other hand, the intensity at ~ -0.8 eV is enhanced in the s -polarized spectrum, indicating d_{xy} orbital character. The parabolic band structure from -0.8 eV to -2.5 eV can be assigned to d_{xy} orbital. These results are consistent with the previous ARPES study [3]. The DMFT calculation also indicates that the intensity at ~ -0.8 eV and at ~ -1.8 eV correspond to d_{xy} and $d_{yz/zx}$ orbital, respectively [3, 4].

Figure 2 (a) shows the angle-integrated photoemission spectra of Ca_2RuO_4 along Γ -S line. The gap size decreases with increasing temperature. To clarify the temperature evolution of the gap, we estimated the gap size by using linear extrapolation from the slope of spectra. The gap size is consistent with that estimated from the optical conductivity [5]. The suppression of the gap size may be caused by the elongation of c -axis. These results imply that the d_{xy} orbital plays a crucial role in the insulator to metal transition.

[1] S. Nakatsuji and Y. Maeno, Phys. Rev. Lett. **84** (2000) 2666.

[2] M. Braden *et al.*, Phys. Rev. B **58** (1998) 847.

[3] D. Sutter *et al.*, Nat. Comm. **8** (2017) 15176.

[4] G. Zhang *et al.*, Phys. Rev. B **95** (2017) 075145.

[5] J. H. Jung *et al.*, Phys. Rev. Lett. **91** (2003) 056403.

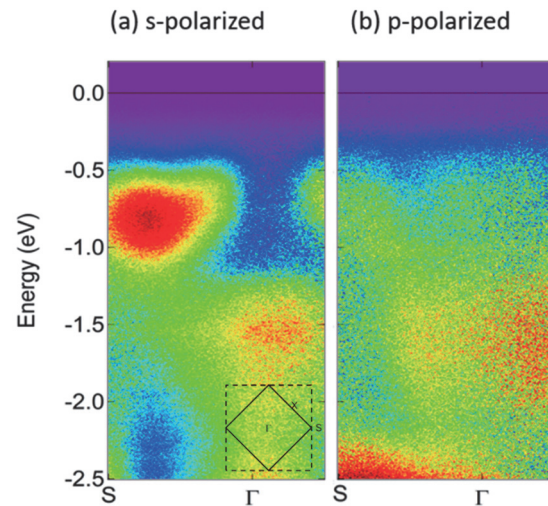


Fig. 1. ARPES spectra along Γ -S line taken at $T = 170$ K using (a) s - and (b) p -polarized light.

size decreases with increasing temperature.

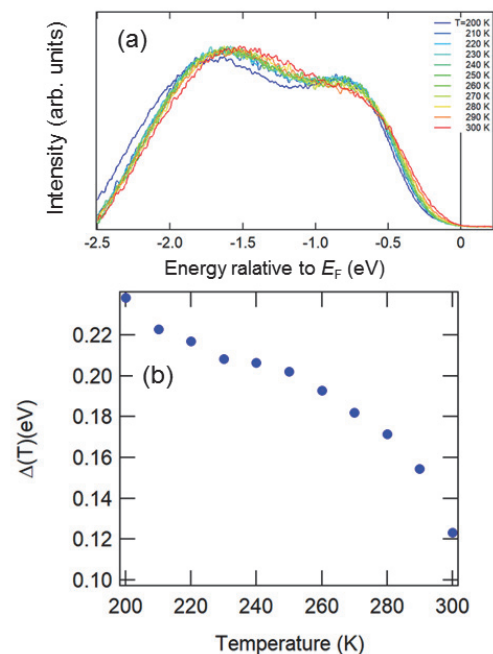


Fig. 2. Temperature dependence of gap structure. (a) Angle-integrated spectra along Γ -S line. (b) Gap size estimated from the spectra in panel (a).

BL7B

Analysis of Luminescence and Scintillation Processes of Organic–inorganic Perovskite-type Compounds Using VUV Excitation Light

N. Kawano¹, M. Koshimizu², G. Okada³, Y. Fujimoto², N. Kawaguchi³,
T. Yanagida³ and K. Asai¹

¹Graduate School of Engineering Science, Akita University, Akita 010-8502, Japan

²Graduate School of Engineering, Tohoku University, Sendai 980-8579, Japan

³Graduate School of Materials Science, Nara Institute of Science and Technology, Ikoma 630-0192, Japan

To develop a scintillator with excellent time resolution, we focused on the phenomena exhibited by confined excitons in nanoscale semiconductors. Among the compounds with a low-dimensional system, scintillation materials based on luminescence from organic–inorganic layered perovskite-type compounds are of particular interest. These hybrid materials have self-organized multiple quantum well structures. An inorganic quantum well exhibits luminescence of confined excitons, and its organic layer acts as a barrier of confinement structures. In the compounds, excitons confined in the inorganic layer have large binding energies and oscillator strengths due to the quantum confinement and the image charge effects.

We have demonstrated that the organic–inorganic layered perovskite-type compounds exhibit efficient scintillation due to exciton emission from the inorganic layer. Among them, $(\text{C}_6\text{H}_5\text{C}_2\text{H}_4\text{NH}_3)_2\text{PbBr}_4$ exhibits fast scintillation decay (~ 10 ns) and efficient luminescence that exceeds 10,000 photons per MeV under synchrotron X-ray (67.4 keV) [1, 2] and gamma-ray irradiation [3]. We reported that the excellent scintillation properties of $(\text{C}_6\text{H}_5\text{C}_2\text{H}_4\text{NH}_3)_2\text{PbBr}_4$ originate from the fast radiative rate of the excitons, which is caused by the lattice distortion in the inorganic layers verified with single-crystal structural analysis [4]. In addition to the effect on the crystal structure, the organic moieties in the organic layers would influence the scintillation properties via possible energy transfer from the organic layers to the inorganic layers. We have reported that the energy transfer slower than the time resolution of the measurement systems (100 ps) and have a negligible contribution to the scintillation properties of the compounds [5]. However, the component of energy transfer faster than the time resolution (100 ps) could have an influence on the scintillation properties of organic–inorganic layered perovskite-type compounds.

In this study, a crystal of $(\text{C}_6\text{H}_5\text{C}_2\text{H}_4\text{NH}_3)_2\text{PbBr}_4$ was fabricated by the poor-solvent diffusion method. Luminescence spectra and decay curves were measured under VUV irradiation at the UVSOR Synchrotron Facility (BL7B; Okazaki, Japan) to analyze the possible contribution of the energy transfer.

Table 1 summarizes the decay time constants and relative intensities (in parentheses) of photoluminescence decay at 410 nm with different

excitation wavelengths. The rise time behavior observed in the luminescence decay curve showed no difference among the excitation wavelengths of 60–300 nm. The decay can primarily be attributed to radiative transition of the Wannier excitons in the inorganic layers. In addition, no excitation peak of benzene such as an intense peak at 180 nm ($^1\text{A}_{1g} \rightarrow ^1\text{E}_{1u}$) in the vacuum ultraviolet region was observed in the excitation spectra measured while monitoring the exciton emissions from the inorganic layer. These results indicate that the effect of energy transfer from the organic layer to the inorganic layer has negligible contribution to the luminescence properties of organic–inorganic layered perovskite-type compounds.

Table 1. Decay time constants and relative intensities (in parentheses) of photoluminescence decay at 410 nm with different excitation wavelengths.

Excitation Wavelength (nm)	First component (ns)	Second component (ns)
60	1.4 (95%)	14 (5%)
150	1.3 (94%)	21 (6%)
180	1.7 (92%)	19 (8%)
250	2.0 (91%)	15 (9%)
300	3.0 (91%)	18 (9%)

[1] S. Kishimoto, K. Shibuya, F. Nishikido, M. Koshimizu, R. Haruki and Y. Yoda, *Appl. Phys. Lett.*, **93** (2008) 261901.

[2] N. Kawano, M. Koshimizu, A. Horiiai, F. Nishikido, R. Haruki, S. Kishimoto, K. Shibuya, Y. Fujimoto, T. Yanagida and K. Asai, *Jpn. J. Appl. Phys.*, **55** (2016) 110309.

[3] N. Kawano, M. Koshimizu, G. Okada, Y. Fujimoto, N. Kawaguchi, T. Yanagida and K. Asai, *Sci. Rep.* **7** (2017) 14754.

[4] N. Kawano, M. Koshimizu, Y. Sun, N. Yahaba, Y. Fujimoto, T. Yanagida and K. Asai, *J. Phys. Chem. C*, **118** (2014) 9101.

[5] N. Kawano, M. Koshimizu, Y. Sun, N. Yahaba, Y. Fujimoto, T. Yanagida and K. Asai, *Jpn. J. Appl. Phys.*, **53** (2014) 02BC20.

BL7B

Anomalous Thermoelectric Response and Charge Dynamics of Pyrochlore $(\text{Eu}_{1-x}\text{Ca}_x)_2\text{Ir}_2\text{O}_7$

J. Fujioka^{1,2}, R. Kaneko¹, M. Masuko¹, K. Ueda¹ and Y. Tokura^{1,3}

¹*Department of Applied Physics and Quantum-Phase Electronics Center (QPEC), University of Tokyo, Tokyo 113-8656, Japan*

²*PRESTO, Japan Science and Technology Agency, Kawaguchi 332-0012, Japan*

³*RIKEN Center for Emergent Matter Science (CEMS), Wako 351-0198, Japan*

The interplay between the relativistic spin-orbit interaction and electron correlation provides a fruitful field to research unconventional quantum phenomena such as the topological semimetal and Kitaev spin liquids. The pyrochlore-type iridates $R_2\text{Ir}_2\text{O}_7$ (R =rare earth elements) is one of candidate materials to study the Mott physics or magnetism of correlated Weyl electron. Wan *et al.*, proposed the possible emergence of antiferromagnetic Weyl semimetallic phase on the verge of Mott transition [1]. The giant negative magnetoresistivity and metallic edge state emerging at the antiferromagnetic domain walls of $\text{Nd}_2\text{Ir}_2\text{O}_7$ have been argued in terms of the magnetic field-induced topological transition and topological edge state of Weyl electrons [2, 3]. Moreover, even in the paramagnetic phase, possible non-Fermi liquid behavior due to the zero-gap semiconducting band or flat-band with long-lived spin moment have been proposed [4]. In this study, we have investigated the charge transport and charge dynamics of hole-doped $\text{Eu}_2\text{Ir}_2\text{O}_7$ to explore the novel non-Fermi liquid behavior.

Figure 1(a) shows the temperature dependence of resistivity for $\text{Eu}_2\text{Ir}_2\text{O}_7$ and its Ca-doped analogs $(\text{Eu}_{1-x}\text{Ca}_x)_2\text{Ir}_2\text{O}_7$. $\text{Eu}_2\text{Ir}_2\text{O}_7$ ($x=0$) exhibits insulating behavior below 300 K and the resistivity shows a kink upon the antiferromagnetic magnetic ordering at 123 K. In the hole doped systems, the resistivity shows a similar behavior and the kink is discernible for $x=0.01$, 0.02 and 0.03. On the other hand, for $x=0.05$ and 0.1, the kink is no longer discernible and paramagnetic metallic behavior subsists down to 2 K.

Figure 1(b) shows the Seebeck coefficient of metallic systems. With decreasing temperature, the Seebeck coefficient is enhanced and reaches 30 $\mu\text{V}/\text{K}$ around 50 K for $x=0.1$. Similar behavior is also observed for $x=0.05$ and 0.2. Such a non-monotonic temperature dependence and relatively large value are not common among conventional correlated metals.

To explore the electronic structure in the paramagnetic metallic state, we show the optical conductivity spectra of $(\text{Eu}_{1-x}\text{Ca}_x)_2\text{Ir}_2\text{O}_7$ in Fig. 2. The charge gap with a magnitude of 0.1 eV is discernible for $x=0$. On the other hand, the gap is closed and a Drude response shows up for $x=0.05$ and 0.2. It should be noted that an absorption peak with narrow width is observed around 0.05 eV besides the broad continuum above 0.1 eV. Such an absorption band suggests the

emergence of flat-band with enhanced density of state (DOS). Since the Seebeck coefficient is sensitive to the DOS, the appearance of flat-band with high-DOS may be related to the anomalous enhancement of Seebeck coefficient.

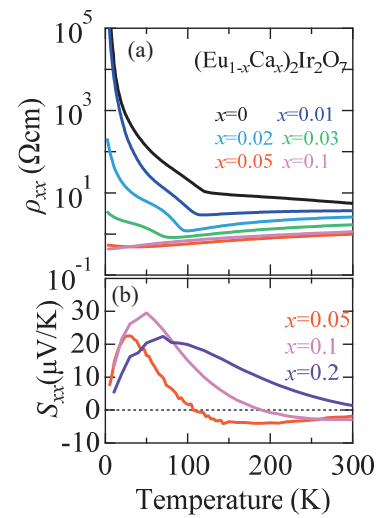


Fig. 1 Temperature dependence of (a) resistivity and (b) Seebeck coefficient.

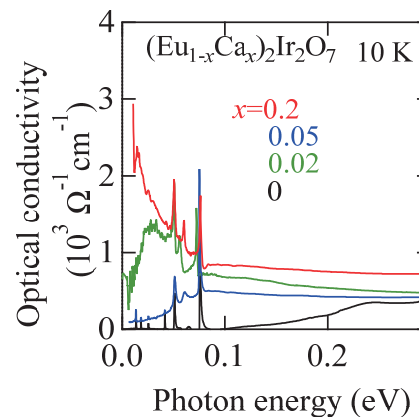


Fig. 2 Optical conductivity spectra at 10 K.

- [1] X. Wan *et al.*, Phys. Rev. B **83** (2011) 205101.
 [2] K. Ueda, *et al.*, Phys. Rev. Lett. **115** (2015) 056402.
 [3] E. Y. Ma, *et al.*, Science **350** (2015) 538.
 [4] H. Shinaoka *et al.*, Phys. Rev. Lett. **115** (2015) 156401.

BL7B

Study of Optical Absorption of Parasitic Transition Metal ions (Fe^{3+} , Cr^{3+}) at Low Temperature in Nonlinear Crystal $\text{YAl}_3(\text{BO}_3)_4$ (YAB) in the 100 – 600 nm Range

E. Lafitte-Houssat^{1,2}, A. Kausas¹, L. Zheng¹, H. Ishizuki¹, G. Aka² and T. Taira¹

¹Laser Research Centre, Institute for Molecular Science, Okazaki 444-8585, Japan

²PSL Research University, Institute de Recherche de Chimie Paris IRCP, Chimie ParisTech, Paris 75005, France

YAB crystals are very promising NLO material for UV applications, one of them being the fourth harmonic generation of Nd^{3+} based lasers at 266 nm. The UV cut-off wavelength is measured to be 170 nm, but Fe^{3+} and Cr^{3+} impurities in the crystals generally cause parasitic UV absorption. The conversion process of YAB crystals is then jeopardized in the deep UV. Low temperature transmittance spectra as function of polarization should allow us to clearly identify transition ions responsible for parasitic optical absorption in the UV range of interest. As absorption band intensities increase at low temperature, the characterization of the peaks should be eased. During our experiment at BL7B, we have studied the influence of temperature on optical transmission for YAB samples within 30 K-300 K temperature range.

Three samples were studied at 300 K to identify the transitions related to transition ions Fe^{3+} and Cr^{3+} , (Fig. 1(a)) in the range of 150 nm to 600 nm. For this scanning, YAB#1 had its Y axis perpendicular to the light polarization, while YAB#2 had its Y axis parallel to the light polarization. The axis for YAB#3 could not be determined. Two absorption bands can be identified around 240 nm and 280 nm. They may be attributed to charge transfer processes from oxygen to iron $\text{O}2\text{p}^5\text{-Fe}3\text{d}^6$: ($e^2t_2^4$, 240 nm) and ($e^3t_2^3$, 280 nm). For YAB#1, there is another absorption around 425 nm, that corresponds to a d-d transition of Cr^{3+} ($^4A_{2g} \rightarrow ^4T_{2g}$), that usually occurs at 425 nm in Cr doped YAB crystals. However, the absence of that transition for the two other samples is not usual. It can be explained by different purities of the starting materials, or by the crucible used for YAB#1 crystal growth (one-month experiment). For the sample YAB#1, we can also notice that the cut-off wavelength is higher than for YAB#2 and YAB#3. This is most likely caused by the higher thickness of the sample. For the three samples, the cut-off wavelength is higher than 170 nm, which is caused by the optical absorption of the transition ions. Also, there is no absorption at 532 nm for all three samples, which confirms that YAB crystals are well suited for SHG from 532 nm to 266 nm.

At low temperature, as thermal motion is reduced, we should be able to better visualize transition ion absorptions. The results we obtained were not totally in accordance with that assumption. For all three samples, we could see that there were few overall differences when the temperature varies, even from 30 K to 300 K range.

The influence of the orientation of the crystal is much more visible and interesting. The results are shown in Fig.1(b) for the sample YAB#2, but they were the same for the other samples. For all the samples, the orientation has an effect in the range 225-350 nm. The absorption at 280 nm is weaker when the Y axis is parallel to light polarization. However, for the transition at 240 nm, it is more visible when the Y

axis is parallel. As the absorption at 266 nm must be limited, the orientation of the crystal must be controlled to have the best performance in frequency conversion. For all the samples, the absorption around 266 nm is weaker when the Y axis is parallel to the polarization of the incoming light. It means that this orientation is to be preferred for FHG experiments with YAB crystals.

We have studied three YAB samples under UV polarized light and their transmission spectra. The parasitic absorption of transition ions Fe^{3+} and Cr^{3+} was confirmed. Charge transfer processes $\text{O}2\text{p}^5\text{-Fe}3\text{d}^6$ were identified around 240 nm and 280 nm, and d-d transitions of Cr^{3+} may be visible in one of the YAB samples. The influence of temperature and the orientation of the crystals was also investigated. The orientation of the crystals influences greatly the transmission profiles, especially for the charge transfer transitions. The scanning under low temperature did not deliver a better characterization but still confirmed the assumptions about parasitic absorptions.

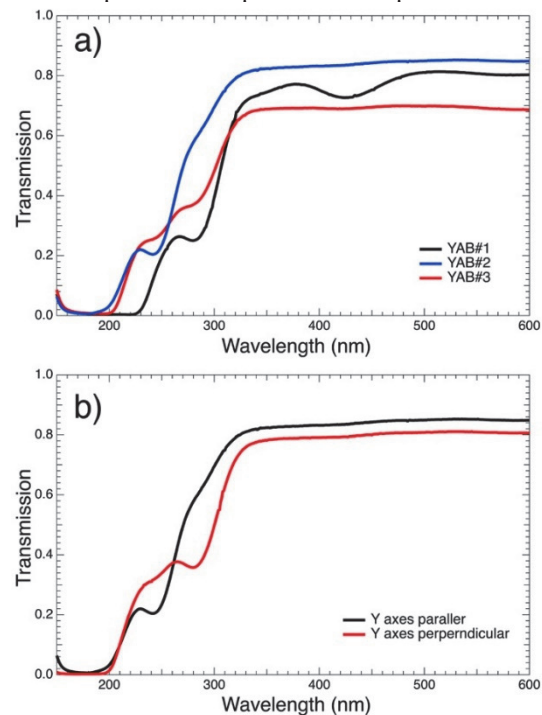


Fig. 2. Optical transmission spectra for YAB#1, YAB#2 and YAB#3 crystals (a) and comparison of crystal orientation for YAB#2 (b).

[1] Y. Wang and R.K. Li, Opt. Materials **32** (2010) 1313.

BL7B

Auger-Free Luminescence in K_2ZnCl_4 Crystals

A. Ohnishi and M. Kitaura

Faculty of Science, Yamagata University, Yamagata 990-8560, Japan

The Auger-free luminescence (AFL) is a peculiar type of intrinsic luminescence in ionic crystals in which the valence excitation through a nonradiative Auger process is forbidden. The AFL is characterized by a high quantum yield and a short lifetime of the order of ns. Therefore, it is very useful as the fast scintillator for high-energy physics, positron emission tomography and so on.

In previous works [1-4], we have studied optical properties of Cs_2ZnCl_4 and Rb_2ZnCl_4 molecular ionic crystals with the use of synchrotron radiation as a light source. We have observed AFL in these crystals. K_2ZnCl_4 is one of molecular ionic crystals and has the same crystal structure as Cs_2ZnCl_4 and Rb_2ZnCl_4 [5]. In this crystal, the outermost core level is supposed to be built up by Zn 3d states, because the K 3p state should be deeper-lying inner shells than the Zn 3d state in comparison with the binding energies of electrons between them. Therefore, it is expected that AFL due to interatomic p-d transitions between the Zn 3d outermost core level and the Cl 3p valence band is observed in K_2ZnCl_4 . In the present study, we have investigated the luminescence of K_2ZnCl_4 crystals under the outermost core excitation, in order to find the existence of AFL.

K_2ZnCl_4 crystals were prepared by evaporating a stoichiometric mixture of solutions of KCl and $ZnCl_2$. The reflection, emission and excitation spectra were measured at the BL7B of UVSOR.

As indicated by a red line in Fig. 1, sharp peaks at 7.3 and 7.9 eV were observed in the reflection spectrum measured for the cleaved surface of K_2ZnCl_4 . The 7.3 and 7.9 eV peaks are assigned to the $n = 1$ and 2 exciton peaks due to the transition from the Cl 3p valence band to the conduction band, respectively. From the positions of the two peaks, the band gap energy (E_g) is estimated to be about 8.0 eV by assuming that the exciton energy levels are hydrogen-like.

From the result of X-ray photoelectron spectroscopy (XPS), it was clear that the outer-most core level in K_2ZnCl_4 is composed of the Zn 3d states. We estimated the energy difference (E_{VC}) between the top of the valence band and that of the outer-most core band by referring to the XPS spectrum. The value of E_{VC} was 6.5 eV. Since this value is smaller than that of E_g , the appearance of AFL due to the interatomic Cl 3p \rightarrow Zn 3d transitions is expected for K_2ZnCl_4 , when a core hole is created in the Zn 3d outer-most band by photo-excitation.

When K_2ZnCl_4 was excited at 10 K with 21.4 eV photons above the value of $E_g + E_{VC}$, three luminescence bands appeared at 5.9, 4.4 and 2.8 eV.

The blue line in Fig. 1 shows the excitation spectrum for the 4.4 eV band. The excitation spectra for the 5.9 and 2.8 eV bands were practically the same as that for the 4.4 eV band. These bands are excited in the energy region above 14.4 eV. The photon energy of 14.4 eV is almost agreement with the energy sum of E_g and E_{VC} . Since this satisfies the condition for the occurrence of AFL, the three bands mentioned above are assigned to the AFL bands due to the radiative recombination of a valence electron and an outermost core hole.

Luminescence decay measurements were also performed using a time-correlated single-photon counting technique under the single bunch operation. It was proved that, at 10 K, the AFL bands are composed of a fast decay component with the lifetime of about 8 ns.

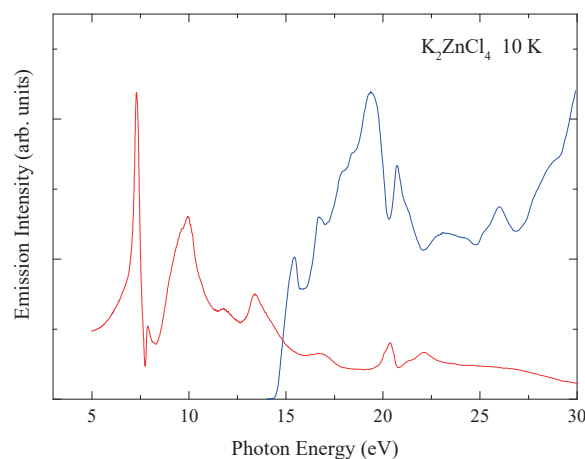


Fig. 1. Excitation spectrum (blue line) at 10 K for the 4.4 eV band in K_2ZnCl_4 . For reference, reflection spectrum is also shown by a red line.

- [1] A. Ohnishi, T. Otomo, M. Kitaura and M. Sasaki, *J. Phys. Soc. Jpn.* **72** (2003) 2400.
- [2] A. Ohnishi, M. Saito, M. Kitaura, M. Itoh and M. Sasaki, *J. Lumin.* **132** (2012) 2639.
- [3] A. Ohnishi, M. Kitaura, M. Itoh and M. Sasaki, *J. Phys. Soc. Jpn.* **81** (2012) 114704.
- [4] M. Kitaura and A. Ohnishi, *Kogaku* **45** (2016) 175 (in Japanese).
- [5] J. A. McGinnery, *Inorg. Chem.* **13** (1974) 1057.

BL7B

Optical Property of Compound Fluoride Materials $\text{Ca}_x\text{Sr}_{1-x}\text{F}_2$ at Low Temperature

K. Suzuki, R. Yamazaki, J. Otani and S. Ono
 Nagoya Institute of Technology, Nagoya 466-8555, Japan

Vacuum ultraviolet (VUV) light source is used in various applications such as surface treatment, optical cleaning of semi-conductor substrates and sterilization. Accordingly, the detector for monitoring the light source is also required. Currently, many researchers developed VUV detectors based on oxide, nitride and diamond. However, the detectors require the filters for cutting off deep-UV when being used for monitoring of the light source. On the other hand, our group is proceeding to development of the VUV detectors using fluorides [1-3]. Some fluorides have extremely wider band gap than oxides and nitrides so that they transmit deep-UV region. Until now, we achieved filterless VUV detectors by applying such fluorides. And spectral response of the detectors varies according to band gap of the material. Therefore, we may realize the detectors possessing arbitrary response region by controlling band gap of the material. Here, we report on controlling band gap of compound fluoride materials $\text{Ca}_x\text{Sr}_{1-x}\text{F}_2$ and the temperature dependence of the band gap of these materials.

$\text{Ca}_x\text{Sr}_{1-x}\text{F}_2$ crystals were grown by Bridgman method and they were controlled composition ratio as $\text{Ca}_{0.85}\text{Sr}_{0.15}\text{F}_2$ and $\text{Ca}_{0.5}\text{Sr}_{0.5}\text{F}_2$. Absorption coefficient was calculated by measuring transmission spectrum of VUV region as shown in Fig.1. Herewith, band gaps of CaF_2 , $\text{Ca}_{0.85}\text{Sr}_{0.15}\text{F}_2$, $\text{Ca}_{0.5}\text{Sr}_{0.5}\text{F}_2$ and SrF_2 were calculated as 10.24, 9.98, 9.83 and 9.73 eV at R.T., respectively. Therefore, the band gap of $\text{Ca}_x\text{Sr}_{1-x}\text{F}_2$ is expanded by increasing composition ratio of CaF_2 in the crystals.

Additionally, the band gap at low temperature (50 - 300K) was obtained by cooling the samples with liquid helium. Solid lines in Fig.2 were calculated from Bose-Einstein type equation as given below

$$E(T) = E(0) - \frac{2a}{\exp\left(\frac{\Theta}{T}\right) - 1}$$

where $E(0)$ is band gap energy at 0 K, a is strength of exciton-phonon interaction, and Θ is average temperature of phonons. As a result of that, the band gaps of CaF_2 , $\text{Ca}_{0.85}\text{Sr}_{0.15}\text{F}_2$, $\text{Ca}_{0.5}\text{Sr}_{0.5}\text{F}_2$ and SrF_2 at 0 K were estimated as 10.69, 10.46, 10.23 and 10.13 eV, respectively.

In summary, we found capable of controlling the band gap of $\text{Ca}_x\text{Sr}_{1-x}\text{F}_2$ and evaluated the band gap of $\text{Ca}_x\text{Sr}_{1-x}\text{F}_2$ at low temperature. The band gap was expanded by increasing composition ratio of CaF_2 in the crystals. Such result shows that we can control the

spectral response of filterless VUV photoconductive detector using $\text{Ca}_x\text{Sr}_{1-x}\text{F}_2$ crystals.

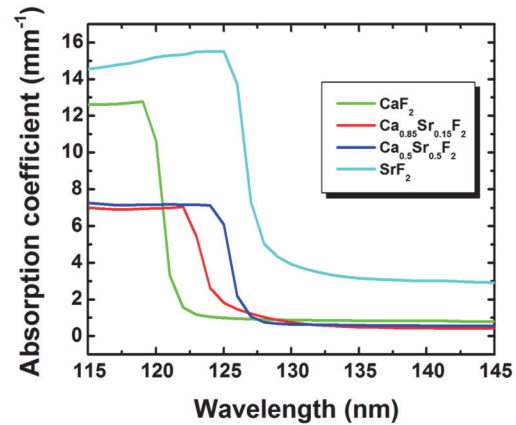


Fig. 1. Temperature characteristic of band gap.

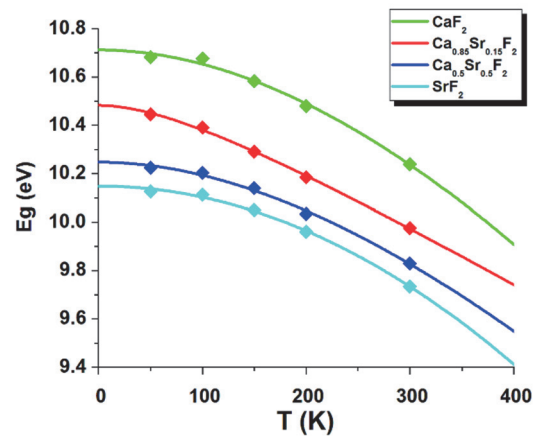
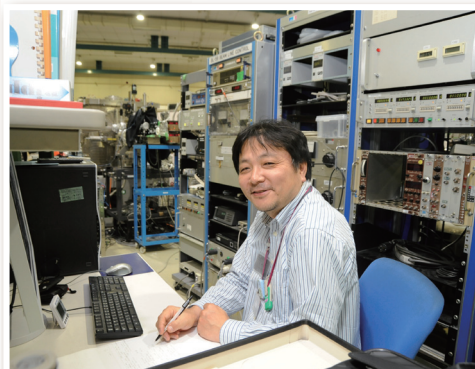
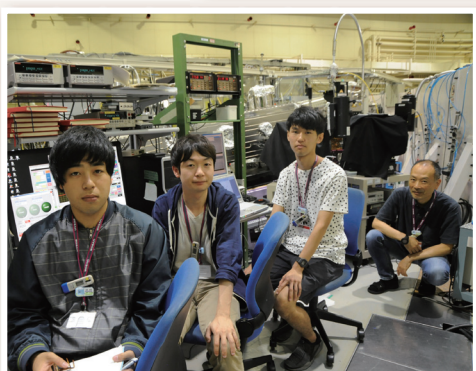
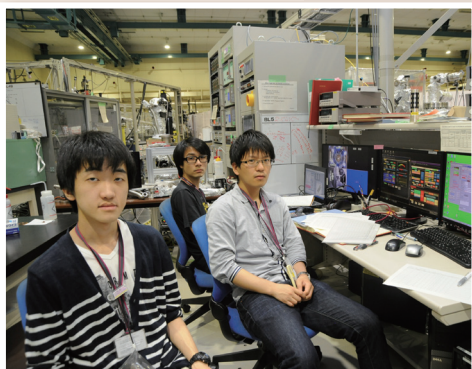
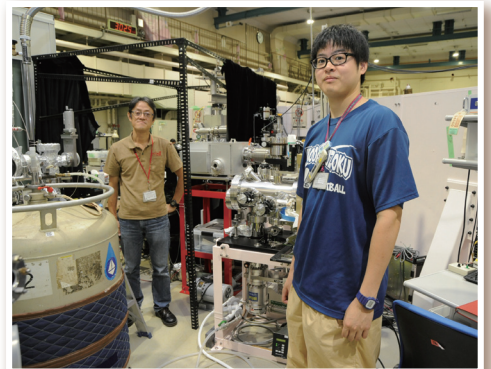
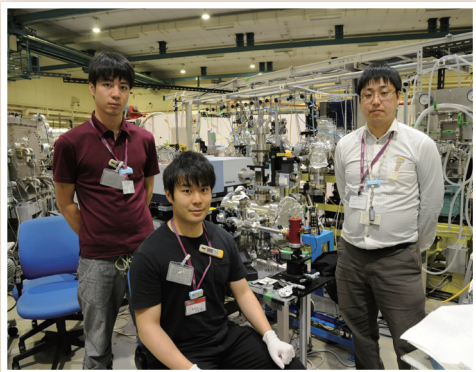
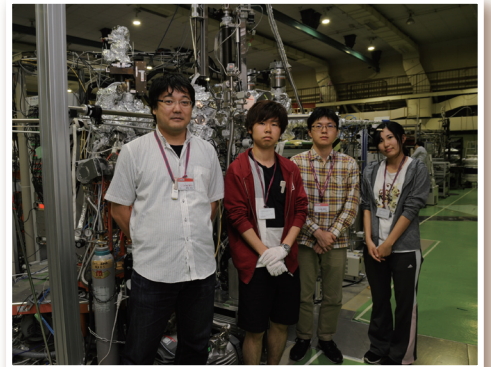
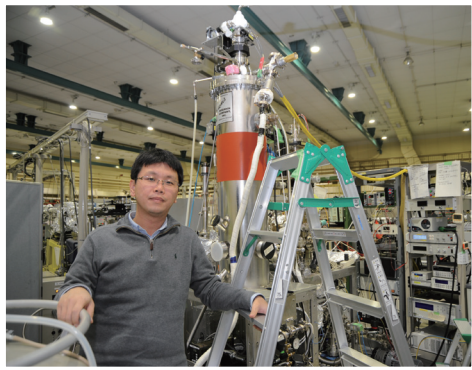
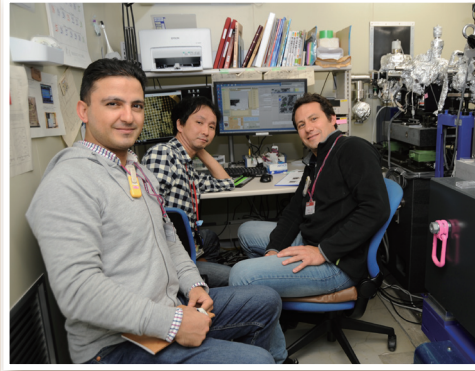
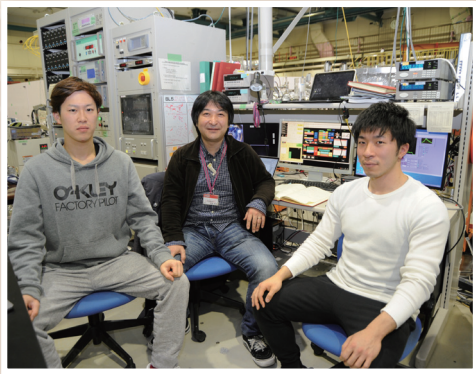


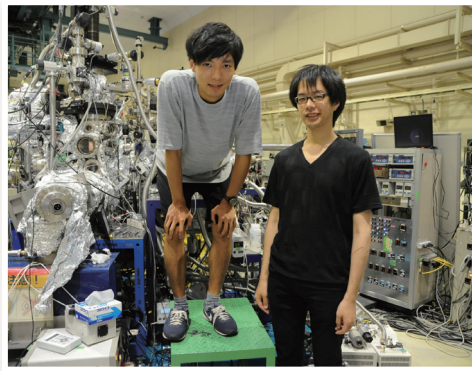
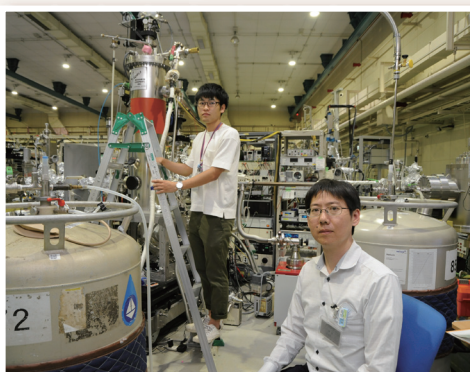
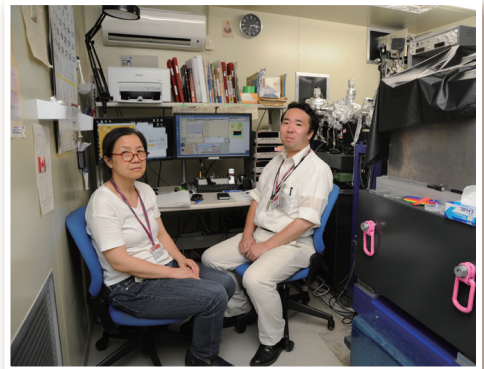
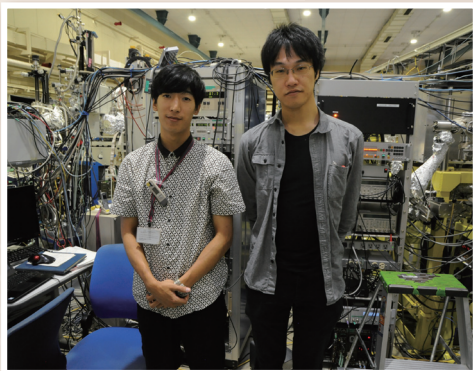
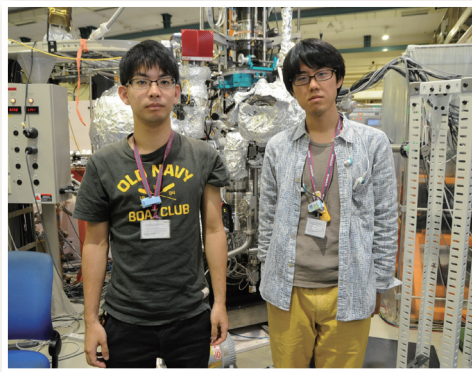
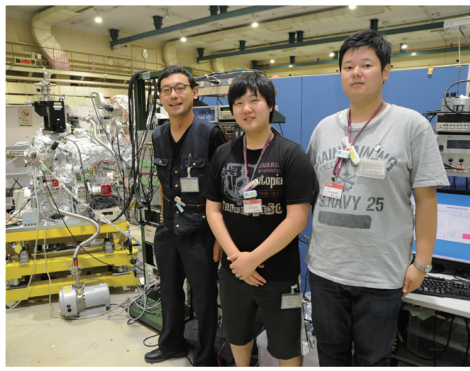
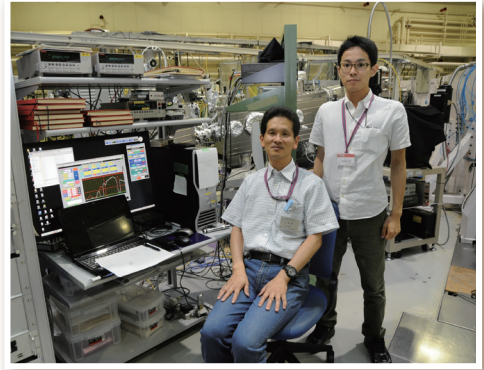
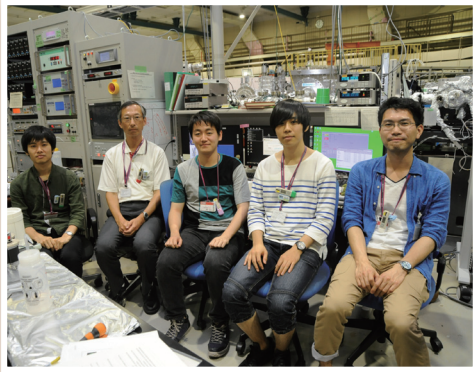
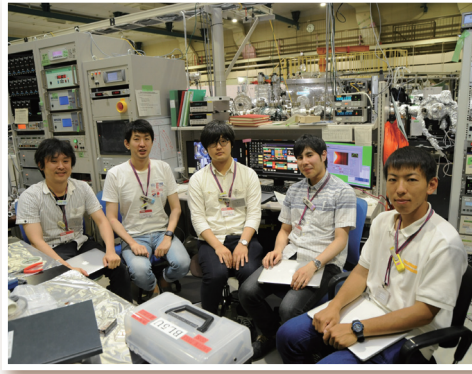
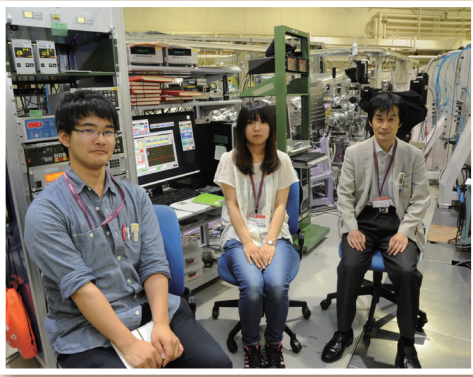
Fig. 2. Temperature characteristic of band gap.

[1] M. Ieda, T. Ishimaru, S. Ono, N. Kawaguchi, K. Fukuda, T. Suyama, Y. Yokota, T. Yanagida and A. Yoshikawa, *Jpn. J. Appl. Phys.* **51** (2012) 062202.
 [2] T. Ishimaru, M. Ieda, S. Ono, Y. Yokota, T. Yanagida and A. Yoshikawa, *Thin Solid Films* **534** (2013) 12.
 [3] M. Yanagihara, H. Ishikawa, S. Ono and H. Ohtake, *Testing and Measurement: Techniques and Applications* (2015) 151.

UVSOR User 2



UVSOR User 3



III-3

Chemistry

BL3U

Microfluidics of Liquid Mixtures for Soft X-ray Absorption Spectroscopy

M. Nagasaka^{1,2}, A. A. Vu^{1,3}, H. Yuzawa¹, N. Takada¹, M. Aoyama¹, E. Rühl³ and N. Kosugi^{1,2}

¹Institute for Molecular Science, Okazaki 444-8585, Japan

²SOKENDAI (The Graduate University for Advanced Studies), Okazaki 444-8585, Japan

³Physikalische Chemie, Freie Universität Berlin, Takustr. 3, D-14195 Berlin, Germany

Microfluidics is a chemical technique to realize highly efficient chemical reactions in liquid phase [1]. Recently, X-ray diffraction in the hard X-ray region has been used for a variety of systems by using microfluidics [2]. However, it is difficult to apply spectroscopic techniques in the soft X-ray region since soft X-rays cannot penetrate a microfluidic cell. Previously, we developed a microfluidic cell for soft X-ray absorption spectroscopy (XAS) of structured liquids [3]. In this study, we have successfully observed a laminar flow between pyridine and water in soft X-ray fluorescence image by improving a microfluidic cell and measured N K-edge XAS in the mixed part of microfluidics to reveal the interaction between water and pyridine in a laminar flow.

The experiments were performed at the BL3U connected to a custom-made microfluidic cell. A T-shape microfluidics setup with the width of 50 μm is made from PDMS resin which is covered by a 100 nm Si_3N_4 membrane. Pyridine and water are mixed in the microfluidics with flow rates of 4 $\mu\text{l}/\text{min}$ by using syringe pumps. The ultrahigh vacuum of the soft X-ray beamline is separated from the microfluidic cell that is kept at atmospheric helium pressure by a 100 nm thick SiC membrane with a window size of $30 \times 30 \mu\text{m}^2$. This window determines the photon beam size [4]. Spatially resolved XAS spectra of the microfluidic cell are measured in the fluorescence yield mode at around 320 eV to 430 eV in N K-edge and at 460 eV to 580 eV in O K-edge, respectively, by using a silicon drift detector.

Figure 1 shows a soft X-ray fluorescence image of the T-shape microfluidic cell excited by soft X-rays at 550 eV. Pyridine (*P*) flows from the upper side, and water (*W*) from the lower side. The water-pyridine mixture (*M*) flows to the right-hand part after the junction of the liquids. Since 550 eV is above the O K-edge, the fluorescence shows high intensity due to water and low intensity at pyridine, respectively. The laminar flow of water and pyridine is observed in the mixed part of the microfluidics.

Figure 2 shows N K-edge XAS spectra at different positions in the mixed part shown in Fig. 1, where the horizontal position is fixed to $X = 600 \mu\text{m}$ and the vertical positions are scanned. From the intensity of the N $1s \rightarrow \pi^*$ transition, the center position of the mixed part is at $Y = 504 \mu\text{m}$. By changing the position from pyridine ($Y = 540 \mu\text{m}$) to the water part ($Y = 460 \mu\text{m}$), the π^* peak shows a spectral shift to the higher photon energy due to the formation of the pyridine-water mixtures [5]. This shift abruptly

occurs at $Y = 500 \mu\text{m}$, indicating clearly the phase separation in the laminar flow.

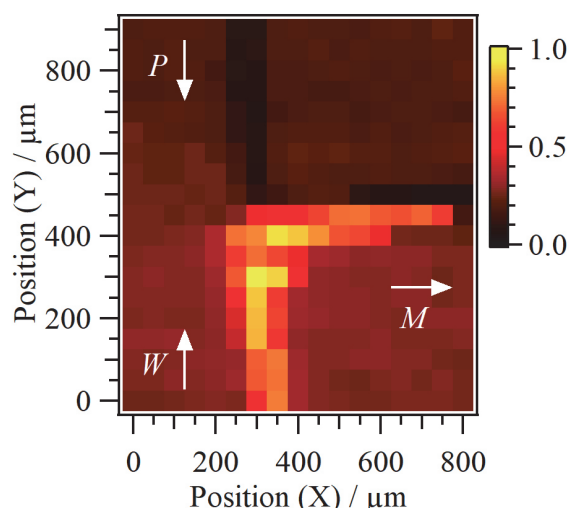


Fig. 1. Soft X-ray fluorescence image of a T-shaped microfluidic cell excited by soft X-rays at 550 eV. A laminar flow is observed in the mixed part.

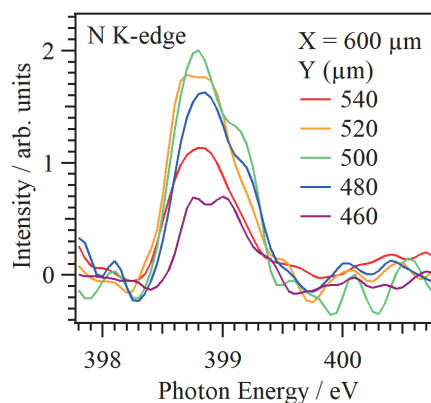


Fig. 2. N K-edge XAS spectra at different positions in the mixed part of the microfluidic flow shown in Fig. 1. The horizontal position is fixed to $X = 600 \mu\text{m}$, and the vertical position is scanned in the mixed part.

- [1] T. Kitamori *et al.*, *Anal. Chem.* **76** (2004) 53.
- [2] B. Weinhausen and S. Köster, *Lab Chip* **13** (2013) 212.
- [3] M. Nagasaka *et al.*, *UVSOR Activity Report* **2016** (2017) 106.
- [4] M. Nagasaka *et al.*, *J. Electron Spectrosc. Relat. Phenom.* **224** (2018) 93.
- [5] M. Nagasaka *et al.*, *Z. Phys. Chem.* *in press*.

BL1U

Molecular Orientation Induced by Irradiation UV to Achiral Dinuclear Schiff Base Metal Complexes-PVA Hybrid Materials

T. Akitsu¹, H. Nakatori¹, S. Yagi¹, H. Sato¹, T. Soejima¹, S. Yamazaki¹,
D. Tadokoro², M. Fujiki³, M. Fujimoto⁴ and M. Katoh⁴

¹Faculty of Sciences, Tokyo University of Science, Tokyo 162-8601, Japan

²Graduate School of Human and Environmental Studies, Kyoto University, Kyoto 606-8501, Japan

³Graduate School of Materials Sciences, NAIST, Nara 630-0192, Japan

⁴UVSOR Synchrotron Facility, Institute for Molecular Science, Okazaki 444-8585, Japan

In recent years, studies on optical vortex light have attracted attention. A light vortex having a spiral wavefront and carrying an orbital angular momentum gives a torque when irradiated on an object. As a result, a phenomenon which cannot be observed with ordinary light is expected. In fact, applied research on azo polymers has been reported.

We have attempted molecular orientation control by irradiating linearly and circularly polarized ultraviolet light to a polymer film in which an azo-dye that undergoes a photoisomerization reaction with a Schiff base metal complex is dispersed [1]. Previous research has revealed that it aligns in one direction by irradiation with linearly polarized ultraviolet light and spirally aligns by irradiation with circularly polarized ultraviolet light. Herein, the purpose of this research is to investigate what will happen if light vortex is irradiated on the complex we have studied so far.

We measured UV-vis spectra of MO (methyl orange, azo-dye), ZnL (Fig. 1), ZnL+MO in PVA (polyvinyl alcohol) aqueous solution. An absorption peak was observed in the vicinity of 280 nm in all the samples. Therefore, the irradiation wavelength of the optical vortex was set to 280 nm. Photo-illumination (both circularly polarized light and optical vortex) of UV light was carried out using UVSOR BL1U.

Prior to actual experiments, we have investigated only PVA films to remove effects of artifact CD peaks due to LD of oriented samples. Difference CD spectra PVA films before and after optical vortex (270 nm, $l=-1, 1$) irradiation corresponding to the $\pi-\pi^*$ band of acetate groups were carefully confirmed to disappear artifact CD peaks just like Fig. 2.

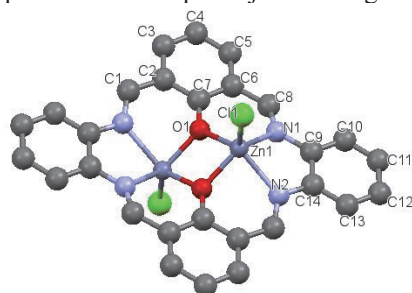


Fig. 1. Crystal structure of ZnL from PXRD data.

As shown in Figs. 3 and 4, not only ZnL+MO

(due to Weigert effect) but also only ZnL (due to orbital angular momentum) could be successfully observed to appear CD peaks after optical vortex irradiation.

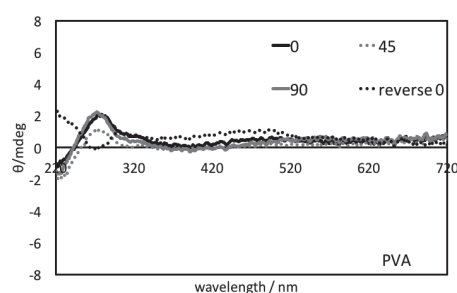


Fig. 2. CD spectra 0°, 45°, 90° reverse side of PVA cast film after optical vortex (280 nm, $l=-1$) irradiation.

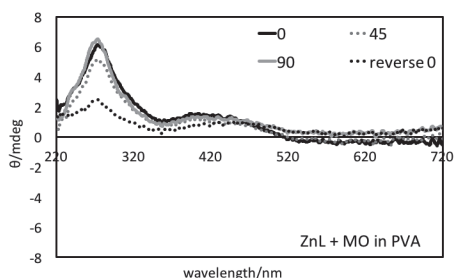


Fig. 3. CD spectra 0°, 45°, 90° reverse side of PVA cast film containing ZnL+MO after optical vortex (280 nm, $l=-1$) irradiation.

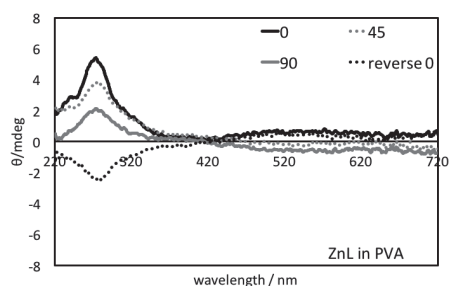


Fig. 4. CD spectra 0°, 45°, 90° reverse side of PVA cast film containing ZnL after optical vortex (280 nm, $l=-1$) irradiation.

[1] N. Sunaga, T. Akitsu, T. Konomi and M. Katoh, MATEC Web of Conferences **130** (2017) 07004.

BL3U, BL4U

XAS Characterizations on NaOH Solutions and Calcium Chlorides in Transmission Mode

Y.-S. Liu¹, P.-A. Glans¹, J. Guo¹, M. Nagasaka², T. Ohgashi² and N. Kosugi²

¹Lawrence Berkeley National Laboratory, 1 Cyclotron Road, Berkeley, CA 94720, USA

²Institute for Molecular Science, Okazaki 444-8585, Japan

The electronic structure of ion solvated in liquids has long been studied owing to its importance in many applications. The related ionic and electronic transportation mechanisms are still far from understood in the microscopic scales, which are crucial for the broad applications ranging from bioscience, pharmacology and energy science such as metal ion batteries.

Here, we are reporting our preliminary results taken at UVSOR in 2016 and 2017 on O K-edge XAS in NaOH solutions and Ca L-edge in CaCl₂ solutions in different solvents (water, methanol and ethanol). The results show that the in-situ capabilities are promising at UVSOR beamlines, especially in transmission mode really provide high quality XAS spectra and stability.

Figure 1 left shows the O K-edge XAS that are taken at UVSOR from the concentrated NaOH solutions. The results are showing that the solvated OH⁻ anion group gives a spectroscopic signature feature at around 532 ~ 533 eV (see enlarged Fig.1 right). This feature has intensity change depending on the concentration corresponding to the increasing of OH⁻ content in the solutions. Most importantly, these results are consistent with our previous experimental study using fluorescence and electron-yield mode measurements at the other synchrotron facilities. In addition, the theoretical calculated XAS spectra of NaOH solutions are to be completed for understanding the ion solvation shell. The results taken at UVSOR could be extremely helpful as the XAS spectra obtained from the transmission geometry removes the so-called saturation effect, which is often been questioned in fluorescence mode.

Figure 2 shows the Calcium L-edge spectra of 1 Molar CaCl₂ in different solvents (water, methanol and ethanol). The experimental Ca L-edges spectra are extremely sensitive to its solvents. However, since Ca²⁺ has a 3d₀ configuration, the pronounced differences between solvents indicating that the polar solvent, i.e. water vs. methanol, plays an important role to its electronic structure. The main differences can be seen from the variation of pre-peak intensities around 348.4 and 351.4 eV. However, the detail solvation shells need to be confirmed and incorporate with theoretical calculations.

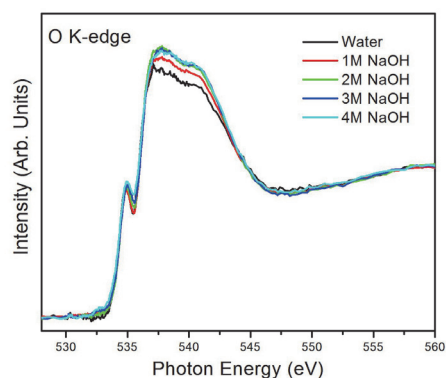


Fig. 1. O K-edge XAS spectra of different concentration NaOH solutions.

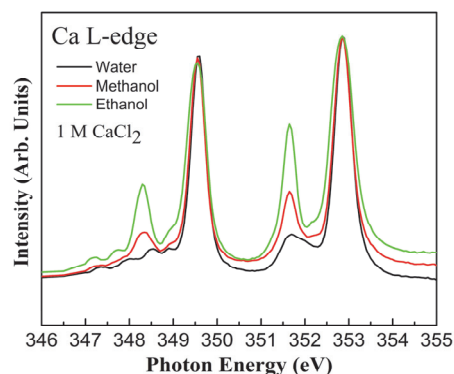


Fig. 2. Ca L-edge XAS spectra in different solvents.

BL3U

Soft X-ray Absorption Spectroscopy of 4-Cyano-4'-pentylbiphenyl Molecules in Liquid, Liquid-crystal and Solid Phases

H. Iwayama^{1,2}¹UVSOR Synchrotron Facility, Institute for Molecular Science, Okazaki 444-8585, Japan²School of Physical Sciences, The Graduate University for Advanced Studies (SOKENDAI), Okazaki 444-8585, Japan

The liquid crystal is one of the most important materials for display devices. In the case of nematic liquid crystals, the rod-shaped organic molecules have no position order, but they self-align to have long-range directional order with their long axes roughly parallel. Since X-ray absorption fine structure (XAFS) spectroscopy is sensitive to a local atomic geometry and the chemical state of the atom of one specific element, XAFS spectroscopy is suitable to investigate structures of liquid crystal materials. However, XAFS measurement of liquid crystal materials is limited to one in a solid phase due to the requirement of high vacuums of a sample chamber. Considering the fact that they work as display device in a liquid-crystal phase, we need to measure XAFS in a liquid-crystal phase. Recently, Nagasaka developed a liquid cell [1], which allows us to measure XAFS spectra of liquid samples. In this work, we measure XAFS of liquid-crystal materials in liquid, liquid-crystal and solid phase with this liquid cell.

Our sample is 4-Cyano-4'-pentylbiphenyl (5cb), which is one of the most popular liquid-crystal materials. A schematic draw of 5cb molecules is shown in Fig. 1. The phase transition temperature of liquid to liquid-crystal and liquid-crystal to solid are 22.5 and 35°C, respectively. The XAFS measurements were carried out at BL3U. After liquid cell which is composed of two Si₃N₄ membranes was filled with the liquid sample, the thickness of liquid sample was optimized by controlling the He gas pressure around the cell. The photon energy was calibrated by using the C-K edge XAS spectrum of the proline thin layer.

Figure 1 shows C K-edge XANES spectra of 5cb sample at three different temperature, which correspond to liquid, liquid-crystal and solid phases. We observed a strong peak at 285 eV, which correspond to a core excitation of C 1s to π^* orbitals of phenyl group. The peak intensities and shapes are different for each phase. Figure 2 shows N K-edge XANES spectra of 5cb molecules. Split peaks at 398.7 and 399.5 eV correspond to a core excitation of N 1s to π^* orbitals of nitrile group. As well as C K-edge XANES spectra, peak intensities of 1s-to- π^* core excitation at N K-edge depend on their phases.

This phase dependence of core excitations reflect the change of molecular alignments between each phases. Our results shows XANES is powerful tool to observe change of a local chemical environment. A more detail analysis is now in progress.



Fig. 1. Schematic draw of 4-Cyano-4'-pentylbiphenyl (5cb) molecules.

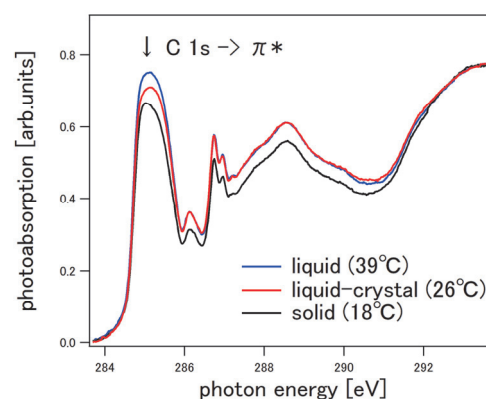


Fig. 2. C K-edge XANES of 5cb molecules at 18 (solid), 26 (liquid-crystal) and 39 °C (liquid).

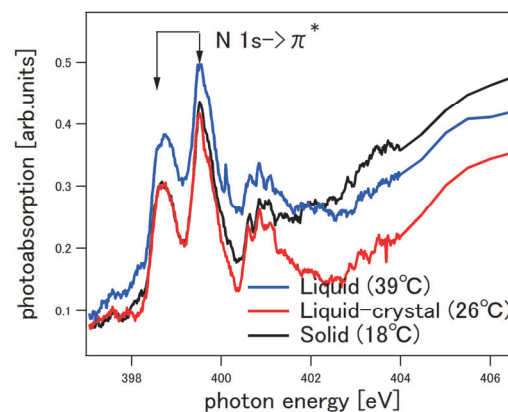


Fig. 3. N K-edge XANES spectra of 5cb samples at 18 (solid), 26 (liquid-crystal) and 39 °C (liquid).

[1] M. Nagasaka, H. Yuzawa and N. Kosugi, *J. pectrosc. Relat. Phenom.* **200** (2015) 293.

BL3U

Temperature Dependence of Interaction around NO_2^- in Aqueous KNO_2 Solution by Soft X-ray Absorption Spectroscopy

H. Yuzawa¹, M. Nagasaka^{1,2} and N. Kosugi^{1,2}

¹Institute for Molecular Science, Okazaki 444-8585, Japan

²School of Physical Sciences, SOKENDAI (The Graduate University for Advanced Studies), Okazaki 444-8585, Japan

Understanding of interactions in aqueous electrolyte solutions is one of the highly attractive research subjects [1]. Recently, our research group has studied the interaction between some cations and water by using O K-edge soft X-ray absorption spectroscopy (XAS) of water in the transmission mode [2]. In the present study, we have investigated the temperature dependence of the interaction around the NO_2^- anion by N and O K-edge XAS.

XAS spectra were measured at BL3U equipped with the liquid cell system in the transmission mode [3]. Aqueous KNO_2 solution sample (Molar ratio is $\text{KNO}_2 : \text{H}_2\text{O} = 1 : 42.6$) was prepared by using the commercial reagent without further purification. After the liquid cell which is composed of two Si_3N_4 membranes and Teflon spacer was filled with the sample, the thickness of the liquid cell was optimized by controlling the He pressure around the cell and N or O K-edge XAS was measured. Temperature in the cell (0 – 70°C) was controlled by the circulation of a liquid heat carrier by using a thermo-chiller, and it is monitored by a thermopile. The photon energy was calibrated by the spectrum of the thin polymer film.

Figure 1 shows N and O 1s $\rightarrow \pi^*$ peaks of NO_2^- in the aqueous KNO_2 solution at various temperatures. In both the N and O K-edges (Fig. 1a, b), the shape of the observed peaks such as half width is not changed by heating from 0 to 70°C. On the other hand, the peak energy shift shows a different behavior to each other. Fig. 2 shows the temperature dependence of the observed peak top energy shift. In the N K-edge XAS, the peak top energy is almost constant, indicating that the interaction around N atoms in NO_2^- is hardly influenced by the investigated temperatures. In the O K-edge XAS, the peak top energy is constant until 40°C, but shows a sudden shift to the lower energy with increasing the temperature from 50 to 70°C.

To investigate this phenomenon in detail, we have also done two types of O K-edge XAS experiments; one is the concentration dependence at 25°C and the other is the temperature dependence by using the concentrated aqueous KNO_2 solution ($\text{KNO}_2 : \text{H}_2\text{O} = 1 : 1.7$, data not shown). In the former, the peak top energy is also shifted to the lower energy with increasing the concentration to pure solid. Since electrolytes in aqueous solution generally decrease the coordination of H_2O and form aggregated structures with increasing the concentration, the observed lower energy shift in Fig. 2b would

correspond to the similar phenomenon, i.e., the decrease of the coordination number of water around NO_2^- in the higher temperature region (50 – 70°C). In the latter, the tendency of the peak energy shift is almost the same as the Fig. 2b. Thus, the observed phenomenon in the temperature dependence of O K-edge XAS, which would arise from the decrease of the H_2O coordination, occur regardless of the formation of KNO_2 aggregate structures.

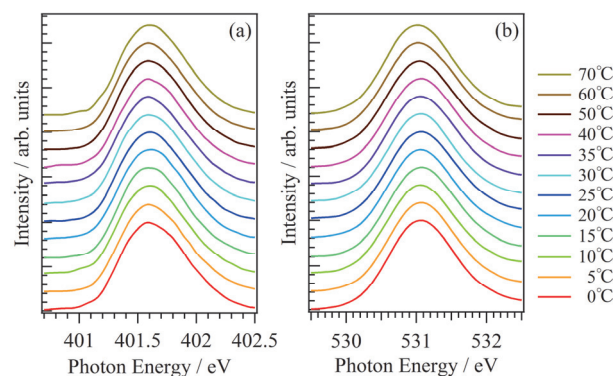


Fig. 1. (a) N K-edge ($1s \rightarrow \pi^*$) and (b) O K-edge XAS ($1s \rightarrow \pi^*$) peaks of NO_2^- in aqueous KNO_2 solution ($\text{KNO}_2 : \text{H}_2\text{O} = 1 : 42.6$) at various temperatures (0 – 70°C).

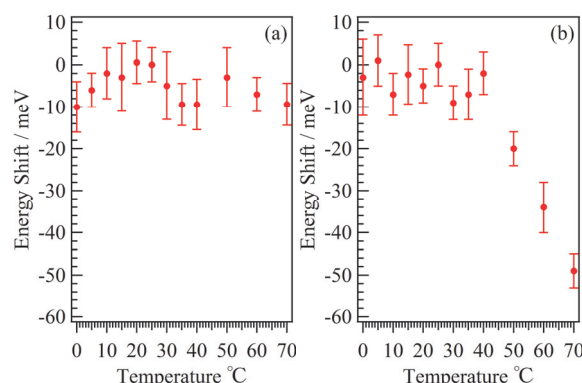


Fig. 2. Temperature dependence of the peak top energy shift in (a) N K-edge and (b) O K-edge XAS from that at 25°C.

[1] Y. Marcus, Chem. Rev. **109** (2009) 1346.

[2] M. Nagasaka *et al.*, J. Phys. Chem. B **121** (2017) 10957.

[3] M. Nagasaka *et al.*, J. Electron Spectrosc. Relat. Phenom. **224** (2018) 93.

BL4U

Characterization of Meso Porous Monolithic Polymers Containing RAFT Agent by Scanning Transmission X-Ray Microscopy (STXM)

D. Arrua¹, A. Khodabandeh¹, T. Ohgashi^{2,3}, N. Kosugi^{2,3} and E. Hilder¹

¹Future Industries Institute, University of South Australia, Building X, Mawson Lakes Campus, GPO Box 2471 Adelaide SA 5001, Australia

²UVSOR Synchrotron Facility, Institute for Molecular Science, Okazaki 444-8585, Japan

³School of Physical Sciences, The Graduate University for Advanced Studies (SOKENDAI), Okazaki 444-8585, Japan

The preparation of hierarchically mesoporous materials exhibiting two or more distinct pore size distributions has found utility in diverse applications, including catalysis and liquid separations [1]. The defining parameters of the 3D network of such system can be adjusted, however this is not a trivial method. Typically, the polymerization is initiated via thermal free radical polymerization which results in the formation of linear polymer chains followed by crosslinking and gelation steps. This mechanism is called polymerization-induced phase separation (PIPS) and the gelation step dictates the resultant morphology and allows for control of the macro- and meso-structure of a continuous piece of porous material known as “monoliths”.

The gelation step can be tuned by using different solvents in the monolith precursor, from well-known organic solvents such as methanol, ethanol and acetone to some less famous large alcohol molecules such as 1-dodecanol. For preparation of percolating macropores, polymeric solvents such as poly(ethylene glycol) with different molecular weights can be used as pore forming materials.

Introducing a RAFT agent (Reversible Addition–Fragmentation chain-Transfer agent) to the above system offered a control over the polymer mechanism as well as on the morphology of the obtained monolithic polymers [2]. Respect to the surface chemistry of the obtained well-defined 3D network, an accurate characterization is required especially when polymeric forming pore agents were utilized [3, 4].

The characterization by STXM of polymeric monolith materials was performed at the BL4U of the UVSOR synchrotron facility. STXM imaging was conducted by focusing on the C 1s core-line signal in NEXAFS. Figure 1 shows the C 1s NEXAFS spectra obtained for three monolithic polymers (A1 with no RAFT agent, A2 and A3 with different amount of RAFT agent). In all these monoliths, polyethylene glycol (PEO *M_w* ~35K) were used as part of pore forming material.

In our first assessment, the components found by STXM were the poly (Sty-co-DVB) monolith domain, and the embedding resin for three different monoliths (A1 to A3, with both 100 nm and 300 nm sections).

The spectrum for the crosslinked styrene-based scaffold has a strong peak at 284.6 eV, which is

characteristic of C 1s → π**C=C* transition in a phenyl ring. On the other hand, there is no strong peak for residue PEO which is expected to retain in the sample. Considering the size of the polymer globules (~50 nm, estimated by scanning electron microscopy (SEM)) in sample A2 and A3 as well as ~200 nm domain between globules (formed via pore forming agent), the export data via the region method could potentially hide the signal of the PEO residue (pore forming material). This study is now in progress.

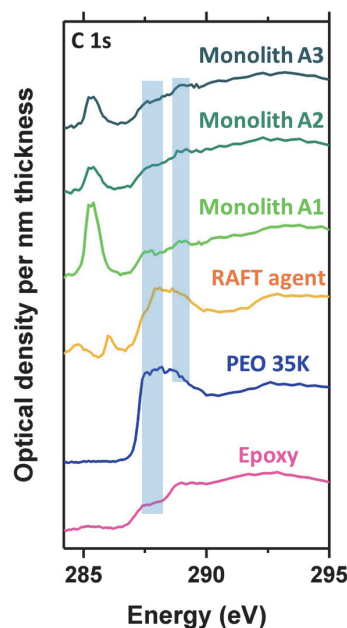


Fig. 1. NEXAFS reference spectra of the epoxy (embedding matrix), PEO *M_w* ~35K, RAFT agent and polystyrene cross-linked monoliths (A1 with no RAFT agent, A2 with RAFT agent (molar ratio between [Initiator] 1: [RAFT] 1) and A3 with RAFT agent (molar ratio between [Initiator] 1: [RAFT] 2) that correspond to 1 nm thickness of each component.

- [1] D. Wu *et al.*, Chem. Rev., **112** (2012) 3959.
- [2] K. J. Barlow *et al.*, Poly Chem, **5** (2014) 722.
- [3] D. Arrua *et al.*, UVSOR Activity Reports **42** (2014) 76.
- [4] A. Khodabandeh *et al.*, Poly Chem, **9** (2018) 213.

BL4B

Metastable CS_2^{2+} States Studied by an Electron-Electron-Ion Coincidence Method

Y. Hikosaka¹ and E. Shigemasa²¹Institute of Liberal Arts and Sciences, University of Toyama, Toyama 939-0364 Japan²UVSOR Synchrotron Facility, Institute for Molecular Science, Okazaki 444-8585 Japan

Doubly-charged positive-ions of molecules are energetically unstable due to the Coulomb repulsion between the two positive charges, and they usually undergo rapid dissociations into fragments. Mass spectroscopy has however identified since long ago the existence of metastable molecular dications having lifetimes of the order of at least microseconds. In this work, we have employed a magnetic-bottle electron spectrometer adapted to ion detection, whose description is elsewhere [1], and have performed an electron-electron-ion coincidence study for the S2p Auger decay of CS_2 , in order to identify the electronic states of the metastable dication.

The magnetic-bottle electron spectrometer is equipped with a strong permanent magnet and a long solenoid coil, and an inhomogeneous magnetic field created in the ionization region forms a magnetic mirror to collect the electrons from almost the whole 4π solid angle. An electrostatic retarder, which consists of a 1.3-m long tube and three Mo meshes (94% transmission each), is installed inside the solenoid tube [2]. For coincidence detection of the counterpart ions, a pulsed high voltage was applied to the ionization region, according to an electron-detection, and the formed ions were introduced into the same microchannel plate detector for electron detection.

A multi-electron ion coincidence measurement was made for CS_2 at a photon energy of 321.4 eV (bandwidth of ~ 150 meV), by applying a retardation of 120 V for electron observations. The top panel of Fig. 1 shows a spectrum of dication states populated after the Auger decay from the S2p core-hole states, which is derived from the energy correlations between photoelectrons and Auger electrons observed in coincidence. The energy resolution allows us to locate different electronic states of CS_2^{2+} , though the vibrational structures known for some specific CS_2^{2+} states are hardly identified. We can examine the ion species produced from these dication states, by inspecting the coincidences among the two electrons and ion(s). The two-dimensional map in Fig. 1 shows the derived correlations, and ion species formed from the individual dication states are presented. Dominant coincidence with CS_2^{2+} is observed for the low-lying dication states around 26-29 eV, and these states are metastable having lifetimes longer than microsecond order. In contrast, dication states lying above 30 eV dissociate, before arriving the detector, mainly into the fragments of S^+ and CS^+ .

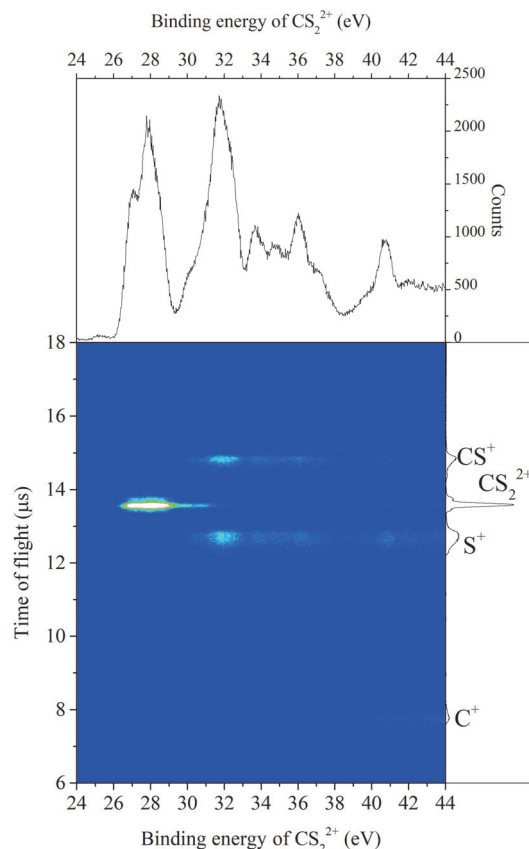


Fig. 1. Two-dimensional map showing the correlations between the CS_2 dication states and time-of-flights of ions, derived from the coincidences among two electrons and ion(s). Top panel shows a spectrum of dication states populated after the Auger decay from the S2p core-hole states. The time-of-flight spectrum of ions is displayed in the right panel.

[1] A. Matsuda *et al.*, Rev. Sci. Instrum. **82** (2011) 103105.

[2] Y. Hikosaka *et al.*, J. El. Spectrosc. Rel. Phemon. **192** (2014) 69.

BL4B

Multi-Electron-Ion Coincidence Spectroscopy: Auger Decay from Xe 4s Core-Hole State

Y. Hikosaka¹ and E. Shigemasa²¹Institute of Liberal Arts and Sciences, University of Toyama, Toyama 939-0364 Japan²UVSOR Synchrotron Facility, Institute for Molecular Science, Okazaki 444-8585 Japan

Auger decay from core-hole states in atoms often produces a variety of multiply-charged ions. Multi-electron coincidence spectroscopy, which is effectively achieved by using a magnetic bottle electron spectrometer, is a useful tool to identify the multiple Auger decay pathways, overcoming the ambiguities resulting from the overlap of Auger lines from different core holes. The benefit of this spectroscopy can be significantly increased when the multi-electrons are observed in further coincidence with ions, because different multi-ionization steps can be isolated by the observed ion charges.

In this work, we have performed multi-electron-ion coincidence spectroscopy to study the Auger decay of Xe 4s core-hole state. The multi-electron-ion coincidence spectrometer utilized in this work is based on a magnetic-bottle time-of-flight electron spectrometer with ion detection capability [1], equipped with an electrostatic retarder to improve the energy resolution in electron observations [2]. A similar multi-electron-ion coincidence setup was developed by Eland *et al.* [3].

A multi-electron ion coincidence measurement was made for Xe at a photon energy of 350 eV (bandwidth of ~90 meV). The black curve in Fig. 1 shows a total Auger electron spectrum observed in coincidence with 4s photoelectron. The formation of the $4d^{-1}5l^{-1}$ states is due to the Coster-Kronig transitions from $4s^{-1}$, and that of $4d^{-2}$ to the super-Coster-Kronig transitions. Structures below 40 eV arise largely from the overlap of the subsequent decays of these $4d^{-1}5l^{-1}$ and $4d^{-2}$ states.

The Auger electron spectra coincident with individual ions are compared in this figure. Clear differences are observed among the spectral features. This observation demonstrates that different Auger pathways are clearly isolated by the coincidence observation including ions. The spectrum coincident with Xe^{3+} ion (shown in red) displays only the structures assignable to the formation of the $4d^{-1}5l^{-1}$ states and their subsequent decays. Since the $4d^{-2}$ states proceed to sequential decays emitting additional two Auger electrons [4], and corresponding structures are isolated in the spectrum coincident with Xe^{4+} ion (blue). The spectrum coincident with Xe^{5+} ion (green), presenting the triple Auger decay of the 4s core-hole state, shows a distribution increasing gradually as decreasing the kinetic energy, where no remarkable Auger structure is seen.

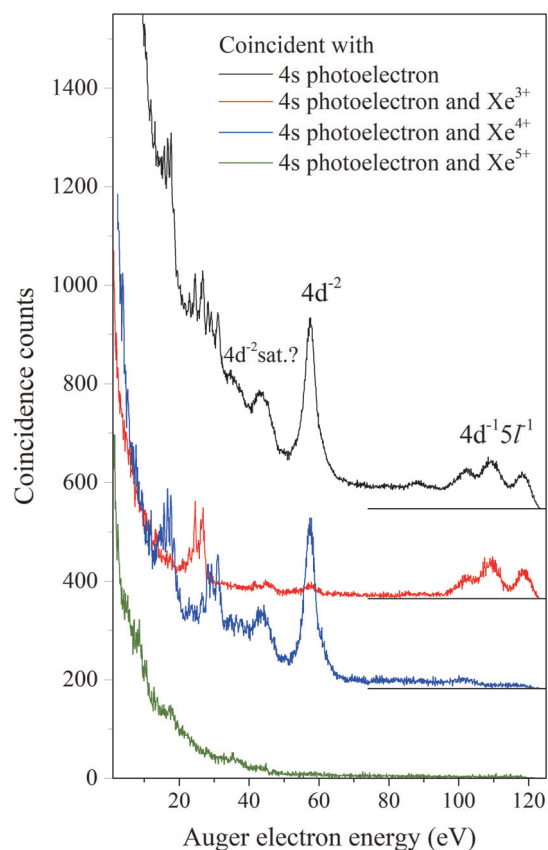


Fig. 1. Auger electron spectrum (black) observed in coincidence with 4s photoelectron, together with the spectra derived by further coincidence with ions of Xe^{3+} (red), Xe^{4+} (blue) and Xe^{5+} (green).

[1] A. Matsuda *et al.*, Rev. Sci. Instrum. **82** (2011) 103105.

[2] Y. Hikosaka *et al.*, J. El. Spectrosc. Rel. Phenom. **192** (2014) 69.

[3] J.H.D. Eland *et al.*, Chem. Phys. Lett. **548** (2012) 90.

[4] Y. Hikosaka *et al.*, Phys. Rev. Lett. **98** (2007) 183002.

BL5B

Zeeman Quantum Beat in Helium Fluorescence Decay Curve

T. Kaneyasu¹, Y. Hikosaka² and H. Iwayama^{3,4}

¹SAGA Light Source, Tosu 841-0005, Japan

²Graduate School of Medicine and Pharmaceutical Sciences, University of Toyama, Toyama 930-0194, Japan

³UVSOR Synchrotron Facility, Institute for Molecular Science, Okazaki 444-8585, Japan

⁴The Graduate University for Advanced Studies (SOKENDAI), Okazaki 444-8585, Japan

When several quantum paths connect the initial and final states of atomic transition, the quantum interference among these paths may cause quantum beat in the physical observables of the system. The quantum beat has been frequently observed in fluorescence decay following coherent excitation of the atomic and molecular system using lasers [1]. In that case, the laser pulse prepares the atomic system in a coherent superposition of the several states. This method can be applied to the atomic excitation using synchrotron radiation because it may cause coherent excitation of several levels within a bandwidth of the monochromatized light. We planned to use the quantum beat phenomena to study the magnetic sublevel population in the vortex-atom interaction [2]. As a first step of the quantum beat study, we observed the Zeeman quantum beat in helium fluorescence decay curve.

The experimental scheme is shown in Fig. 1. The experiments were performed at BL5B. The fluorescence decay curve was measured using the VUV pulse provided by the single bunch operation of the UVSOR ring. We observed the UV or visible fluorescence following the $1s \rightarrow np$ ($n=4-7$) excitation of helium atoms at the VUV wavelength region. A weak magnetic field of several tens of Gauss was applied to the interaction region. The direction of the magnetic field was parallel to the photon propagation axis. This magnetic field induced the Zeeman shift of the magnetic sublevels $M_j = \pm 1$ which caused the interference in the decay paths. Thus it was expected that the fluorescence decay curves show beat structure which oscillates at frequency 2ω according to the Zeeman shift energy of $\hbar\omega$.

Figure 2 shows the measured decay curves following the $1s \rightarrow 6p$ excitation. In accordance with the interference model described above, we found that the beat structure was superimposed on the decay curve and its oscillating frequency increased when the solenoid coil current increased. The observed beat frequency agrees well with the Zeeman shift estimated by the magnetic field measurement. Furthermore the beat structure vanished when the magnetic field was parallel to the electric field vector of the VUV pulse (not shown here). This is because the dipole-allowed magnetic sublevel is limited to $M_j=0$ in this configuration. These results strongly support the reliability of the quantum beat measurement using the synchrotron radiation.

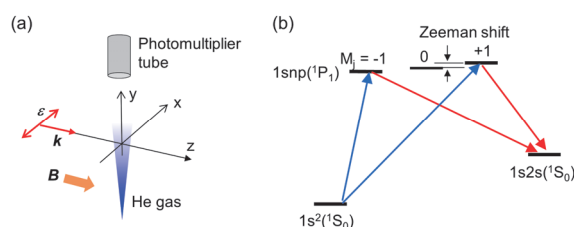


Fig. 1. (a) Experimental setup for observing the helium Zeeman quantum beat. The magnetic field was produced by solenoid coils. Helium atoms were excited by the VUV pulses of 178 ns repetition. The UV or visible fluorescence was detected by a photomultiplier tube. (b) Energy level diagram of the helium atom and excitation/decay pathways in the present study.

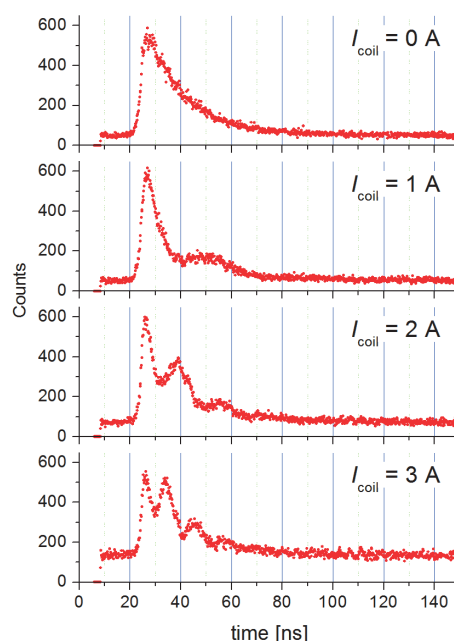


Fig. 2. Fluorescence decay curves of the $1s6p$ excited state of helium. The wavelength of the excitation pulse was set to 51.2 nm while the wavelength of the fluorescence was 345 nm.

[1] H. Bitto and J.R. Huber, *Opt. Comm.* **80** (1990) 185.

[2] A. Afanasev *et al.*, *Phys. Rev. A* **88** (2013) 033841.

BL6U

Mass Spectra of Xenon Difluoride in Coincidence with the F KVV and Xe M₄₅N₄₅N₄₅ Auger Electrons

M. Kono^{1,2,3}, F. Yamashita⁴, H. Iwayama^{5,6}, K. Okada⁴ and E. Shigemasa^{5,6}

¹School of Science and Technology, Kwansei Gakuin University, Sanda 669-1337, Japan

²Senri International School of Kwansei Gakuin, Minoh 562-0032, Japan

³RSPE, Australian National University, Canberra, ACT 2601, Australia

⁴Graduate School of Science, Hiroshima University, Higashi-Hiroshima 739-8526, Japan

⁵UVSOR Synchrotron Facility, Institute for Molecular Science, Okazaki 444-8585, Japan

⁶School of Physical Sciences, The Graduate University for Advanced Studies (SOKENDAI), Okazaki 444-8585, Japan

Xenon difluoride attracts the attention of X-ray spectroscopists because it has similar binding energies among Xe 3d_{5/2}, Xe 3d_{3/2} and F 1s subshells [1]. Southworth *et al.* [2] have recently measured the partial ion yield curves of XeF₂ and found that the charge state distribution of Xe^{q+} shifts down compared to the Xe atom case. Our previous study [3] has been concerned with the Auger spectra to get an insight into the molecular electronic states leading to the production of Xe^{q+}. The results show that at the σ* resonance the F KV₀V₀ peak is most intense, while the Xe M₅N₄₅N₄₅ transitions are dominant at the shape resonance. Here the symbol V₀ means outer-valence orbitals. By comparison of our results with the study by Southworth *et al.*, there exists a strong correlation between the Auger transitions and fragmentation channels. In order to justify this directly, here we conducted the Auger-electron-photoion coincidence (AEPICO) measurements.

The present experiments were performed on the soft X-ray beamline, BL6U, and its setup has been described elsewhere [4]. In brief, a monochromatized light beam of synchrotron radiation was irradiated at right angles to the effusive beam of the sublimated XeF₂ sample. The pressure of the main chamber was kept at 1.0 × 10⁻³ Pa during all the measurements. Auger electrons traveling through a double toroidal analyzer tube were detected with a position sensitive detector. Pass energies of the analyzer were set to 400 eV. Each electron detection triggered a pulse of electric field applied across the interaction region, extracting photoions toward a time-of-flight mass spectrometer. The coincidence data were obtained as list-mode files, containing a series of the detected electron positions and the ion-arrival time and positions. The photon energy was set at 707.3 eV in this study.

Mass spectra of the photoions coincident with particular Auger electrons can be obtained by extracting the electron kinetic-energy region of interest from the acquired data. The most abundant photoion is F⁺ for both the F KV₀V₀ and Xe M₄N₄₅N₄₅ regions, while the charge distribution of Xe^{q+} differs from each other. The Xe M₄N₄₅N₄₅ AEPICO spectrum is shown in Fig. 1. The maximum

yield of Xe^{q+} comes at the trivalent ion, which is in contrast with the atomic Xe case where the exclusive production of Xe⁴⁺ is observed [5]. Based on the proposed transition channel for the Xe⁴⁺ production following the M₄₅N₄₅N₄₅ Auger process of Xe [5], the lower-charged Xe ions are presumably formed through similar transition channels leading to the electron configurations with the holes in the 5π_u and 10σ_g orbitals. Since the latter orbital has an F 2p character, the charge(s) can be put on fluorine as well, accounting for the formation of the F⁺ and F²⁺ ions.

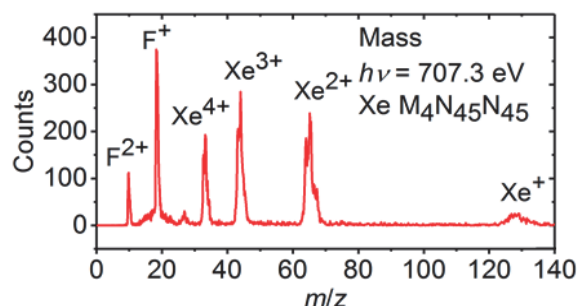


Fig. 1. The photoion mass spectrum of xenon difluoride in coincidence with the Xe M₄N₄₅N₄₅ Auger electrons. The spectral data were acquired at the photon energy of 707.3 eV.

[1] T. X. Carroll, R. W. Shaw Jr., T. D. Thomas, C. Kindle and N. Bartlett, *J. Am. Chem. Soc.* **96** (1974) 1989.

[2] S. H. Southworth, R. Wehlitz, A. Picón, C. S. Lehmann, L. Cheng and J. F. Stanton, *J. Chem. Phys.* **142** (2015) 224302.

[3] F. Yamashita, M. Kono, H. Iwayama, K. Okada and E. Shigemasa, *UVSOR Activity Report* **44** (2017) 111.

[4] R. Tateishi, T. Kaneda, H. Iwayama, M. Kono, K. Okada and E. Shigemasa, *UVSOR Activity Report* **43** (2016) 104.

[5] Y. Tamenori, K. Okada, S. Nagaoka, T. Ibuki, S. Tanimoto, Y. Shimizu, A. Fujii, Y. Haga, H. Yoshida, H. Ohashi and I. H. Suzuki, *J. Phys. B: At. Mol. Opt. Phys.* **35** (2002) 2799.

BL6U

Site-specific Production of H_3^+ by Core Ionization of CH_3Cl

H. Fujise^{1,2}, H. Iwayama^{1,2} and E. Shigemasa^{1,2}

¹UVSOR Synchrotron Facility, Institute for Molecular Science, Okazaki 444-8585, Japan

²School of Physical Sciences, The Graduate University for Advanced Studies (SOKENDAI), Okazaki 444-8585, Japan

The trihydrogen cation, H_3^+ , is an interesting molecule which plays a key role in reactions that lead to complex molecules characterizing interstellar clouds [1]. H_3^+ can be produced from fragmentation reactions of several hydrocarbon molecules using intense laser fields [1], soft X-rays [2], and electron impact [3]. Previous results, irradiating soft X-rays to chloromethane, CH_3Cl , suggested that H_3^+ was preferentially produced and related to the site-specific Auger final states obtained after the core ionization of the Cl 2p electron [4]. However, the detailed production mechanism is still unknown. In this study, we investigate the site-specific production mechanism of H_3^+ , and its responsible ionic state of $\text{CH}_3\text{Cl}^{2+}$, by core ionization with soft X-rays and Auger-electron-ion coincidence measurements, as well as comparing the results with deuterated chloromethane, CD_3Cl .

Experiments were performed on the soft X-ray BL6U. Radiation from the undulator was monochromatized and focused onto the interaction region of an Auger-electron-ion coincidence spectrometer. The target gas was introduced into the interaction region by effusion from a capillary tube: produced Auger-electrons were energy-analyzed by the double toroidal analyzer (DTA). Ions in the interaction region were extracted towards the ion momentum spectrometer by an applied pulsed electric field, according to each electron detection. The electron pass energy of the DTA was set to 200 eV, and the corresponding energy resolution was ~ 1.9 eV. The photon energy used for Cl 2p core ionization was 220 eV.

Figure 1(a) shows the total Auger spectrum and coincidence Auger spectrum after the Cl 2p core ionization of CH_3Cl . The coincidence spectrum is extracted from the total Auger spectrum, using the time-of-flight information of H_3^+ . The vertical lines above the experimental data are the theoretically calculated Auger final states, along with their valence electron configuration, which are listed on the right. The coincidence Auger spectrum has a single peak at ~ 31 eV, which is hardly observed in the case of the C 1s core ionization [4]. This indicates that the H_3^+ formation process occurs site-specifically through the Cl 2p core ionization, with a relation with the $3e^-$ Auger final states. To give further insight into the molecular dynamics of the dissociation mechanism of H_3^+ , a comparison experiment was conducted, using deuterated chloromethane, CD_3Cl . Figure 1(b) shows

the total Auger and coincidence Auger spectra after the Cl 2p core ionization of CD_3Cl . The coincidence Auger spectrum in Fig. 1(b) has a similar spectral profile compared to the CH_3Cl case in Fig. 1(a), where the only difference seen is the lower coincidence detection rate of the D_3^+ fragment ions. The similar spectral profile strongly suggests the same $3e^-$ Auger final states involved in the dissociation mechanism. Furthermore, because the deuterium atom is twice as heavy than the hydrogen atom, molecular motion around the deuterium atom is repressed. The lower abundance of D_3^+ implies that molecular deformation due to vibrational motion around the C-D bond is suppressed, which resulted in decreasing the abundance of D_3^+ .

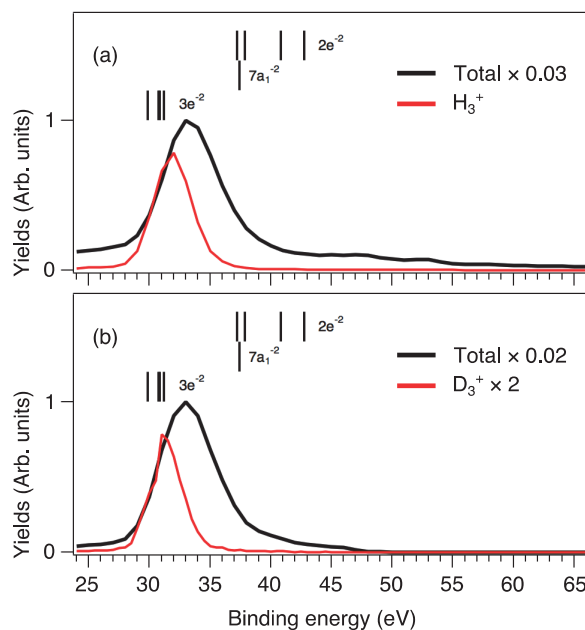


Fig. 1. Total Auger spectra (black) and coincidence Auger spectra (red) following Cl 2p core ionization from (a) CH_3Cl and (b) CD_3Cl .

- [1] J. H. D. Eland, *Rapid Commun. Mass Spectrom.* **10** (1996) 1560
 [2] S. Pilling *et al.*, *Mon. Not. R. Astron. Soc.* **375** (2007) 1488.
 [3] K. Hoshina *et al.*, *J. Chem. Phys.* **129** (2008) 104302.
 [4] H. Iwayama and E. Shigemasa, *UVSOR Activity Report 2015* **43** (2016) 107.

BL6U

Intermolecular Coulombic Decay of Core Excited Nitrogen Molecular Clusters

H. Iwayama^{1,2}¹UVSOR Synchrotron Facility, Institute for Molecular Science, Okazaki 444-8585, Japan²School of Physical Sciences, The Graduate University for Advanced Studies (SOKENDAI), Okazaki 444-8585, Japan

Intermolecular Coulombic decay is an efficient electronic relaxation of excited molecules placed in a loosely bound chemical system (such as a hydrogen bonded or van-der-Waals-bounded cluster). This decay process ionize neighboring molecules to excited one and eject low-energy electrons, which play an important role in DNA damage induced ionizing radiation. Recently, it was proposed that emission site and energy of the electron released during this process can be controlled by coupling the ICD to a resonant core excitation [1]. These properties may have consequences for fundamental and applied radiation biology. In this work, we investigated ICD process of core excited nitrogen molecule clusters by using Auger-electron ion coincidence technique. Since ICD process lower the double ionization threshold, we measured binding energy of Auger states corresponding to double ionizations. Compared to isolated nitrogen molecules, we observed lowering of double ionization threshold for nitrogen molecular clusters.

The Auger-electron-ion coincidence measurements were performed on the undulator BL6U at UVSOR. The Auger electrons and product ions were measured in coincidence by a double toroidal electron analyzer (DTA) and an ion momentum spectrometer, respectively. The pass energy of DTA was set to 400 eV. All signals from the ion and electron delay-line detectors were recorded with an 8ch TDC board. The photon energy was tuned to 401.1 eV, which corresponds to the resonance energy of the N 1s $\rightarrow\pi^*$ excitation for isolated and clustered nitrogen[1]. Nitrogen clusters were produced by supersonic expansion through a 100- μm nozzle at 220K. The stagnation pressure is 8 bar. The average cluster size was estimated to be ~ 10 molecules per cluster.

Figure 1 shows time-of-flight mass spectra for (a) molecular nitrogen and (b) clustered nitrogen. For molecular nitrogen, we observed parent molecular ions of N_2^+ and fragment ions of N^+ . For clustered nitrogen, we observed cluster fragment ions of $(\text{N}_2)_n^+$ ($n \geq 2$) and $(\text{N}_2)_n\text{N}^+$ ($n \geq 1$) in addition to N_2^+ and N^+ ions.

To investigate double ionization thresholds, we explore the events where we detected two fragment ions in coincidence with an Auger electron. Figure 2 shows Auger spectra in coincidence with two fragment ions for (a) isolated and (b) clustered nitrogen. The binding energy distribution of Auger states resulting in double ionizations for nitrogen

molecular clusters are significantly lower than isolated nitrogen molecules. The enhancement around binding energy of 45 eV corresponds to the ICD process of core excited nitrogen molecular clusters. Analysis in more detail is in progress.

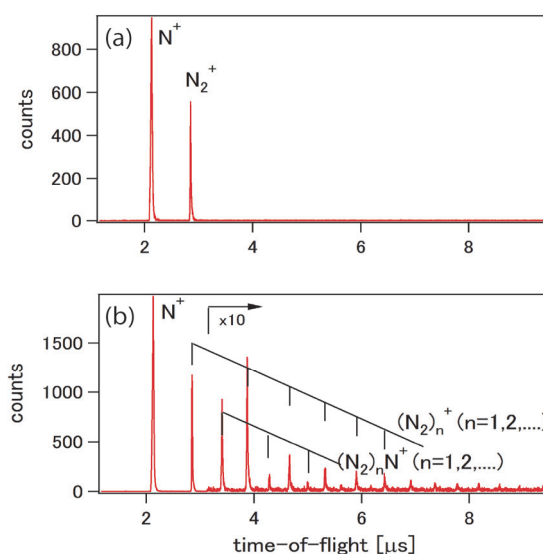


Fig. 1. Time-of-flight mass spectra for (a) N_2 molecules and (b) clusters.

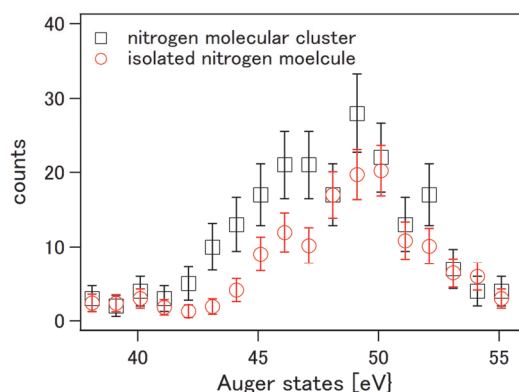


Fig. 2. Coincidence Auger spectra with two fragment ions for nitrogen molecules and clusters.

[1] K. Gokhberg, *et al.*, Nature **505** (2014) 661.

[2] R. Flesch, *et al.*, Phys. Rev. Lett. **86** (2001) 3767.

BL6B

Microfluidics of Liquid Mixtures for Infrared Microscopy

M. Nagasaka^{1,2}, A. A. Vu^{1,3}, H. Yuzawa¹, N. Takada¹, M. Aoyama¹, E. Rühl³ and N. Kosugi^{1,2}

¹Institute for Molecular Science, Okazaki 444-8585, Japan

²SOKENDAI (The Graduate University for Advanced Studies), Okazaki 444-8585, Japan

³Physikalische Chemie, Freie Universität Berlin, Takustr. 3, D-14195 Berlin, Germany

Microfluidics is a chemical technique to realize highly efficient chemical reactions in the liquid phase [1]. Recently, X-ray diffraction in the hard X-ray regime has been used for a variety of systems by using microfluidics [2]. Previously, we applied infrared (IR) microscopy to characterize microfluidic flows [3], but the microfluidic channel was not completely sealed at that time. Recently, we have improved the microfluidic cell for soft X-ray absorption spectroscopy and successfully observed a laminar flow in the mixed part of the microfluidic system [4]. In this study, we have used it for IR microscopy.

The experiments were performed by using the IR microscopy setup IRT-7000 at BL6B. A T-shape microfluidics setup with the width of 50 μm is made from PDMS resin which is covered by a 100 nm Si_3N_4 membrane. The spatial resolution of $30 \times 30 \mu\text{m}^2$ is reached by using a $\times 16$ Cassegrain mirror. IR spectra are taken by detecting the reflected infrared light by an MCT detector.

Figure 1 shows IR spectra of pyridine and water taken from the mixed part of the microfluidic cell, at positions shown in Fig. 2. The IR spectra correspond to the OH stretching vibration of water around 3392 cm^{-1} and the CH stretching vibration of the pyridine ring around 2936 cm^{-1} , respectively. The absorbance of water and pyridine at different positions is obtained from the fitting results of the IR spectra to both the vibrational peaks.

Figure 2(a) shows the 2D image of the absorbance of water. Pyridine (*P*) flows from the upper side, and water (*W*) from the lower side. The water-pyridine mixture (*M*) flows to the right-hand part after the junction of the liquids. In the mixed part of the microfluidic flow, the absorbance of water shows high intensity at $Y = 120 \mu\text{m}$. On the other hand, Figure 2(b) shows the 2D image of the absorbance of pyridine, which shows high intensities at $Y = 150 \mu\text{m}$. These results suggest that the mixed part of the microfluidic flow is evidently laminar between $Y = 120$ and $150 \mu\text{m}$. IR microscopy enables us to observe both chemical compounds separately by selecting their respective vibrational modes.

[1] T. Kitamori *et al.*, *Anal. Chem.* **76** (2004) 53.

[2] B. Weinhausen and S. Köster, *Lab Chip* **13** (2013) 212.

[3] M. Nagasaka *et al.*, *UVSOR Activity Report* **2016** (2017) 116.

[4] M. Nagasaka *et al.*, in this volume.

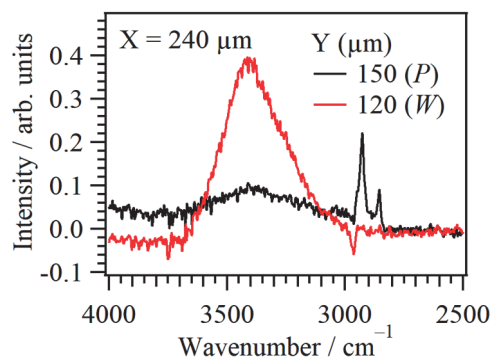


Fig. 1. IR spectroscopy of pyridine (*P*) and water (*W*) in the mixed part of the T-shape microfluidic cell, at positions shown in Fig. 2.

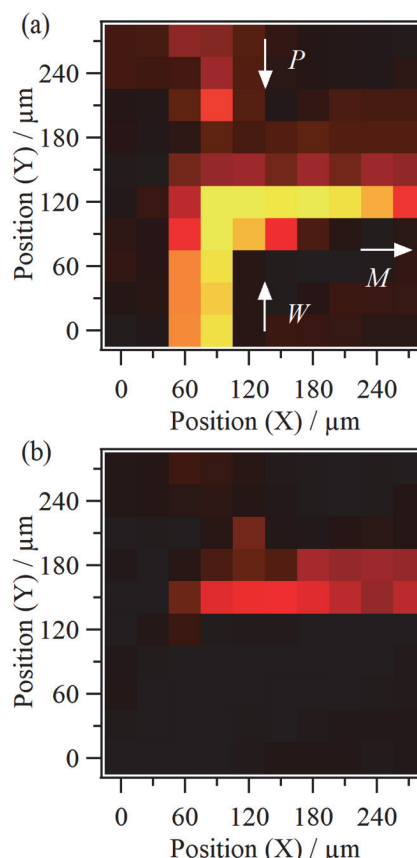
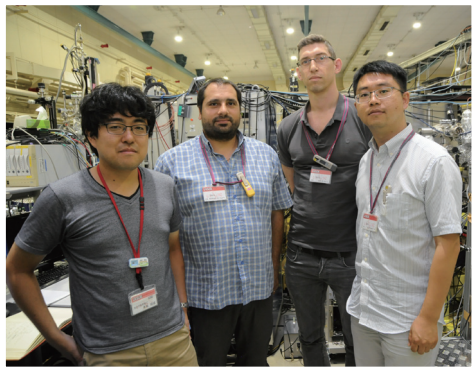
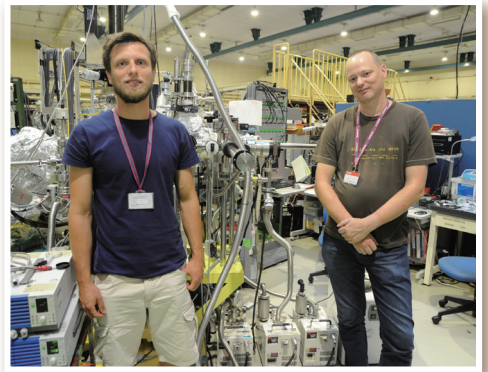
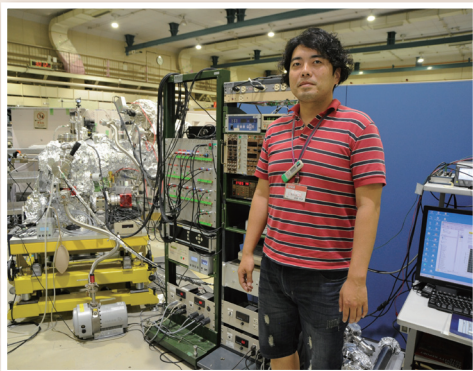
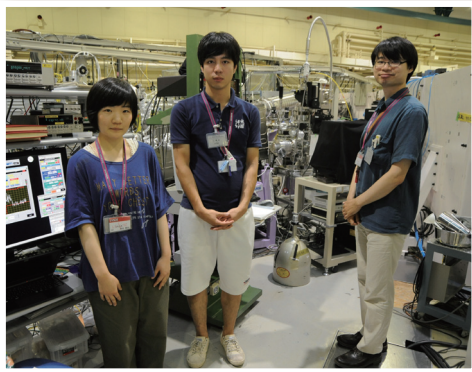
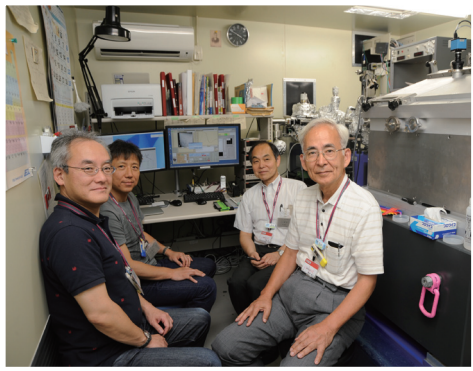
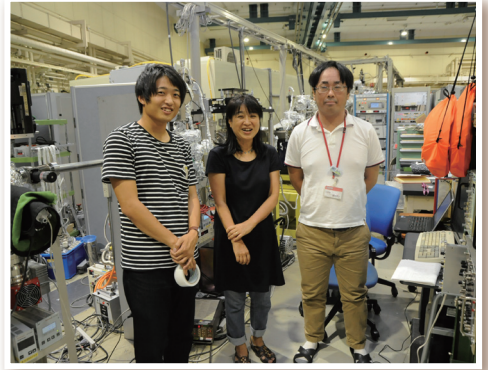
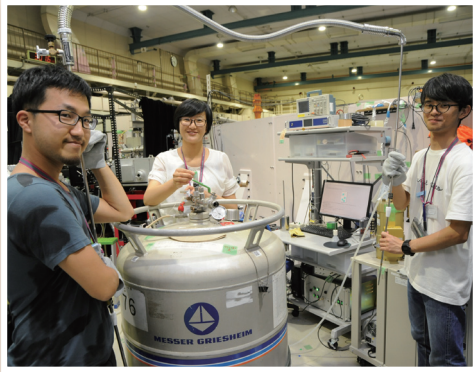
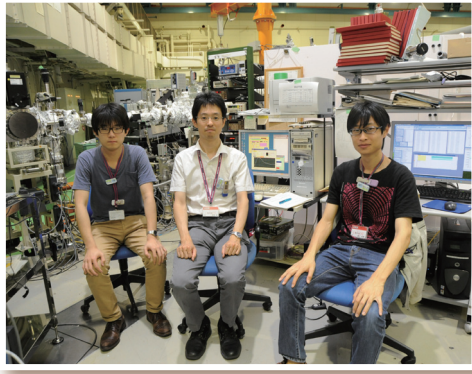
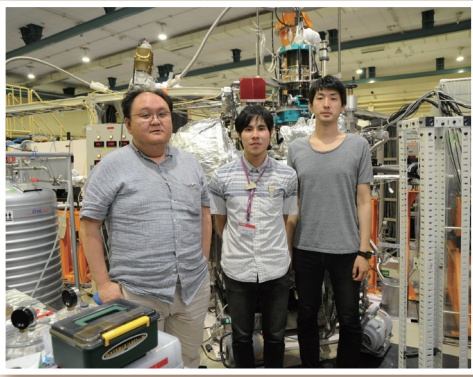


Fig. 2. The 2D images of the absorbance of (a) water and (b) pyridine in the T-shape microfluidic cell obtained from IR spectra at different positions.

UVSOR User 4



III-4

Surface,
Interface and
Thin Films

BL6U

Anomalous Interfacial Interaction at Polycyclic Aromatic Hydrocarbon Monolayers on Graphene Layer

H. Yamane and N. Kosugi

Institute for Molecular Science, Okazaki 444-8585, Japan

Two-dimensional sp^2 carbon layer, graphene, has a honeycomb network, which induces unique low-dimensional electronic properties such as an in-plane high carrier mobility (ca. 15,000 cm^2/Vs at 300 K). The ABAB-stacking graphene multilayer shows the electronic structure of the single-crystalline graphite. As the graphene sheet can be obtained simply by multiple peeling of graphite with the sticky tape, the interlayer (out-of-plane) interaction in graphite is dominated by the weak π - π interaction. Therefore, organic/graphite interfaces have been regarded as an archetypal model system for electronic and structural studies of physisorbed organic molecules. On the other hand, hexa-*peri*-hexabenzocoronene [HBC, see inset of Fig. 1(b)] is a molecular unit graphene. In the present work, we have succeeded to observe the anomalous interfacial interaction in the HBC monolayers on graphene and graphite by angle-resolved photoemission spectroscopy (ARPES).

The present experiment was performed at BL6U. The photon energy ($h\nu$) for ARPES was 50 eV, which can probe $k_z = na_z^*$ for graphite. The single layer graphene (SLG) and the single crystalline graphite (SCG) were grown on a 6H-SiC(0001) substrate by annealing at 1150°C under the Si flux and 1600°C, respectively [1]. The surface crystallinity of SLG and SCG was characterized using low-energy electron diffraction (LEED) and ARPES.

Figure 1 shows the LEED image and ARPES (E - k_{\parallel}) map around the K point in the Γ -K direction for (a) HBC/SLG and (b) HBC/SCG at 20 K. The LEED images indicate the $p(\sqrt{31}\times\sqrt{31})R9.0$ ordered structure for both interfaces. The E - k_{\parallel} map shows a well-known π -band dispersion of graphene and graphite (π_{Gr}) around the K point. The highest occupied molecular orbital (HOMO)-derived peak of HBC appears at different binding energy (E_b) position depending on the substrate; $E_b = 2.1$ eV for HBC/SLG and $E_b = 1.8$ eV for HBC/SCG. The charge transfer from SiC through the graphene layer might exist at HBC/SLG.

It is of note that the HOMO-derived peak shows a dispersion for both interfaces, which does not depend on the graphene layer thickness. As shown in Fig.2(a), the HOMO-derived peak at HBC/SCG disperses to the lower- E_b side with increasing k_{\parallel} from 1.56 \AA^{-1} to 1.86 \AA^{-1} . The total dispersion width is 105 meV. Furthermore, the HOMO-derived peak involves the vibrational satellites at the higher- E_b side, which also show the dispersive behavior with respect to the 0-0 transition peak, as shown in Fig. 2(b). The observed evidence suggests that the upper (bottom) HOMO band with the anti-bonding (bonding) character around

$k_{\parallel} = 1.82$ \AA^{-1} (1.58 \AA^{-1}) can effectively couple with high (low) frequency phonons.

Since such dispersive behaviors for HOMO and its vibrational satellites are not observable for iron-phthalocyanine/SLG [2] and HBC/Au(111) [3], the molecule-substrate interfacial π - π coupling can play a crucial role in the MO delocalization.

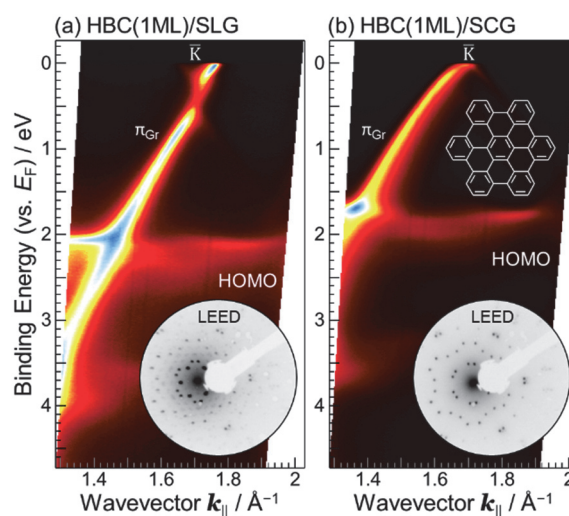


Fig. 1. LEED image and ARPES (E - k_{\parallel}) map around the K point in the Γ -K direction for (a) HBC/SLG and (b) HBC/SCG, measured at $h\nu = 50$ eV and $T = 20$ K.

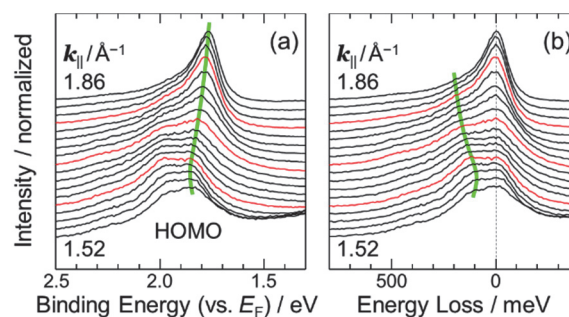


Fig. 2. Energy distribution curves for the HOMO region at HBC/SCG with the k_{\parallel} step of 0.02 \AA^{-1} , wherein the energy scale is measured from (a) the Fermi level and (b) the 0-0 transition peak.

[1] I. Forbeaux, J.-M. Themlin and J.-M. Debever, Phys. Rev. B **58** (1998) 16396.

[2] M. Scardamaglia *et al.*, J. Phys. Chem. C **117** (2013) 3019.

[3] H. Yamane and N. Kosugi, to be published.

BL2B

ARUPS of DNTT on a-TES Film Prepared on Copper Oxide

K. K. Okudaira and S. Nomoto

Graduate School of Science and Engineering, Chiba University, Chiba 263-8522, Japan

An organic thin-film transistor (OTFT) is likely to have suitable applications requiring large-area coverage, structural flexibility and low-cost. However, there are still many issues such as low mobility to be addressed for practical organic electronics. To achieve high mobility it is important to improve the charge injection efficiency at the interface between the metal electrode and the organic semiconductor layer and charge transfer probability. Self-assembled monolayers (SAMs) has been introduced on metal electrode in order to modify the work function of the metal [1].

A triazine-based molecular adhesion agent (a-TES : 6-triethoxysilyl propylamino-1,3,5- triazine- 2,4-dithiol (TES)) was used for preparing thin film like self- assembly monolayers on metal surface as well as SiO₂ insulator layer.

In this work we used a-TES modified copper oxide substrate and examined the molecular orientation of dinaphtho[2,3-b:2',3'-f]thieno[3,2-b]thiophene (DNTT) thin films thermally deposited on the surface by angle- resolved ultraviolet photoelectron spectroscopy (ARUPS) measurements. To obtain the quantitative analysis on the molecular orientation; we compare observed take-off angle dependence of π band and calculated ones by the independent-atomic-center (IAC)/ MO approximation [2].

ARUPS measurements were performed at the BL2B of the UVSOR. The take-off angle (θ) dependencies of photoelectron spectra were measured with the photon energy ($h\nu$) of 28 eV. We use a-TES modified copper oxide (CuO) and CuO as substrate. Copper substrate was subjected to ultrasonic cleaning for 10 minutes in acetone, isopropanol, and then ozone cleaning for 30 minutes. a-TES modified CuO substrate was obtained by dipped in 0.1% solution at 20 °C for 30 minutes. DNTT was deposited on 1.5 nm on both substrates.

We observed take-off angle (θ) dependence of HOMO peak in UPS of DNTT deposited on CuO and a-TES/(CuO) and (thickness of 1.5 nm).

The HOMO peaks of DNTT on CuO and on a-TES/C appear at binding energy of about 1.2 eV and 1.5eV, respectively. The HOMO peaks of DNTT both on SiO₂ and on a-TES/SiO₂ show intense peaks at higher take- off angle ($\theta = 60^\circ$), and at lower θ these intensities become small. For DNTT/CuO, HOMO intensity at $\theta = 38^\circ$ (about 40°) is almost same as that at $\theta = 60^\circ$. On the other hand, for DNTT/a-TES/CuO, HOMO intensity at $\theta = 40^\circ$ is smaller than that at $\theta = 60^\circ$. Due to the difference of θ dependence of HOMO peak of DNTT on CuO and on a-TES/CuO, it is found that the molecular orientation of DNTT on CuO is different from that on a-TES/CuO. The difference of

surface energy of a-TES and CuO indicates that the surface modification by a-TES affects the molecular orientation of organic semiconductor layer, which would have an effect on the characteristics of OTFT such as mobility.

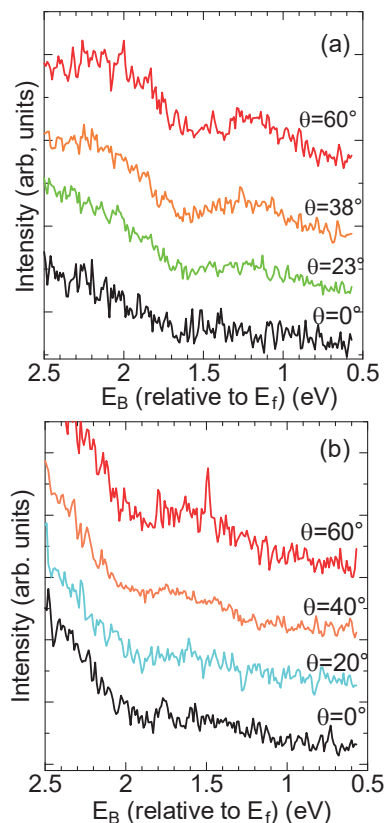


Fig. 1. ARUPS of DNTT(1.5nm)/CuO (a) and DNTT(1.5nm)/a-TES/CuO (b).

- [1] F. Wang *et al.*, *Nanoscale Res. Lett.* **6** (2011) 483.
 J. -P. Hong *et al.*, *Appl. Phys. Lett.* **92** (2008) 143311.
 [2] N. Ueno *et al.*, *J. Chem. Phys.* **99** (1993) 7169.

BL2B

Phase Stability of Quasi-1 Dimensional Columnar Structure of Tin-phthalocyanine Films

Y. Kashimoto¹, H. Ichikawa¹ and H. Yoshida^{1,2}

¹ Graduate School of Engineering, Chiba University, Chiba 263-8522, Japan

² Molecular Chirality Research Center, Chiba University, Chiba 263-8522, Japan

In organic semiconductors, the carrier transport occurs through the overlap of molecular orbitals. The intermolecular orbital interaction results in the split of energy levels. For the highest occupied molecular orbital (HOMO), the split of lead phthalocyanine (PbPc) dimer has been observed by ultraviolet photoelectron spectroscopy (UPS) [1]. Similar splitting can be observed for lowest unoccupied molecular orbital (LUMO) using low-energy inverse photoelectron spectroscopy (LEIPS) [2].

Recently, we demonstrated that tin-phthalocyanine (SnPc) film grows layer by layer into a quasi-1D columnar structure on graphite. From the low energy electron diffraction and UV-visible absorption measurements, we concluded that the structure is similar to the monoclinic phase of PbPc crystal [3]. We applied UPS and LEIPS to the SnPc films with the thickness between 2 and 5 monolayers (MLs). The observed characteristic broadening of peaks were interpreted as the energy level splits due to the intermolecular electronic coupling [4]. The initial aim of this study was to observe an energy-momentum dispersion relation of splitted HOMO peaks of SnPc bilayer using energy-dependent UPS. In the momentum space, the intensities of the two components are expected to vary [5] which should be decisive evidence of our interpretation.

In the experiment, a highly oriented pyrolytic graphite (HOPG) was cleaved in air and annealed at 873 K for 2 hours in vacuum. The 2 ML thick SnPc film was prepared by the vacuum deposition onto the HOPG at room temperature (300 K) for the UPS study.

Figure 1 shows energy-dependent UPS spectra. We observed a peak at 1.5 eV and a shoulder at 1.3 eV at the photon energy $h\nu$ of 40 eV at 25 min after the film preparation. The line shape is similar to our previous UPS results [4] suggesting that the spectral features originate from the split of SnPc dimer interaction. Subsequently, we measured the spectra at different photon energies, $h\nu = 105, 85$ and 70 eV. The line shapes became a single broad peak without shoulder. Finally, we measured again the spectrum at $h\nu=40$ eV 205 min after the sample preparation. The observed spectrum is completely different from the previous one as shown in Fig. 1.

The SnPc film shows polymorphs. When SnPc is deposited at the room temperature, the 1D columnar structure is observed. However, a different film having a head-to-tail molecular arrangement is observed when the film is prepared on a substrate at elevated

temperature or the film is annealed after the deposition [4]. This indicates that the 1D columnar structure is a metastable and transformed to the more stable head-to-tail arrangement. The relation of the two phases is similar to the monoclinic [3] and triclinic [6] phases of PbPc.

The observed difference in the spectral line shapes in this work is most likely due to the phase transition of Sn bilayer though the reason is not clear at the moment. Our previous UPS measurement was made at 290 K which is 10 K lower than the temperature of the present work at BL2B. This subtle difference may cause the phase transition. Also the contamination on the HOPG surface may affect the stability of the 1D-columnar phase.

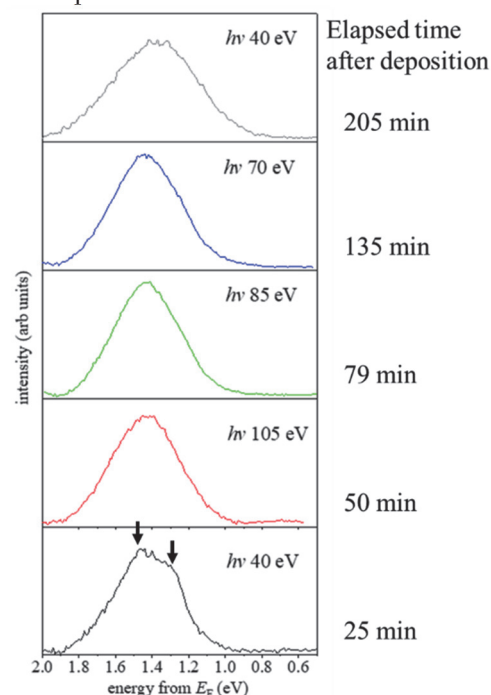


Fig. 1. Energy-dependent UPS spectra of 2 ML SnPc film on HOPG. Spectral features changed by elapsed time after deposition.

- [1] S. Kera *et al.*, Phys. Rev. B **75** (2007) 121305.
- [2] H. Yoshida, Chem. Phys. Lett. **539–540** (2012) 180.
- [3] Ukei, Acta Cryst. B **29** (1973) 2292.
- [4] Y. Kashimoto *et al.*, (submitted).
- [5] Moser, J. Electron Spectrosc. Relat. Phenom. **214** (2017) 29.
- [6] Iyechika *et al.*, Acta Cryst. B **38** (1982) 766.

BL2B

Internal Electric Potential Distributions in Metallo-phthalocyanine Thin Films: Magnesium Phthalocyanine and Aluminum Phthalocyanine Chloride

Y. Nakayama

Department of Pure and Applied Chemistry, Tokyo University of Science, Noda 278-8510, Japan

Phthalocyanines have been used as hole transporting materials in various prototypical organic semiconductor devices such as organic solar cells [1]. A striking point of metallo-phthalocyanines is the tunability of their electronic properties, e.g., energy gap width (color), molecular shape, and permanent dipole moment, by switching the metal species at the center of the ligand ring. In the present work, we conducted photoelectron spectroscopy (PES) measurements on thin films of two kinds of metallo-phthalocyanine molecules (Fig. 1), magnesium phthalocyanine (MgPc) and aluminum phthalocyanine chloride (AlClPc), to study electronic states of these materials.

MgPc and AlClPc thin film were deposited in a step-by-step manner under ultra-high vacuum (base pressure below 2×10^{-7} Pa) conditions onto Au-coated Si substrates. It should be noted that the Au/Si substrates had been prepared in a separate system and transferred in the ambient atmosphere, so that the surface of these was not clean but contained some contaminants. PES measurements were conducted at BL2B of UVSOR, IMS. The excitation photon energy was fixed at 120 eV throughout this work. In order to avoid any unfavorable shift or broadening of the spectra due to sample charging or radiation damage, measurement duration of each spectrum was minimized and also the photon flux was reduced to restrict the photoemission current not to exceed 100 pA. All the measurement were carried out in the normal emission geometry and at room temperature.

As shown in Fig. 2, the vacuum level and Mg2p states shifted to the lower energy side in increasing the MgPc thickness suggesting a downward band bending in the MgPc film toward the surface. The similar trend was previously reported for CuPc [2, 3]. In contrast, AlClPc exhibited substantially no (or slightly upward [4]) band bending in its thin film. As a result of this existence/absence of the band bending, the hole transporting state of MgPc shifted closer to the Fermi level as approaching the substrate (Fig. 3(a)), which is advantageous for extraction of holes to the Au electrode, whereas that of AlClPc are almost constant regardless of the film thickness (Fig. 3(b)).

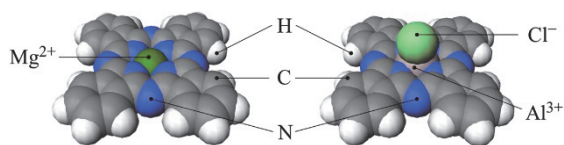


Fig. 1. Structures of MgPc (left) and AlClPc (right).

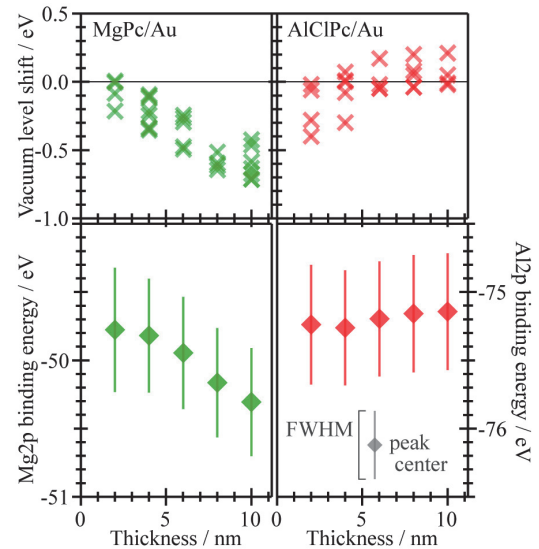


Fig. 2. Vacuum level shifts (upper panels) and core level peak positions (lower panels) of MgPc (left panels) and AlClPc (right panels) thin films on Au substrates plotted as a function of the film thickness.

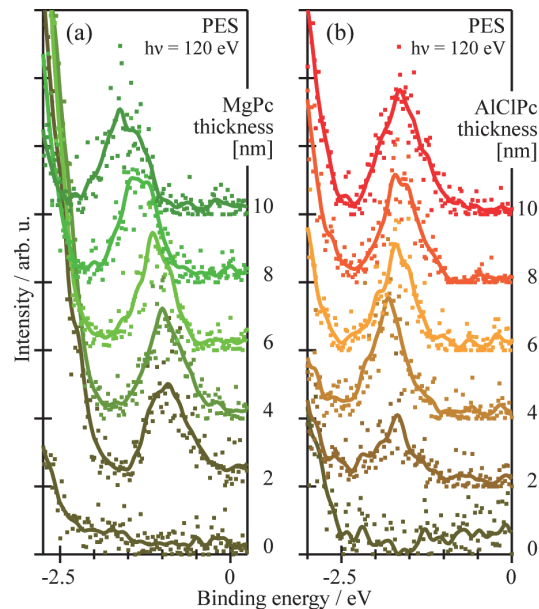


Fig. 3. Evolution of the PES spectra of the (a) MgPc and (b) AlClPc thin films.

- [1] C. W. Tang, *Appl. Phys. Lett.* **48** (1986) 183.
- [2] H. Yamane *et al.*, *J. Appl. Phys.* **99** (2006) 093705.
- [3] Y. Nakayama *et al.*, *Adv. Energy Mater.* **4** (2014) 1301354.
- [4] M.-K. Lin *et al.*, *Phys. Rev. B* **95** (2017) 085425.

BL2B

Effects of Water Exposure on Materials for Organic Light Emitting Diodes

Y. Nakayama, F. Minagawa and M. Hikasa

Department of Pure and Applied Chemistry, Tokyo University of Science, Noda 278-8510, Japan

Deterioration of organic semiconductor materials is a common drawback for organic electronic devices. Humidity is widely believed as a major factor that degrades functionalities of the materials, yet accurate mechanisms how water molecules impact the electronic states of the organic semiconductor materials are still not well understood. In the present works, effects of exposure to H₂O on representative organic materials for light emitting diodes (Fig. 1), 2,2',7,7'-tetrakis(*N,N*-di-*p*-methoxyphenylamino)-9,9'-spirobifluorene (spiro-OMeTAD) as a hole transporter [1], tris(8-hydroxyquinolino)aluminium (Alq₃) as an electron transporter and emitter [2], and dipyrazino[2,3-*f*:2',3'-*h*]quinoxaline-2,3,6,7,10,11-hexacarbonitrile (HATCN) as a hole injector [3], are studied by photoelectron spectroscopy (PES).

10 nm-thick spiro-OMeTAD, Alq₃, and HATCN were deposited onto Au/Si substrate in ultra-high vacuum conditions. Each sample was subsequently exposed to H₂O up to the dosage of 10⁸ L (1 L = 1 × 10⁻⁶ Torr·s) in a step-by-step manner. PES measurements were conducted at BL2B of UVSOR.

Figure 2 shows variation in the work function values of these three materials plotted as a function of dosage of H₂O. It was revealed that spiro-OMeTAD exhibits reduction of the work function by exposure to H₂O, whereas the work function of the Alq₃ thin film was preserved at the pristine value even after a 10⁸ L dosage of H₂O. For the HATCN case, the work function exhibited irregular jumps, which may be ascribed to position by position inhomogeneity of the HATCN film. However, the similar trend to the case of spiro-OMeTAD can be recognized, which supports reduction of the work function of HATCN due to exposure to the ambient atmosphere.

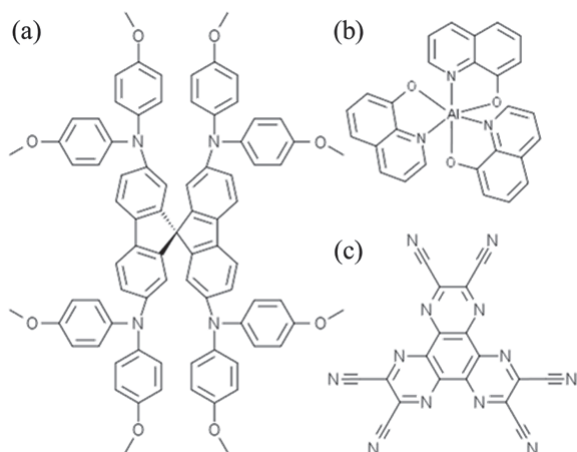


Fig. 1. Molecular structures of (a) spiro-OMeTAD, (b) Alq₃, and (c) HATCN.

PES spectra in the highest occupied molecular orbital (HOMO) regions of the spiro-OMeTAD and Alq₃ films evolved upon exposure to H₂O as shown in Fig. 3, in which each spectrum is plotted with respect to the vacuum level. The HOMO positions in these spectra are substantially maintained independent of the H₂O dosage, namely the water vapor in this dosage range does not rise any significant effects to the ionization energies of spiro-OMeTAD and Alq₃. The Fermi level (E_F) separated away from the HOMO of spiro-OMeTAD in increasing the dosage of H₂O, which may result in a disadvantage for the efficiency for hole injection into this material from electrodes.

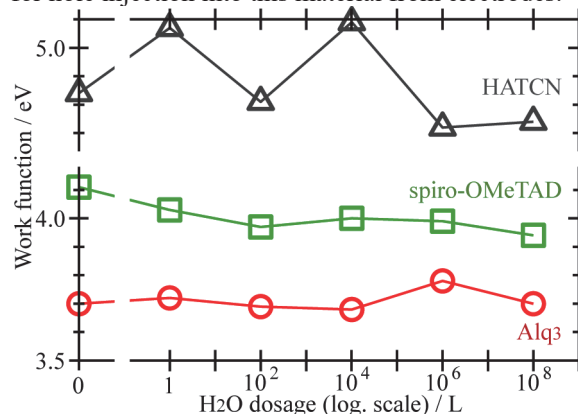


Fig. 2. Work function variation on exposure to H₂O.

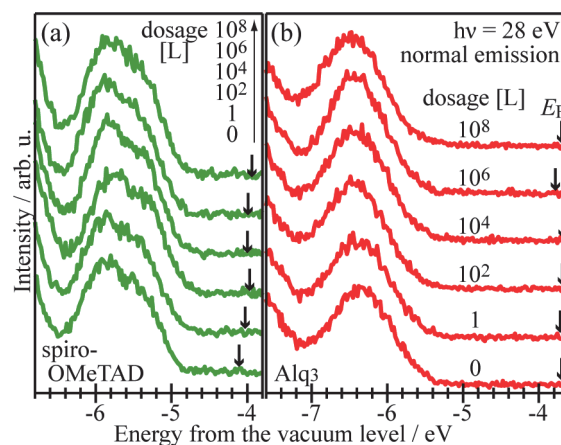


Fig. 3. Evolution of the PES spectra of 10 nm-thick (a) spiro-OMeTAD and (b) Alq₃ thin films upon exposure to H₂O. The E_F positions are indicated by downward arrows on the respective spectra.

[1] O. A. Jaramillo-Quintero *et al.*, *J. Phys. Chem. Lett.* **6** (2015) 1883.

[2] C. W. Tang *et al.*, *Appl. Phys. Lett.* **51** (1987) 913.

[3] S. Park *et al.*, *Appl. Phys. Lett.* **97** (2010) 063308.

BL3U

Cobalt Oxide Catalyst Containing Glycine Molecule Studied by Operando O K-edge XAFS Measurement

M. Yoshida^{1,2,*}, T. Hiue³, M. Nagasaka⁴, H. Yuzawa⁴, N. Kosugi⁴ and H. Kondoh³

¹Yamaguchi University, Yamaguchi, 755-8611, Japan

²Cooperative Research Fellow, Institute for Catalysis, Hokkaido University, Sapporo 001-0021, Japan

³Keio University, Yokohama 223-8522, Japan

⁴Institute for Molecular Science, Okazaki 444-8585, Japan

Electrochemical water splitting using renewable energies such as solar, wind, and hydroelectric powers is one of the promising methods for sustainable hydrogen production. In this system, oxygen evolution reaction (OER) limits the efficiency of overall water splitting due to the high overpotential. Thus, the development of highly active OER electrocatalyst is strongly required. Recently, Nocera and co-workers reported cobalt-phosphate-based catalyst (Co-P_i) could function as the efficient OER catalyst [1]. On the other hand, our group found that nickel oxide clusters were integrated by amino acids and the catalytic activity was enhanced [2]. Herein, we examined whether the OER activity was improved by addition of organic molecules to Co-P_i, and the function of the organic molecule was investigated using operando UV-vis absorption, X-ray absorption fine structure (XAFS), and infrared absorption spectroscopy in an attenuated total reflection mode (ATR-IR).

A Teflon electrochemical cell was equipped with a Pt wire counter electrode and a Ag/AgCl reference electrode for all electrochemical experiments. Cobalt oxide thin films were electrodeposited on an indium tin oxide (ITO), a Pt/Pd thin film, or a Au thin film in potassium phosphate (K-P_i) containing Co(NO₃)₂ and glycine (Co-Gly). The prepared sample was investigated using operando UV-vis absorption, XAFS, and ATR-IR.

Constant potential electrolysis was conducted in a potassium phosphate (K-P_i) aqueous electrolyte. The OER current of Co-Gly was higher than that of Co-P_i, indicating that the glycine molecule enhanced the OER activity of Co-P_i. To assess the film thickness of these catalysts, the operando UV-vis absorption spectra were taken and we found that the glycine molecule promoted the electrodeposition of cobalt oxide catalyst. Next, to investigate the local structure of Co species in the Co-Gly, Co K-edge extended X-ray absorption fine structure (EXAFS) spectra were taken for Co-Gly and CoOOH reference powder. This result suggested that the local structure of Co species in the Co-Gly was composed of an edge-sharing CoOOH octahedral clusters a few nanometers in size. Moreover, to observe the glycine species in Co-Gly, ATR-IR spectra were obtained and two upward bands attributed to the adsorbed glycine species was observed during the electrodeposition of Co-Gly

catalysts.

Finally, operando O K-edge XAFS spectra for Co-Gly were taken under electrochemical control with transmission mode at BL3U in the UVSOR Synchrotron, according to the previous works [3]. An absorption peak assigned to CoOOH was observed around 530 eV. Meanwhile, when the electrode potential was changed from 0.5 V to 1.0 V, a peak attributed to the CoO₂ species was observed around 529 eV as the active species for OER process.

In conclusion, we found that the glycine molecule combined between cobalt oxide clusters composed of CoOOH octahedral structure and the OER activity was enhanced because the number of active reaction sites (CoO₂) increased.

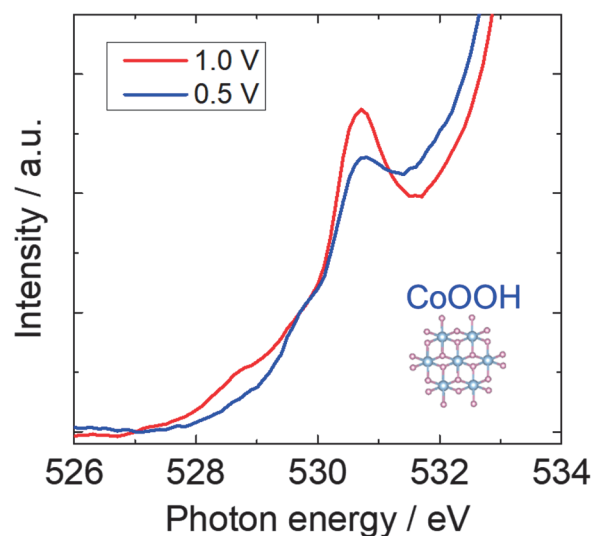


Fig. 1. Operando O K-edge XAFS spectra for Co-Gly catalyst.

[1] D. G. Nocera *et al.*, *Science* **321** (2008) 1072.

[2] M. Yoshida* *et al.*, *J. Phys. Chem. C* **121** (2017) 255.

[3] (a) M. Nagasaka *et al.*, *J. Phys. Chem. C* **117** (2013) 16343. (b) M. Yoshida* *et al.*, *J. Phys. Chem. C* **119** (2015) 19279.

BL3B

Effects of UV Irradiation and Annealing on the Oxygen Vacancies in Solution-processed IGZO Thin Films

Y. Takamori^{1,3}, T. Morimoto^{1,3}, N. Fukuda³ and Y. Ohki^{1,2}

¹Waseda University, Tokyo 169-8555, Japan

²Research Institute for Materials Science and Technology, Waseda University, Tokyo 169-8555, Japan

³Flexible Electronics Research Center (FLEC), National Institute of Advanced Industrial Science and Technology (AIST), Tsukuba 305-8565, Japan

We fabricated solution-processed IGZO thin film transistors (TFTs) [1], and found that the drain current in the TFTs decreases by UV irradiation and recovers by thermal annealing. In this paper, the mechanism of this phenomenon was analyzed by photoluminescence (PL) and XPS measurement.

The IGZO precursor solution was prepared by dissolving nitrate hydrates of In, Ga and Zn with a molar ratio of 6:1:3 in a solvent consisting of 2-methoxyethanol and 2, 2, 2-trifluoroethanol with a volume ratio of 4:1. This solution was spin-coated on a 300-nm thick thermally oxidized SiO₂ fabricated on a p-type Si substrate, and sintered at 250 °C on a hot plate in air for 1 h. Then, Al electrodes were vacuum-evaporated onto the IGZO film to fabricate a bottom-gate top-contact TFT with a channel length of 50 μm and a channel width of 500 μm.

Figure 1 shows transfer characteristics of the IGZO TFTs at drain voltage $V_D = 40$ V. Their drain currents decrease by 7.21 eV UV irradiation from a Xe₂* excimer lamp (UER20-172, Ushio) and recover by the subsequent thermal annealing at 250 °C on a hot plate in air for 30 min.

Figure 2 shows broad PL spectra of the IGZO films, excited by 4.6-eV photons at 10 K. The intensity of this PL peak centered at nearly 2.25 eV increases by the UV irradiation and decreases by the subsequent thermal annealing. This PL originates from oxygen vacancies [2]. Next, XPS O 1s peaks observed in the IGZO films were separated into three components by Gaussian fitting. The lowest component O_I at 530.2 eV is due to lattice oxygens. The middle component O_{II} at 531.7 eV is due to oxygens in oxygen-deficient regions. The highest component O_{III} at 532.7 eV is due to loosely bound oxygens on the surface of the films, such as -CO₃, adsorbed H₂O, or adsorbed O₂ [3]. Figure 3 shows the intensity ratio of each component. The O_{II} increases by the UV irradiation and decreases by the subsequent thermal annealing.

We have reported that oxygen vacancies can act as electron scattering centers and that the increase of oxygen vacancies occurs as the Ga content in solution-processed IGZO films increases. Namely, oxygen vacancies decrease the drain current [2]. These results indicate that the decrease in drain current induced by the UV irradiation is also due to the increase in number of oxygen vacancies.

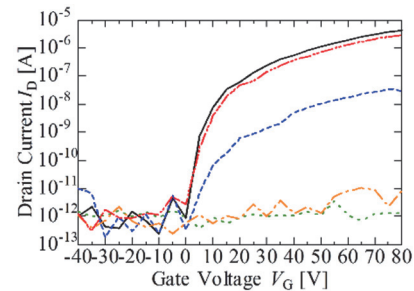


Fig. 1. Transfer characteristics of the IGZO TFTs at $V_D = 40$ V before the UV irradiation (—), after the UV irradiation for 1 (---), 5 (···), and 10 min (-·-), and after the subsequent thermal annealing (-·-).

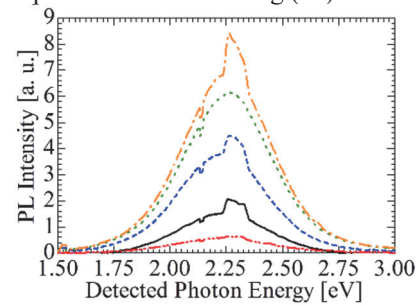


Fig. 2. PL spectra of the IGZO thin films, excited by 4.6-eV photons at 10 K before the UV irradiation (—), after the UV irradiation for 1 (---), 5 (···), and 10 min (-·-), and after the subsequent thermal annealing (-·-).

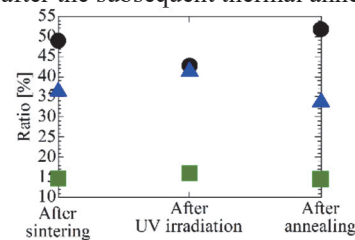


Fig. 3. Intensity ratios of the three components of XPS O 1s peaks: O_I due to lattice oxygens (●), O_{II} due to oxygens in oxygen-deficient regions (▲), and O_{III} due to loosely bound oxygens on the surface of the IGZO films (■), before and after the UV irradiation for 10 min, and after the subsequent thermal annealing.

[1] S. Ogura *et al.*, *Flex. Print. Electron.* **1** (2016) 045001.

[2] Y. Ochiai *et al.*, *UVSOR Activity Report* **44** (2017) 128.

[3] G. H. Kim *et al.*, *Thin Solid Films*, **517** (2009) 4007.

BL4B

Substrate-symmetry Driven Electronic and Magnetic Modifications in a Monatomic Layer Iron Nitride

T. Miyamachi¹, T. Hattori¹, S. Nakashima¹, Y. Takagi^{2,3}, T. Yokoyama^{2,3} and F. Komori¹

¹*Institute for Solid State Physics, University of Tokyo, Kashiwa 277-8581, Japan*

²*Department of Materials Molecular Science, Institute for Molecular Science, Okazaki 444-8585, Japan*

³*Department of Structural Molecular Science, The Graduate University for Advanced Studies (SOKENDAI), Okazaki 444-8585, Japan*

Iron nitrides have a variety of compositions and crystal structures depending on the nitrogen concentration. Especially, the iron rich Fe₄N phase attracts great attention toward practical application for its high coercivity and room temperature ferromagnetism in the form of thin films [1]. Fe₄N thin films can be grown on Cu(001) with alternating Fe- and Fe₂N- planes in the fcc Fe sublattice with a N atom centered in the cubic cell. At the thinnest limit, i.e., a monatomic layer, the Fe₂N plane preferentially grows on the surface and the surface reconstruction from the square c(2×2) lattice in bulk to the p4gm(2×2) one takes place, which is so called clock reconstruction [1, 2].

Using scanning tunneling microscopy (STM) and low energy electron diffraction (LEED), we have recently revealed the high stability of the p4gm(2×2) lattice in the monatomic layer Fe₄N (Fe₂N) due to the strong bonding between Fe and N atoms [3,4]. Furthermore, with the help of x-ray absorption spectroscopy/x-ray magnetic circular dichroism (XAS/XMCD) and the first principles calculations, the strong in-plane magnetic anisotropy observed for the Fe₂N is successfully associated with the change in the distribution of Fe 3d electrons by the electronic hybridization with Cu (001) [5]. In this work, taking the advantage of the robust surface lattice of the Fe₂N, we intend to tune its magnetic properties by changing the supporting substrate symmetry from fourfold Cu(001) to threefold Cu(111). This can modify the degrees of the binding and thus of the electronic hybridization between the Fe₂N and the substrate.

The growth and structural properties of the Fe₂N on Cu(111) were pre-checked by STM before XAS/XMCD [6]. Likewise on Cu(001) [3-5], N⁺ ions with an energy of 500 eV were firstly bombarded to the clean Cu(111) surface and Fe was additionally deposited at room temperature. By subsequent annealing at 620 K, well-ordered Fe₂N was grown on the surface. We find that the Fe₂N keeps the clock reconstruction even on Cu(111), while the moiré pattern additionally appears on the surface due to the slight lattice distortion of the Fe₂N. Note that the

sample quality for XAS/XMCD is confirmed from the consistency of Fe₂N LEED patterns in STM and XAS/XMCD measurements.

The measurements were performed at BL4B in UVSOR by total electron yield mode at B = ± 5 T and T = 6.2 K. The XMCD spectra are obtained at the normal (NI: θ = 0°) and the grazing (GI: θ = 55°) geometries by detecting μ₊ - μ₋, where μ₊ (μ₋) denotes the XAS recorded at Fe L-adsorption edges with the photon helicity parallel (antiparallel) to the sample magnetization. Note that θ is the angle between the sample normal and the incident x-ray.

We find that the XMCD intensity is slightly greater in the GI geometry than in the NI geometry. This reveals that the magnetic easy axis of the Fe₂N on Cu(111) is towards in-plane direction as in the case on Cu(001). However, the spin magnetic moment of the Fe₂N on Cu(111) is quantitatively evaluated to be ~ 0.5 μ_B/atom from XMCD sum rules, which is considerably smaller than that on Cu(001) of ~ 1.1 μ_B/atom [5]. Furthermore, the magnetization curves of the Fe₂N on Cu(111) recorded in the NI and GI geometries behave in a similar fashion, while the strong in-plane magnetic anisotropy is confirmed for the geometry dependence of the magnetization curve on Cu(001) [5]. The results indicate that changing the symmetry of the supporting substrate from Cu(001) to Cu(111) modifies electronic properties of the Fe₂N especially for Fe 3d states, and accordingly magnetically weakens the Fe₂N.

In future work, combining results of XMCD with those of STM and the first principles calculations, we will discuss the impacts of the atomic-scale distortion and surface inhomogeneity including moiré corrugation on the electronic and magnetic properties of the Fe₂N on Cu(111).

[1] J. M. Gallego *et al.*, Phys. Rev. B **70** (2004) 115417.

[2] Y. Takagi *et al.*, Phys. Rev. B **81** (2010) 035422.

[3] Y. Takahashi *et al.*, Phys. Rev. Lett. **116** (2016) 056802.

[4] K. Ienaga *et al.*, Phys. Rev. B **96** (2017) 085439.

[5] Y. Takahashi *et al.*, Phys. Rev. B **95** (2017) 224417.

[6] T. Hattori *et al.*, Phys. Rev. M *accepted*.

BL4B

Interfacial Spin and Orbital Magnetic Moments and their Anisotropies in Pd Studied by X-ray Magnetic Circular Dichroism in Co/Pd Multilayers

J. Okabayashi^{1,*}, Y. Miura² and H. Munekata³

¹Research Center for Spectrochemistry, The University of Tokyo, Tokyo 113-0033, Japan

²Electrical Engineering and Electronics, Kyoto Institute of Technology, Kyoto 606-8585, Japan

³Laboratory for Future Interdisciplinary Research Science and Technology, Tokyo Institute of Technology, Yokohama 226-8503, Japan

Ultrathin Co/Pd multilayers are artificial nanomaterials that exhibit perpendicular magnetic anisotropy (PMA), due to the spin-orbit interactions, achieved through interfacial chemical bonding. Extensive efforts have been made for studying interfaces of ultra-thin magnetic multilayers and nanostructures. Studies on Co atoms performed using X-ray magnetic circular dichroism (XMCD) have suggested the enhancement of orbital magnetic moments at the interfacial Co that is adjacent to Pd. It has been reported that the PMA emerges due to the cooperative effects between spin moments in *3d* TMs and large spin-orbit interactions in the non-magnetic *4d* or *5d* TMs. However, the interfacial PMA, including the anisotropic orbital magnetic moments, has not been fully understood for both Co and Pd sites. Bruno and van der Laan theoretically proposed an orbital moment anisotropy in *3d* TMs within the second-order perturbation of the spin-orbit interaction for more than half-occupied electrons [1]. However, in the case of strong spin-orbit coupling in *4d* or *5d* TMs, the validity of this perturbative formula has been debated [2]. In order to study the mechanisms of PMA in Co/Pd multilayers, the orbital magnetic moments contributions of each element have to be explicitly considered. It is challenging to study the anisotropy of the orbital magnetic moments of both Co and Pd elements using one specific experiment, due to the challenges in detection of the induced magnetic moments, of Pd in particular.

For the interfacial Pd, the magnetic dipole contribution through the quadrupole interactions between dipoles is assessed quantitatively. We focus on the anisotropy of orbital moments at the Co/Pd interfaces using XMCD and first-principles density functional theory (DFT) calculations, which provide the element- and layer-resolved contributions that reveal the mechanism of PMA.

We prepared the sample of Co/Pd multilayered structures: Co (0.69 nm)/Pd (1.62 nm) for PMA with stacking five periods on the Si substrates [3]. Sample surfaces were sputtered by Ar ions before the XMCD measurements in order to remove the oxygen contamination. We performed XMCD experiments at BL4B, UVSOR, Institute of Molecular Science. Total electron yield mode by directly detecting the sample current was adopted. A magnetic field of ± 5 T was applied along the direction of the incident polarized soft x-ray.

We successfully observed clear XMCD signals in Pd

M-edges after the removal of surface contamination as shown in Fig. 1. Although the XAS line shapes overlap with those of O *K*-edge absorption, clear XMCD signals induced by the proximity with Co layers are observed. The Pd *M*-edge XMCD line shapes are almost identical, which suggests isotropic orbital moments in Pd, within the detection limits. This indicates that the isotropic finite orbital moments in Pd do not directly contribute to the PMA. On the other hand, clear Co *L*-edge XAS and XMCD with angular dependence reveal the enhancement of orbital moments in the surface normal direction because of PMA.

Next, we discuss the quadrupole-like contribution of the interfacial Pd layer. Our Pd XMCD results indicate that the Pd orbital moments induced at the interface are isotropic. Note that the magnetic dipole term m_T is an order of magnitude smaller than the orbital moments, i.e., less than $0.005 \mu_B$, comparable with the detectable limits. Therefore, the relatively large spin-orbit coupling constant and small Pd exchange splitting contribute to the appearance of PMA by means of quadrupole-like interactions through the interfacial proximity effects. Furthermore, these results are well explained by DFT calculations.

We acknowledge to Prof. T. Yokoyama, Dr. Y. Takagi, and Dr. K. Uemura for the technical supports at BL4B.

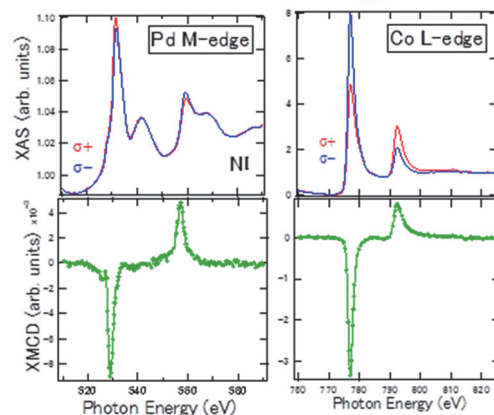


Fig. 1. XAS and XMCD of Pd *M*-edge and Co *L*-edge in perpendicularly magnetized Co/Pd multilayer.

- [1] P. Bruno, Phys. Rev. B **39** (1989) 865.
- [2] C. Andersson *et al.*, Phys. Rev. Lett. **99** (2007) 177207.
- [3] K. Yamamoto *et al.*, IEEE TRANSACTIONS ON MAGNETICS **49** (2013) 3155.

*e-mail: jun@chem.s.u-tokyo.ac.jp

BL4B

Magnetic Properties of Magnetic Ionic Liquid Thin Films Prepared on Cu(001) and Ferromagnetic Co/Cu(001)

K. Eguchi¹, T. Yokoyama^{2,3} and K. Awaga¹¹Department of Chemistry, Nagoya University, Nagoya 464-8602, Japan²Department of Materials Molecular Science, Institute for Molecular Science, Okazaki 444-8585, Japan³School of Physical Sciences, The Graduate University for Advanced Studies (SOKENDAI), Okazaki 444-8585, Japan

Ionic liquids (ILs), which consist of mobile cations and anions at near-room temperature, have attracted much attention in a wide range of applications because of their unique properties such as low melting points, non-volatility, and high capacitance. ILs are generally non-magnetic; however, incorporating magnetic ions into ILs at room temperature yields paramagnetic ILs [1, 2]. Magnetic susceptibility measurements have been performed to understand the magnetic properties of magnetic ILs [1, 2]. However, to the best of our knowledge, their magnetic properties on metal substrates have not been reported. This study investigates the magnetic properties of 1-ethyl-3-methylimidazolium tetrachloroferrate ([Emim][FeCl₄], Fig. 1(a)) thin films prepared on Cu(001) using X-ray magnetic circular dichroism (XMCD) measurements. These measurements were also performed for [Emim][FeCl₄] thin films prepared on ferromagnetic Co/Cu(001) to examine the magnetic interaction between trivalent Fe ions in FeCl₄⁻ and Co thin films at the interfaces.

A commercially available [Emim][FeCl₄] (Tokyo Chemical Industry) was deposited on Cu(001) and Co(3 ML)/Cu(001) [3] at room temperature using a pulse valve under ultrahigh vacuum ($P \sim 10^{-7}$ Pa) conditions. The thickness of [Emim][FeCl₄] was set as 0.8 ML by controlling the opening time of the pulse valve. X-ray absorption spectroscopy (XAS) and XMCD measurements were performed using an XMCD system ($P < 1 \times 10^{-8}$ Pa, $B = 7$ T, and $T = 3.8$ K). XMCD spectra were obtained by the total electron yield detection mode in a magnetic field of ± 5 mT or ± 5 T at a temperature of 6.5 K and an X-ray incidence angle of 55° with respect to the surface normal.

The [Emim][FeCl₄] thin film prepared on Cu(001) showed an XMCD signal at the Fe *L*-edge in a magnetic field of 5 T (Fig. 1(b)). The effective spin (m_{spin}) and orbital (m_{orb}) magnetic moments of the trivalent Fe ion in the thin film were calculated using the sum rules [4,5], wherein $m_{\text{spin}} = 1.82 \mu_B$ and $m_{\text{orb}} = 0.15 \mu_B$; here, the number of *d*-holes was assumed as 5. Considering the Brillouin function at $T = 6.5$ K and $B = 5$ T, the value of m_{spin} is almost identical to the magnetic moment of $2.03 \mu_B$ for $S = 3/2$. The magnetic property of the [Emim][FeCl₄] thin film prepared on Co/Cu(001) was similar compared with that prepared on Cu(001), indicating weak magnetic interactions of Fe with Co at $T = 6.5$ K (Figs. 1(c) and 1(d)).

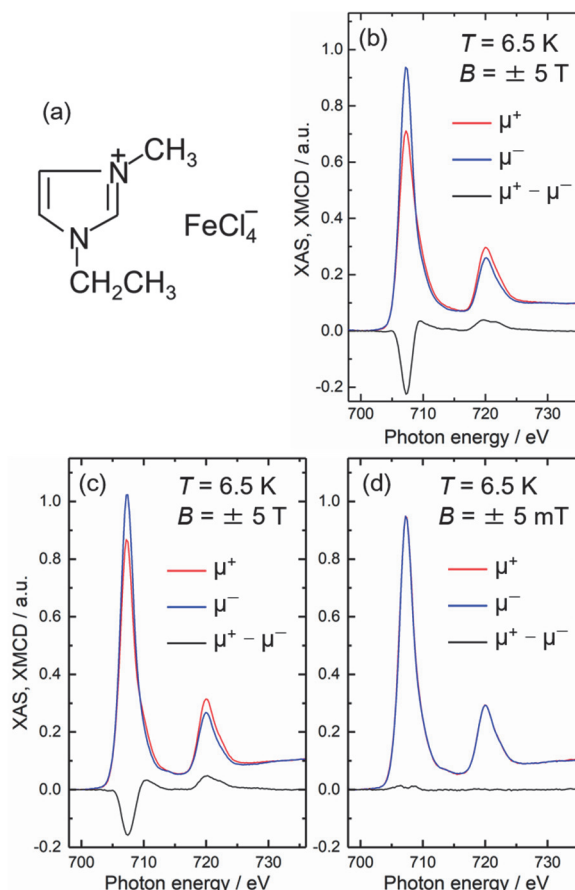


Fig. 1. (a) Chemical structure of [Emim][FeCl₄]. Fe *L*-edge X-ray absorption and X-ray magnetic circular dichroism spectra of [Emim][FeCl₄] on (b) Cu(001) and (c,d) Co (3 ML)/Cu(001).

- [1] S. Hayashi and H. Hamaguchi, Chem. Lett. **33** (2004) 1590.
- [2] Y. Yoshida, *et al.*, Bull. Chem. Soc. Jpn. **78** (2005) 1921.
- [3] K. Eguchi, *et al.*, J. Phys. Chem. C **118** (2014) 17633.
- [4] B.T. Thole, *et al.*, Phys. Rev. Lett. **68** (1992) 1943.
- [5] P. Carra, *et al.*, Phys. Rev. Lett. **70** (1993) 694.

BL4B

XMCD Measurements on a Magnetic Topological Heterostructure: Mn and Te Deposited Bi_2Te_3

S. Kusaka¹, K. Yokoyama¹, Y. Uemura², T. Yokoyama² and T. Hirahara¹

¹Department of Physics, Tokyo Institute of Technology, Tokyo 152-8551, Japan

²Department of Materials Molecular Science, Institute for Molecular Science, Okazaki 444-8585, Japan

Topological insulators (TI) are extensively studied recently due to its peculiar properties [1]. The Dirac-cone surface states of TI are protected by time-reversal symmetry (TRS) and backscattering among these surface states is prohibited. But when TRS is broken by application of a magnetic field or incorporating magnetic materials, a gap opening in the Dirac cone is expected and an intriguing phase called the quantum anomalous Hall state can be realized [2]. This phase is expected to show even more exotic phenomena such as the topological magnetoelectric effect. To realize such state, two types of sample fabrication techniques have been employed up to now: (1) magnetic doping while growing the single crystal or thin film of TI [3], and (2) magnetic impurity deposition on the surface of TI [4]. While method (1) was successful and showed evidence of the TRS violation, no one has succeeded using method (2), which should be a more direct way to examine the interaction between the topological surface states and magnetism. Recently, we have succeeded in inducing a gap in the TI Dirac surface states by a new method called ‘magnetic extension’ [5]. An ordered Mn layer was incorporated into the topmost quintuple layer of a prototypical TI, Bi_2Te_3 by Mn and Se deposition and a $\text{MnBi}_2\text{Se}_4/\text{Bi}_2\text{Se}_3$ heterostructure was formed. Due to the large wave function overlap between the Dirac cone and the ferromagnetic Mn layer, a large gap of 85 meV was observed and its origin was ambiguously assigned to the ferromagnetic nature of MnBi_2Se_4 as proven by XMCD measurements [6].

We have recently found that we can also employ magnetic extension to break the time reversal symmetry of another prototypical TI, Bi_2Te_3 . We deposited Mn and Te on Bi_2Te_3 and found a clear gap opening of ~ 70 meV at the Dirac point. In the present work, we have performed XMCD measurements at BL-4B to experimentally prove that this system is ferromagnetic. Figure 1 shows the X-ray absorption (XAS) spectra and the corresponding XMCD spectra at 5 T (~ 5 K). One can find clear XMCD peaks at the Mn L_3 and L_2 edges. The measurements were also performed at remanence, and the result is shown in Fig. 2. Although very weak, one can find a dip structure at the L_3 edge and this shows that this system is indeed ferromagnetic.

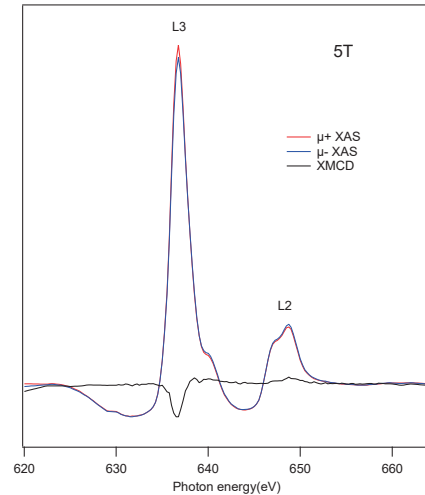


Fig. 1. XAS and XMCD spectra at 5 T.

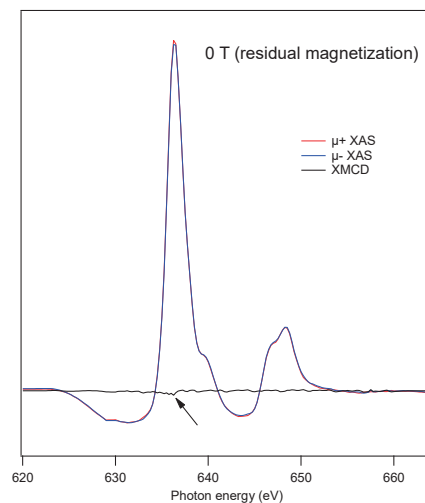


Fig. 2. XAS and XMCD spectra at 0 T (residual magnetization).

- [1] M. Hasan and C. Kane, *Reviews of Modern Physics* **82** (2010) 3045.
- [2] X.-L. Qi and S.-C. Zhang, *Reviews of Modern Physics* **83** (2011) 1057.
- [3] For example, C. Z. Chang *et al.*, *Science* **340** (2013) 167.
- [4] For example, M. Ye *et al.*, *Physical Review B* **85** (2012) 205317.
- [5] M. Otrokov *et al.*, *2D Mater.* **4** (2017) 025082.
- [6] T. Hirahara *et al.*, *Nano Letters* **17** (2017) 3493.

BL4B

Oxygen Induced Magnetic Transition in Single Layer Iron Film

T. Nakagawa¹, T. Nomitsu¹, S. Mizuno¹ and T. Yokoyama²

¹ Department of Molecular and Material Sciences, Kyushu University, Kasuga, Fukuoka 816-0955, Japan

² Institute for Molecular Science, Okazaki 444-8585, Japan

Molecular adsorption on magnetic thin films changes the magnetic anisotropy and the magnetization easy axis through the modification of the magnetic orbital moment, and thus induces a spin reorientation transition (SRT). It is not clear, however, whether molecular adsorption induces magnetic transitions, except the SRT, such as a ferromagnetic to antiferromagnetic transition since the exchange interaction is larger compared with the magnetic anisotropy energy.

Experiments were performed in the x-ray magnetic circular dichroism (XMCD) endstation with the base pressures of 4×10^{-8} Pa for sample preparation and better than 1×10^{-8} Pa for XMCD measurement. Single Fe layers were grown on W(110). Oxygen was dosed with the sample kept at the room temperature, via a variable leak valve at 2×10^{-7} Pa. The Fe films exposed up to 150 L (1 L = 1.3×10^{-4} Pa s) oxygen were examined by XMCD. The oxygen coverage was estimated by the appearance of an ordered 3×2 structure with 0.33 ML oxygen on Fe/W(110) using low energy electron diffraction [1]. Fe *L* edge XMCD was taken with a circularly polarized light (circularly polarization ~ 0.6) at $H = \pm 5$ T at a sample temperature of 6 K. NEXAFS spectra were measured at $H = 0$ T. All the measurements were performed for a grazing incidence angle of 30° from the surface.

Figure 1 (a) shows magnetization curves measured at Fe *L* edge. On the clean single layer Fe, the magnetization curve exhibits hysteresis and a large coercivity of ~ 2 T. With increasing the oxygen coverage, the magnetization and the coercivity decrease up to 0.33 ML oxygen coverage. At 0.33 ML, the Fe film is not ferromagnetic, and it is likely paramagnetic. The oxygen adsorption of 0.6 ML restores the Fe film to the ferromagnetic state with ~ 2 T coercivity. Further increase of the oxygen coverage, leading to the formation of iron oxide, transforms the Fe film to a non-ferromagnetic state.

In order to investigate the origin of the magnetic transition, we have measured NEXAFS spectra of O *K* edge with increasing the oxygen coverage. Figure 1(b) shows NEXAFS for the oxygen coverage of 0.33, 0.6 and 1 ML. For all the coverages studied the oxygen dissociates on the Fe film. At 0.33 ML, the peak at 530 eV is assigned to the transition to O(2p). The peak shifts to a higher energy with increasing the oxygen coverage. This energy shift is due to the strong hybridization between O 2p and Fe 3d, which would drive the transition from the paramagnetic to ferromagnetic state.

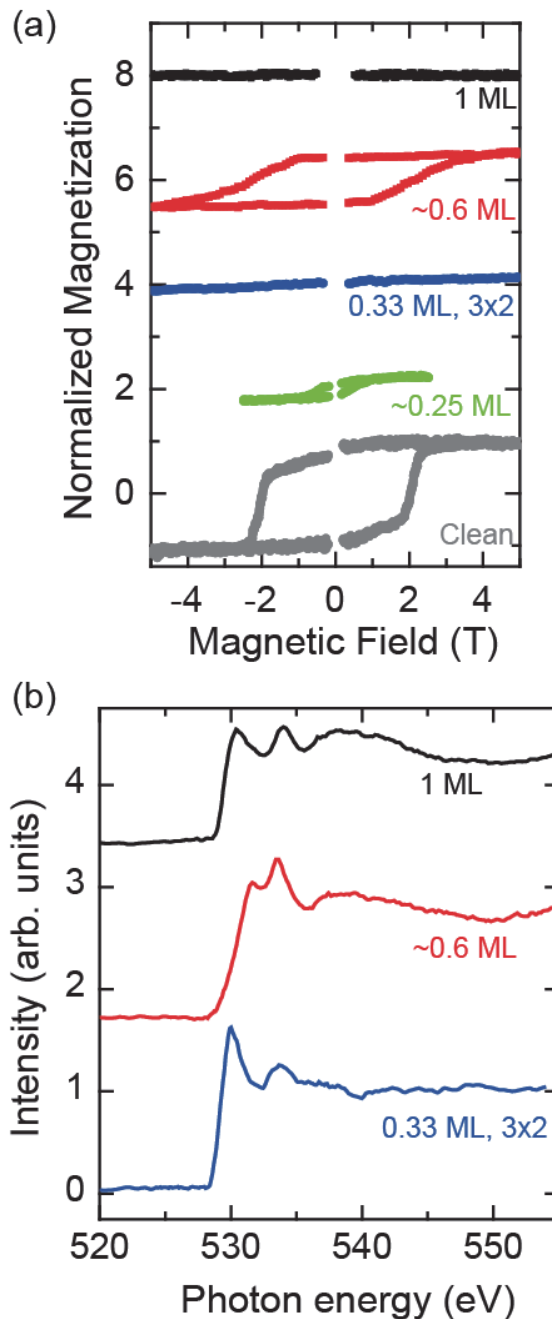


Fig. 1. (a) Magnetization curves measured at Fe-L edges. (b) NEXAFS for oxygen K edge. Indicated inside are the oxygen coverages.

[1] K. Feindl *et al.*, Surf. Sci. **617** (2013) 183.

BL5U

Change in the Electronic Structure of Fe₂P(10-10) Induced by Phosphorus Segregation: Soft X-ray Photoemission Spectroscopy Study

H. Motoyama¹, Y. Sugizaki¹, Y. Shimato¹, T. Yoshida¹, T. Takano¹ and K. Edamoto^{1,2}

¹Department of Chemistry, Rikkyo University, Tokyo 171-8501, Japan

²Research Center for Smart Molecules, Rikkyo University, Tokyo 171-8501, Japan

The surface properties of transition metal phosphides (TMPs) have attracted much attention because of their high catalytic performance for HDS and HDN for petroleum fuels. It has been found that Ni₂P has the highest catalytic activity among TMPs while that of Fe₂P is extremely low [1]. Therefore, in order to elucidate the origin of the high catalytic activity of TMPs, it is useful to explore the difference in the surface electronic structures of Ni₂P and Fe₂P. In this work, we investigated the phosphorus segregation process and its effect on the electronic structure of Fe₂P(10-10).

Our previous Auger electron spectroscopy (AES) study revealed that the P atoms on Fe₂P(10-10) are selectively removed by Ar⁺ ion sputtering. When the sputtered surface is subsequently annealed, the intensity ratio of P LMM and Fe MVV peaks in AES spectra decreases with elevating annealing temperature up to 400 °C, and increases at temperatures higher than 400 °C, as shown in the inset of Fig. 1. The P 2p spectrum of Fe₂P(10-10) after Ar⁺ ion sputtering, which was measured under a highly surface sensitive condition ($h\nu=170$ eV), is shown in Fig. 1. The spectrum can be fit by seven components denoted as $\alpha - \eta$. The δ peak is assigned as a bulk component [2]. The analyses of annealing temperature dependence of the spectra show that the ϵ' , ζ , η peaks should be associated with weakly bonded surface species which would be formed through the sputtering, and α , β , γ , ϵ peaks are associated with surface P atoms segregated from the bulk. (The ϵ' and ϵ peaks are thought to be observed in the same binding energy region accidentally.) The former species are easily removed by annealing at lower than 400 °C, and the latter species are increased in intensities by annealing at higher than 300 °C, which are consistent with the AES results shown in the inset of Fig. 1.

Figure 2 shows the valence band spectra of Fe₂P(10-10) after Ar⁺ ion sputtering and subsequent annealing at various temperatures at 300 – 700 °C. The band observed at 0 – 4 eV is associated with the Fe 3d – P 3p hybrid band [2]. As shown in Fig. 2, the spectral shape of the band in the vicinity of E_F is not changed by the segregation of P atoms induced by heating above 400 °C, suggesting that the Fe 3d states are not stabilized by the bonding with segregated P atoms. This is contrary to the case of Ni₂P surfaces where the Ni 3d states are stabilized through the bonding with segregated P atoms forming a pseudo gap around E_F [3]. These results suggest that the stabilization of the

active metal sites through the bonding with P atom is crucial to maintain the activity during HDS through preventing the accumulation of S atoms on active metal sites.

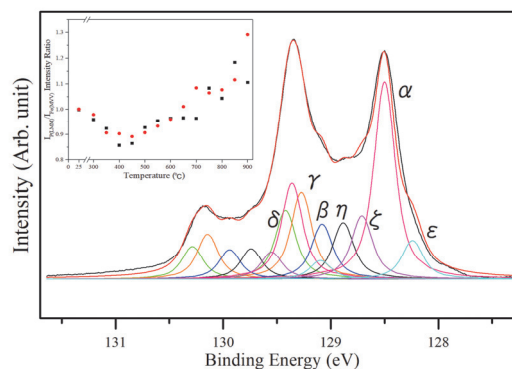


Fig. 1. The P 2p spectrum of Fe₂P(10-10) fit by Voigt functions. The change in the P LMM and Fe MVV Auger peak intensity ratio as a function of annealing temperature is shown in the inset.

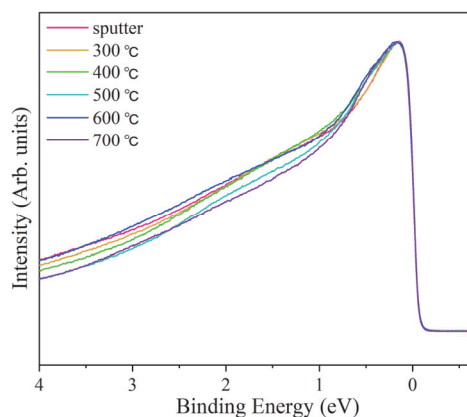


Fig. 2. Valence band spectra of Fe₂P(10-10) after Ar⁺ ion sputtering and subsequent annealing at various temperatures at 300 – 700 °C.

- [1] S. T. Oyama *et al.*, *Catal Today* **143** (2009) 94.
- [2] Y. Sugizaki *et al.*, *Surf. Sci.* **664** (2017) 50.
- [3] K. Edamoto, *Appl. Surf. Sci.* **269** (2013) 7.

BL5U

Valence-Band Electronic Structures of Ultra-Thin Fe Layers on Rashba-Split Au (111) Surfaces

J. Okabayashi^{1*}, K. Tanaka² and S. Mitani³

¹Research Center for Spectrochemistry, The University of Tokyo, Tokyo 113-0033, Japan

²UVSOR Synchrotron Facility, Institute of Molecular Science, Okazaki 444-8585, Japan

³National Institute for Materials Science, Tsukuba 305-0047, Japan

When ferromagnetic transition metals (TMs) are deposited on the Rashba-type spin-orbit coupled surface, novel properties such as perpendicular magnetic anisotropy (PMA) are emerged at the interfaces, which are derived from the symmetry broken spin-orbit effects. The gold Au (111) surfaces have been investigated extensively by means of scanning tunneling microscopy and angle-resolved photoemission spectroscopy (ARPES) because this surface exhibits the large Rashba-type spin-orbit splitting. Large spin-orbit interaction in the heavy element of gold provides the wide varieties for the topological physics and spin-orbit coupled sciences at the surfaces and interfaces. The Rashba splitting of 110 meV in Au (111) surface was reported firstly by LaShell *et al.* [1]. Recently, the interfaces between Au(111) and other heavy elements such as Bi or Ag have been extensively investigated [2,3]. Here, we focus on the interfaces between ferromagnetic materials and Au(111) interfaces because the thin Fe layers on the heavy elements are expected to exhibit the PMA induced by the Rashba-type spin-orbit interaction.

The spin-orbit coupling between the ferromagnetic 3d TMs Fe or Co and 5d heavy TM elements of non-ferromagnetic materials such as Pt and Au has been utilized for the PMA through the proximity at the interfaces. It is believed that the future researches concerning not only spins but also orbitals are recognized as the *spin-orbitronics*. Therefore, to clarify the origin of the PMA at these interfaces is a crucial role. The relationship between Au (111) Rashba-type spin-orbit interaction and PMA in 3d TMs has not been clarified explicitly. In order to investigate the orbital-resolved states in the Fe films showing the PMA, ARPES at the interfaces becomes powerful techniques through the photon-energy and polarization dependences in each 3d orbital. By using ARPES, we aim to understand the orbital-resolved electronic structures at the magnetic interfaces on the Rashba-type Au (111) surface in order to develop the researches of novel PMA using spin-orbit coupled interfaces.

We prepared the clean Au (111) surface for the Fe deposition. The commercialized single-crystalline 100-nm-thick Au (111) films on Mica were used. At the BL5U in UVSOR, we repeated the Ar-ion sputtering at 1-2 kV accelerating voltage and subsequent annealing at 400 °C under the high vacuum conditions. After the sample preparation, the Fe layer

was deposited at room temperature and then annealed. By *in-situ* transferring the samples into the ARPES chamber, we performed ARPES at 10 K using the photon energies of 45 and 120 eV because of the large cross-section of Au (111) surface states and detections of Fe 3p and Au 4f intensity ratios, respectively.

Figure 1 displays the Fe deposition dependence on Au (111). As shown in Fig. 1a, the intensity ratio between Fe 3p and Au 4f peaks systematically changes. The Au (111) surface clearly exhibits the Rashba-type surface states (Fig. 1c). The Fe 3d states appear near the Fermi level (E_F) and the surface states disappear as shown in Fig. 1d. As shown in Fig. 1b, with increasing the Fe layer thickness, spectral line shapes cannot be explained by the overlap between Fe and Au, suggesting that the chemical bonding at the interface is modulated from the Au (111) surface and Rashba-type spin-orbit interaction affects to the Fe layer. Therefore, the interfacial chemical reaction between Fe and Au brings the novel properties on the ultrathin Fe electronic structures.

We acknowledge Dr. S. Ideta in IMS for technical supports of data analyses. This work was in part supported by KAKENHI Kiban(S) project.

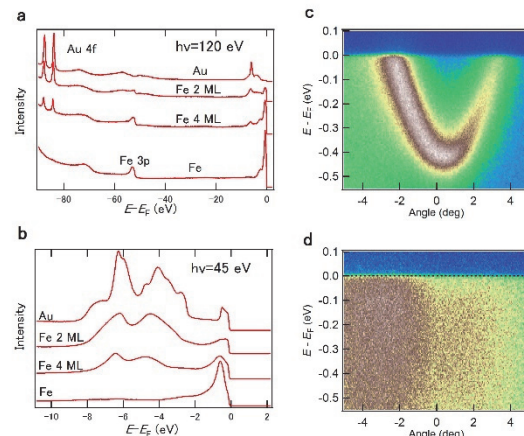


Fig. 1. Photoemission spectra for various Fe deposited layers. **a.** Angle-integrated wide-range spectra taken at 120 eV. **b.** valence-band spectra taken at 45 eV. **c.** ARPES near E_F in Au surface taken at 45 eV. **d.** ARPES near E_F after 2 ML Fe deposition taken at 45 eV.

- [1] S. LaShell *et al.*, Phys. Rev. Lett. **77** (1996) 3419.
 [2] C. Tusche *et al.*, Ultramicroscopy **159** (2015) 620.
 [3] B. Yan *et al.*, Nature Commun. **6** (2015) 10167.

*e-mail: jun@chem.s.u-tokyo.ac.jp

BL5U

Photoelectron Angular Distribution Maps of Perfluoropentacene on Ag (111)

T. Yamaguchi^{1,2}, S. Ouchi³, M. Meissner¹, T. Ueba^{1,2}, R. Shiraishi^{1,2}, S. Ideta^{1,4}, K. Tanaka^{1,4}
and S. Kera^{1,2,3}

¹School of Physical Sciences, The Graduate University for Advanced Studies (SOKENDAI), Okazaki 444-8585

²Department of Photo-Molecular Science, Institute for Molecular Science, Okazaki 444-8585, Japan

³Graduate School of Engineering, Chiba University, Chiba 263-8522, Japan

⁴UVSOR Synchrotron Facility, Institute for Molecular Science, Okazaki 444-8585, Japan

The interface between a molecular semiconductor and a metal greatly affects the electronic properties of the molecular film and it is thus of great importance to fundamentally study the large variety of effects taking place at such an interface. Photoelectron angular distribution (PAD) maps generated from angle-resolved ultraviolet photoemission spectroscopy (ARUPS) provide insight into the orbital shapes of adsorbed molecules. By comparing experiments with theoretical data allows us to discuss the origin of modifications of orbitals and the implications for the electronic properties of the film. Here, we aimed to test the suitability of BL5U with the deflector mode for this purpose, using monolayers of perfluoropentacene (PFP) adsorbed on Ag(111).

We prepared monolayers of PFP on Ag(111) by annealing slightly thicker films at 130 °C for 10 min. These samples were then measured at room temperature as well as at 5 K, using different photon energies of 60 eV and 120 eV. An exemplary PAD map is shown in Fig. 1a for a sample that is tilted away from the normal-emission geometry, such that the Γ point is outside the upper left corner of the image. The arc-like feature in the center belongs to the Ag sp-band, whereas the feature in the center belongs to the second-highest occupied molecular orbital (HOMO^{-1}). The $\bar{\Gamma}\bar{K}$ direction of Ag(111) is aligned horizontally.

By probing the photoelectrons at different binding energies, we generated three-dimensional energy-versus-angle data, enabling us to discuss spectroscopic details and dispersion behavior of the films. Fig. 1b shows a cut through that data in the direction indicated by the red line in panel a. The HOMO and HOMO^{-1} are marked by horizontal lines.

Building on experiences from a previous beamtime at BL5U, we aimed to reduce film damages due to the intense beam by measuring during single-bunch operation. Obviously, however, there are low-energy shoulders next to both the HOMO and HOMO^{-1} , which is a typical indication of molecules broken up by the irradiation. Moreover, the field of view (FoV) of this setup is quite limited compared to the angular dimensions of typical molecular orbitals. It is sufficient to discuss fine features of individual orbital lobes. However, a stitching of images taken under different rotation/tilting angles of the sample in order to obtain a more complete PAD map is hardly possible or meaningful due to the changing beam incidence angle.

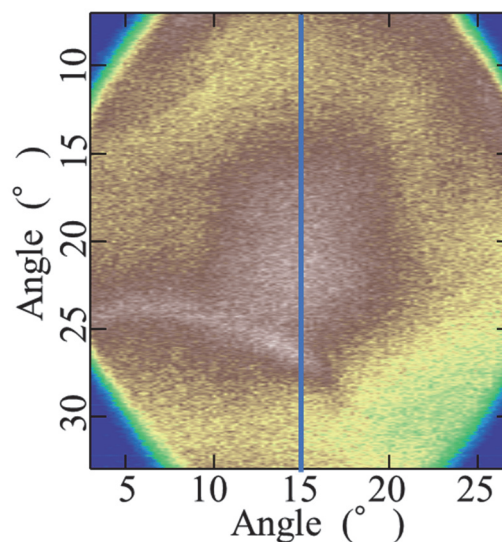


Fig. 1. Angle-resolved photoelectron map of HOMO^{-1} for monolayer PFP on Ag(111) at $h\nu= 60$ eV. The blue line marks the cut direction for the image in Fig. 2.

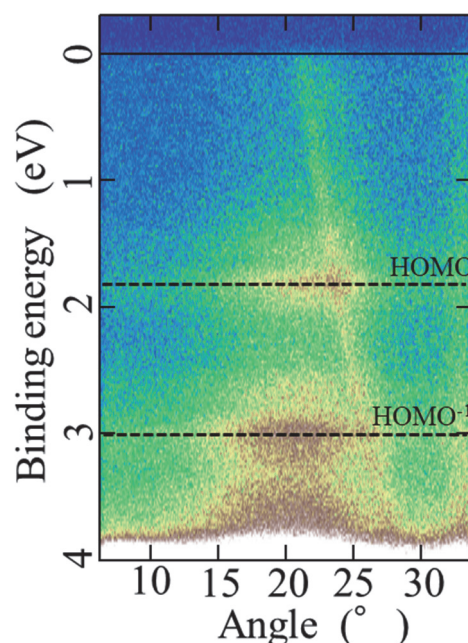


Fig. 2. Binding energy versus emission angle in the direction highlighted in Fig. 1, overlaid by the horizontally integrated energy distribution curve. The HOMO and HOMO^{-1} of PFP are marked by horizontal dashed lines.

BL5U, BL7U

Electronic Structure of Mn and Te Deposited Bi_2Te_3 : A New Magnetic Topological Heterostructure

K. Yokoyama¹, Y. Okuyama¹, S. Ideta², K. Tanaka² and T. Hirahara¹¹Department of Physics, Tokyo Institute of Technology, Tokyo 152-8551, Japan²UVSOR Synchrotron Facility, Institute for Molecular Science, Okazaki 444-8585, Japan

Topological insulators (TI) are extensively studied recently due to its peculiar properties [1]. The Dirac-cone surface states of TI are protected by time-reversal symmetry (TRS) and backscattering among these surface states is prohibited. But when TRS is broken by application of a magnetic field or incorporating magnetic materials, a gap opening in the Dirac cone is expected and an intriguing phase called the quantum anomalous Hall state can be realized [2]. This phase is expected to show even more exotic phenomena such as the topological magnetoelectric effect. To realize such state, two types of sample fabrication techniques have been employed up to now: (1) magnetic doping while growing the single crystal or thin film of TI [3], and (2) magnetic impurity deposition on the surface of TI [4]. While method (1) was successful and showed evidence of the TRS violation, no one has succeeded using method (2), which should be a more direct way to examine the interaction between the topological surface states and magnetism. Recently, we have succeeded in inducing a gap in the TI Dirac surface states by a new method called ‘magnetic extension’ [5]. An ordered Mn layer was incorporated into the topmost quintuple layer of a prototypical TI, Bi_2Se_3 by Mn and Se deposition and a $\text{MnBi}_2\text{Se}_4/\text{Bi}_2\text{Se}_3$ heterostructure was formed. Due to the large wave function overlap between the Dirac cone and the ferromagnetic Mn layer, a large gap of 85 meV was observed [6].

In the present work, we have tried to employ magnetic extension to break the TRS in another prototypical TI, Bi_2Te_3 . We deposited Mn and Te on Bi_2Te_3 and measured its electronic structure. Figures 1 (a) and (b) show the band dispersion of the surface states of the pristine Bi_2Te_3 and the sample with Mn and Te deposited on top measured at 30 K ($h\nu = 8$ eV). The Dirac-cone surface states are massless in (a) with no gap. On the other hand, one can find a clear gap of ~ 70 meV at the Dirac point in (b) as indicated by the energy distribution curve, meaning that it has turned into a massive Dirac cone. This result shows that we have successfully induced TRS breaking in the surface states of Bi_2Te_3 . However, comparison with *ab initio* calculations [5] showed that the formed structure is not $\text{MnBi}_2\text{Te}_4/\text{Bi}_2\text{Te}_3$ and a structural study is under way to determine the real crystal structure of the system.

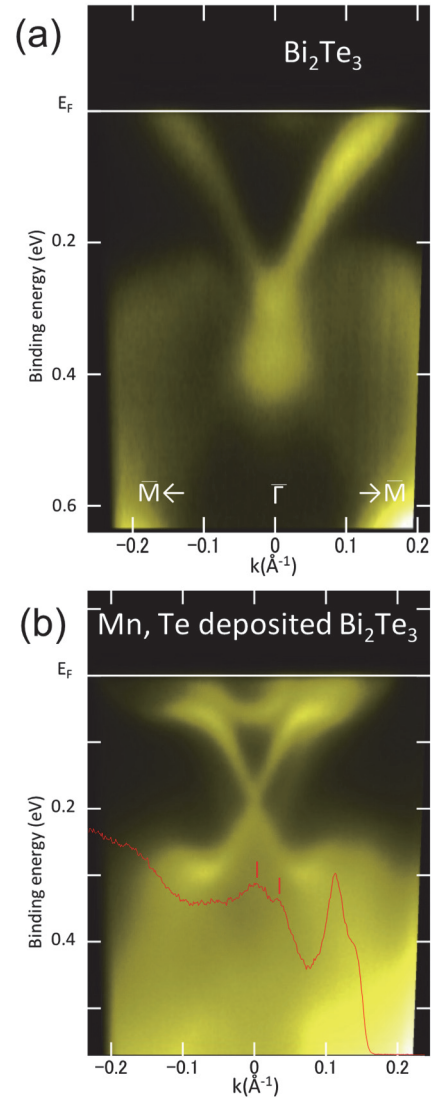


Fig. 1. The band dispersion of Bi_2Te_3 (a), and that with Mn and Te deposition (b), respectively, measured at 30 K with $h\nu = 8$ eV photons of *p*-polarization.

[1] M. Hasan and C. Kane, *Rev. Mod. Phys.* **82** (2010) 3045.

[2] X.-L. Qi and S.-C. Zhang, *Rev. Mod. Phys.* **83** (2011) 1057.

[3] For example, C. Z. Chang *et al.*, *Science* **340** (2013) 167.

[4] For example, M. Ye *et al.*, *Phys. Rev. B* **85** (2012) 205317.

[5] M. Otkrov *et al.*, *2D Mater.* **4** (2017) 025082.

[6] T. Hirahara *et al.*, *Nano Letters* **17** (2017) 3493.

BL5B

Optical Properties of Amorphous Arsenic Trisulfide

K. Hayashi

Department of Electrical, Electronic and Computer Engineering, Gifu University, Gifu 501-1193, Japan

Amorphous chalcogenide semiconductor materials, such as a-As₂S₃, a-As₂Se₃ and a-Se etc., show a variety of photo-induced phenomena. These materials are expected as materials for optoelectronic devices. A lot of work have been done on the photo-induced phenomena of these amorphous semiconductor materials and various mechanisms have been proposed for these photo-induced phenomena [1-3]. However, the details of the mechanisms are still unknown. For device applications, it is necessary to sufficiently understand the fundamental properties of these materials. The interest has been attracted for the change of the optical properties in the energy region of the visible light. We are interesting for the changes of the optical properties in the higher energy region. To our knowledge, little attention has been given to photo-induced changes at the vacuum ultra-violet (VUV) absorption spectrum. In previous reports, we reported the photo-induced change at VUV transmission spectra of as-deposited evaporated amorphous As₂Se₃ thin films [4]. In this report, we measure the VUV transmission spectra on as-deposited evaporated amorphous As₂S₃ thin films.

Samples used for the measurement of the VUV transmission spectra were amorphous As₂S₃ thin films prepared onto aluminum thin films by conventional evaporation technique. Typical thickness of the amorphous film and the aluminum film were around 200 nm and 100 nm, respectively. The measurements were carried out at room temperature at the BL5B of the UVSOR Synchrotron Facility of the Institute for Molecular Science. And the spectrum was measured by using the silicon photodiode as a detector. Two pinholes of 1.5 mm in a diameter were inserted between the monochromator and sample to remove stray light. The intensity of the VUV light was monitored by measuring the total photoelectron yield of a gold mesh.

Figure 1 shows the transmission spectra of as-deposited a-As₂S₃ thin film at room temperature in the wavelength range (a) 7.5-8.9nm and (b) 25-30nm. Several peaks were observed at this wavelength range. The absorption peaks around 7.7nm correspond to the 2*p* core level of S atom. Other peaks correspond to the 3*p* and 3*d* core level of As atom. The broad structures observed in the absorption spectra. The origin of each component is not clear now. I would like to clarify the origin of each component in the future. Further analysis of these spectra is now in progress. We pay attention to the photo-induced effects near this wavelength range. We now are investigating photo-induced change on these spectra. The detailed experiments and analysis will be done in the next step.

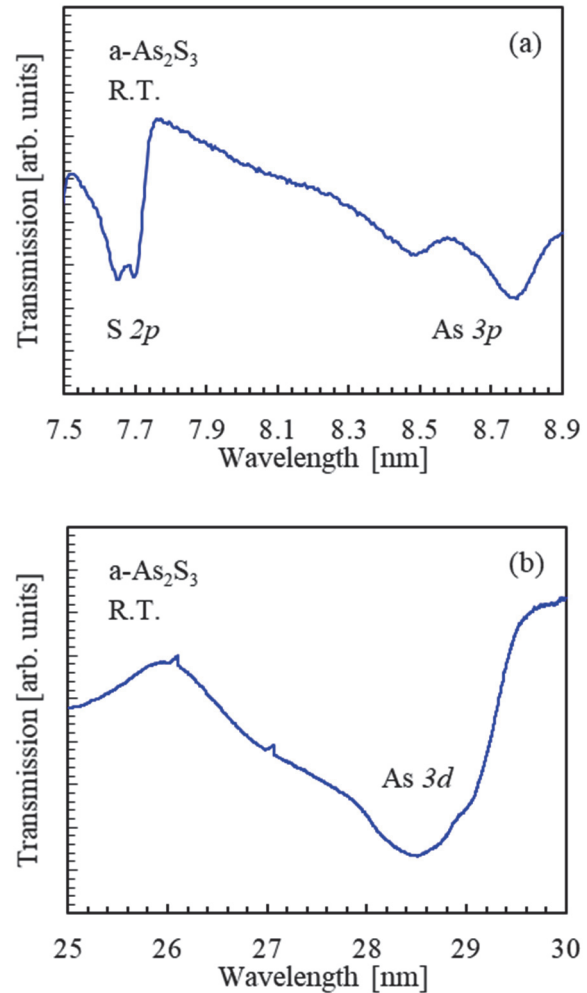


Fig. 1. The transmission spectra of as-deposited a-As₂S₃ thin film in the wavelength range (a) 7.5-8.9nm and (b) 25-30nm.

- [1] K. Tanaka, *Rev. Solid State Sci.*, **4** (1990) 641.
- [2] K. Shimakawa, A. Kolobov and S. R. Elliott, *Adv. Phys.*, **44** (1995) 475.
- [3] K. Tanaka, *Encyclopedia of Nanoscience and Nanotechnology*, **7** (2004) 629.
- [4] K. Hayashi, *UVSOR Activity Report 2014* **42** (2015) 134.

BL6U

Band Engineering of Silicene-Ge Alloy

A. Fleurence¹, T. Yonezawa¹, H. Yamane², N. Kosugi² and Y. Yamada-Takamura¹
¹*School of Materials Science, Japan Advanced Institute of Science and Technology, Nomi 923-1292, Japan*
²*Institute for Molecular Science, Okazaki 444-8585, Japan*

Alloying plays an important role for applications as it gives solution to tune the properties of materials. For instance, the band gap can be tuned in bulk SiGe alloy by means of the concentration of Ge atoms [1].

Silicene is a graphene-like buckled honeycomb structure made of silicon atoms featuring π bands at the K points of its Brillouin zone [2]. As a two-dimensional material, silicene is of high interest for Si-based nanoelectronics.

Silicene only exists in epitaxial forms. Among them, epitaxial silicene on ZrB₂ thin films grown on Si(111) has the particularity to form in a spontaneous and self-terminating way by segregation of Si atoms from the silicon substrate [3]. Epitaxial silicene adopts a silicene- $(\sqrt{3}\times\sqrt{3})$ reconstructed unit cell in which 5 Si atoms are in the same plane and a single atom is protruding. This silicene is semiconducting as a 350 meV-wide gap is opened in the Dirac cones [3].

We demonstrated by means of scanning tunneling microscopy at our home laboratory that the deposition of germanium on silicene can give rise to a silicene-Ge alloy resulting from the incorporation of Ge atoms into the silicene lattice [4].

The experiments done at the BL6U of UVSOR were aimed at determining the evolution of the band structure of this silicene-Ge alloy with the concentration of Ge atoms.

Water-cooled mini K-cell, which we used for the experiments in our home-based setup, was installed in the preparation chamber of the end station for evaporating Ge. Epitaxial silicene samples were prepared on-site by annealing ZrB₂/Si(111) samples at 800 °C under ultrahigh vacuum [2]. Ge growths were realized with a substrate temperature of 350 °C. All photoemission spectra were recorded at 15 K.

The core-level of Fig. 1(a) shows a single Ge 3d component which indicates that the Ge atoms are incorporated in a unique site in the silicene lattice. The saturation of this peak for a Ge coverage of about 1/6 monolayer (ML) silicene points out that Ge atoms occupy the protruding sites in the silicene lattice. More importantly, a clear effect of the Ge atoms on the band structure was found as the top of the valence band shifts up monotonously with the concentration. Figs. 1(c) and (d) compare angle-resolved photoemission (ARPES) spectra of pristine silicene and of silicene-Ge alloy at saturation. In the latter, the top of the band is shifted by 160 meV above that of pristine silicene.

These experiments provide an experimental demonstration of the possibility of band gap engineering in SiGe two-dimensional materials as for their bulk counterparts.

This work was supported by the Joint Studies

Program (No. 206, 2017-2018) of the Institute for Molecular Science.

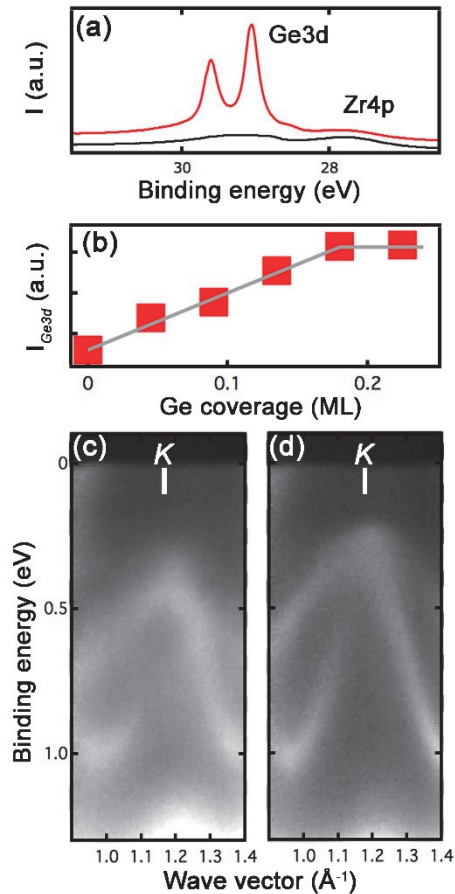


Fig. 1. (a): Core-level spectra ($h\nu=80$ eV) in the Zr 4p and Ge 3d region before and after deposition of 0.04 ML Ge on silicene. (b): Evolution of the Ge3d peak with the Ge coverage. (c) and (d) ARPES spectra ($h\nu=45$ eV) of pristine silicene and after deposition of 0.18 ML Ge.

- [1] J. C. Bean, Proc. IEEE **80** (1992) 571.
 [2] K. Takeda and K. Shiraiishi, Phys. Rev. B **50** (1994) 14916.
 [3] A. Fleurence *et al.*, Phys. Rev. Lett. **108** (2012) 245501.
 [4] Y. Awatani, *et al.*, Bulletin of the American Physical Society, 2016 March Meeting, T1.307.

BL6U

Self-Encapsulation of Epitaxial Silicene on ZrB₂ under a h-BN Monolayer

A. Fleurence¹, T. Yonezawa¹, M. P. de Jong², M. W. Ochapski², H. Yamane³,
N. Kosugi³ and Y. Yamada-Takamura¹

¹*School of Materials Science, Japan Advanced Institute of Science and Technology, Nomi 923-1292, Japan*

²*MESA+ Institute for Nanotechnology, University of Twente, 7500 AE Enschede, The Netherlands*

³*Institute for Molecular Science, Okazaki 444-8585, Japan*

Silicene, as a graphene-like silicon two-dimensional material has great expectation to give solution to scale down further the Si-based nanotechnologies. Even if a first transistor based on silicene could be fabricated [1], its quick oxidation in air indicates that silicene encapsulation is a crucial point to address for processing it routinely and fabricate reliable devices.

Silicene only exists in epitaxial forms. Among them, epitaxial silicene on ZrB₂ thin films grown on Si(111) has the particularity to form in a spontaneous and self-terminating way by the segregation of Si atoms from the silicon substrate [2].

It is also possible to fabricate a monocrystalline h-BN single layer covering the entire ZrB₂ thin film surface [3]. The deposition of silicon on this h-BN/ZrB₂ surface gives rise to a surface structure resembling that of epitaxial silicene. Si2*p* core-level and band structure, indicate that a silicene layer similar to that observed on bare ZrB₂ surface intercalates between the ZrB₂ thin film and the h-BN layer.

The purpose of these experiments at BL6U was to determine whether the h-BN layer is capable of preventing the oxidation of silicene.

Epitaxial silicene and oxide-free h-BN samples were prepared on-site by annealing at 800 °C under ultrahigh vacuum ZrB₂/Si(111) [2] and h-BN/ZrB₂/Si(111) samples we elaborated at our home laboratory. Silicon was evaporated by heating a piece of silicon in front of the h-BN/ZrB₂ surface held at room temperature (RT). Core-level spectra in the Si2*p* region were recorded with a surface-sensitive photon energy of $h\nu=130$ eV at RT.

The comparison of the core-level spectra of pristine silicene before and after a 5 min exposure to air (Figs. 1(a) and (b)) shows that the typical spectrum of silicene has turned into a Si oxide peak, which confirms the destruction of silicene in air. The spectrum recorded after deposition of silicon on h-BN/ZrB₂ is visible in Fig. 1(c). It differs from that of Fig. 1(a) due to an excess of silicon forming amorphous islands. Most importantly, after exposure to air with duration up to 60 min (Figs. 1(d)-(e)), the silicene component remains while a small oxide peak appears. It can be noticed that the line shape of the silicene component now more closely resembles that of pristine silicene, which indicates that the silicon oxide peak corresponds to the excess of Si.

The fact that the spontaneously encapsulated silicene survived an exposure long enough to allow for taking silicene in air opens the way to the possibility of processing silicene *ex-situ* in a controlled

environment.

This work was supported by the Joint Studies Program (No. 206, 2017-2018) of the Institute for Molecular Science.

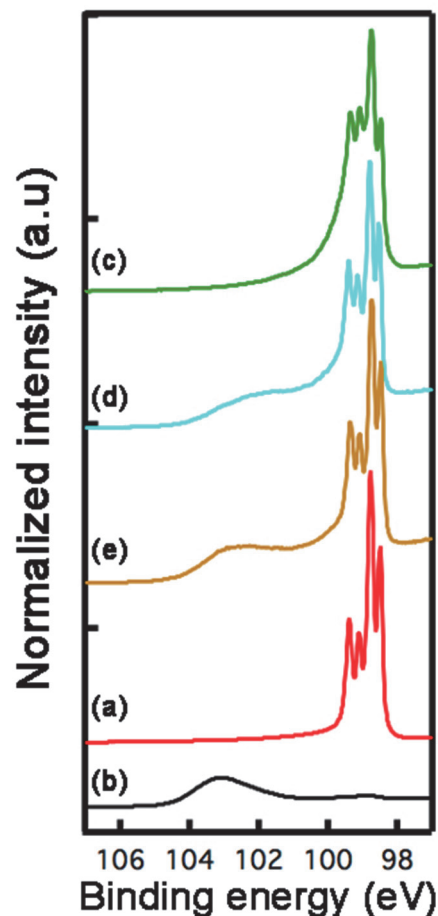


Fig. 1. (a) and (b): Normalized core-level spectra ($h\nu=130$ eV) in the Si2*p* region before and after a 5 min exposure to air of unencapsulated silicene. (c): Core-level spectrum of intercalated silicene. (d) and (e): Core-level spectra of intercalated silicene recorded after 5 and 60 min exposures to air.

[1] L. Tao *et al.*, *Nature Nanotech.* **10** (2015) 227.

[2] A. Fleurence *et al.*, *Phys. Rev. Lett.* **108** (2012) 245501.

[3] Z.-T. Wang *et al.*, *J. Appl. Phys.* **100** (2006) 033506.

BL6U

Thin-film Structure Depending on the Sulfur Substitution of Phenanthro-dithiophene Isomers

S. Ouchi¹, C. Numata¹, T. Yamaguchi^{2,3}, M. Meissner³, T. Ueba^{2,3}, H. Yamane^{2,3},
N. Kosugi^{2,3}, H. Yoshida¹, K. Hyodo⁴, Y. Nishihara⁴ and S. Kera^{1,2,3}

¹ Graduate School of Engineering, Chiba University, Chiba 263-8522, Japan

² Institute for Molecular Science, Okazaki 444-8585, Japan

³ The Graduate University for Advanced Studies (SOKENDAI), Okazaki 444-8585, Japan

⁴ Research Institute for Interdisciplinary Science, Okayama University, Okayama 700-8530, Japan

Even a subtle difference of intermolecular interaction can impose a large change in molecular ordering and electronic properties at organic semiconductor/metal interface. We examined two picene analogues, phenanthro-dithiophene isomers (PDT1 and PDT2), where the sulfur atoms are substituted differently as shown in Fig.1. We investigated the effect of the isomeric structure on the thin film structure as well as the electronic state.

The Au(110) substrate was cleaned by the repeated cycles of the Ar-ion sputtering and the subsequent annealing at 873 K. The monolayer (ML) films were prepared by the vacuum deposition onto the clean Au(110) surface at 300 K. The deposition rate was 0.05 nm/min. After depositing the ML, the PDT1 and PDT2 samples were annealed at 373 K.

Figure 2 shows the LEED images of PDT1 and PDT2 MLs on Au(110). Before the annealing, no sharp spots appear, while the sharp spots appear after the annealing for the PDT1 film. On the other hand, exhibits the stripe pattern for both as-grown and annealed films. The observed LEED images indicate that the PDT1 molecules on Au(110) form a long-range ordered structure in two directions, while the PDT2 molecules on Au(110) form it in only one-dimensional ordered structure. This difference is caused by a different intermolecular interaction assisted by the larger permanent dipole of PDT1.

Figure 3 shows the comparison of XPS spectra of the MLs of PDT1 and PDT2 ($h\nu = 335$ eV). The upper panel (a) show the spectra before the annealing and the bottom panel (b) show the one after the annealing. While no differences are discernible between PDT1 and PDT2 for the as-grown film, two changes are clearly observed in the spectra upon the annealing. First, the binding energy of PDT1 is smaller than that of PDT2 by about 100 meV in S2p spectra. Second, comparing C1s spectra, we also observed the binding energy shift of 30 meV and the different line shapes between PDT1 and PDT2. The observed XPS spectra indicate that the interaction between gold and sulfur of the PDT1 is stronger than that of the PDT2.

Understanding the relationship between the substitution position of the sulfur and the thin film structure more precisely, we would discuss the impacts of the thin film structure on the electronic states.



Fig. 1 Molecular structures of PDT1 (left) and PDT2 (right).

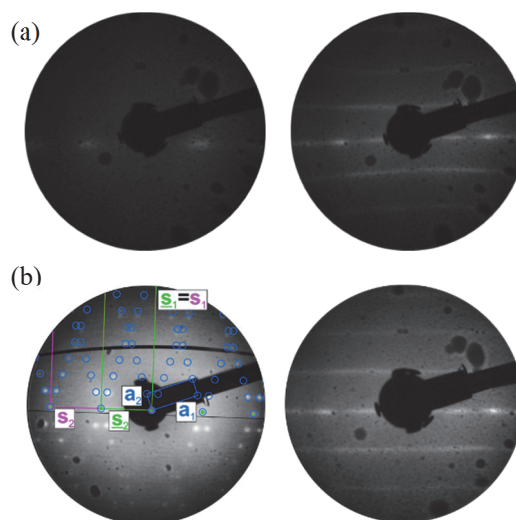


Fig. 2 Comparison of LEED images of PDT1 (left) and PDT2 (right). (a) before the annealing, (b) after the annealing.

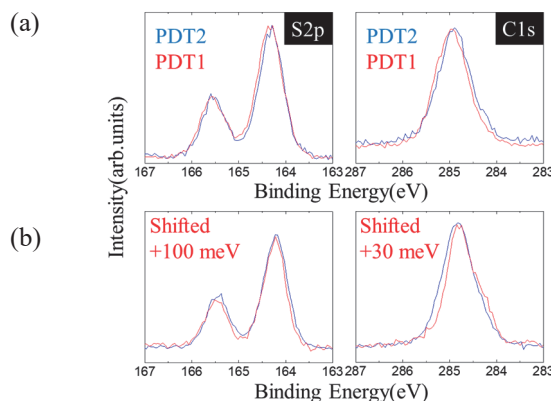


Fig. 3 Comparison of XPS spectra of PDT1 (red) and PDT2 (blue) MLs on Au(110). (a) before the annealing, (b) after the annealing (S2p and C1s peaks are aligned by 100 meV and 30 meV, respectively).

BL6U

Effects of Surface Adsorbates on the Electronic Structure of Excitonic Insulator Ta_2NiSe_5

 K. Fukutani¹, R. Stania¹, J. Jung^{1,2}, H. Yamane³, N. Kosugi³ and H. W. Yeom^{1,2}
¹Center for Artificial Low Dimensional Electronic Systems, Institute for Basic Science (IBS), Pohang 37673, Republic of Korea

²Department of Physics, Pohang University of Science and Technology (POSTECH), Pohang 37673, Republic of Korea

³Department of Photo-Molecular Science, Institute for Molecular Science, Okazaki 444-8585, Japan

Bound pairs of conduction band electrons and valence band holes, so-called excitons, can be formed within solids as a meta-stable state induced by external excitations, such as light irradiation. On the other hand, it has also been proposed theoretically for more than half a century that, for narrow-gap semiconductors and semimetals, a finite number of excitons can condense in the ground state to form what is called an excitonic insulator [1, 2]. However, due to number of experimental difficulties, the direct elucidation of such excitonic condensate was revealed only recently [3].

Ta_2NiSe_5 is among the few materials that are proposed to be excitonic insulators, and a number of studies have recently been performed to explore the nature of excitonic phase of this material, including the presence of many-body band gap near the Fermi level [4], band gap tuning by chalcogen substitutions [5], and layer-confined nature of excitonic phases [6].

Our previous studies on Ta_2NiSe_5 , utilizing the low-energy photon source, revealed that some surface adsorbates on this material induce a renormalization of the excitonic band structure. While the small excitonic radii in the surface-normal direction and their, layer-confined nature likely makes it possible for the surface adsorbates to modify the excitonic insulator phase at the topmost surface, the detailed mechanisms by which the renormalization occurs required further investigation.

In our experiments conducted at BL6U at UVSOR, the excitonic insulator phase of Ta_2NiSe_5 was investigated using the angle-resolved photoelectron spectroscopy (ARPES). As shown in Fig. 1(a), the unusual flattening of the topmost valence band is observed, which is believed to be a signature of the excitonic condensate for $T < T_c$. Our ARPES data also reveal the band structure perpendicular to the quasi-one-dimensional atomic chain as shown in Fig. 1(b) indicating small, yet finite inter-atomic chain interactions. Upon adsorption of potassium (K) as surface dopants, the Ta 4f core levels are seen to shift towards higher binding energy by ~ 40 meV (see Fig. 2), indicating that K adsorption results in the electron-doping at the surface. While further investigations, including model calculations, are required to make definite conclusions, the experimental results obtained at BL6U likely indicate the change in the free carrier concentration induced by the surface dopants screens the attractive Coulomb interaction between the

electrons and holes, thereby modifying the binding energy of excitons at condensate.

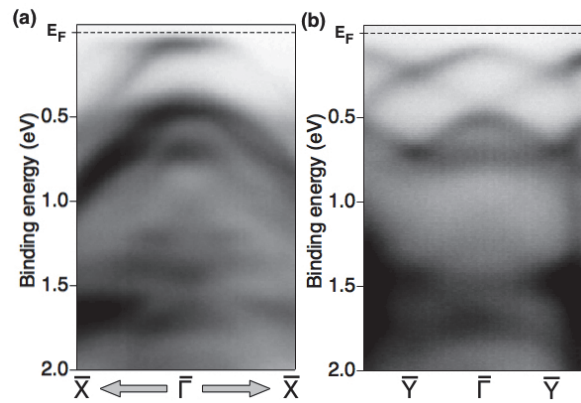


Fig. 1. (a) The ARPES band mapping taken at photon energy of $h\nu = 60$ eV along the Γ -X direction (parallel to the quasi-one-dimensional atomic chain) and (b) along the Γ -Y direction (perpendicular to the atomic chain). The sample temperature was maintained at $T = 40$ K.

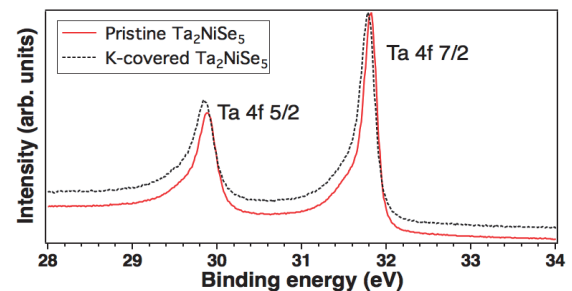


Fig. 2. The evolution of the Ta 4f core level spectra with upon K adsorption, taken at $h\nu = 60$ eV, $T = 40$ K. The both spin-orbit split pair of Ta 4f core levels are seen to move towards the higher binding energy with K adsorption, indicating the n -type doping on the sample surface.

- [1] N. F. Mott, *Phil. Mag.* **6** (1961) 287.
- [2] W. Kohn, *Phys. Rev. Lett.* **19** (1967) 439.
- [3] C. Monney *et al.*, *Phys. Rev. B* **79** (2009) 045116.
- [4] Y. Wakisaka *et al.*, *Phys. Rev. Lett.* **103** (2009) 026402.
- [5] Y. F. Lu *et al.*, *Nat. Commun.* **8** (2017) 1.
- [6] S. Y. Kim *et al.*, *ACS Nano* **10** (2016) 8888.

BL7U

Photoelectron Angular Distribution of Anthradithiophene on Graphite Investigated by Low-energy Angle Resolved Photoelectron Spectroscopy

T. Yamaguchi^{1,2}, M. Meissner², T. Ueba^{1,2}, R. Shiraishi^{1,2}, S. Ideta^{1,3},
K. Tanaka^{1,3} and S. Kera^{1,2}

¹*School of Physical Sciences, The Graduate University for Advanced Studies (SOKENDAI), Okazaki 444-8585*

²*Department of Photo-Molecular Science, Institute for Molecular Science, Okazaki 444-8585, Japan*

³*UVSOR Synchrotron Facility, Institute for Molecular Science, Okazaki 444-8585, Japan*

Ultraviolet photoelectron spectroscopy (UPS) is a very useful technique for studying the electronic structure of surfaces and interfaces. However, UPS with low energy photons is not well understood theoretically and experimentally because of the complicated photoemission process. For instance, resonances excitation between initial states and final states occur which cause unexpected scattering due to the relatively long dwell time of low-energy electrons at the surface/interface (potential trapping in intermediate states) [1]. Moreover, the asymmetric parameter of the photoelectron intensity greatly depends on the photon energy ($h\nu$). In this work, we investigated the photoelectron angular distribution (PAD) of the highest occupied molecular orbital (HOMO) for anthradithiophene (ADT), using low-energy angle-resolved UPS (LE-ARUPS), aiming to improve the understanding of the photoemission process in the low energy region at organic-metal interfaces.

Highly oriented pyrolytic graphite (HOPG) as the substrate was cleaned by annealing at 600 K for 2 h. An ADT molecule film of 5 Å was deposited on the HOPG at room temperature in a custom UHV chamber designed for organic layer deposition.

Figures 1 (a) and (c) show a LE-ARUPS intensity

map and energy distribution curves, respectively, taken at $h\nu = 21$ eV. The HOMO peak was observed at 1.40 eV and around -1.5 \AA^{-1} in Fig. 1 (a). Around the Γ point, there is no momentum dependence of the HOMO intensity. This is a typical PAD of the HOMO of the π -conjugated, planar molecules in a flat-lying orientation.

Figures 1 (b) and (d) show a LE-ARUPS intensity map and energy distribution curves, respectively, taken at 11 eV. It is impossible to observe the main HOMO-intensity lobe by 11 eV due to the low kinetic energy of the photoelectrons. Even though the photons come from right side of the image, the HOMO intensity at 0.5 \AA^{-1} is 3 times stronger than that at -0.5 \AA^{-1} . Moreover, a sudden change of intensity occurs at the Γ point. The direction of the p-polarized incident beam normally causes the opposite intensity distribution as found in Fig. 1 (a).

We clearly observed an interesting difference of PAD between $h\nu = 21$ eV and 11 eV which will be caused by non-trivial multi-particle events in the photoemission. The multiple scattering theory will be helpful to understand the origin of the PAD, hence to reveal the modification of the molecular orbital upon weak interactions.

[1] S. Tanaka *et al.*, *Sci. Rep.* **3** (2013) 3031.

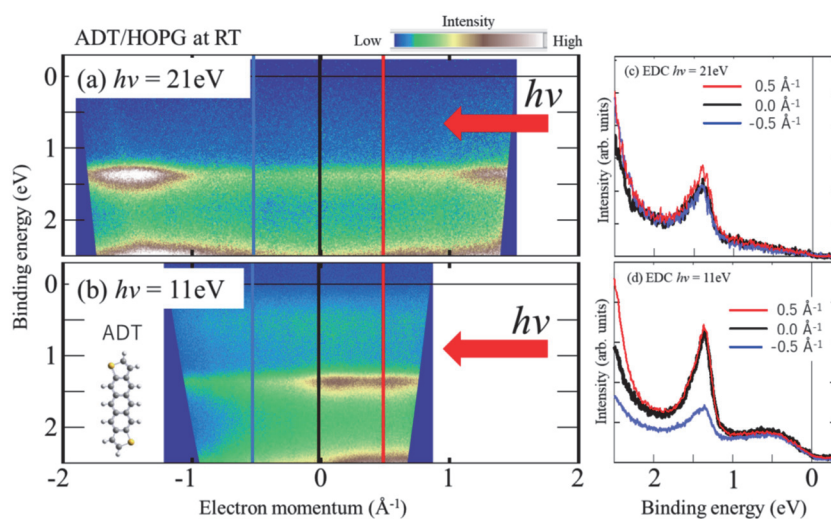
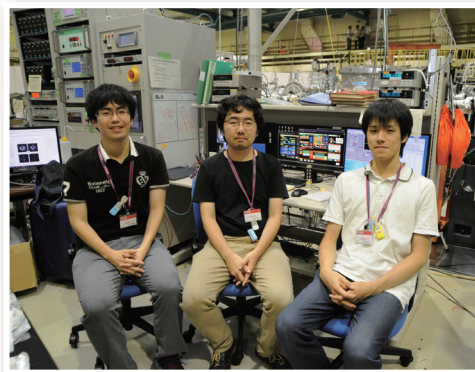
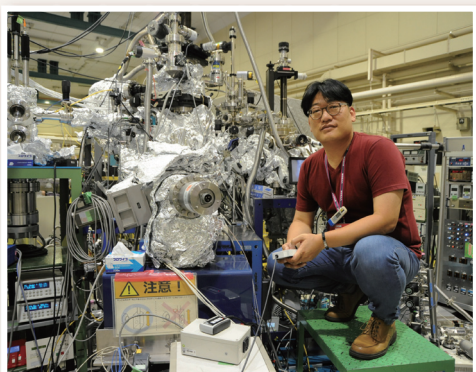
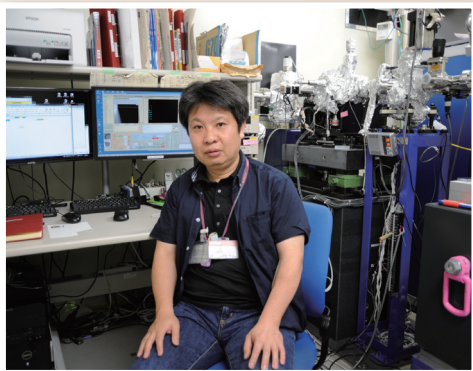
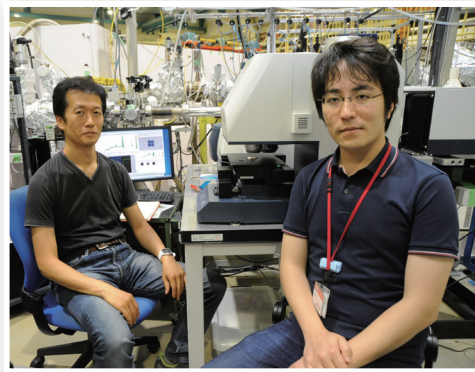
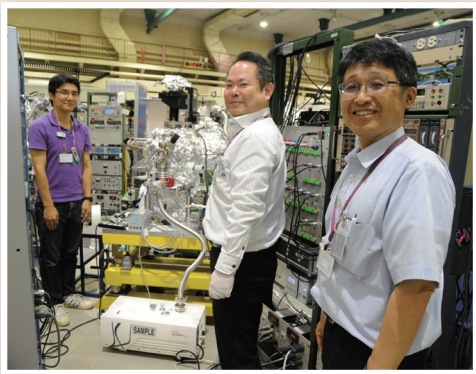
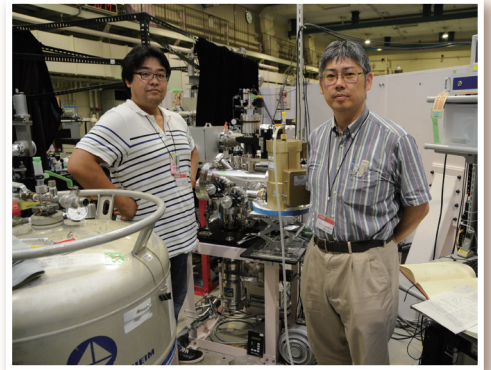
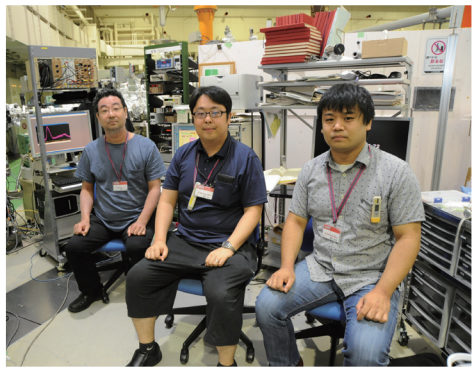
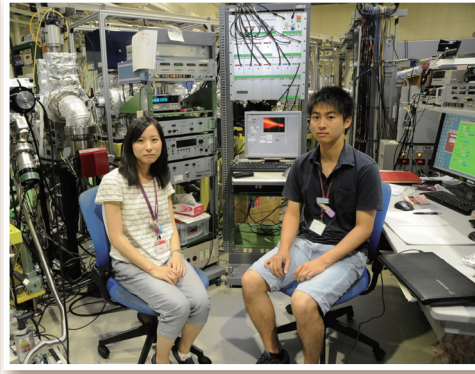
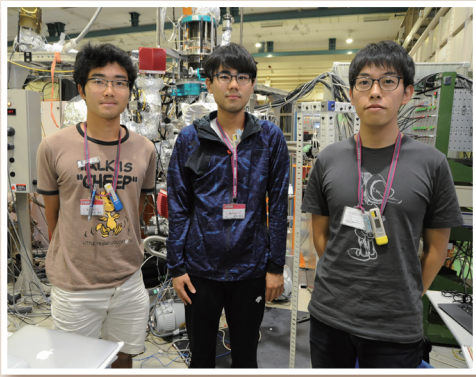
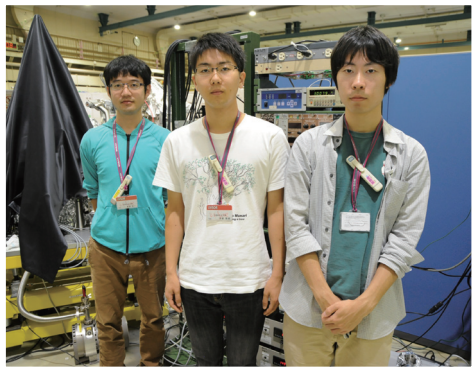
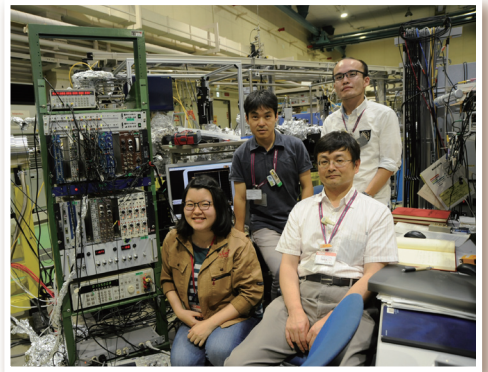
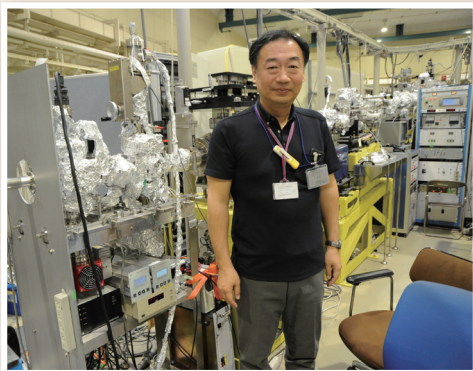
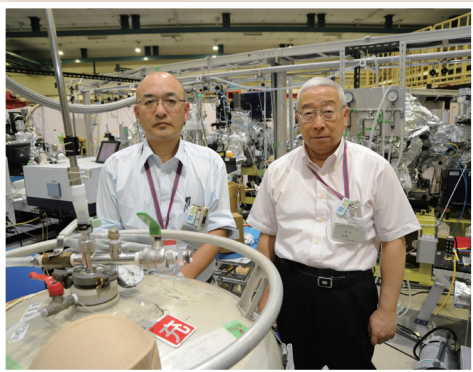
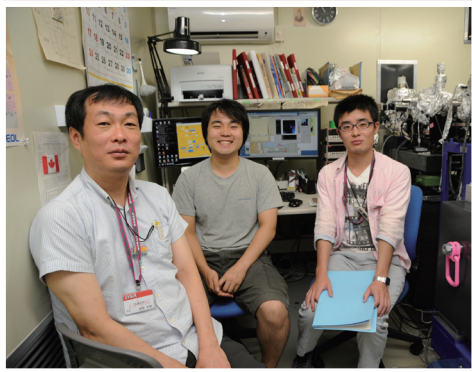
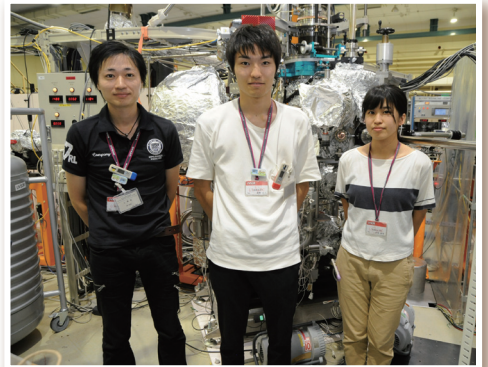
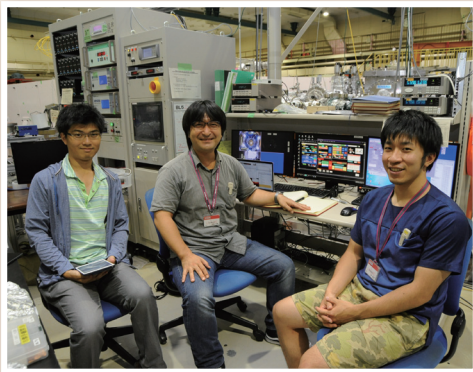
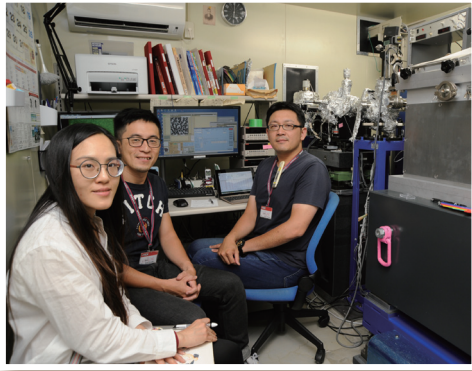


Fig. 1. LE-ARUPS intensity map for ADT/HOPG taken at room temperature using $h\nu = 21$ eV (a) and 11 eV (c). Both images were prepared by combining 8 and 7 images taken every 12° . Energy distribution curves at -0.5 \AA^{-1} , 0.0 \AA^{-1} and 0.5 \AA^{-1} taken for $h\nu = 21$ eV (b) and 11 eV (d). Red arrows represent the incident light direction. The structure of the ADT molecule is shown as an inset in (b).

UVSOR User 5



UVSOR User 6



The background is a solid purple color with several geometric patterns. A large, semi-transparent circular graphic is centered on the right side, featuring concentric rings and a dotted border. Diagonal lines and a grid of small dots are also visible in the lower-left quadrant.

III-5

Life, Earth and
Planetary Sciences

BL1U

Optical Activity Emergence in Amino-Acid Films by Vacuum-Ultraviolet Circularly-Polarized Light Irradiation (I) - Experimental Setup -

J. Takahashi¹, K. Matsuo², Y. Izumi², K. Kobayashi¹, M. Fujimoto³ and M. Katoh³

¹*Faculty of Engineering, Yokohama National University, Yokohama 250-8501, Japan*

²*Hiroshima Synchrotron Radiation Center, Higashi-Hiroshima 739-0046, Japan*

³*UVSOR Synchrotron Facility, Institute for Molecular Science, Okazaki 444-8585, Japan*

The origin of homochirality in terrestrial bioorganic compounds (dominant L-amino acid and D-sugar) is one of the most mysterious issues that remain unresolved in the study of the origin of life. Because bioorganic compounds synthesized in abiotic circumstances are intrinsically racemic mixtures of equal amounts of L- and D-bodies, it is hypothesized that chiral products originated from asymmetric chemical reactions. These types of asymmetric reactions could have possibly been derived from physically asymmetric excitation sources in space, that is “chiral radiation”, and the chiral products would have been transported to primitive Earth resulting in terrestrial biological homochirality (Cosmic Scenario) [1]. Eventually, terrestrial observations of circularly-polarized light (CPL) radiation due to scattering by interstellar dust clouds in star formation regions have been reported [2].

Several ground experiments have already examined asymmetric photochemical reactions in simple biochemical molecules by CPL. We reported optical activity emergence in solid-phase films of racemic mixtures of amino acids by CPL irradiation of 215 nm in wavelength from free electron laser (FEL) of UVSOR-II [3].

Recently, we are carrying out the measurement of CPL irradiation wavelength dependence of optical activity emergence by tuning undulator gap conditions. We have already also reported the optical activity emergence by using CPL irradiation of 230, 215, and 203 nm in wavelength from undulator BL1U of UVSOR-III [4].

Presently, we are trying to introduce optical activity by vacuum ultraviolet (VUV) CPL irradiation in shorter wavelength than 200 nm. As for the sample, we formed thin solid films of racemic DL-alanine on fused quartz substrates using a thermal-crucible vacuum evaporator from crystal powders of DL-alanine as a sublimation source. Sublimation temperature was in the range of 150~200°C and pressure of the vacuum chamber was approximately 10^{-2} Pa throughout the evaporation process. In order to introduce optical activity into the racemic film, we irradiate them with CPL introduced from undulator BL1U of UVSOR-III. The samples were set in a vacuum sample chamber preventing VUV CPL attenuation by air absorption in shorter wavelength than 200 nm (Fig.1). On the beam entrance side of the vacuum sample chamber, a gate valve with a vacuum-sealed MgF₂ window was mounted. The irradiated CPL

wavelengths were 180, 155, and 120 nm corresponding to photon absorption bands of alanine molecule. The irradiated photon number was measured with photoelectron current of a silicon photodiode (International Radiation Detectors, Inc.) settled at the sample position. The typical energy dose calibrated by quantum efficiency of the silicon photodiode was approximately 50mWhour.

In order to clarify the optical anisotropy of the films before and after VUV CPL irradiation, we measured the synchrotron radiation (SR) circular dichroism (CD) at beamline BL-12 of Hiroshima Synchrotron Radiation Center (HiSOR). In order to delete the effects of linear dichroism (LD) and/or linear birefringence (LB) components, dependence on sample rotation angle (0, 45, 90, and 135degrees) of the CD spectra was measured.

Through the VUV CPL irradiation experiments and the detailed analysis of SR-CD spectra, we are aiming to clarify full mechanism of the optical activity emergence, which potentially has relevance to the origin of terrestrial biological homochirality.

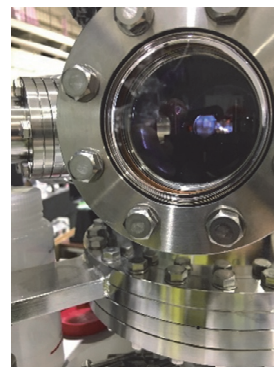


Fig. 1. Photo of VUV CPL irradiation experiment on BL1U using a vacuum sample chamber.

- [1] W. A. Bonner, *Orig. Life Evol. Biosph.* **21** (1991) 59.
- [2] T. Fukue *et al.*, *Orig. Life Evol. Biosph.* **40** (2010) 335.
- [3] J. Takahashi *et al.*, *Int. J. Mol. Sci.* **10** (2009) 3044.
- [4] K. Matsuo *et al.*, *UVSOR Activity Report* **44** (2017) 157.

BL1B, BL7B

Giant Thermal Effect of Vibration Modes of Single-Crystalline Alanine

 Z. Mita¹, H. Watanabe^{1,2} and S. Kimura^{1,2}
¹ Graduate School of Frontier Biosciences, Osaka University, Suita, 565-0871, Japan

² Department of Physics, Graduate School of Science, Osaka University, Toyonaka, 560-0043, Japan

Amino acids are the most basic molecules of living bodies. Since almost all amino acids are chiral materials, they have enantiomers, L- and D-form. Although amino acids are well-known, fundamental physical properties have hardly been studied. Owing to the crystal structure, strong anisotropy of optical constants and ferroelectricity are expected. However, the optical measurements using single-crystalline samples have never been studied so far, neither the temperature dependence. Here we report the temperature-dependent anisotropic reflectivity spectra of single-crystalline L-alanine that has the simplest molecular structure among amino acids having chirality.

We have grown the single crystal by using the solvent evaporation method and confirmed to be orthorhombic structure reported previously [1]. Polarized optical spectra from the terahertz (THz) to vacuum-ultraviolet (VUV) regions have been measured by using BL1B [2] and BL7B [3] at UVSOR-III and laboratorial equipments. Temperature dependence of anisotropic reflectivity spectra in the THz region are shown in Fig. 1. Some peaks owing to molecular vibrations appear. The optical spectra are strongly anisotropic and all of these peaks have large temperature dependency. For instance, the intensity of the peak appearing at the photon energy of about 15 meV (indicated by a red square in Fig. 1) in the configuration of the electric vector parallel to the c -axis ($E // c$) increases 4 times larger with decreasing temperature from 300 K to 10 K. The obtained reflectivity spectra were converted to the optical conductivity spectra by using the Kramers-Kronig analysis. The temperature-dependent peak at 15 meV is shown in Fig. 2.

To explain the temperature dependence, we adopt the Morse potential that is one of the simplified potentials having anharmonicity [4]. Here, we assume the Boltzmann distribution for oscillators' occupation. Assuming the multiple excitation among energy levels, the temperature dependence of the peak in Fig. 2 can be reproduced by using the summation of Lorentz functions owing to the excitations. The results reproduce well as shown by thin lines in Fig. 2. Furthermore, using the parameters obtained from the simulation, the bottom energy of the Morse potential can be evaluated as 822 meV at 10 K and 675 meV at 300 K. The change of the potential shape is the origin of the giant thermal effect of the molecular vibrations of single-crystalline L-alanine.

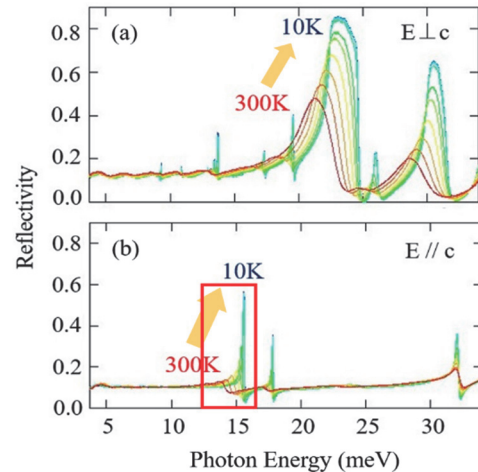


Fig. 1. Anisotropic reflectivity spectra at temperatures from 10 to 300 K in THz regions perpendicular (a) and parallel (b) to the c -axis.

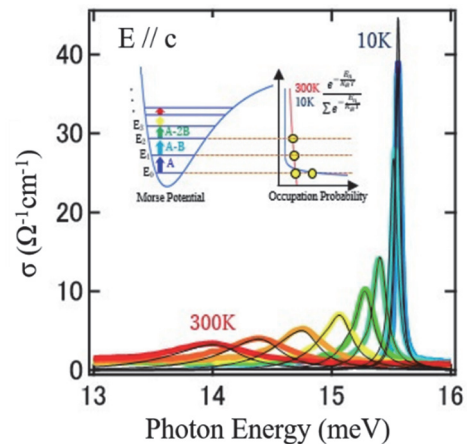


Fig. 2. Temperature-dependent optical conductivity [$\sigma(\omega)$] spectra of the 15 meV peak (thick lines). Thin lines are the simulation results using a simplified anharmonic Morse potential.

[1] M. Fleck and A. M. Petrosyan, *Salts of Amino Acids-Crystallization Structure and Properties* (Springer, 2014) p. 26.

[2] S. Kimura, E. Nakamura, K. Imura, M. Hosaka, T. Takahashi, M. Katoh, *J. Phys.: Conf. Ser.* **359** (2012) 012009.

[3] K. Fukui, H. Miura, H. Nakagawa, I. Shimoyama, K. Nakagawa, H. Okamura, T. Nanba, M. Hasumoto, T. Kinoshita, *Nucl. Instrum. Meth. Phys. Res. A* **467-468** (2001) 601.

[4] P. M. Morse, *Phys. Rev.* **34** (1929) 57.

BL3U

Novel Insights to Cloud Water Microphysics Using Synchrotron-excited XAS

J. J. Lin¹, G. Michailoudi¹, H. Yuzawa², H. Iwayama^{2,3}, M. Nagasaka^{2,3},
M. Huttula¹, N. Kosugi^{2,3} and N. L. Prisle¹

¹Nano and Molecular Systems Research Unit, University of Oulu, Oulu 90041, Finland

²UVSOR Synchrotron Facility, Institute for Molecular Science, Okazaki 444-8585, Japan

³School of Physical Sciences, The Graduate University for Advanced Studies (SOKENDAI), Okazaki 444-8585, Japan

Cloud droplets in the atmosphere are complex aqueous mixtures of organic and inorganic constituents, but their exact composition and the nature of aqueous phase molecular interactions are extremely challenging to quantify [1]. Amphiphilic compounds present in the organic aerosol fraction are known to self assemble into micelles, but direct chemical information on the aqueous phase interactions of amphiphilic monomers and their aggregate structures has been lacking.

Two types of samples were analyzed with synchrotron radiation X-ray absorption spectroscopy using the liquid cell setup at BL3U [2]: 1) cloud water collected from October 10-14 at the Finnish Meteorological Institute Pallas-Sodankylä Global Atmosphere Watch station in the sub-Arctic region in Finnish Lapland as part of the 7th Pallas Cloud Experiment from September 1 to November 30; and 2) organic micellar systems composed of n-octanoic acid, n-decanoic acid, and sodium n-decanoate dissolved in water at varying multiples of their critical micelle concentration (CMC). A summary of the samples measured is given in Table 1.

For the cloud water samples, both the oxygen K-edge in the 528-550 eV range and the carbon K-edge in the 280-300 eV range were studied. Unfortunately, due to the apparently very low concentration of organic material in the cloud water, presumably from very clean Arctic conditions, any difference between cloud water spectra and pure water spectra could not be detected. Another batch of the cloud water sample will be subject to various complementary analyses to confirm this.

For the aqueous organic micellar solutions, the carbon K-edge in the 280-300 eV range was studied. Photon energies in the 280-285 and 290-300 eV range were scanned at 0.1 eV resolution while photon energies in the 285-290 eV range were scanned at 0.02 eV resolution in order to specifically capture the aliphatic R(CH)R' and carboxylic C(=O)OH carbon absorption peaks from monomers to identify shifts in peak location due to the difference in chemical environment between monomers and micelles in solution.

Preliminary absorption spectra at the C 1s absorption edge for sodium n-octanoate in water at various concentrations along with pure octanoic acid are shown in Fig. 1. Background absorption due to

water and the cell membranes have been removed. For all the samples, one main peak is observed at around 289 eV. For sodium n-octanoate solution below the CMC, the absorption spectra before and after the main feature are less than those solutions above the CMC. Interestingly, the higher the sodium n-octanoate concentration in solution, the more the absorption spectra start to resemble that of pure octanoic acid. The measurements hold promise for detecting the aqueous-phase interactions of organic monomer and micellar structures compounds in solution.

Table 1. Summary of samples measured

Sample	CMC [mM]	Concentrations	Number of scans
Cloud Water	—	—	5
n-octanoic acid	140. [3]	0.75, 1.25, 2, 3, 4, 6, and 8 times CMC; pure	15
Sodium n-octanoate	340.0 [4]	0.75, 2, 3, 4, and 5 times CMC	7
Sodium n-decanoate	94.0 [4]	2, 3, 4, 6, and 8 times CMC	10

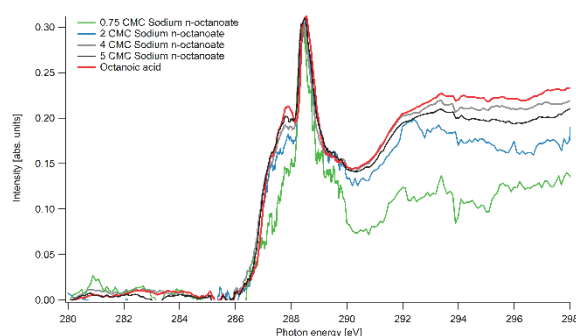


Fig. 1. Preliminary absorption spectra for sodium n-octanoate solutions at various concentrations together with that of pure octanoic acid.

- [1] T. Kurtén *et al.*, *J. Phys. Chem. A* **119** (2014) 4509.
 [2] M. Nagasaka *et al.*, *J. Electron Spectrosc.* **177** (2010) 130.
 [3] A. N. Campbell and G. R. Lakshminarayanan, *Can. J. Chem.* **43** (1965) 1729.
 [4] K. Quast, *Miner. Eng.* **19** (2010) 582.

BL4U

Feasibility Study of Sulfur Speciation High-spatial Resolution Mapping in Extraterrestrial Organics by STXM-XANES

M. Ito¹, R. Nakada¹, H. Suga², T. Ohigashi³, Y. Kodama⁴ and H. Naraoka⁵

¹ Kochi inst. for Core Sample Res., JAMSTEC, Nankoku 783-8502, Japan

² Hiroshima University, Higashihiroshima 739-0046, Japan

³ UVSOR Synchrotron Facility, Institute for Molecular Science, Okazaki 444-8585, Japan

⁴ Marine Works Japan LTD., Japan

⁵ Kyushu University, Fukuoka 819-0395, Japan

Sulfur is one of the major elements in terrestrial and extraterrestrial organics. The elemental compositions of the Murchison IOM (insoluble organic matter) are proposed to be C₁₀₀H₇₀O₂₂N₃S₇ [1] or C₁₀₀H₄₈N_{1.8}O₁₂S₂ [2]. Because sulfur shows a wide range in oxidation state (-2 to +6) with both electropositive and electronegative elements, reduced and oxidized sulfur species have been found in various carbonaceous chondrites [3, 4]. Therefore, understanding of speciation of sulfur and its distribution within organics in a carbonaceous chondrite may provide the secondary alteration processes of thermal metamorphism and aqueous alteration in the parent body.

Synchrotron based X-ray absorption near edge spectroscopy (XANES) is a powerful analytical tool to characterize and quantify chemical speciation, functional group and bonding environment of the sample. In the field of cosmochemistry, many researches were carried out to identify functional groups of C, N and O in extraterrestrial organics (i.e., IOM in carbonaceous chondrites [5], cometary returned sample [6], organics found in Hayabusa Category-3 particles [7], organics in IDPs [8], and organic component extracted from halite grain in Monahans LL chondrite [9]). However, sulfur study using XANES in the extraterrestrial organics is very rare [3, 10].

In this study, we report preliminary results of sulfur speciation measurements by L₃-edge XANES of series sulfur bearing terrestrial organics to obtain reference spectra, and of S, N, C and O-XANES in the FIB section of the Murchison CM2 carbonaceous chondrite (147 x 187 pixels, 22 x 28 μm²: spatial resolution = 150 nm) using scanning transmission X-ray microscope (STXM) at Inst. Mole Sci. UVSOR BL4U. We also took a sulfur image

(L₃-edge XANES) of organics extracted from Asuka881458 CM2 chondrite for comparison in terms of sulfur distribution and speciation.

We show nine reference sulfur L₃-edge spectra measured by the STXM. Reference sulfur bearing organics are sodium lauryl sulfate, sodium methanesulfonate, dibenzothiophene, thianthrene, DL-methionine, DL-methionine sulfone, L-cysteic acid, L-cystein, and L-cystine (Fig. 1). These organics show different absorption curves which related to sulfur related chemical bond (e.g., sulfate, sulfone, thiol).

We successfully obtained high resolution sulfur STXM images of both FIB sections of Murchison and organics from Asuka881458. We will continue to measure another primitive chondrite for understanding of diversity of organics based on sulfur speciation. We plan to combine sulfur isotope imaging with NanoSIMS for same sections that used in this study.

[1] L. Remusat, EPJ Web of Conferences **18** (2011) 05002.

[2] Gilmour, Meteorites, Comets, and Planets, Treatise on Geochemistry (2005) 269.

[3] Orthous-Daunay *et al.*, EPSL **300** (2010) 321.

[4] W. J. Cooper *et al.*, Science **277** (1997) 1072.

[5] G. D. Cody *et al.*, Meteor Planet Sci. **43** (2011) 353.

[6] S. A. Sanford *et al.*, Science **314** (2006) 1720.

[7] H. Yabuta *et al.*, EPS **66** (2014) 156.

[8] G. J. Flynn *et al.*, Geochim Cosmochim Acta **67** (2003) 4791.

[9] Chan *et al.*, Science Advance **4** (2018) eaao3521.

[10] M. Bose *et al.*, Meteor Planet Sci. **52** (2017) 546.

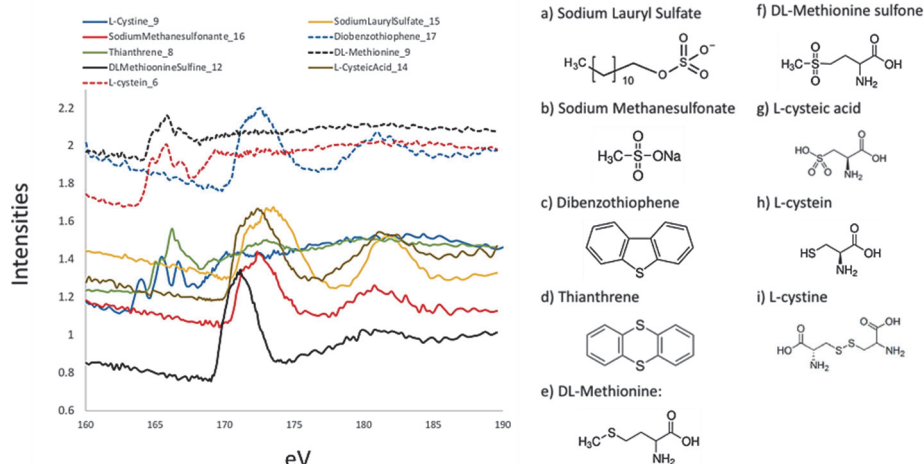


Fig. 1. Sulfur bearing organics of L₃-edge STXM-XANES spectrum

BL4U

Organic Vein in a Primitive Clast in the Carancas Meteorites

Y. Kebukawa¹, M. E. Zolensky², T. Ohigashi³ and Y. Inagaki³

¹Faculty of Engineering, Yokohama National University, Yokohama 240-8501, Japan

²ARES, NASA Johnson Space Center, Houston, TX 77058, USA

³UVSOR Synchrotron Facility, Institute for Molecular Science, Okazaki 444-8585, Japan

Primitive xenolithic clasts are often found in various groups of meteorites [e.g., 1, 2]. These xenoliths sometime contain unique carbonaceous matter. We have been analyzed these using scanning transmission X-ray microscopes (STXM) combined with other microscopic techniques [3-5]. Some of these could be candidates of primordial trans-Neptunian object (TNOs) that have been scattered by giant planetary migration. It was suggested that numerous bodies were injected from outer Solar System into the main asteroid belt, where modeling shows they can successfully reproduce the observed D/P-type asteroid populations [e.g., 6]. After implantation, some of the D/P-asteroids would have collided with parent body(s) of ordinary chondrites (S-type asteroids). Some of the fragments from D/P-asteroids left in the ordinary chondrite parent body(s) and eventually could be delivered to Earth as meteorites [7]. The Carancas meteorite is a H4-5 ordinary chondrite that contains a primitive xenolithic clast rich in organic matter.

We are conducting coordinated analysis of organic matter in the clast using various methods [8]. 100 nm-thick FIB sections were prepared from the clast using a Quanta 3d field-emission gun FIB instrument at NASA JSC. We investigated the FIB sections with C,N,O-X-ray absorption near-edge structure (XANES) using the STXM at BL4U of UVSOR.

Figure 1 shows a carbon map containing ~10 μm C-rich vein in the clast from Carancas meteorite. C-XANES spectrum of the C-rich vein shows 285.0 eV absorption designed to aromatic carbon and 286.5 eV absorption designed to ketone (C=O), as well as a weak absorption at 288.7 eV assigned to carboxyl/ester [(C=O)O] (Fig. 2). The N-XANES shows absorption at 398.6, 399.7 and 401.1 eV. The 398.6 and 399.7 eV can be attributed to imine/nitrile/pyridine groups, and 401.1 eV can be attributed to amide/pyrrole groups [e.g., 9].

The C-XANES features confirmed that the clast was not subjected to thermal metamorphism in the Carancas H4-5 parent body. The C-XANES of the organic vein is distinguished from that of typical primitive chondritic insoluble organic matter (IOM), and dominated in C=O structures. It indicates that the organic matter is originated in relatively oxygen rich condition. The vein-like morphology indicates that fluid was involved during formation of this structure. Thus the organic vein is formed during aqueous alteration in the clast parent body.

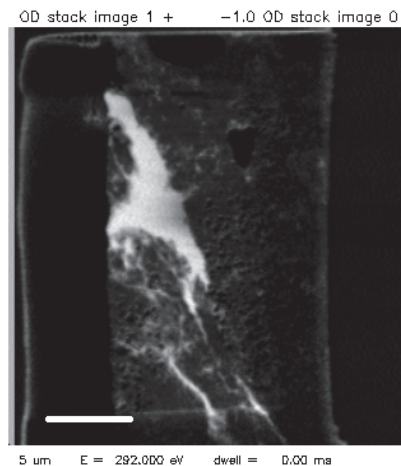


Fig. 1. Carbon map obtained from a FIB section from the clast in the Carancas meteorite. The white area is organic vein-like structure. The map was derived with 292 eV and 280 eV images. The scale bar is 5 μm .

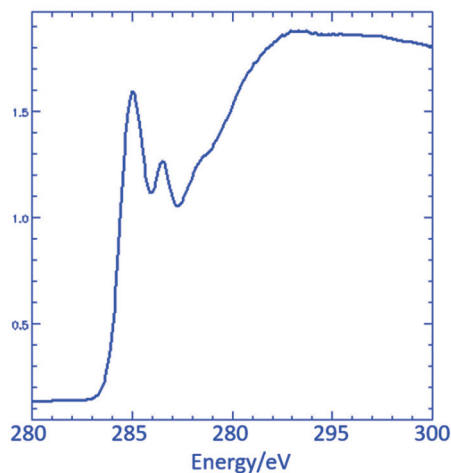


Fig. 2. The C-XANES spectrum obtained from the organic vein in the clast from the Carancas meteorite.

- [1] A. J. Brearley, *Geochim. Cosmochim. Acta* **54** (1990) 831.
- [2] M. Zolensky *et al.*, *Meteoritics* **27** (1992) 596.
- [3] Y. Kebukawa *et al.*, *Geochim. Cosmochim. Acta* **196** (2017) 74.
- [4] Q. H. S. Chan *et al.*, *Sci. Adv.* **4** (2018) eaao3521.
- [5] Y. Kebukawa *et al.*, *Nat. Astro.* Submitted.
- [6] H. F. Levison *et al.*, *Nature* **460** (2009) 364.
- [7] M. Zolensky *et al.*, LPSC abst. (2018) 1789.
- [8] Q. H. S. Chan *et al.*, LPSC abst. (2018) 1191.
- [9] P. Leinweber *et al.*, *J. Synchrotr. rad.* **14** (2007) 500.

BL4U

Direct Observation of the Basalt-cell Interface by STXM -Study on the Mechanism of Microbial Alteration of Oceanic Crust-

S. Mitsunobu^{1,2}, Y. Ohashi² and T. Ohigashi³¹Department of Agriculture, Ehime University, Matsuyama 790-8566, Japan²Institute for Environmental Sciences, University of Shizuoka, Shizuoka 422-8526, Japan³UVSOR Synchrotron Facility, Institute for Molecular Science, Okazaki 444-8585, Japan

Alteration of oceanic basalts is an important water-rock interaction ubiquitously occurring in the vast oceanic crust. The alteration of oceanic basalt has a significant impact on Earth's climate on a geological timescale by providing a sink for atmospheric CO₂ through carbonization of oceanic basalts (e.g., Standigel et al., 1989; Sleep & Zahnle, 2001). The fresh basalt rock contains abundant Fe (roughly 9 wt.%) and its dominant species is ferrous iron (Fe(II)) and Fe(II)/Fe_{total} ratio in fresh basalt ranges between 82 and 90% [1]. Hence, when the oceanic basalts are exposed to oxidative conditions (e.g., oxygen-saturated seafloor), the Fe(II) in basalts is gradually oxidized to Fe(III) in the alteration process on a geological timescale even at low temperature in deep seafloor [2]. Recent studies have noticed that oceanic microbes (mainly bacteria and archaea) play a significant role to the oxidation of Fe(II) in the basalt. Also, microbial Fe(II) oxidation accelerate the whole alteration process of oceanic crust [2], as the rate of biogenic Fe(II) oxidation is generally more rapid than that of abiotic (chemical) oxidation. There have been considerable efforts to identify mechanisms of the oxidation of Fe(II) involved in the oceanic basalt. However, little is known on the mechanism of microbial Fe(II) in the basalt alteration, because direct chemical speciation of metals and biomolecules at mineral-microbe interface has been difficult due to high spatial resolution in analysis.

Here, we investigated the mechanisms of the Fe(II) oxidation in basalt alteration by scanning transmission X-ray microscopy (STXM) based C and Fe near edge X-ray absorption fine structure (NEXAFS) analyses at UVSOR BL4U. The basalt samples used in the study was the basalt glass samples incubated for 12 months at deep seafloor (the depth of water: ca. 700 m) in Izu-Ogasawara bonin.

Figure 1 shows the STXM-based merged Fe/C image and C 1s NEXAFS. The C NEXAFS showed that the spectrum measured at bacteria cell-basalt interface in the incubated basalt glass contains a significant peak specific for acidic polysaccharides like alginate, addition to the other biomolecules (protein, DNA, and lipid), and this spectral feature was not found in those of the other area. This finding indicates that the bacteria on the basalt glass produce the polysaccharide-rich extracellular polymeric substances (EPS) at the cell-basalt interface. The biogenic polysaccharides often form a strong complex

with Fe ion under wide pH region [3]. Thus, our finding obtained by C NEXAFS analysis imply that observed bacteria could produce the polysaccharides to enhance the dissolution of basalt by the complexation and/or mediate contact between the cell and basalt surface. These findings could be important information for understanding key mechanism of biogenic alteration of ocean crust, basalt.

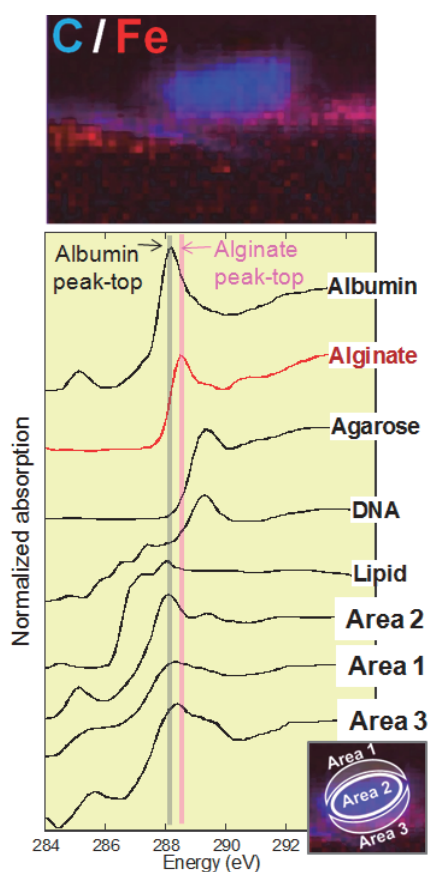


Fig. 1. STXM-based C and Fe images (upper) and C 1s NEXAFS spectra (bottom).

[1] A. Bezos and E. Humler, *Geochim. Cosmochim. Acta* **69** (2005) 711.

[2] W. Bach and K.J. Edwards, *Geochim. Cosmochim. Acta* **67** (2003) 3871.

[3] S. Mitsunobu *et al.*, *Chem. Lett.* **44** (2015) 91.

BL4U

3-Dimensional Observation of a Cell Nucleus by Using a Scanning Transmission X-ray Microscope

T. Ohigashi^{1,2}, A. Ito³, K. Shinohara³, S. Tone⁴, Y. Inagaki¹ and N. Kosugi^{1,2}¹UVSOR Synchrotron Facility, Institute for Molecular Science, Okazaki 444-8585, Japan²School of Physical Sciences, The Graduate University for Advanced Studies (SOKENDAI), Okazaki 444-8585, Japan³School of Engineering, Tokai University, Hiratsuka, 259-1292, Japan⁴Graduate School of Advanced Science and Technology, Tokyo Denki University, Hatoyama, 350-0394, Japan

Apoptosis is a process of a programmed cell death observed in many biological processes. Nuclear condensation and DNA fragmentation occur during execution of apoptosis and this process is classified into 3 stages. Generally, apoptosis is observed by using fluorescence microscope with staining process but high resolution image, chemical compositions and 3-dimensional (3D) structure are still unclear. Then, we use a scanning transmission X-ray microscopy (STXM). In these years, we have been developing computed tomography (CT) to perform 3D spectroscopy by changing the energy of the X-ray [1, 2]. By using this technique, 3D distributions of protein and DNA of an isolated cell nucleus were observed.

As the sample preparation, isolated nuclei from HeLa S3 cells were attached on a slide glass using cell adhesive agent, Cell-Tak (Fisher Scientific), and were fixed by glutaraldehyde. After critical point drying process, the isolated cell nucleus was glued on a tip of a tungsten needle. The sample was mounted on a CT sample cell.

Experiment was performed at BL4U. To perform CT, a focal depth of a Fresnel zone plate (FZP) should be longer than thickness of the sample to assume paths of the X-rays through the sample as a parallel beam. Therefore, the FZP with smaller NA was used instead of higher spatial resolution. In this experiment, the FZP with the outermost zone width of 45 nm was used and the focal depth of 5.2 μm at 400 eV is nearly enough length for a cell nucleus.

NEXAFS spectra of DNA and histone as protein around N K-edge are shown in Fig.1. These spectra show remarkable difference on $1s-\pi^*$ transition so that they were used as reference spectra. In CT measurement, 41 X-ray transmission images (energy stack) were acquired by changing the X-ray energy from 397 to 410 eV. 50 energy stacks were acquired by rotating the sample 3.6° each (180° rotation in total). Then, a size of one image was $8 \times 8 \mu\text{m}^2$ with 50×50 pixels and a dwell time was 2 ms per a pixel.

For reconstruction of 3D chemical distributions, the X-ray transmission images of the energy stack were aligned and 2D distributions of DNA and protein were obtained by fitting their reference spectra to each energy stack by using aXis2000 software. Sinograms were extracted from data sets of the 2D distributions of DNA and protein respectively and cross sectional images were reconstructed by home-made filtered

back-projection algorithm. The reconstructed 3D distribution of DNA and 2D distributions of DNA and protein are shown in Fig. 2. While the 2D distribution of DNA in Fig. 2(b) shows distinct sub-nuclear structures (shown by arrows), presumably nucleoli, that of protein in Fig. 2(c) shows only the compartment like structures and less protein in the nucleoli.

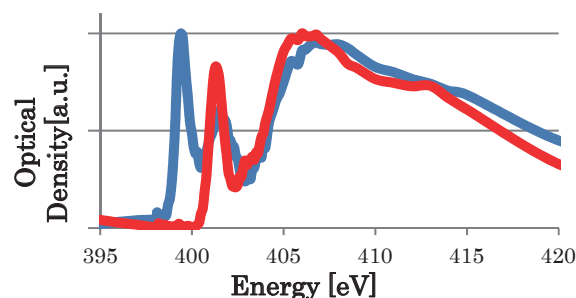


Fig. 1. NEXAFS spectra of DNA (blue) and protein (red) at N K-edge.

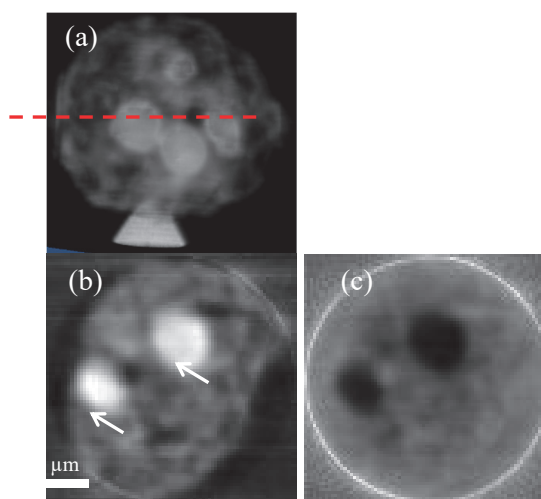


Fig. 2. (a) 3D volume projection image of distribution of DNA and 2D distribution of (b) DNA and (c) protein at the dashed line in (a).

[1] T. Ohigashi, Y. Inagaki, A. Ito, K. Shinohara and N. Kosugi, UVSOR Activity Report **44** (2017) 39.

[2] T. Ohigashi, Y. Inagaki, A. Ito, K. Shinohara and N. Kosugi, J. Phys.: Conf. Ser. **849** (2017) 012044.

BL4U

Investigation of Carbonaceous Materials Inside Moderately Shocked Ureilite Using STXM-XANES System

M. Uesugi¹, T. Ohgashi² and Y. Inagaki²

¹Japan Synchrotron Radiation Research Institute, JASRI, Sayo 679-5198, Japan

²UVSOR Synchrotron Facility, Institute for Molecular Science, Okazaki 444-8585, Japan, Japan

Ureilite is a unique class of meteorite which shows small carbonaceous materials inside veins or sometime inclusion like structure, inside the rocky matrix [1-3]. It shows iron-sulfide inclusions or veins, indicating that the meteorite would not come from differentiated asteroids (Fig. 1). On the other hand, silicate materials inside the ureilite shows igneous texture, and their composition is similar to peridotite of Earth, those formed from highly differentiated mantle. On the other hand, oxygen isotopic composition of the ureilite shows close relation with the carbonaceous chondrites, most primitive class of meteorites. In addition, existence of carbonaceous materials also indicates their relation. However, abundance of the carbonaceous materials inside the ureilite is much higher than carbonaceous chondrites, and the carbon material includes euhedral graphite and 100 μ m-sized diamond inclusions, those rarely found in carbonaceous chondrites. It is interesting that ureilites those showing low impact features do not show diamond inclusions. It might indicate that diamond inclusions inside the carbonaceous material would be formed by heavy shock on the asteroids. However, those carbonaceous material shows noble gas content. It is unlikely that long-heated and highly-shocked materials contain such abundant noble gas. Thus, origin of carbonaceous materials inside the ureilite is still unknown, though it might have important information for the time series of evolution of carbonaceous chondrites.

We investigated Kenna meteorite, a ureilite which shows moderately shocked texture, using x-ray diffraction computed tomography (XRD-CT) at SPring-8, in order to investigate the relation between the shock degree and characteristics of carbonaceous materials. We found that distribution of several different phases of carbonaceous materials inside the meteorite, those are not reported previously.

In this study, we investigated the carbonaceous materials inside Kenna meteorite using scanning transmitted x-ray microscope and x-ray absorption near edge analysis (STXM-XANES), to investigate and identify the phases of carbonaceous materials included inside the meteorite. We lifted up several ultrathin-sections from several points of the meteorite using Focused ion beam (FIB), and investigated the difference of the molecular structure of the carbon phases. Figure 2 shows the result for the STXM-XANES analysis of a thin section of carbonaceous materials picked up from the vein of the meteorite. It shows quite complicated structure of graphite,

diamond, amorphous and some unknown phases.

Unfortunately, we could not find the specific phases appeared in the XRD-CT image in this investigation yet. After the analysis of UVSOR, we plan to investigate same sections by transmission electron microscope (TEM) and electron diffraction system, for high resolution analysis.

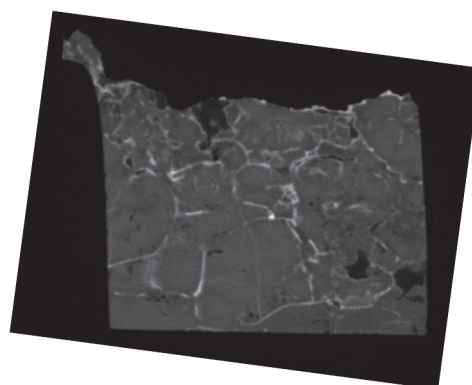


Fig. 1. An X-ray CT image of Kenna meteorite. The width of the sample is 3mm. White veins are iron-sulfide and dark portions are carbonaceous inclusions. Some of veins also includes carbonaceous material.

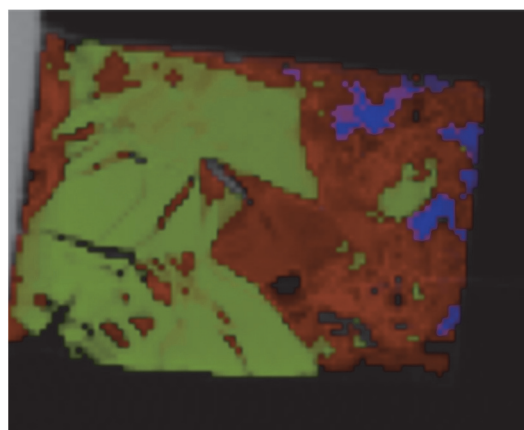


Fig. 2. Mapping of carbonaceous materials. (green: amorphous, red: graphite, blue: diamond, black: unknown). The width of the section is 20 μ m.

[1] J. L. Berkley, G. J. Taylor, K. Kell, G. E. Harlow and M. Pnzn, *Geochim. Cosmochim. Acta*, **44** (1980) 1579.

[2] H. Takeda, *Earth Planet. Sci. Lett.* **81** (1987) 358.

[3] H. Takeda, *Earth Planet. Sci. Lett.* **93** (1989) 181.

BL4U

Silica-bearing Minerals in Martian Meteorites

H. Suga¹, N. Shiraishi¹, N. Sago¹, M. Miyahara¹, T. Ohigashi², Y. Inagaki², A. Yamaguchi³,
N. Tomioka⁴, Y. Kodama⁵ and E. Ohtani⁶

¹Department of Earth and Planetary Systems Science, Graduate School of Science, Hiroshima University,
Higashi-Hiroshima 739-8526, Japan

²UVSOR Synchrotron Facility, Institute for Molecular Science, Okazaki 444-8585, Japan

³National Institute of Polar Research, Tokyo 190-8518, Japan

⁴Kochi Institute for Core Sample Research, Japan Agency for Marine-Earth Science and Technology, Nankoku
783-8502, Japan

⁵Marine Works Japan, Nankoku 783-8502, Japan

⁶Department of Earth Sciences, Graduate School of Science, Tohoku University, Sendai 980-8578, Japan

Nakhlite is a unique Martian meteorite clan because it has stark evidence for a rock-fluid reaction occurred on the Mars. Olivine [(Mg,Fe)₂SiO₄] occurs in Nakhlite. One of representative evidence for the rock-fluid reaction in Nakhlite is “iddingsite”, which is the alteration texture formed in and around the olivine grain. Varied kinds of secondary minerals occur in the iddingsite [e.g., 1]. The mineral species, assemblages, compositions and chemical species of the secondary minerals depend on several parameters such as the temperature and pH of the fluid. Accordingly, Nakhlite allows us to elucidate the physicochemical properties of the fluid existed on ancient Martian surface and its origin. Many previous studies propose that sulfate minerals exist on the Martian surface [e.g., 2]. When sulfate minerals dissolve into solution, sulfate anion and hydrogen ion occur in the solution, which decreases the pH value in the solution. Silica precipitates through the dissolution of olivine under very low pH condition (pH = 0~3); $(\text{Mg,Fe})_2\text{SiO}_4 + 4\text{H}^+ \rightarrow \text{Si}(\text{OH})_4 + 2(\text{Mg,Fe})^{2+}$. Si L_{III}-edge XANES allows us to clarify chemical bonding state around Si [2]. However, Si-XANES was not taken from a natural sample, because the transmittance of the Si L_{III}-edge energy (around 100 eV) is very low. Hence, we attempt to take Si-XANES from the iddingsite in Nakhlite.

Nakhlites, the Yamato (Y) 000593 and Yamato (Y) 000749 were used for this study. Several portions including the iddingsite were extracted by FIB. We prepared the FIB foils having two different thicknesses (Fig. 1). We obtained O-, S- and Fe-XANES from the thick portion, whereas Si- and S-XANES from the thin portion. The foils were observed with TEM/STEM-EDS after STXM analysis.

Laihunite, ferrihydrite, amorphous or poor crystallized silica-rich portion and iron sulfate were identified as a secondary mineral in the iddingsite through TEM/STEM-EDS and STXM analysis. Based on S-XANES, sulfur included in the iron sulfate is hexavalent (Fig. 2(b)). Considering TEM/STEM-EDS analysis and selected area electron diffraction (SAED) patterns, the iron sulfate is natrojarosite [NaFe₃(SO₄)₂(OH)₆]. Si L_{III}-edge XANES spectrum were successfully obtained from the poor crystallized silica-rich portion besides montmorillonite and opal as a reference material (Fig. 2(a)). The Si-XANES obtained from the poor crystallized

silica-rich portion appears to be montmorillonite (clay mineral: smectite group), which is supported by the SAED patterns. It is likely that the dissolved Si under low pH condition precipitates as clay mineral.

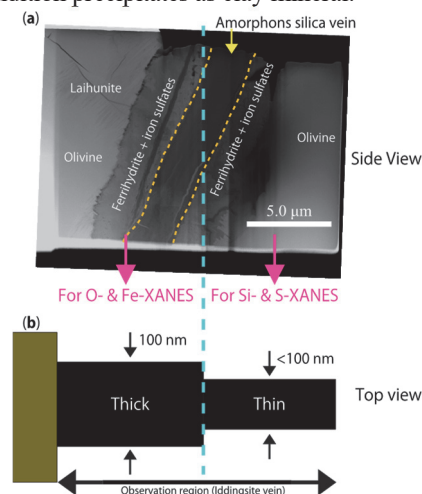


Fig. 1. The FIB foil extracted from the iddingsite in Y 000749. **a)** HAADF-STEM image. The yellow dotted line shows the distribution of the silica-rich portion. **b)** A schematic of cross-section of the FIB foil.

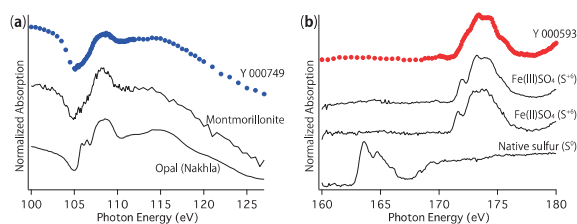


Fig. 2. Representative XANES spectrum. **a)** Si-XANES obtained from the poor crystallized silica-rich portion (blue). Reference spectrum are also shown. **b)** S-XANES obtained from the iron sulfate coexisting with ferrihydrite in Y 000593 (red). Reference spectrum are also shown.

[1] H. Suga *et al.*, Goldschmidt Conference 2017 (2017) 3814pdf.

[2] J. M. Lewis *et al.*, *Astrobiology* **15** (2015) 247.

[3] L. A. J. Garvie and P. R. Busek, *Am. Mineral.* **84** (1999) 946.

BL4U

Quantitative Mapping of DNA and Protein in Human Chromosome by Spectromicroscopy with STXM Using Combined NEXAFS Measured at the C, N, and O-K Edges

A. Ito¹, K. Shinohara¹, T. Ohigashi^{2,3}, S. Tone⁴, M. Kado⁵, Y. Inagaki² and N. Kosugi^{2,3}¹*School of Engineering, Tokai University, Hiratsuka 259-1292, Japan*²*UVSOR Synchrotron Facility, Institute for Molecular Science, Okazaki 444-8585, Japan*³*SOKENDAI (The Graduate University for Advanced Studies), Okazaki 444-8585, Japan*⁴*Graduate School of Science & Engineering, Tokyo Denki University, Hatoyama 350-0394, Japan*⁵*Kansai Photon Science Institute, Nat. Inst. Quantum and Radiological Sci. Technol., Kizugawa 619-0215, Japan*

Spectromicroscopy using scanning transmission X-ray microscope (STXM) has been applied to DNA and protein distributions in biological specimens such as chromosome and sperm at the C-K absorption edge [1, 2]. We proposed the use of a unique NEXAFS peak of DNA at the N-K absorption edge for DNA imaging [3], and in our previous study using STXM at BL4U, we obtained DNA and histone, a nuclear protein, distributions in mammalian cells using NEXAFS at the N-K absorption edge [4].

In the present study, to extend the usefulness of the unique DNA peak we developed the procedure for quantitative mapping of DNA, protein and other biomolecules. In addition, the resultant images were compared with the results obtained by the widely used analytical method named as SVD (Singular Value Decomposition).

We used chromosomes for the mapping of DNA, histone and other biomolecules, because they have rather simple molecular composition, DNA and histone. Cultured Chinese Hamster Ovary (CHO) cells were treated with colcemid to stop cell cycle at the beginning of mitotic phase, then mitotic cells that were detached from culture dish were collected and fixed with the mixed solution of ethanol and acetic acid (3:1). The fixed chromosomes were dropped on formvar membrane, and then dried in air. For spectromicroscopy, we measured NEXAFS of DNA, histone, a lipid, phosphatidylcholine (PC), at the C, N, and O-K edges. The image and spectrum analyses were performed using aXis2000 software.

Our procedure to obtain molecular maps is as follows: Images obtained at three absorption edges are combined to form one image stack file. NEXAFS spectra are also combined to form one spectrum. DNA image is obtained by the difference between images on and below the unique DNA peak at the N-K edge. Then DNA stack file is formed by scaling normalized DNA NEXAFS spectrum with the DNA peak height by DNA quantity in each pixel of DNA image. DNA stack file is subtracted from the image stack file. Since the resultant image stack file has no DNA component, the similar procedure can be applied to obtain a stack file of other molecules one by one using possible specific NEXAFS peak for each molecule.

Figure 1 shows chromosome image by STXM at 400 eV. The calculated DNA, histone and PC images

are shown in Fig. 2a. The discrete distribution of DNA was observed, which possibly reflects band structure in a chromosome. In Fig. 2b images of the same molecules obtained by SVD method were shown for comparison. The images are not so resolved compared with images by our method, and the molecular contents were largely different (data not shown). SVD method may not be suitable for applying straightly to biological specimens with complex molecular composition.

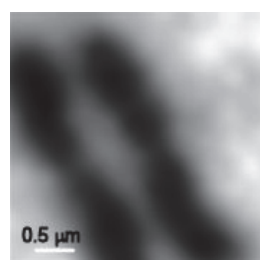


Fig. 1. STXM image of chromosomes of CHO cells at 400 eV.

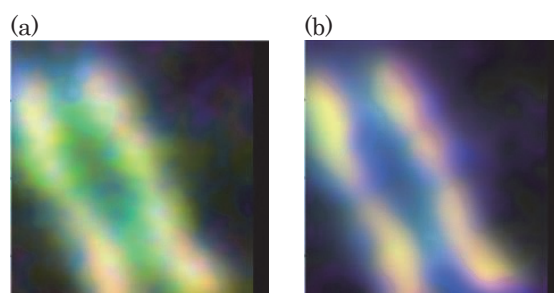


Fig. 2. RGB expression of molecular distribution in chromosomes.

DNA, protein, PC are displayed with red, green and blue, respectively. (a) present method, (b) SVD

- [1] H. Ade et al., *Science*, **258** (1992) 972.
- [2] X. Zhang et al., *J. Struct. Biol.*, **116** (1996) 335.
- [3] K. Shinohara, A. Ito, K. Kobayashi, In: *X-Ray Microscopy and Spectromicroscopy*, Springer-Verlag, Berlin/Heidelberg (1998), pp. III-157-III-161.
- [4] A. Ito, T. Ohigashi, K. Shinohara, S. Tone, M. Kado, Y. Inagaki and N. Kosugi, *UVSOR Activity Report 2015* **43** (2016) 143.

BL4U

Chemical Bonding State Change of Phosphodiester Bonds in Plasmid DNA

T. Ejima¹, T. Ohigashi², M. Kado³ and S. Tone⁴

¹IMRAM, Tohoku University, Sendai 980-8577, Japan

²UVSOR Synchrotron Facility, Institute for Molecular Science, Okazaki 444-8585, Japan

³Takasaki Adv. Rad. Res. Inst., QST, Takasaki 370-1292, Japan

⁴Sch. of Sci & Technol., Tokyo Denki University, Hatoyama 350-0394, Japan

During the apoptotic process, phosphodiester bonds in DNA are cleaved then DNA strand is broken [1]. When the chemical bonding state change of the phosphodiester bond can be observed according to progress of the DNA cleavage, the DNA cleavage in a cell-nucleus will be visualized by utilizing the chemical bonding state change of the phosphodiester bond. In advance of the visualization of the DNA cleavage, the P-L_{2,3} absorption edge structure of plasmid DNA is investigated, and the results of the edge structures are compared with those of some phosphate materials, such as di-nucleotide, tri-nucleotide, AMP, and cAMP.

Measured samples were a commercially available plasmid DNA that was air-dried as it was on a 50nm thick SiN membrane and that was cleaved with EcoRI and air-dried on a same 50 nm thick SiN membrane. X-ray absorption spectroscopy measurement was made in STXM at BL4U of UVSOR. Energy resolution $E/\delta E$ was >1000 and spatial resolution was 50 nm. Measured spectra are shown in Fig. 1.

Spectral shapes of measured P - L_{2,3} XAS spectra can be reproduced by 6 peaks, which are indicated by alphabets designated in the figure. Energy positions and peak intensities of corresponding peaks between the spectra are similar to each other except for peak D. Spectral structures of di-nucleotide, tri-nucleotide, AMP, and cAMP show similar shape and are composed of 6 peaks at the same energy range. When the spectral shapes are compared with that of KH₂PO₄ [2], which spectral shape show the six peaks, which spectral shape show the six peaks, the peaks A and B, the peaks C and D, and the peaks E and F will be originated from P3s+O2p, P3p+O2p, and P3d+O2p, respectively.

Peak intensity of peak D will be increased as the result of DNA-cleavage reaction. The comparison of the spectral shapes between the measured spectra and that of KH₂PO₄ suggest that the difference of the DNA cleavage is associated with the P3p+O2p bonds, and that state of DNA cleavage in cell-nucleus may be visualized by the intensity difference of peak D.

This work was supported by Grants-in-Aid for Scientific Research (JSPS Kakenhi, Grant Number: 16H03902 and 17K190210). Prof. K. Shinohara and Prof. A. Ito are thanked for discussions. Y. Inagaki is thanked for assistance of the measurements.

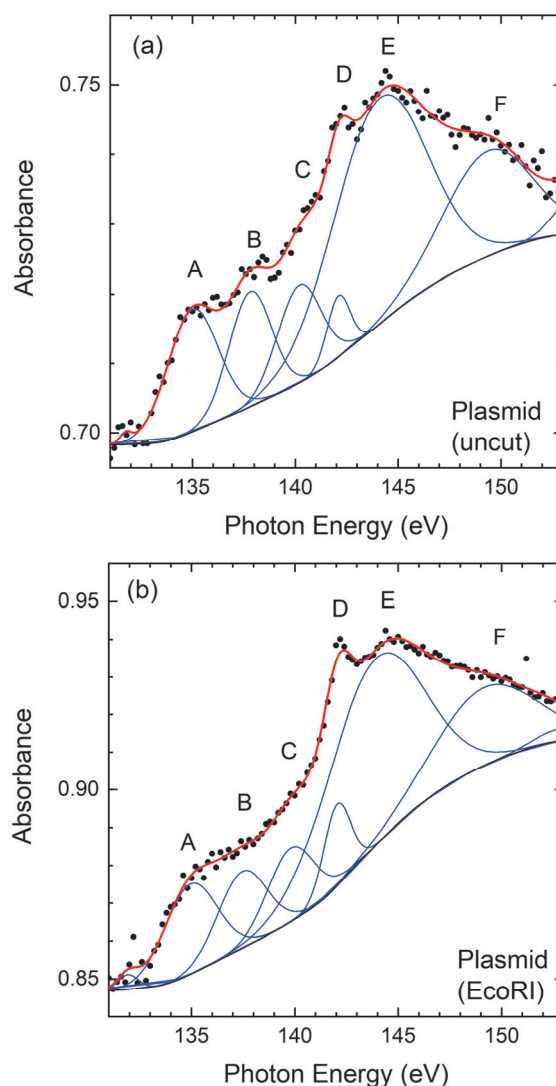


Fig. 1. P-L_{2,3} XAS spectrum of plasmid DNA that air-dried as it is, (a), and that cleaved with EcoRI and air-dried, (b). Dots represent the measurement results, blue curves are deconvolution results, and red curves, the summation of the peaks.

[1] S. Tone *et al.*, *Exp. Cell Res.* **313** (2007) 3635.

[2] S. O. Kucheyev, *et al.*, *Phys. Rev. B* **70** (2004) 245106.

BL4U

Investigation of Origin and Evolution of Extraterrestrial Materials by Visualizing Molecular Structure and Construction of Analytical Scheme with Facility-crossing Collaboration of Hayabusa2 Returned Samples

M. Uesugi¹, M. Ito², N. Tomioka², K. Uesugi¹, A. Yamaguchi³, N. Imae³, T. Ohigashi⁴, N. Shirai⁵, Y. Karouji⁶, T. Yada⁶, M. Abe⁶ and Y. Inagaki⁴

¹Japan Synchrotron Radiation Research Institute (JASRI/SPring-8), Sayo 679-5198, Japan

²Japan Agency for Marine-Earth Science and Technology (JAMSTEC), Nankoku 783-8502, Japan

³National Institute of Polar Research (NIPR), Tachikawa 190-0014, Japan

⁴UVSOR Synchrotron Facility, Institute for Molecular Science (IMS), Okazaki 444-8585, Japan

⁵Tokyo Metropolitan University, Hachioji 192-0364, Japan

⁶Japan Aerospace Exploration Agency (JAXA), Sagami-hara 252-5210, Japan

Extraterrestrial sample curation center (ESCuC) of Japan aerospace exploration agency (JAXA) organized a special team for the development of techniques and devices for the handling, transfer and analysis of samples returned by Hayabusa2 spacecraft, from 2015 under the agreements of collaboration. The special team constitutes of members of institutes those having state-of-the-art analytical instruments and experiences of curatorial works of precious natural samples, but beyond the specialists of the extraterrestrial materials [1-2].

We started development of new analytical protocols of extraterrestrial materials, which includes method of sample transfer, sample separation and data sharing, through the rehearsals of the curation works for the initial description of Hayabusa2-returned samples using extraterrestrial materials. Currently, 5 Antarctic micrometeorites (AMMs) provided by national institute of polar research (NIPR) were imaged by synchrotron radiation computed tomography (SR-CT) and x-ray diffraction (XRD) at SPring-8, and investigated by high resolution field emission scanning electron microscopy and energy dispersive spectroscopy (FE-SEM-EDS) system at institute for molecular sciences (IMS) (Fig. 1). Through the series of non-destructive analysis, we selected Antarctic micrometeorites those having similar characteristics of carbonaceous chondrites.

In this study, we formed thin sections of two AMMs selected by the results of non-destructive analyses, using focused ion beam (FIB) for the characterization of organic materials by scanning transmitted x-ray microscopy and x-ray absorption near edge structure analysis (STXM-XANES) at BL4U. One section for a fragment of AMM, TT006cT0009-1-1 was analyzed by nano-scale secondary ion mass spectrometry (NanoSIMS) before the STXM-XANES, and obtained isotopic mapping images of the light elements such as hydrogen, carbon, nitrogen and oxygen by at Japan agency for marine-earth science and technology (JAMSTEC). After NanoSIMS analysis, the section was fabricated by FIB again, to make ultrathin section for the STXM-XANES analysis. Other sections were prepared without NanoSIMS analysis.

Figure 2 shows STXM image of TT006cT0009-2-1 obtained using a NanoAnalysis linkage grid (Kochi

grid) developed in our activity. We could safely prepare the sample in atmosphere shielding environment using glovebox and sample loading system equipped at BL4U, and investigated the ultrathin-section without paper tape. Further result of our analyses will be reported by subsequent papers (in prep).

After the STXM-XANES analysis, the ultrathin-sections will be analyzed by transmission electron microscopy (TEM), for high resolution analysis of nano-scale textures and crystal structures inside the AMMs.

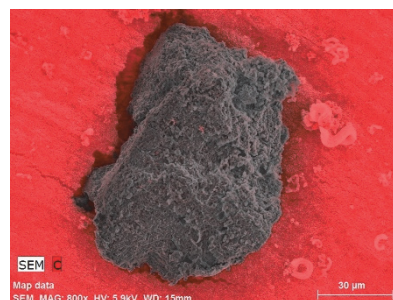


Fig. 1. An energy dispersion spectroscopy image of TT006cT0009-2. Red shows carbon distribution.

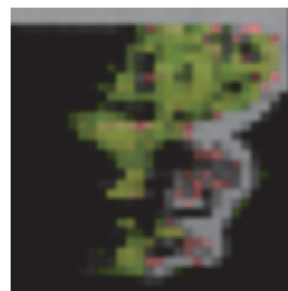


Fig. 2. A STXM-XANES image of an ultrathin-section of TT 006cT0009-2. Green portion shows region enriched in graphene, and red portion shows region enriched in carboxyl and poor in graphene.

[1] M. Uesugi *et al.* Abstract Hayabusa symp. (2016) #1129

[2] M. Uesugi *et al.* Abstract Hayabusa symp. (2017) #1129

BL4U

Probing the Penetration of Tofacitinib and Tofacitinib Citrate in Inflamed Murine Skin by Soft X-Ray Spectromicroscopy

K. Yamamoto¹, A. Klossek¹, J. Berkemeyer¹, T. Ohigashi², F. Rancan³, R. Flesch¹, A. Vogt³, U. Blume-Peytavi³, M. Radbruch⁴, H. Pischon⁴, A. D. Gruber⁴, L. Mundhenk⁴, N. Kosugi² and E. Rühl¹

¹Institute for Chemistry and Biochemistry, Freie Universität Berlin, Takustr. 3, 14195 Berlin, Germany

²UVSOR Synchrotron Facility, Institute for Molecular Science, Okazaki 444-8585, Japan

³Charité Universitätsmedizin, 10117 Berlin, Germany

⁴Veterinary Pathology, Freie Universität Berlin, 14163 Berlin, Germany

The penetration of hydrophilic and hydrophobic drugs into human skin is systematically investigated by label-free detection employing soft X-ray microscopy. The FDA-approved anti-inflammatory drug tofacitinib citrate ($C_{16}H_{20}N_6O \cdot C_6H_8O_7$, molecular weight 504.49 g/mol), marketed under the name Xeljanz, is chosen as a hydrophilic drug, which acts as a JAK inhibitor by interfering with the JAKSTAT signaling pathway. It is a low molecular weight drug that is commonly used for oral drug delivery for treating e.g. rheumatoid arthritis. Its use for treating plaque psoriasis is currently under investigation [1]. We also included the free base of tofacitinib ($C_{16}H_{20}N_6O$, molecular weight 312.37 g/mol) as a hydrophobic complement to tofacitinib citrate. This enables us to investigate the influence of hydrophilicity on dermal drug penetration.

The experiments made use of excised murine skin, which was inflamed and exposed to tofacitinib citrate and the free base obtained from LC Labs for penetration times between 10 and 1000 min, similar to earlier work using dexamethasone as a drug [2-3].

Spectromicroscopy studies were performed at the BL4U at UVSOR III using a scanning X-ray microscope. The chemical selectivity for probing the drugs in EPON-fixed skin was achieved by exciting the samples selectively at the O 1s-edge in the pre-edge regime, i.e. at 528 eV (pre-edge) and 531.8 eV, respectively, corresponding to the O 1s $\rightarrow \pi^*$ transition of the drugs. Figure 1 shows the O 1s regime of fixed murine skin, tofacitinib, and tofacitinib citrate.

Figure 1. This provides chemical selectivity for label-free probing of tofacitinib. Differential absorption maps corresponding to the drug distribution as a function of depth were derived similar to our previous work [2-3]. Figure 2 shows the drug distribution in the top skin layers, consisting of stratum corneum (SC) and viable epidermis (VE). There are distinct differences between the drug distributions after 100 min penetration time. The hydrophilic drug tofacitinib citrate is primarily found in the top layers of the stratum corneum and no drug is found in deeper skin layers (see Fig. 2(a)). In contrast, the free base is found in deeper layers of the stratum corneum and in the viable epidermis (see Fig. 2(b)). There, the drug is

preferably found in the thin membranes of the keratinocytes surrounding the cell nuclei. This corresponds to the site of action of this drug. The present results also indicate that topically applied hydrophobic drugs can more efficiently penetrate the top layers of skin than the hydrophilic analogue.

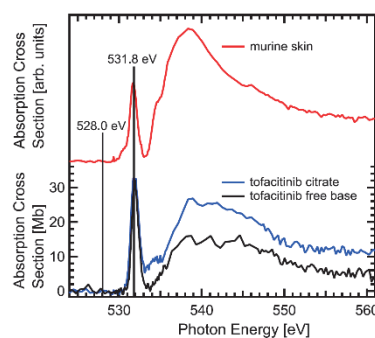


Fig. 1. X-ray absorption of tofacitinib citrate, the free base, and fixed murine skin near the O 1s-edge.

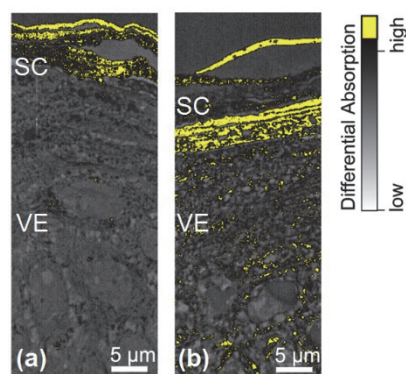


Fig. 2. Differential absorption of (a) tofacitinib citrate and (b) the free base of tofacitinib penetrating the top skin layers of murine skin for 100 min, respectively. High drug concentration is indicated by yellow color.

[1] V. Di Lernia *et al.*, Drug Design Develop. Therap. **10** (2015) 533.

[2] K. Yamamoto *et al.*, Anal. Chem. **87** (2015) 6173.

[3] K. Yamamoto *et al.*, Eur. J. Pharm. Biopharm. **118** (2017) 30.

BL4U

Chemical Mapping Individual Atmospheric Nanoparticles

X. Kong^{1*}, M. Huttula¹, J. J. Lin¹, P. Corral Arroyo², T. Ohigashi³,
N. Kosugi^{3,4}, Z. Wu⁵ and N. L. Prisle¹

¹Nano and Molecular Systems Research Unit, University of Oulu, Oulu 90041, Finland

²Laboratory of Environmental Chemistry, Paul Scherrer Institute, CH-5232 Villigen PSI, Switzerland

³UVSOR Synchrotron Facility, Institute for Molecular Science, Okazaki 444-8585, Japan

⁴School of Physical Sciences, The Graduate University for Advanced Studies, Okazaki 444-8585, Japan

⁵State Key Joint Laboratory of Environmental Simulation and Pollution Control, College of Environmental Sciences and Engineering, Peking University, 100871, China

*now at Department of Chemistry and Molecular Biology, University of Gothenburg, Gothenburg, Sweden

During the STXM beamtime, chemical maps were drawn for two laboratory-generated aerosol samples and one ambient urban aerosol sample.

The laboratory-generated aerosols were produced by the atomization of solutions of sodium n-decanoate and sodium chloride. Particles of 150, 200, and 300 nm were generated from solutions with 0.5 and 0.8 mass fraction of sodium n-decanoate and particles of 30, 50, 80 nm, and polydisperse samples were generated from solutions of 0.25 mass fraction of sodium n-decanoate.

The urban aerosol samples were collected from October 2017 to January 2018 in a winter campaign jointly operated by Peking University and the University of Gothenburg. Sampling was carried out at the Peking University Atmosphere Environment Monitoring Station on the roof of a six-floor building on the campus of Peking University located in the northwestern urban area of Beijing. A SKC 4-stage cascade impactor was used to collect particles with cut-off sizes of 250 and 500 nm that were impacted onto Formvar films.

The urban aerosol samples were examined at the adsorption edges of carbon, nitrogen, sulfur, silicon, chlorine, and potassium. Figure 1 shows the optical density of a particle at the carbon and nitrogen edges. At 284.5 eV, the C=C double bond is shown as the bright area [1], which indicates two soot components located at the two poles of the particle. The spatial resolution of the image is 30 nm. The detailed carbon edge spectrum indicates that the soot particles are well aged. In addition, the potassium L-edge indicates that K⁺ ions are present and located in the area between the soot particles. The absorption maxima of the ammonium functional group are around 401 eV, and according to the panel (b) the NH₄⁺ mainly stays between the soot particles, like K⁺. From panel (c) it seems that the NO₃⁻ is spread all over the particle. Further quantitative analysis will be performed to calculate the mixing ratio.

The carbon edge adsorption spectrum contains rich information about the functional groups and the oxidation states. Figure 2 shows (a) the carbon spectra of aged soot particles at the carbon edge from 280 eV to 320 eV, where the spectra of different colors are taken from different places of the particle, but they are very consistent except for the amplitudes that is correlated to

the particle thickness of the examined regions. Panel (b) shows the spectra of laboratory-generated soot coated by α -pinene (in red) and naphthalene SOA (in black) from literature [2], where the featured peaks excellently match the sampled particle shown in panel (a). The STXM method at BL4U seems to be perfectly suited for the study of both ambient and laboratory nanoparticles.

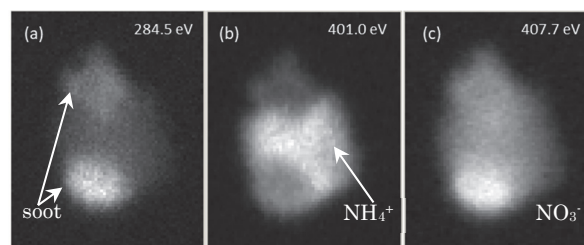


Fig. 1. Optical density at various photon energies. The bright areas indicate where the excited functional groups are located. (a) soot; (b) NH₄⁺; (c) NO₃⁻.

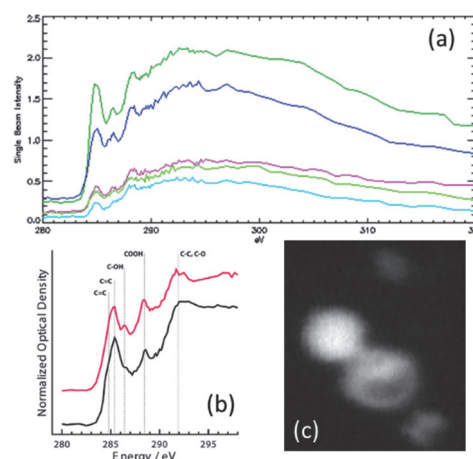


Fig. 2. (a) carbon K-edge adsorption spectra of sampled urban particles; (b) STXM spectra of laboratory-generated soot coated by α -pinene (red) and naphthalene SOA (black) [2]; (c) STXM image of the particles at 286.6 eV.

[1] R. C. Moffet, A.V. Tivanski and M.K. Gilles, “Fundamentals and Applications in Aerosol Spectroscopy” (CRC Press; Boca Raton, FL, 2011).

[2] J. C. Charnawskas *et al.*, *Faraday Discussions*, **200** (2017) 165.

BL4U

STXM Studies of Abnormal Ultrastructural Features in FINCA Disease

E.-V. Immonen^{1,2}, T. Ohigashi³, I. Miinalainen⁴, M. Patanen¹, R. Hinttala^{2,4},
J. Uusimaa^{2,4}, N. Kosugi³ and M. Huttula¹

¹Nano and Molecular Systems research unit, P.O. Box 3000, 90014 University of Oulu, Finland

²PEDEGO Research Unit and Medical Research Center Oulu, University of Oulu and Oulu University Hospital,
PO Box 5000, 90014 University of Oulu, Finland

³UVSOR Synchrotron Facility, Institute for Molecular Science, Okazaki 444-8585, Japan

⁴Biocenter Oulu, PO Box 5000, 90014 University of Oulu, Finland

In this work, we have used scanning transmission X-ray imaging technique at BL4U to study human tissue samples exhibiting abnormal ultrastructural features related to FINCA disease. Recently, a novel, fatal cerebropulmonary disease in children was characterized with fibrosis, neuro- degeneration and cerebral angiomas (FINCA disease) [1]. The disease course is progressive with multiorgan manifestations, leading to death before the age of two years. Studies on autopsy samples revealed interstitial fibrosis and previously undescribed granuloma-like lesions in the lungs, and hepatomegaly related to widespread microvacuolar hepatocyte fatty degeneration and hepatocellular necrosis. All patients had a combination of mutations in the *NHLRC2* gene encoding an NHL repeat containing protein 2 that is ubiquitously present in various types of tissues, from animals to bacteria. Still, no published results exist on the functional role of the *NHLRC2*.

In order to learn more about the pathomechanism behind FINCA disease, multidisciplinary approaches are called for. These, among others, include morphological and chemical analysis of the subcellular features in the liver autopsy samples taken from the FINCA patients. However, conventional imaging techniques, such as electron microscopy, possess severe pitfalls when it comes to chemical imaging, requiring the utilization of the STXM method. Thus, we have performed the first proof-of-principle STXM studies on subcellular structural characteristics related to storage diseases.

The samples (approximately 150-200 nm thick) were prepared at Biocenter Oulu, Finland using standard methods in transmission electron microscopy (TEM), and placed on Butvar film coated copper grids. In addition, sections adjacent to ones selected for STXM imaging were imaged using TEM, allowing the comparison of these methods as shown in Fig. 1.

The measurements concentrated on C 1s edge, and we have observed several abnormal ultrastructural features in various tissues of a FINCA patient. Figure 1 shows an example of a liver sample, where these abnormal features include large vacuoles of unknown origin (marked as U in Fig. 1). According to carbon K-edge absorption profile, these vacuoles have a chemical signature that differs from other organelles (Fig. 1C). Further studies will focus on verifying the origin and identifying the accumulated compounds.

This can be useful in finding novel biomarkers in future for example storage diseases.

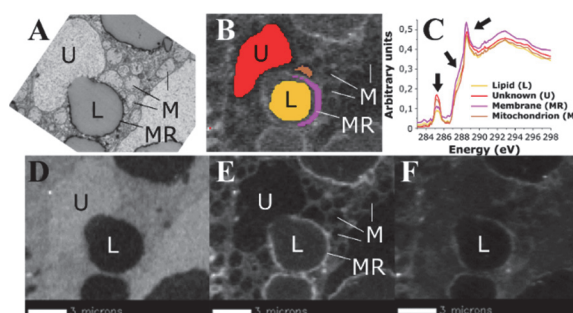
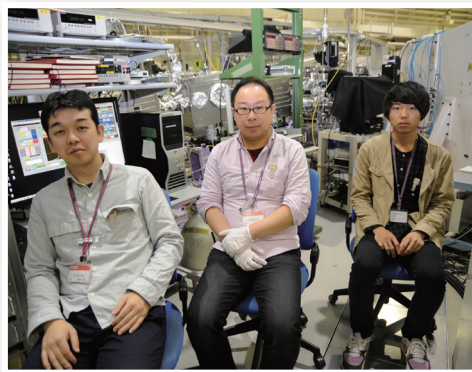
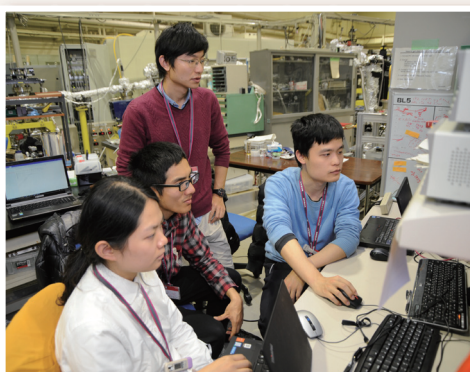
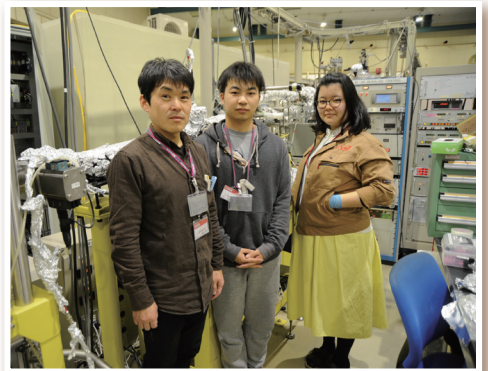
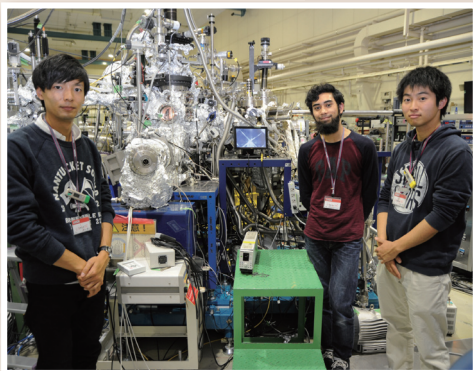
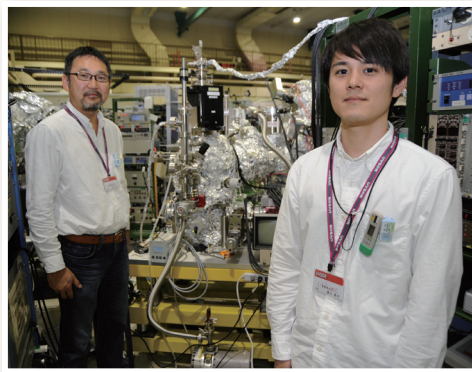
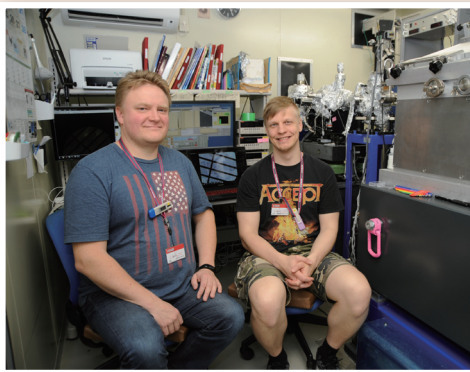
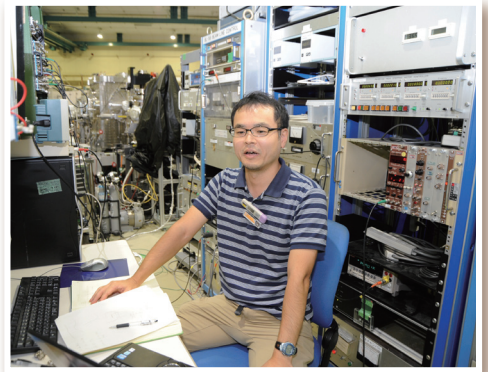
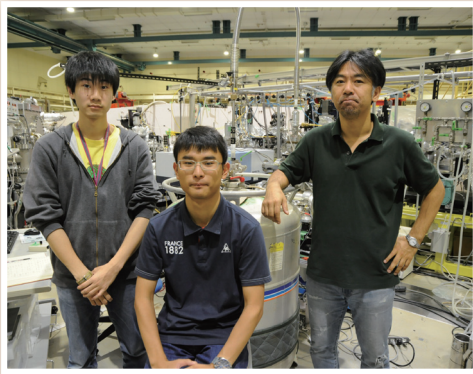
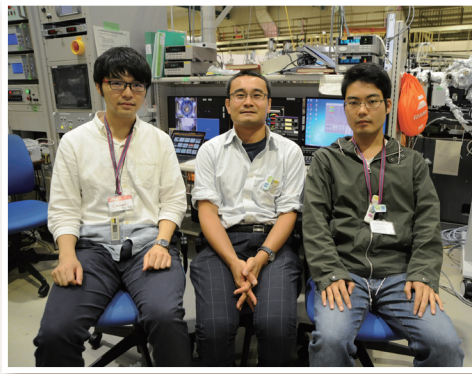
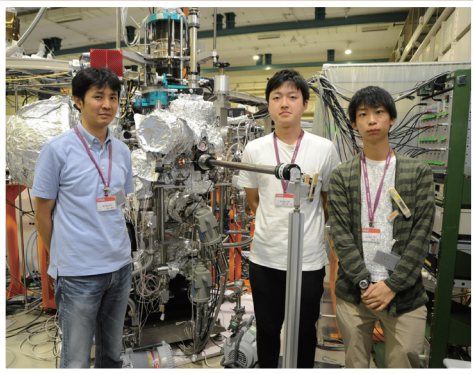


Fig. 1. A) A TEM image showing organelles (lipid vesicles L, their membrane MR, mitochondria M, and an unknown structure U, within a hepatocyte. B) An STXM image of the same region with $h\nu = 287$ eV. Subcellular features used for collecting region specific absorption spectra are marked with colors. C) Absorption spectra from regions in B. The arrows indicate the most prominent spectral differences. D) STXM image stack from an energy range 285-286 eV (1st arrow in C). E) Energy range 286-288 eV (2nd arrow in C). F) 288-297 (3rd arrow in C).

[1] J. Uusimaa, R. Kaarteenaho, T. Paakkola, H. Tuominen, M. K. Karjalainen, J. Nadaf, T. Varilo, M. Uusi-Mäkelä, M. Suo-Palosaari, I. Pietilä, A. E. Hiltunen, L. Ruddock, H. Alanen, E. Biterova, I. Miinalainen, A. Salminen, R. Soininen, A. Manninen, R. Sormunen, M. Kaakinen, R. Vuolteenaho, R. Herva, P. Vieira, T. Dunder, H. Kokkonen, J. S. Moilanen, H. Rantala, L. M. Noguee, J. Majewski, M. Rämetsä, M. Hallman, R. Hinttala, *Acta Neuropathol.* (2018). In press. <https://doi.org/10.1007/s00401-018-1817-z>

UVSOR User 7



The background is a solid red color with several abstract geometric patterns. A large, semi-transparent circular graphic is centered on the page, featuring concentric rings and a dotted border. Diagonal lines and a grid of small dots are also visible in the lower half of the image.

IV

List of Publications

List of Publications

K. Asami, J. Ueda, M. Kitaura and S. Tanabe

“Investigation of Luminescence Quenching and Persistent Luminescence in Ce³⁺ Doped (Gd,Y)₃(Al,Ga)₅O₁₂ Garnet Using Vacuum Referred Binding Energy Diagram”, J. Lumin., **198** (2018) 418.

T. Brandenburg, R. Golnak, M. Nagasaka, K. Atak, S. S. N. Lalithambika, N. Kosugi and E. F. Aziz

“Impacts of Conformational Geometries in Fluorinated Alkanes”, Sci. Rep., **6** (2016) 31382.

F. Bussolotti, J. Yang, T. Yamaguchi, K. Yonezawa, K. Sato, M. Matsunami, K. Tanaka, Y. Nakayama, H. Ishii, N. Ueno and S. Kera

“Hole-Phonon Coupling Effect on the Band Dispersion of Organic Molecular Semiconductors”, Nature Commun., **8** (2017) Article number: 173.

A. Hara and T. Awano

“Ground-State Splitting of Ultrashallow Thermal Donors with Negative Central-Cell Corrections in Silicon”, Jpn. J. Appl. Phys., **56** (2017) 068001.

T. Hirahara, S. V. Eremeev, T. Shirasawa, Y. Okuyama, T. Kubo, R. Nakanishi, R. Akiyama, A. Takayama, T. Hajiri, S. Ideta, M. Matsunami, K. Sumida, K. Miyamoto, Y. Takagi, K. Tanaka, T. Okuda, T. Yokoyama, S. Kimura, S. Hasegawa and E. V. Chulkov

“Large-Gap Magnetic Topological Heterostructure Formed by Subsurface Incorporation of a Ferromagnetic Layer”, Nano Lett., **17** (2017) 3493.

S. Hosokawa, K. Matsuki, K. Tamaru, Y. Oshino, H. Aritani, H. Asakura, K. Teramura and T. Tanaka

“Selective Reduction of NO over Cu/Al₂O₃: Enhanced Catalytic Activity by Infinitesimal Loading of Rh on Cu/Al₂O₃”, Mol. Catal., **442** (2017) 74.

H. Iwayama, C. L'eonard, F. Le Qu'ere, S. Carniato, R. Guillemin, M. Simon, M. N. Piancastelli and E. Shigemasa

“Different Time Scales in the Dissociation Dynamics of Core-Excited CF₄ by Two Internal Clocks”, Phys. Rev. Lett., **119** (2017) 203203.

T. Kaneyasu, Y. Hikosaka, M. Fujimoto, H. Iwayama, M. Hosaka, E. Shigemasa and M. Katoh

“Observation of an Optical Vortex Beam from a Helical Undulator in the XUV Region”, J. Synchrotron Rad., **24** (2017) 934.

M. Katoh, M. Fujimoto, N. S. Mirian, T. Konomi, Y. Taira, T. Kaneyasu, M. Hosaka, N. Yamamoto, A. Mochihashi, Y. Takashima, K. Kuroda, A. Miyamoto, K. Miyamoto and S. Sasaki

“Helical Phase Structure of Radiation from an Electron in Circular Motion”, SCIENTIFIC REPORTS, **7** (2017) Article number:6130.

N. Kawano, M. Koshimizu, G. Okada, Y. Fujimoto, N. Kawaguchi, T. Yanagida and K. Asai

“Luminescence Properties of Organic Inorganic Layered Perovskite-type Compounds under Vacuum Ultraviolet Irradiation”, Jpn. J. Appl. Phys., **57** (2018) 02CA03.

S. Kimura, H. Yokoyama, H. Watanabe, J. Sichelschmidt, V. Süß, M. Schmidt and C. Felser
“Optical signature of Weyl Electronic Structures in Tantalum Pnictides TaPn (Pn = P, As)”, Phys. Rev. B., **96** (2017) 075119.

M. Mori, D. Nakauchi, G. Okada, Y. Fujimoto, N. Kawaguchi, M. Koshimizu and T. Yanagida
“Scintillation and Optical Properties of Ce³⁺-doped CaGdAl₃O₇ Single Crystals”, J. Lumin., **186** (2017) 93.

M. Nagasaka, H. Yuzawa and N. Kosugi
“Interaction between Water and Alkali Metal Ions and Its Temperature Dependence Revealed by Oxygen KEdge Xray Absorption Spectroscopy”, J. Phys. Chem. B, **121** (2017) 10957

M. Nagasaka, T. Ohigashi and N. Kosugi
“Development of In-Situ/Operando Sample Cells for Soft X-ray Transmission Spectromicroscopy at UVSOR-III Synchrotron”, SRN, **30** (2) (2017) 3.

M. Nagasaka, H. Yuzawa, T. Horigome and N. Kosugi
“Reliable Absorbance Measurement of Liquid Samples in Soft X-Rayabsorption Spectroscopy in Transmission Mode”, J. Electron Spectrosc Relat. Phenom., **224** (2018) 93.

D. Nakauchi, G. Okada, M. Koshimizu, N. Kawaguchi and T. Yanagida
“Radioluminescence and Thermally-Stimulated Luminescence Properties of Pr:CaSiO₃ Crystals”, Physica B, **530** (2018) 38.

T. Ohigashi, Y. Inagaki, A. Ito, K. Shinohara and N. Kosugi
“Investigation of Measurement Condition for 3-Dimensional Spectroscopy by Scanning Transmission X-ray Microscopy”, J. Phys.: Conf. Ser., **849** (2017) 012044.

H. Oinuma, S. Souma, D. Takane, T. Nakamura, K. Nakayama, T. Mitsuhashi, K. Horiba, H. Kumigashira, M. Yoshida, A. Ochiai, T. Takahashi and T. Sato
“Three-Dimensional Band Structure of LaSb and CeSb: Absence of Band Inversion”, Phys. Rev. B, **96** (2017) 041120.

Y. Okuyama, Y. Sugiyama, S. Ideta, K. Tanaka and T. Hirahara
“Growth and Atomic Structure of Tellurium Thin Films Grown on Bi₂Te₃”, Applied Surface Science, **398** (2017) 125.

T. Petit, L. Puskar, T. Dolenko, S. Choudhury, E. Ritter, S. Burikov, K. Laptinskiy, Q. Brustowski, U. Schade, H. Yuzawa, M. Nagasaka, N. Kosugi, M. Kurzyp, A. Venerosy, H. Girard, J.-C. Arnault, E. Osawa, N. Nunn, O. Shenderova and E. F. Aziz
“Unusual Water Hydrogen Bond Network around Hydrogenated Nanodiamonds”, J. Phys. Chem. C, **121** (2017) 5185.

K. Shinohara, T. Ohigashi, S. Toné, M. Kado and A. Ito
“Quantitative Study of Mammalian Cells by ScanningTransmission Soft X-ray Microscopy”, J. Phys.: Conf. Ser., **849** (2017) 012003.

H. Suga, S. Kikuchi, Y. Takeichi, C. Miyamoto, M. Miyahara, S. Mitsunobu, T. Ohigashi, K. Mase, K. Ono and Y. Takahashi
“Spetially Resolved Distribution of Fe Species around Microbes at the Submicron Scale in Natural Bacteriogenic Iron Oxdes”, Microbes Environ, **32** (2017) 283.

K. Takemoto, M. Yoshimura, T. Ohigashi, Y. Inagaki, H. Namba and H. Kihara
“Application of Soft X-ray Microscopy to Environmental Microbiology of Hydrosphere”, *J. Phys.: Conf. Ser.*, **849** (2017) 012010.

N. Tatemizo, Y. Miura, K. Nishio, S. Hirata, F. Sawa, K. Fukui, T. Isshiki and S. Imada
“**Band Structure and Photoconductivity of Blue-Green Light Absorbing AlTiN Films**”, *J. Mater. Chem. A*, **5** (2017) 20824.

H. Yamane and N. Kosugi
“**High Hole-Mobility Molecular Layer Made from Strong Electron Acceptor Molecules with Metal Adatoms**”, *J. Phys. Chem. Lett.*, **8** (2017) 5366.

T. Yanagida, M. Koshimizu, Y. Fujimoto, K. Fukuda, K. Watanabe, G. Okada and N. Kawaguchi
“**Scintillation Properties of Eu and Alkaline Metal Co-doped LiCaAlF₆**”, *J. Lumin.*, **191** (2017) 22.

T. Yanagida, Y. Fujimoto, M. Koshimizu, N. Kawano, G. Okada and N. Kawaguchi
“**Comparative Studies of Optical and Scintillation Properties between LiGaO₂ and LiAlO₂ Crystals**”, *J. Phys. Soc. Jpn.*, **86** (2017) 094201.

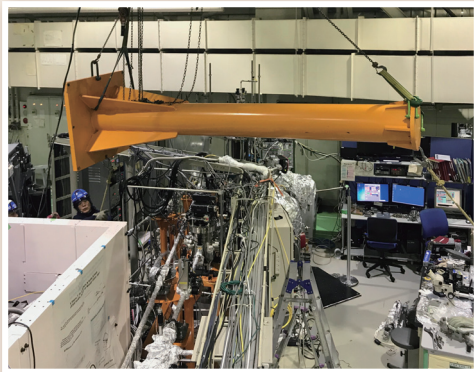
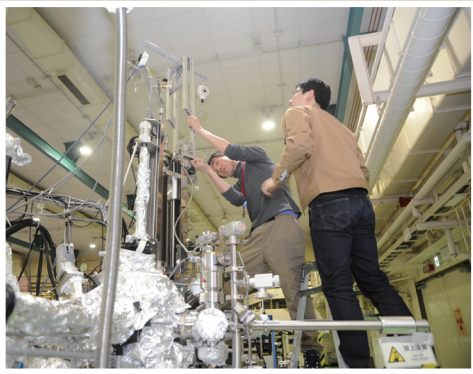
T. Yanagida, Y. Fujimoto, M. Koshimizu, N. Kumamoto, G. Okada and N. Kawaguchi
“**Scintillation and Dosimeter Properties of LiAlSi₂O₆ and LiAlSi₄O₁₀ Crystals**”, *Sensors and Materials*, **29** (2017) 1399.

T. Yanagida, M. Koshimizu, N. Kawano, G. Okada and N. Kawaguchi
“**Optical and Scintillation Properties of ScAlMgO₄ Crystal Grown by the Floating Zone Method**”, *Mater. Res. Bull.*, **95** (2017) 409.

M. Yoshida, Y. Mitsutomi, T. Mineo, M. Nagasaka, H. Yuzawa, N. Kosugi and H. Kondoh
“**Direct Observation of Active Nickel Oxide Cluster in Nickel–Borate Electrocatalyst for Water Oxidation by In Situ O K-Edge X-ray Absorption Spectroscopy**”, *J. Phys. Chem. C*, **119** (2015) 19279.

S. Yoshizawa, E. Minamitani, S. Vijayaraghavan, P. Mishra, Y. Takagi, T. Yokoyama, H. Oba, J. Nitta, K. Sakamoto, S. Watanabe, T. Nakayama and T. Uchihashi
“**Controlled Modification of Superconductivity in Epitaxial Atomic Layer-Organic Molecule Heterostructures**”, *Nano Lett.*, **17** (2017) 2287.

UVSOR Staff Works & Year End Party



The background features a large, stylized graphic of concentric circles and radial lines, resembling a sunburst or a stylized 'V' shape. The circles are composed of dashed lines and small dots, creating a textured, layered effect. The overall color palette is a range of warm, earthy browns and oranges.

V

Workshops

UVSOR Symposium 2017

Date: October 28-29, 2017

Place: Okazaki Conference Center

October 28th (Sat.)

< Session 1, Chair: **M. Katoh** >

- 13:00 – 13:05 Opening remarks
M. Fujimoto (UVSOR)
- 13:05 – 13:25 Present Status of UVSOR and Other Synchrotron facilities in Japan and the World
N. Kosugi (UVSOR)
- 13:25 – 13:45 Optical Vortex from a Helical Undulator at UVSOR-III
M. Hosaka (Nagoya Univ.)
- 13:45 – 14:05 Development of Analytical Method of Extraterrestrial Organic Materials Using Synchrotron Radiation for Analysis of Hayabusa2 Returned Samples
M. Uesugi (JASRI)
- 14:05 – 14:25 Coffee Break
- 14:25 – 15:30 Poster Short Presentation

< Session 2, Chair: **K. Tanaka** >

- 15:30 – 15:50 Study on Band Structures of 3d-transition Metal Doped AlN Films for Highly Efficient Artificial Photosynthesis Devices
S. Imada (Kyoto Institute of Technology)
- 15:50 – 16:20 [invited] Observing Two-dimensional Materials Using Synchrotron Radiation: Crucial Role of Photoemission Spectroscopy in Silicene Research
Y. Yamada-Takamura (JAIST)
- 16:20 – 18:30 Poster Session
- 18:30 – 20:00 Banquet

October 29th (Sun.)

< Session 3, Chair: **H. Iwayama** >

- 9:00 – 9:20 Electronic Structure of Detwinned $\text{Ba}_{1-x}\text{K}_x\text{Fe}_2\text{As}_2$ Using Angle-Resolved Photoemission Spectroscopy
S. Ideta (UVSOR)
- 9:20 – 9:40 Charge Transport in Organic Semiconductor Crystal: Impacts of Electron-phonon Coupling
S. Kera (IMS)
- 9:40 – 10:00 Electronic States of Topological Line-node Semimetals Studied by High Resolution ARPES
D. Takane (Tohoku Univ.)
- 10:00 – 10:20 Coffee Break

< Session 4, Chair: **T. Ohigashi** >

- 10:20 – 10:40 Local Structure Observation of Aqueous Salt Solutions by Soft X-ray Absorption Spectroscopy
H. Yuzawa (IMS)
- 10:40 – 11:00 Mars Surface Conditions Deduced from Alteration Products in Martian Meteorites
M. Miyahara (Hiroshima Univ.)
- 11:00 – 12:00 Discussion and closing remarks

< Poster Presentation >

- P01 Molecular Orientation of Schiff Base Ni(II), Cu(II), Zn(II) Binuclear Complexes in PVA Films by Optical Vortex UV Light Irradiation
T. Soejima (Tokyo Univ. of Science)
- P02 Measurement of 2D Isotope Distribution by LCS Gamma-ray 2
H. Zen (IAE, Kyoto Univ.)
- P03 Optical Activation of Amino Acids by Circularly Polarized Light Irradiation
K. Matsuo (HiSOR, Hiroshima Univ.)
- P04 In-situ XAFS Measurements of Manganese Oxide Oxygen Evolution Catalysts
M. Yoshida (Keio Univ.)
- P05 Elucidation of the Role of Phosphate and Borate Ions Adsorbing Onto Cobalt Oxygen Evolving Catalysts by in-situ Observations
H. Kurosu (Keio Univ.)
- P06 Effect of the Addition of Organic Molecules to Cobalt Oxide Electrocatalyst for Oxygen Evolution and its Elucidation of the Function
T. Hiue (Keio Univ.)
- P07 Local Structures of Aqueous Solutions Studied by Soft X-ray Absorption Spectroscopy
M. Nagasaka (IMS)
- P08 Advanced Analyses in Scanning Transmission X-ray Microscopy at UVSOR- III Synchrotron
T. Ohigashi (UVSOR)
- P09 Detail Investigation to Carbonaceous Materials in the Allende CV3 Meteorite Using Microscopic Methods Based on STXM
H. Suga (Hiroshima Univ.)
- P10 Feasibility Study of Sulfur Speciation High-spatial Resolution Mapping in Extraterrestrial Organics by STXM-XANES
M. Ito (Kochi Inst. for Core Sample Res., JAMSTEC)
- P11 Electronic Structure of a Bi Atomic Chain on Low Symmetric InAs (110) Surface
T. Nakamura (Osaka Univ.)
- P12 Experimental Observation of Electronic Structure of SmO Thin Film Studied by Photoemission Spectroscopy
Y. Sakai (Nagoya Institute of Technology)
- P13 Band Dispersion of Bi₂Te₃ with Mn and Te Deposition and its Temperature Dependence
K. Yokoyama (Tokyo Institute of Technology)

- P14 Observation of Four-fold Rotational Symmetry Breaking in a Pseudogap Phase of the Cuprate Superconductor Bi2212 Using ARPES
S. Nakata (Univ. of Tokyo)
- P15 Site-specific Production of H_3^+ by Core Ionization of CH_3Cl
H. Fujise (UVSOR, The Graduate Univ. for Advanced Studies)
- P16 Molecular Orientation and Electronic States of Thin Film of Phenanthro-dithiophene Derivatives on Au(110)
S. Ouchi (Chiba Univ.)
- P17 The Evolution of Aggregation Structure and Electronic State Depending on Annealing Time and Temperature of $SnCl_2Pc$
C. Numata (Chiba Univ.)
- P18 Electronic Structure and Magnetic Properties of a Topological Insulator/magnetic Insulator Ultrathin Film Heterostructure
Y. Okuyama (Tokyo Institute of Technology)
- P19 Observation of Dirac Cone in $NiTe_2$ by Angle Resolved Photoelectron Spectroscopy
M. Nishino (Osaka Univ.)
- P20 Electronic Structure of $Sr_{1-x}Ca_xFe_2(As_{1-y}P_y)_2$ ($x = 0.08, y = 0.25$) Revealed by Angle Resolved Photoemission Spectroscopy
T. Adachi (Osaka Univ.)
- P21 Resonant Scattering Phenomena of an Electron Excited from the Graphite Surface Affected by the Organic Monolayer
T. Yamaguchi (IMS, The Graduate Univ. for Advanced Studies)
- P22 Systematic Angle-resolved Photoemission Study of the Phase Transition in the Electronic Structure of $(TMTTF)_2X$
T. Ito (SRRC, Nagoya Univ.)
- P23 The Bandgap Energy and Optical Properties of Ce-doped $(Gd, La, Y)_2Si_2O_7$ Scintillator
T. Horiai (IMR, Tohoku Univ.)
- P24 XMCD Study of Ferro Orbital Ordered System: FeV_2O_4
J. Okabayashi (Univ. of Tokyo)
- P25 Vacuum Ultra-Violet Absorption Spectra of Amorphous Compound Semiconductors
K. Hayashi (Gifu Univ.)
- P26 Anisotropic Metal-to-Insulator Transition of RuAs Probed by Polarized Infrared Spectroscopy
Y. Nakajima (Osaka Univ.)
- P27 Establishment of Infrared Microscopic Imaging Method by Concentration of Aspartic Acid
J. Hibi (Osaka Univ.)
- P28 Infrared Absorption of Trapped Electron Centers in $Ce:Gd_xLu_{3-x}Al_2Ga_3O_{12}$ Crystals
T. Yagihashi (Yamagata Univ.)
- P29 Visualizing Hidden Electron Trap Levels in GAGG:Ce Crystals
M. Kitaura (Yamagata Univ.)
- P30 Study on Band Structures of 3d-transition Metal Doped AlN Films for Highly Efficient Artificial Photosynthesis Devices
N. Tatemizo (Kyoto Institute of Technology)

- P31 Evaluation of Response Wavelength Characteristic of Vacuum Ultraviolet Detector Based on Fluorides
R. Yamazaki (Nagoya Institute of Technology)
- P32 Giant Thermal Effect of Vibration Modes of Single-crystalline Alanine
Z. Mita (Osaka Univ.)
- P33 Measurement of the Stokes Parameters of BL7B by Using the VIS-VUV Region Spectroscopic Ellipsometer
F. Sawa (Univ. of Fukui)
- P34 Excitation Spectrum of Laser Irradiated α -CN_x Thin Films
K. Imamura (Univ. of Fukui)
- P35 CEES Measurements of the 3d-transition Metal Doped AlN Film
W. Kamihigoshi (Univ. of Fukui)
- P36 LO Phonon Replicas in Localized Exciton Emission of AlGa_{0.5}N Alloys
S. Hirata (Univ. of Fukui)

Beam Physics 2017 and Young Researchers Meeting

IMS Workshop “New Applications of Quantum Beam to Material and Life Science”

Date: November 16-18, 2017

Place: Okazaki Conference Center

November 16th (Thu.)

12:50 – 13:00 Opening remarks

M. Katoh (UVSOR)

< General session 1, Chair: **M. Katoh** (UVSOR) >

13:00 – 13:30 Electron Orbit Analysis in Standing-wave Cavity at Low Energy Region

T. Miyajima (KEK)

13:30 – 14:00 Investigation of Multibeam Operation with CW Superconducting Linear Accelerator

M. Shimada (KEK)

14:00 – 14:30 Numerical Analysis of Interaction between Electron Bunches and Double RF System Using Macro Particle Method and Semi-analytical Method

N. Yamamoto (KEK)

14:30 – 15:00 Optimization of Beam Shape by Emittance Exchange

M. Kuriki (Hiroshima Univ.)

15:00 – 15:15 Coffee Break

< Special session 1, Chair: **S. Miyamoto** (Univ. of Hyogo) >

15:15 – 16:00 [invited] New Development of Muon Science

Y. Miyake (KEK)

16:00 – 16:30 Recent Status of STXM in UVSOR

T. Ohgashi (UVSOR)

16:30 – 16:45 Coffee Break

< Special session 2, Chair: **Y. Takashima** (Nagoya Univ.) >

16:45 – 17:30 [invited] Slow Positron Generation and Application at Slow Positron Facility of KEK

T. Hyodo (KEK)

17:30 – 18:15 [invited] One-shot Imaging Cryo Electron Microscope Realized with Electron Beam Innovation by GaN Semiconductor

T. Nishitani (Nagoya Univ.)

18:30 – 20:30 Banquet

November 17th (Fri.)

< Special session 3, Chair: **S. Kashiwagi** (Tohoku Univ.) >

9:00 – 9:30 Generation of Optical Vortex by Synchrotron Radiation

M. Hosaka (Nagoya Univ.)

9:30 – 10:15 [invited] New Development of Electron Beam Carrying Orbital Angular Momentum

A. Saitoh (Nagoya Univ.)

10:15 – 10:30 Coffee Break

< Special session 4, Chair: **T. Miyajima** (KEK) >

10:30 – 11:00 Pinpoint Damage Method of Organelle with Small Generator of Ion Microbeam Using Glass Capillary

T. Ikeda (RIKEN)

11:00 – 11:30 New Development of Material Science by Infrared Free Electron Laser

A. Irizawa (Osaka Univ.)

11:30 – 12:00 Demonstration of Isotope CT Imaging by Measurement of Nuclear Resonance Fluorescence Absorption of Quasi-monochromatic Gamma-ray

H. Zen (Kyoto Univ.)

12:00 – 13:00 Lunch

< General session 2, Chair: **M. Kuriki** (Hiroshima Univ.) >

13:00 – 13:30 Laser Stripping Injection for the Next Generation High-intensity Proton Accelerator

H. Harada (J-PARC)

13:30 – 14:00 Development of Neutron Beam Source for Plasma Heating in NIFS

M. Kisaki (NIFS)

14:00 – 14:30 Realization of Muon RF Linear Acceleration

M. Otani (KEK)

14:30 – 15:00 Laser-driven Ion Acceleration

Y. Sakaki (QST)

15:00 – 15:15 Coffee break

< General session 3, Chair: **M. Hosaka** (Nagoya Univ.) >

15:15 – 15:45 LUCX Pre-bunched e-beam Generation and Its Application to THz Experimental Studies

A. Alexander (KEK)

15:45 – 16:15 Generation of CEP-stabilized Several Cycle Optical Pulse in FEL Cavity

R. Hajima (QST)

16:15 – 16:45 Science of Small SR Ring and Next Light Source at HiSOR

K. Kawase (Hiroshi Univ.)

16:45 – 17:30 [Invited] Introduction of the Newly Established Tabletop Synchrotron Radiation Center and Research on Active Hydrogen Water

H. Yamada (Ritsumeikan Univ.)

17:30 – 17:40 Closing remarks

R. Hajima (QST.)

18:00 – 21:00 Banquet

[Opening Ceremony of Young Researchers Meeting & Laboratory Introduction]

Chair: **K. Sakagami** (Waseda Univ.)

November 18th (Sat.)

< Young session 1, Chair: **N. Yamamoto** (KEK) >

- 9:00 – 9:15 Research on High Durability NEA-GaAs Cathode
K. Masaki (Waseda Univ.)
- 9:15 – 9:30 Design Study of Electron-driven ILC Positron Source
H. Nagoshi (Hiroshima Univ.)
- 9:30 – 9:45 Development of Fresnel-type Pinpoint Laser Sighting Method for Cell Irradiation by Glass Capillary
K. Sato (Toho University)
- 9:45 – 10:00 Development of Laser Microbeam Pinpoint Irradiation Method with Glass Capillary Optics: Measurement of Beam Power Density Distribution
H. Hirose (Toho Univ.)
- 10:00 – 10:15 Study of THz-wave Generation Target by Coherent Cherenkov Radiation
T. Yuichi (Waseda Univ.)
- 10:15 – 10:30 Sub-picosecond Bunch Length Measurement Using Cherenkov Radiation from Low Refractive Silica Aerogel Thin Film
Y. Saito (Tohoku Univ.)
- 10:30 – 10:45 Coffee break

< Young session 2, Chair: **H. Zen** (Kyoto Univ.) >

- 10:45 – 11:00 Irradiation Effect Evaluation of PoMS Short Pulse Electron Beam Pulse Radiolysis
T. Uchida (Waseda Univ.)
- 11:00 – 11:15 Development of Laser System for Crab Crossing Laser-Compton Scattering
R. Morita (Waseda Univ.)
- 11:15 – 11:30 Measurement of Photonuclear Reaction Neutron by LCS Gamma-ray
Y. Morimoto (Univ. of Hyogo)
- 11:30 – 11:45 Generation of Laser Compton Scattering Gamma-ray and Material Research Using Pair Production Positron
K. Sugita (Univ. of Hyogo)
- 11:45 – 12:00 Experimental Study on Beam Kinematics in Harmonic Cavity of UVSOR
J. Hasegawa (Nagoya Univ.)
- 12:00 – 12:15 Development of Laser Driven Ion Beam Diagnostic System with Photostimulable Phosphor detector - Aiming for Ion Estimation by Machine Learning Method
T. Miyahara (Kyushu Univ.)
- 12:15 – 13:00 Lunch

< Young session 3, Chair: **S. Matsuba** (Hiroshima Univ.) >

- 13:00 – 13:15 Evaluation of Wakefield Influence on Beam Dynamics in Bunch Compressor of Particle Accelerator
D. Tomita (Muroran Institute of Technology.)
- 13:15 – 13:30 Simulation Modeling of three-dimensional electromagnetic Field in cERL Injector Cavity
T. Hotei (SOKENDAI)

- 13:30 – 13:45 Research on Nondestructive Beam Monitor for Longitudinal Measurement of Next Generation High-intensity Beam
K. Moriya (J-PARC)
- 13:45 – 14:00 Investigation of Beam-intensity Dependence of Closed Orbit Distortion (COD) at J-PARC MR
A. Kobayashi (J-PARC,)
- 14:00 – 14:15 Study on Endohedral Fullerene Production Using Laser Ablation Method
Y. Fujiwara (NIFS)
- 14:15 – 14:30 Development of Stable High QE CsK₂Sb Cathode
L. Guo (UVSOR)
- 14:30 – 14:45 Wavefront Observation of Vortex Radiation from Helical Undulator
M. Fujimoto (UVSOR)
- 14:45 – 15:00 Study on Polarization-variable Coherent THz Radiation Generation from Crossed Undulator
H. Saito (Tohoku Univ.)
- 15:00 – 15:10 Coffee break
- 15:10 – 15:20 Closing remarks of Young Reserchers Meeting
- 15:20 – 16:20 Facility tour

The 1st Research Meeting of Natural Vortex Photon Science

Date: May 26-27, 2017

Place: Okazaki Conference Center

May 26th (Fri.)

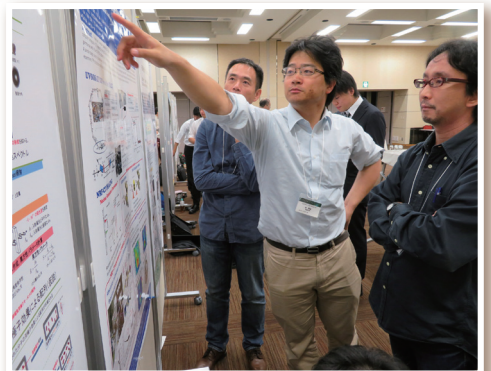
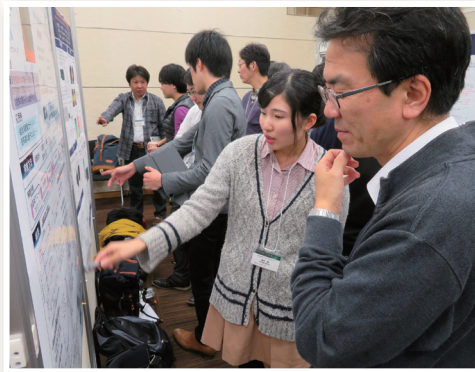
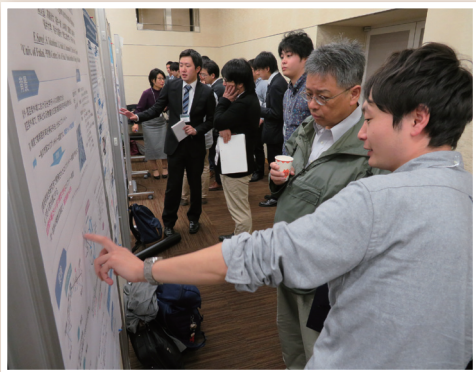
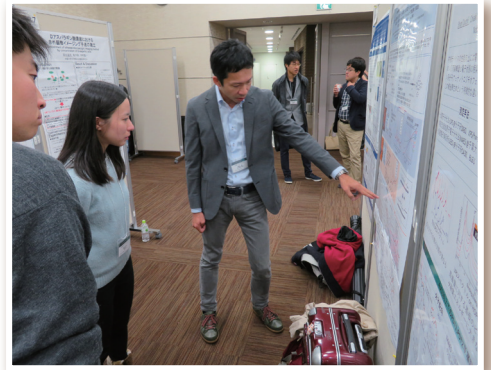
- 13:00 – 13:05 Opening Remarks
S. Tanaka (Osaka Pref. Univ.)
- 13:05 – 13:35 Outline of New Natural Science Project Developed by Optical Vortex,
Vortex Radiation Damping and Time Symmetry Violation
S. Tanaka (Osaka Pref. Univ.)
- 13:35 – 14:05 Theory of Spontaneous Emission by Complex Eigenvalue Problem
K. Kamiyoshi (Osaka Pref. University)
- 14:05 – 14:35 Vortex Photons from Electrons in Circular Motion
M. Katoh (UVSOR)
- 14:35 – 14:50 Coffee break
- 14:50 – 15:20 Calculation of Angular Momentum of Field Using Multipole Expansion of Radiation Field
from Relativistic Charged Particle
H. Kawaguchi (Muroran Institute of Technology)
- 15:20 – 15:50 Wavefront Geometry from Maxwell Equation
D. Tarama (Ritsumeikan Univ.)
- 15:50 – 16:20 Simulation of Optical Vortex Generated from Helical Undulator
M. Hosaka (Nagoya Univ.)
- 16:20 – 16:35 Coffee break
- 16:35 – 17:05 Verification of Vorticity of Cyclotron Radiation and Enhancement of Intensity
S. Kubo (NIFS)
- 17:00 – 17:35 Gamma-ray Vortex in Space Nuclear Physics
T. Hayakawa (QST)
- 17:35 – 18:05 Compton Scattering by Gamma-ray Vortex
T. Maruyama (Nihon Univ.)
- 18:05 – 18:35 Possibility and Problem of Nonlinear Compton Scattering Experiment at Kansai Photon
Science Institute of QST
M. Kando (QST)
- 19:00 – 21:00 Banquet

May 27th (Sat.)

- 9:00 – 9:30 Resonance Impurity State in Quantum Wire
H. Nakamura (NIFS)

9:30 – 10:00	Research on EUV Vortex Interaction with Atom and Molecule T. Kaneyasu (SAGA-LS)
10:00 – 10:30	Flow Measurement by Doppler Absorption Spectroscopy Using Vortex Laser S. Yoshimura (NIFS)
10:30 – 11:00	Frequency Shift of Lamb Dip in Saturated Absorption Spectroscopy and Measurement of Beam-crossing Gas Flow M. Aramaki (Nihon Univ.)
11:00 – 11:15	Coffee break
11:15 – 11:45	Generation and Measurement of Asymmetric Structure with Optical Vortex and Circular Polarization as Excitation Light Source M. Fujiki (NAIST)
11:45 – 12:15	Azimuthal Structure Formation of Polymer by Vortex Synchrotron Radiation Irradiation D. Tadokoro (Kyoto Univ.)
12:15 – 12:45	Study on Biomolecule Structure with Synchrotron Radiation Circular Dichroism Spectroscopy and Expectation for Optical Vortex Source K. Matsuo (HiSOR)
12:45 – 12:50	Closing remarks S. Kubo (NIFS)
13:00 – 14:00	Facility tour

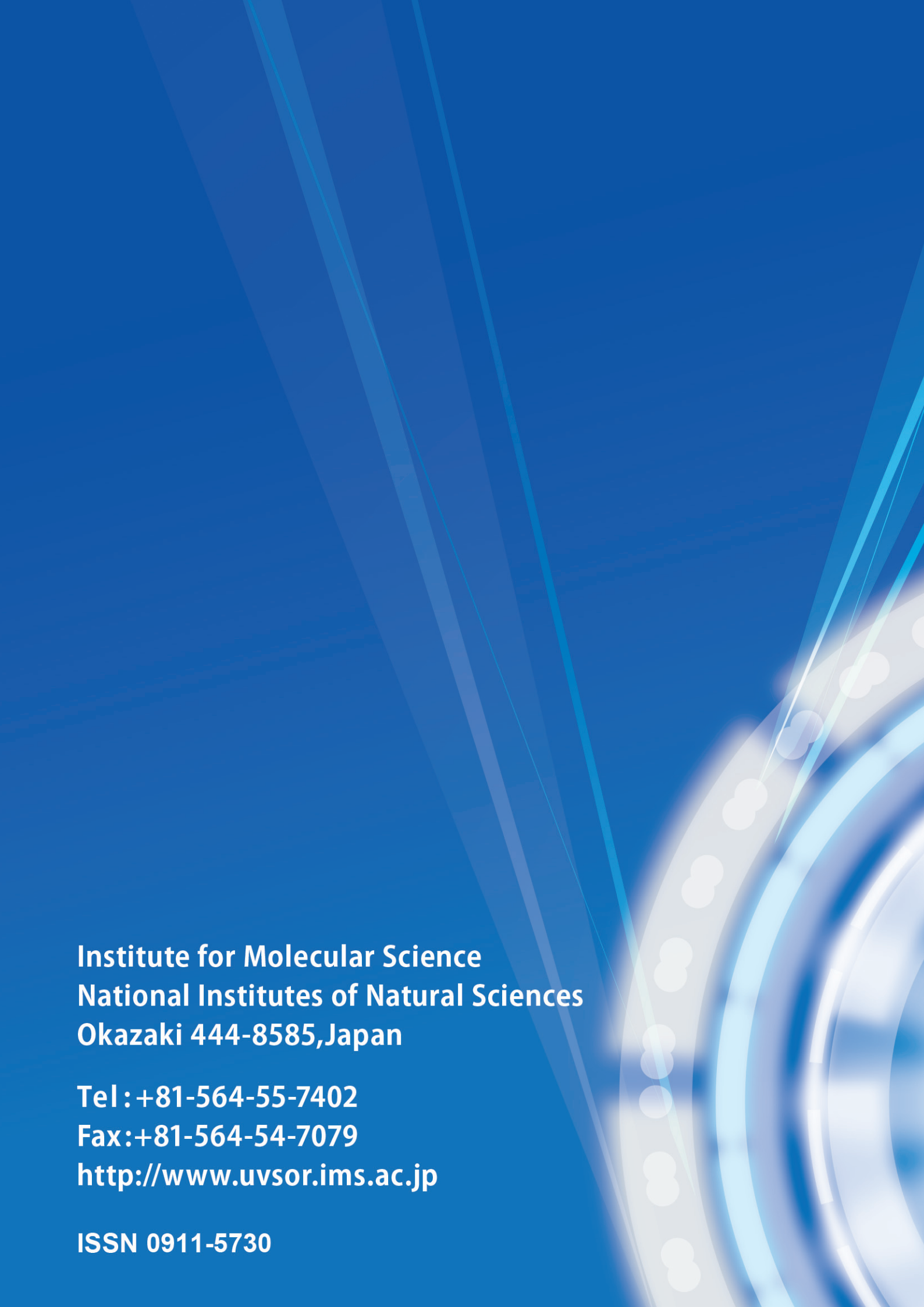
UVSOR Symposium 2017







Editorial Board : M. Fujimoto T. Ohigashi M. Sakai H. Hagiwara I. Inagaki



**Institute for Molecular Science
National Institutes of Natural Sciences
Okazaki 444-8585, Japan**

Tel: +81-564-55-7402

Fax: +81-564-54-7079

<http://www.uvsor.ims.ac.jp>

ISSN 0911-5730